Transactions of the ASME, Journal of Fluids Engineering (ISSN 0098-2202) is published monthly by The American Society of Mechanical Engineers, Three Park Avenue, New York, NY 10016. Periodicals postage paid at New York, NY and additional mailing offices.
POSTMASTER: Send address changes to Transactions of the ASME, Journal of Fluids Engineering, c/o THE AMERICAN SOCIETY OF MECHANICAL ENGINEERS, 22 Law Drive, Box 2300, Fairfield, NJ 07007-2300.
CHANGES OF ADDRESS must be received at Society headquarters seven weeks before they are to be effective. Please send old label and new address.

Journal of Fluids Engineering

Published Monthly by ASME

VOLUME 132 • NUMBER 2 • FEBRUARY 2010

RESEARCH PAPERS

Flows in Complex Systems

Fundamental Issues and Canonical Flows

Multiphase Flows

(Contents continued on inside back cover)

This journal is printed on acid-free paper, which exceeds the ANSI Z39.48-1992 specification for permanence of paper and library materials. ♾™
♻ 85% recycled content, including 10% post-consumer fibers.

Journal of Fluids Engineering **Volume 132, Number 2** **FEBRUARY 2010**

The ASME Journal of Fluids Engineering is abstracted and indexed in the following:

Applied Science & Technology Index, Chemical Abstracts, Chemical Engineering and Biotechnology Abstracts (Electronic equivalent of Process and Chemical Engineering), Civil Engineering Abstracts, Computer & Information Systems Abstracts, Corrosion Abstracts, Current Contents, Ei EncompassLit, Electronics & Communications Abstracts, Engineered Materials Abstracts, Engineering Index, Environmental Engineering Abstracts, Environmental Science and Pollution Management, Excerpta Medica, Fluidex, Index to Scientific Reviews, INSPEC, International Building Services Abstracts, Mechanical & Transportation Engineering Abstracts, Mechanical Engineering Abstracts, METADEX (The electronic equivalent of Metals Abstracts and Alloys Index), Petroleum Abstracts, Process and Chemical Engineering, Referativnyi Zhurnal, Science Citation Index, SciSearch (The electronic equivalent of Science Citation Index), Shock and Vibration Digest, Solid State and Superconductivity Abstracts, Theoretical Chemical Engineering

A Method to Generate Propulsor Side Forces

Stephen A. Huyer[1]
e-mail: stephen.huyer@navy.mil

Amanda Dropkin

James Dick

David Beal

Naval Undersea Warfare Center,
Code 8233,
Building 1302/2,
Newport, RI 02874

A computational study was performed to investigate a method to generate vehicle maneuvering forces from a propulsor alone. A ducted, preswirl propulsor was configured with an upstream stator row and downstream rotor. During normal operation, the upstream stator blades are all situated at the same pitch angle and preswirl the flow into the propulsor while generating a roll moment to counter the moment produced by the rotor. By varying the pitch angles of the stator blade about the circumference, it is possible to both generate a mean stator side force and subsequently vary the axial velocity and swirl that is ingested into the propulsor. The rotor then generates a side force in response to the inflow. Both potential flow and fully viscous 3D Reynolds averaged Navier–Stokes (RANS) computations were used to predict the stator forces, velocity field, and rotor response. Potential flow methods were used for initial examination of a wide variety of stator configurations. The most promising were then modeled using RANS. The RANS inflow was then computed and used as velocity boundary conditions during rotor blade design using potential flow methods. Blade parameters including blade number, rake, skew, and a combination of the two were varied to characterize their effects. RANS was used to then validate the final propulsor design. Computations demonstrated that total side force coefficients on the order of 0.1 and moment coefficients about the stator leading edge of 0.066 could be generated by the propulsor alone. This translates to an additional 50% control authority at 3 kn for current Navy 21″ unmanned undersea vehicles. [DOI: 10.1115/1.4000745]

Keywords: maneuvering, propulsor, hydrodynamics, experimental fluid dynamics, computational fluid dynamics

1 Introduction

Standard navy torpedoes and unmanned undersea vehicles (UUVs) utilize a single propulsor at the stern coupled with control surfaces to provide the vehicle with necessary forces and moments to offer control. At higher speeds, this combination generally is satisfactory in terms of offering sufficient control. At low speeds (with the extreme being zero forward velocity, e.g., Bollard condition), control surface effectiveness is significantly diminished. There are several operations where low speed control is vitally important for UUV mission requirements. These include UUV recovery, station keeping, and synthetic aperture sonar.

Side forces have been generated using thrust vectoring [1]. In this case, the thrust is redirected off axis to generate side forces for control. To meet low speed requirements, the midsized autonomous research vehicle (MARV) utilizes tunnel thrusters to offer lateral and vertical controls [2]. The difficulty is that this method is most effective for zero speeds. As the flow velocity is increased, tunnel thruster effectiveness is significantly diminished (20% effectiveness above 5 kn). The tunnel thrusters also increase the parasitic drag of the MARV so that maximum velocities are reduced. As tunnel thrusters also take up considerable volume that could otherwise be used for energy or payload, alternative methods of control are highly desirable. If the control can be offered by the propulsor alone, that is very attractive.

Another concept is referred to as the Haselton bow propulsor, which was first introduced in the 1960s by Haselton [3]. In this original concept, a pair of propellers, one at the bow and one at the stern, is used in tandem to provide vehicle control. Side forces are generated via cyclic pitch actuation similar to that used for helicopter rotors. The design utilizes a swashplate so that the angle of attack is varied over a single propeller rotation. For example, if maximum angle attack is reached at 0 deg and minimum at 180 deg, the higher thrust force at 0 and lower thrust force at 180 deg will generate a moment couple. By adding rake and skew to the propeller, it is then possible to generate a substantial side force component. The disadvantage is that the Haselton bow propulsor concept remains mechanically complex for implementation on undersea vehicles. In addition, placing a propulsor at the bow of the vehicle interferes with the forward look sonar that is used on most UUVs and torpedoes.

Geometrically, side forces can also be produced by altering the inflow velocity field into the propulsor. This technique effectively varies the inflow swirl circumferentially using a fixed but adjustable upstream stator row. The effective blade angle of attack is modified in three ways, as follows: (1) physical propeller pitch angles; (2) axial flow velocity; and (3) circumferential flow velocity. The proposed methodology offers an alternative way to generate side forces and moments that may be implemented for undersea vehicle maneuvering and control.

This article summarizes the computations used to evaluate a method to generate side forces utilizing the propulsor alone. The concept examines an upstream stator row with variable blade pitch around the circumference and a downstream rotor. Initial stator blade designs were evaluated using potential flow methods to provide estimates of the induced velocities and stator forces. Final designs were downselected and evaluated using a commercial Reynolds averaged Navier–Stokes (RANS) code, FLUENT®. The 3D viscous flow field was computed and used to provide velocity boundary conditions for a downstream rotor. The induced rotor forces were then computed using potential flow methods. Rotor design parameters included an investigation of blade number, rake, skew, and a combination of rake and skew. Steady and unsteady forces were computed for the rotor with final designs selected to maximize the rotor side forces. FLUENT® was then used

[1]Corresponding author.

Contributed by the Fluids Engineering Division of ASME for publication in the JOURNAL OF FLUIDS ENGINEERING. Manuscript received October 24, 2008; final manuscript received November 25, 2009; published online February 3, 2010. Assoc. Editor: Chunill Hah.

to fully evaluate the final rotor blade row designs.

2 Methodology

2.1 PUF/PBD Code. Initial calculations of the induced stator flow for a variety of pitch configurations as well as investigations regarding the rotor blade design were performed using potential flow methods. This approach utilized a modified version of the propulsor unsteady flow (PUF) code developed at the Massachusetts Institute of Technology (MIT) over the past three decades. The lifting surface theory approach utilizes a vortex lattice method to compute for the unsteady flow. Thin blade, inviscid flow with no separation is assumed and the vorticity on the propulsor blade and wake is discretized as a set of panels. For more details, refer to Refs. [4,5]. The author also has several references of application of this methodology [6–8]. A summary of the methodology is given below.

The blade geometry is generated from a table of blade coordinates, and then uniquely defined using B-spline surface meshes. B-splines allow the surface of the blade to be described by very few points. The blade surface may then be discretized so the spatial resolution is sufficient for an accurate computation of the flow. In the present calculations, typical blade resolution consists of 21 points in both chordwise and spanwise directions.

2.1.1 Lifting Surface Theory. The flow is assumed to be incompressible and inviscid, and the domain is assumed to be unbounded. The propulsor is assumed to consist of a set of thin blades at small angles of attack so separated flow effects may be neglected. These assumptions allow for the vorticity to be confined to the surface and the wake with the remainder of the flow assumed irrotational. These assumptions allow for the use of potential flow theory. The potential flow problem satisfies Laplace's equation

$$\nabla^2\varphi = 0 \tag{1}$$

where φ is the velocity potential and the perturbation velocity due to the potential flow is defined as

$$\mathbf{v}_p = \nabla\varphi \tag{2}$$

In the present formulation, the contribution to the velocity potential is from the surface only. For a point $\mathbf{x}$, source point $\boldsymbol{\xi}$, surface S, and surface normal $\mathbf{n}$, this is defined as

$$-2\pi\varphi(\vec{\mathbf{x}}) = \int_S\int \frac{1}{|\vec{\mathbf{x}}-\vec{\boldsymbol{\xi}}|}\vec{\mathbf{n}}(\vec{\boldsymbol{\xi}})\nabla_{\xi}\varphi(\vec{\boldsymbol{\xi}}) - \varphi(\vec{\boldsymbol{\xi}})\vec{\mathbf{n}}(\vec{\boldsymbol{\xi}})\nabla_{\xi}\frac{1}{|\vec{\mathbf{x}}-\vec{\boldsymbol{\xi}}|}dS \tag{3}$$

Taking the gradient of Eq. (3) with respect to $\mathbf{x}$ yields the perturbation velocity. Assuming that the surface is infinitely thin, the upper and lower surfaces of the blade coincide so the governing set of equations becomes

$$\int_{S_B}\int \mu(\boldsymbol{\xi})\mathbf{n}(\mathbf{x})\left[\nabla_x\left(\mathbf{n}(\boldsymbol{\xi})\nabla_{\xi}\frac{1}{|\mathbf{x}-\boldsymbol{\xi}|}\right)\right]dS_B = \int_{S_W}\int \mu_W(\boldsymbol{\xi})\mathbf{n}(\mathbf{x}) \times\left[\nabla_x\left(\mathbf{n}(\boldsymbol{\xi})\nabla_{\xi}\frac{1}{|\mathbf{x}-\boldsymbol{\xi}|}\right)\right]dS_W - 2\pi\mathbf{n}(\mathbf{x})\mathbf{u}_{\text{in}}(\mathbf{x}) \tag{4}$$

Here, $\mu(\boldsymbol{\xi})$ is defined as the potential jump across the surface and $\mu_w(\boldsymbol{\xi})$ is the potential jump in the wake, the subscripts B and W refer to the blade and wake, respectively, and $\mathbf{u}_{\text{in}}$ is the inflow velocity. To numerically describe the flow, the blade surface is discretized as using sources (to account for thickness effects) and a distribution of vorticity on the camber surface and wake. Equation (4) forms a matrix set of equations, and the normal velocity (no-flux) boundary conditions are enforced and $\mu(\vec{\boldsymbol{\xi}})$ is solved at each time step.

The Kutta condition requires the velocity at the trailing edge to be finite. To satisfy this, an implicit Kutta condition is imposed where control points are placed at the trailing edge and the boundary condition $\mathbf{n}(\mathbf{x})\mathbf{u}_{\text{in}}(\mathbf{x})$ is satisfied. Also, the dynamic boundary condition states that there is no pressure jump across the trailing vortex wake. This is satisfied by requiring that the vortex sheets be advected by the local flow velocity. These vortex sheets formed at the trailing edge of the blade lattice are advected using the circumferentially averaged inflow velocity field, thus forming the wake structure. The wake is modeled with a distance of 2.5 radii downstream of the blade trailing edge and is used to account for the wake induced velocities on the blade. The far wake structure is modeled as a single helical vortex structure, defined as the ultimate wake.

The code computes for the blade forces based on the effects of surface pressure force, viscous force, leading edge suction forces, and unsteady force. The viscous forces account for skin friction due to finite viscosity, and the leading edge suction forces are required due to the assumption of zero blade thickness. Viscous forces are computed via a user supplied empirical drag coefficient for the blade. The pressure force is obtained from Joukowski's law for individual panels and then integrated over the entire blade surface. This force may be expressed as

$$d\mathbf{F}_J = \rho dA(\mathbf{V}\times(\mathbf{n}\times\boldsymbol{\nabla}_s\mu)) \tag{5}$$

Here, $\mathbf{V}$ is the total velocity at the panel control points, ρ is the density, dA is the panel area and $\mathbf{n}$ is the panel unit normal. The gradient of the potential jump along the surface governs the blade force.

The unsteady velocity potential contribution to the force is given by the derivative of the velocity potential. Since the source contribution is steady, the only contribution to the potential is from the vortices. Since the blade forces are computed after the solution has converged, the code uses a central five-point differentiation formula to numerically solve for the unsteady potential contribution.

In order to account for the effect of the body and the duct on the blade forces, image vortices modeling the body and duct walls are used. The number of vortices used is 1/3rd the number of spanwise points used along the chord. For example, if 21 spanwise points are used, then a layer of 7 image vortices are used to model the effect of the hub and duct. This models the effect of the surface, but the overall effect of the body and duct is already included in the velocity inflow file used to establish the velocity boundary conditions on the blade.

The PUF code capability was extended to accept a fully unsteady turbulent inflow. In this manner, inflows that evolve in space and time can be input into the force prediction code to better simulate the unsteady forces and radiated noise. Details of the modification are found in Refs. [6,9]. Two separate potential flow codes were used in this study. The first, the propeller blade design code (PBD 14.3) was used to design the rotor blades. This code requires a circumferentially averaged 2D inflow with swirl to provide the velocity boundary conditions necessary for the blade calculations. The user prescribes a spanwise circulation distribution to provide the design thrust. The blade shape is then adjusted to minimize the normal velocity component. PBD 14.3 was used to design the downstream rotor blade shapes. The second is the modified form of the PUF code (MPUF). MPUF requires the full 3D inflow velocity field to provide the velocity boundary conditions on the blade row. MPUF was used to provide initial estimations of the induced velocity fields and blade forces produced by the upstream stator row as well as to fully evaluate the unsteady forces produced by the downstream rotor designs.

2.2 RANS Solver (FLUENT®). The commercial code FLUENT® was used as the RANS solver [10]. There is an extensive library of references regarding RANS development and implementation that will not be repeated here. Specific solver settings and grid resolution will be summarized. A steady 3D implicit flow solver was used to compute for the flow for the upstream stator row. The solution methodology utilizes a finite volume formulation with a

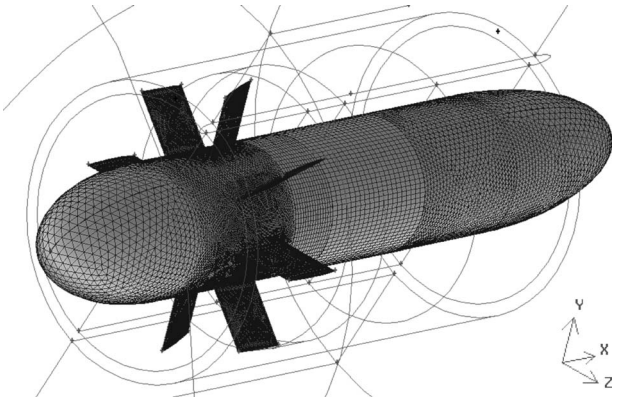

Fig. 1 FLUENT surface mesh depicting the body and stator geometries

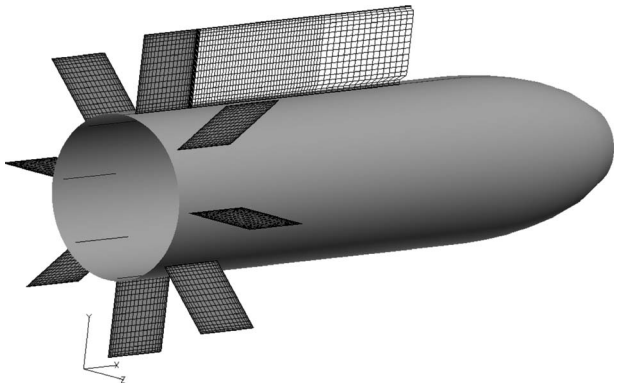

Fig. 2 Vortex lattice of the stator blade row and wake on the first blade with the main body (not including the nose region)

mixture of tetrahedral and brick elements as defined by the grid generator, GAMBIT®. These computations employed a realizable k-ε turbulence model with boundary layer resolution on both the afterbody and duct to $y+=1$. Wall functions were used to define the boundary layer on the stator blades. Second order upwind solutions of the advection term and turbulent kinetic energy were used. A standard semi-implicit method for pressure linked equations (SIMPLE) algorithm was used to solve for the pressure-velocity coupling term.

A full 3D solution incorporating every blade in the stator and rotor blade rows was necessary due to the fact that each stator blade is at a different angle of attack, resulting in a circumferential variation in the flow into the rotor. This was very computationally intensive so only select cases were run. An example of the surface mesh used in the solution is shown in Fig. 1. The surfaces were defined using a mix of triangular and quadrilateral elements.

3 Results

Nondimensional quantities are used throughout this study with length and velocity scales relative to the maximum blade radius and freestream velocity, respectively.

3.1 Stator Row Design. A relatively simple symmetrical stator blade was designed with zero rake and skew distribution and constant chord. The stator blades have a maximum radius of 1.0 at the tip, a minimum radius of 0.5 at the root, and a chord length of 0.5. Standard blade design practices also place the maximum thickness at the midchord point. For these computational studies, a NACA 66 series symmetrical airfoil section with 5% thickness was used. The stator blade airfoil sections were chosen to be symmetrical due to positive and negative pitch angles. Due to the symmetry condition, PBD 14.3 was not needed to optimize the stator blade shape. The blade pitch angles vary in sinusoidal fashion around the circumference. Mathematically, the angle of attack variation can be expressed as

$$\alpha_{\text{blade}} = \alpha_{\text{mean}} + A \sin \theta \tag{6}$$

For these studies, a mean swirl velocity of 0.0 was the design point. Consequently, the mean angle of attack of the stator blades was 0.0 with a variation in the angle of attack about the circumference determined by the pitch amplitude parameter A in Eq. (6). The number of blades in the blade row was also examined as an independent variable.

The body and duct were also designed for this problem. In this case, the axisymmetric version of FLUENT® was used. The maximum body radius was 0.5 (nondimensionalized by propeller radius) with a spherical leading edge and an ellipsoidal afterbody sufficient to eliminate flow separation. The inner portion of the duct was located at a radius of 1.0 and had a nondimensional thickness of 0.1. A spherical leading edge and ellipsoid trailing edge sufficiently long to eliminate separation were incorporated. FLUENT® flow computations for this configuration at a Reynolds number of 1×10^6 confirmed no flow separation for the afterbody section or duct trailing edge. The stator blade row was also placed two body radii downstream of the nose so that effects due to flow acceleration around the nose were minimal. The duct area was sufficiently long to accommodate both the stator row as well as the downstream rotor, with a total length of 2.5 (normalized by the blade radius). The stator blade row leading edge is located 0.6 blade radii downstream of the duct leading edge. The body geometry can be seen in Fig. 1. It should be noted that the calculations assumed that there was no gap between the stator blade tip and the duct.

3.2 MPUF Stator Flow Computations. The vortex lattice of the stator blade row, wake from the base blade, and the main body are shown in Fig. 2. The 2D axisymmetric version of FLUENT® was used to compute the stator inflow and account for the effects of both the body and the duct. The nominal inflow was assumed to be swirl-free and was then rotated through the full 360 deg circumference in 2 deg increments to create the required 3D inflow. Blade row numbers of 8 and 12 blades were examined. The pitch amplitude A (Eq. (1)) was varied between 0 deg and 30 deg, and calculations were performed to approximate the potential amount of swirl that could be produced. Circumferential velocity profiles were then plotted in the wake a distance of 0.25 stator blade radii (R_{stator}) downstream of the stator trailing edge. The steady-state force produced by the stator row was also computed. Figure 3 shows the circumferential velocity distributions for an eight bladed stator row with 30 deg pitch amplitude at spanwise locations from the near root ($r/R_{\text{stator}}=0.59$) station toward the tip

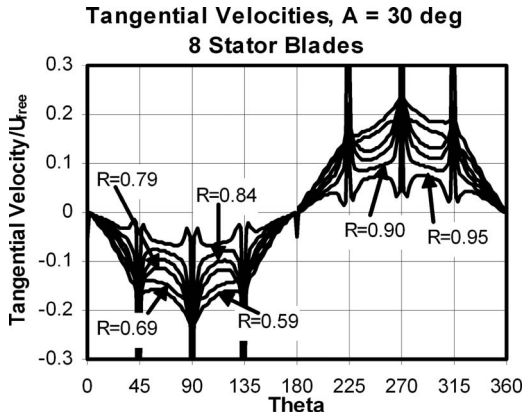

Fig. 3 Tangential velocity distributions normalized by the freestream velocity at span locations from 0.58 to 0.94

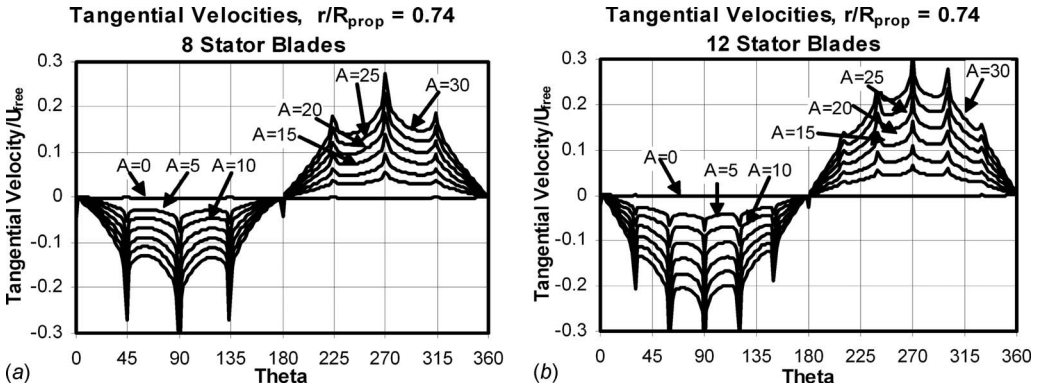

Fig. 4 Tangential velocity distributions normalized by the freestream velocity for eight- and 12-blade stator rows for a range of pitch amplitudes *A*

$(r/R_{\text{stator}}=0.95)$. As can be seen, the MPUF code predicts the largest circumferential velocities at the root diminishing outward toward the tip. Typical midspan velocities appear to diminish by approximately 20% compared with the root velocities. Near the tip, the velocities are on the order of half the root velocities. An artifact of the induced velocities is the spike in velocity proximal to the blade wakes. This is due to the nature of the infinitely thin vortex sheet in the wake and is not physically realistic. The actual wake boundary layer vorticity shed from the stator blades is confined in a finitely thick region, whose thickness is dependent on the flow Reynolds number. For this reason, FLUENT® is used to compute the rotor inflow for specific test cases. MPUF is useful as a first approximation to the magnitude of swirl and stator blade row forces.

The effect of pitch amplitude A was examined for the eight- and 12-blade stator rows at a span location of 0.74 (Fig. 4). As expected, the circumferential velocities increase with A with maximum velocities varying between 0.05 for $A=6$ deg to approximately 0.2 for $A=30$ deg (eight-blade stator row). Velocities are increased on the order of 15% for the 12-blade stator row. The wake signature can also clearly be seen in the plots.

3.3 FLUENT Computations. FLUENT® is a commercial RANS solver that incorporates viscosity and turbulence into the solution, and is therefore more representative of the flow physics. Unlike the potential flow method described above, no assumptions are made regarding viscosity, flow separation, confinement of vorticity, or blade thickness. For these computations, the only assumption is that the flow is steady in time. A grid convergence study was performed to establish grid independence in the solution and to lend confidence to the flow predictions. Drag coefficient of the entire model with the 12-blade stator row at $A=10$ deg was used as an indicator, and results are plotted in Fig. 5. The grid was refined in the inner duct region and grid independence appears established with 3.93×10^6 cells. This grid resolution was used for all subsequent calculations.

Figure 6 shows the axial flow velocity component at $x/R_{\text{rotor}}=0.75$, corresponding to a distance of 0.25 (or $\frac{1}{2}$ stator chordlength) downstream of the stator trailing edge for the eight-blade stator row. The velocity distributions are in the y-z plane and are colored based on the scale to the left with flow velocities ranging between 0 (blue) and 125% freestream (red). The flow for the 10 deg pitch amplitude is shown on the left and 20 deg on the right. In both cases, the axial flow is higher on the left side of the disk compared with the right, which is due to the downwash produced by the lifting stator blade row. The stator wakes can also be seen as indicated by the velocity defect. For $A=20$ deg, however, there are reverse flow velocities in the stator wakes at 12:00 and 6:00 indicating flow separation. This could not be predicted using MPUF due to the potential flow assumptions. This demonstrates that the 20 deg case is too extreme a pitch angle as flow separation must be avoided.

Figure 7 plots the circumferential velocity distributions for the same conditions as in Fig. 6. It is immediately clear that the velocities are higher for $A=20$ deg compared with 10 deg. In both cases, the maximum and minimum velocities are biased to the left side of the disk due to the geometry of the stator blades and induced flow. What is interesting is that there does not appear to be a significant stator wake signature as was seen for the MPUF computations. The wake signature appears only in the axial velocity distributions. This is due to the fact that the vorticity is no longer confined to an infinitely thin sheet.

Based on these initial runs, additional test cases were computed using FLUENT® for 12-blade stator rows for $A=20$ deg and 15 deg. Significant flow separation was still seen for $A=20$ deg, but appeared minimal for $A=15$ deg. This suggests that $A=15$ deg is the limiting condition for this configuration. Figure 8 plots the

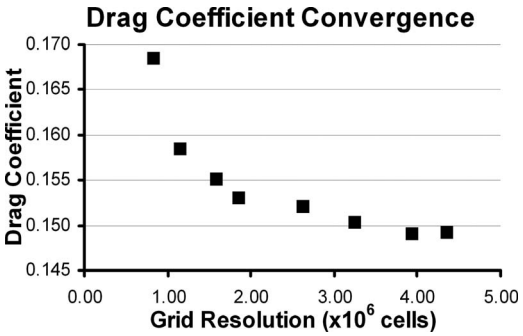

Fig. 5 Drag coefficient convergence with increased grid resolution

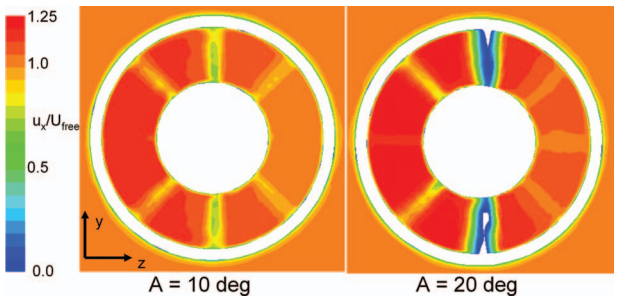

Fig. 6 FLUENT® calculations highlighting the axial velocity distributions (normalized by the freestream velocity) in the rotor inflow plane ($x/R_{\text{rotor}}=0.75$) due to the eight-blade stator row

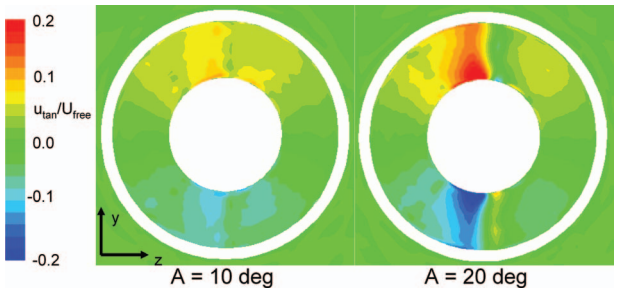

Fig. 7 FLUENT® calculations highlighting the tangential velocity distributions (normalized by the freestream velocity) in the rotor inflow plane ($x/R_{rotor}=0.75$) due to the eight-blade stator row

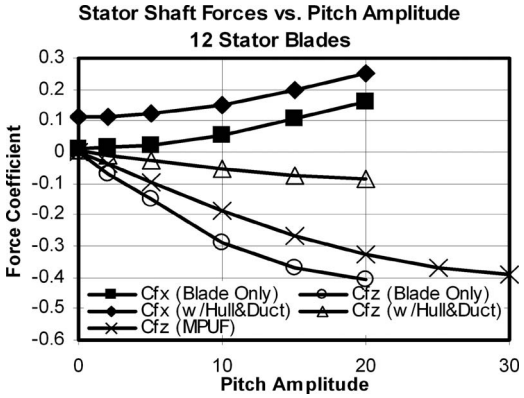

Fig. 9 FLUENT® predictions of the mean propulsor force coefficients produced by the stator blade row with hull and duct influences. MPUF calculations shown for comparison are for the blades only.

axial and circumferential velocity distributions. As can be seen, the circumferential velocities approach ±20% freestream values. For the 12-blade case, the wake signatures can more clearly be seen. This is due to the downwash produced by the individual blades and is made more evenly distributed with the 12-blade configuration. The axial velocities are increased on the left side of the disk, indicating that the blade loading and the velocity defects in the wake can clearly be seen.

The stator side force coefficients are plotted in Fig. 9 for both FLUENT® and MPUF runs. Force coefficient is defined as $C_f = F/(1/2\rho V^2 \pi R_{prop}^2)$. Due to the stator configuration, the y-forces are zero with finite x- (drag) and z-forces. The plots show, that for the blade alone, the z-forces are on the order of four times larger for RANS compared with MPUF. Upon inclusion of the reactionary forces from the hull and duct, however, the sum of the side forces due to the stator drop from −0.4 to −0.072.

3.4 Unsteady Rotor Forces. PBD 14.3 was used to optimize the rotor blade sections for a variety of rake, skew, and blade number configurations. The rotors are shown in Fig. 10. Geometrically, the rotor leading edge was situated 0.25 rotor radii ($R_{rotor}=R_{stator}$) downstream of the stator trailing edge ($\frac{1}{2}$ stator chord). The rotor blade chord length $C_{blade}/R_{rotor}=0.5$ was kept constant over the span and for all blade configurations. Where indicated, the total rake ($c_{x\,total}/R_{rotor}$, where $c_{x\,total}$ is the blade displacement in the x-direction) has a spanwise distribution computed as

$$c_x = c_{x\,total} \sin((\pi/2)(r - r_o)/(R_{rotor} - r_o)) \quad (7)$$

Here, c_x is evaluated from the root radius r_o to the maximum rotor radius. The skew distribution selected had a tangential variation in the leading edge of the rotor, which can be described by

$$\theta_{skew} = \theta_{sk\,total} 0.5[1.0 - \cos(\pi(r - r_o)/(R_{rotor} - r_o))] \quad (8)$$

Similar to the rake, the skew angle is evaluated from the root radius to the maximum rotor radius. As was the case of the stator, the computations assume that there is no gap between the rotor tip and the duct.

The axisymmetric version of FLUENT® was used to compute for the required 2D velocity boundary conditions downstream of the stator blade row. In this case, the design point was for zero stator blade angle of attack, making the flow computations straightforward with zero swirl. The blade circulations were prescribed to be zero, thus establishing a zero thrust condition as the design point. This was chosen in order to minimize the coupling of the rotor on the flow field produced by the stator and to better satisfy the frozen wake assumptions used in these calculations. As the purpose of this study was to investigate propulsor side force generation, these limitations were deemed acceptable.

After the various blade shapes were established, MPUF was used to compute the fully unsteady blade forces due to the upstream stator blade row. The full 3D FLUENT® stator calculations

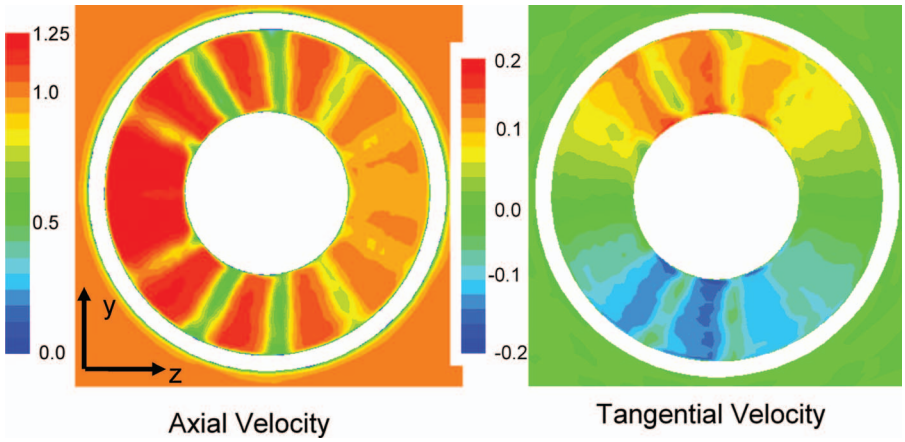

Fig. 8 FLUENT® calculations highlighting the axial and tangential velocity distributions (normalized by the freestream velocity) in the rotor inflow plane ($x/R_{rotor}=0.75$) due to the 12-blade stator row for $A=15$ deg

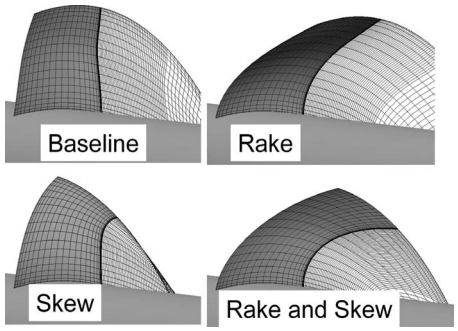

Fig. 10 Baseline, rake, skew, and rake and skew rotor geometries

were used to provide the necessary unsteady inflow velocity boundary conditions on the downstream rotor blade row. While the velocity field is steady in time, unsteady forces are produced on the downstream rotor as the individual blades rotate through the circumferentially varying upstream wakes. The unsteady side force coefficients are presented in Fig. 11 to demonstrate the effect of inflow on a nine-bladed rotor with 30 deg skew $0.4*R_{\text{rotor}}$ total rake. In all cases, unsteady forces are seen due to the difference between the individual blade wakes. The frequency identically matches the blade number giving rise to what is referred to as the blade rate effect. This effect appears largest for the $A=15$ deg and decreases with decreasing pitch amplitude. In all cases, the z-force is in a direction opposite to that produced by the stator.

Rotor blade parameters were examined for the $A=15$ deg case. This case was chosen so that the blade shape parameters could be

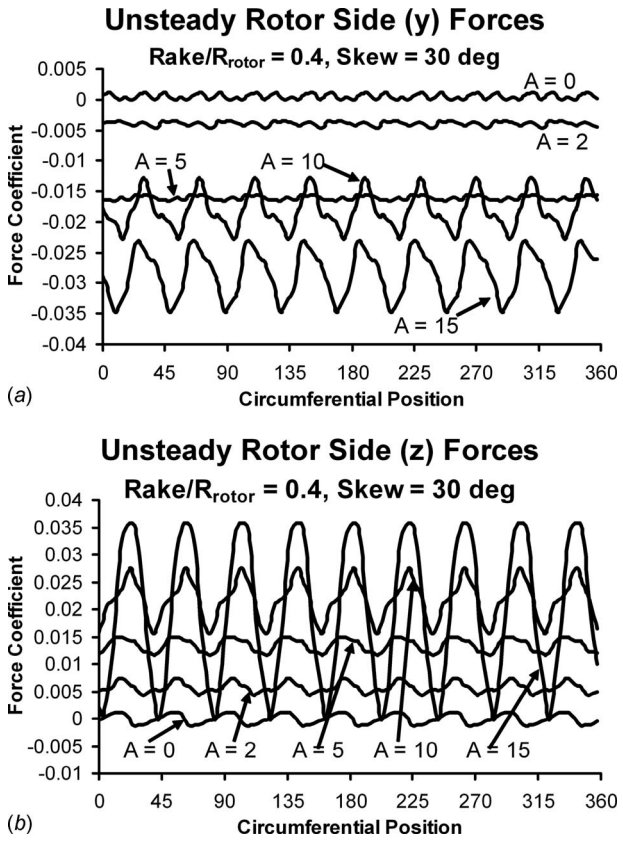

Fig. 11 Unsteady side force coefficients for varying stator pitch amplitudes *A*. Forces are for the Rake/R_{rotor}=0.4, 30 deg skew, nine-blade rotor configuration

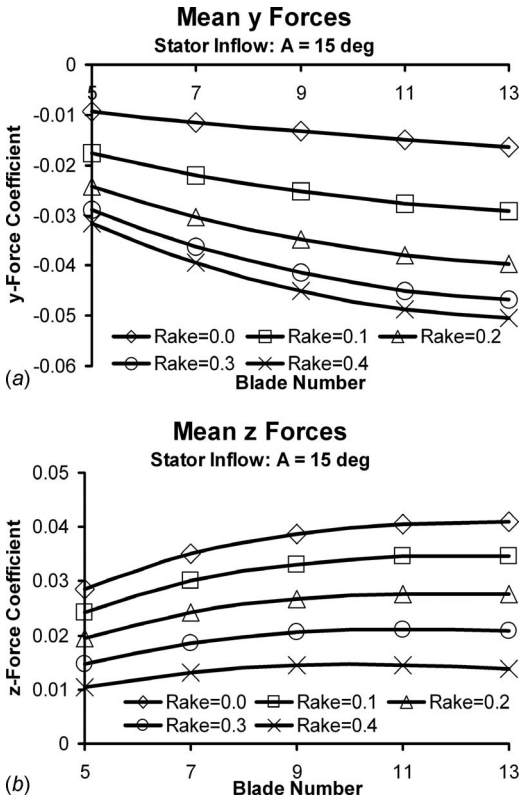

Fig. 12 Mean *y*- and *z*-force coefficients as a function of the blade number for the range of rakes examined

selected to minimize the large unsteady forces produced. The effect of rake, skew, and combination of the two were examined for a range of blade numbers from 5 to 13. In addition, only odd rotor blade numbers were examined as even blade numbers resulted in a substantial increase in unsteady forces, likely resulting from phase interaction between the stator wakes (12) and the even rotor blade number. Mean y- and z-force values are plotted in Fig. 12 for blade numbers of 5–13 for a range of rake values from 0.1 to 0.4 relative to the rotor radius (Rake=$c_{x\ \text{total}}/R_{\text{rotor}}$). Overall, an increase in the blade number results in increased force magnitudes. This appears as an asymptotic increase reaching a limit at a blade number of 13. An increase in rake increases the negative y-force component and decreases the positive z-force component.

Figure 13 plots the mean y- and z-force coefficients for blade skew angles from 0 to 40 deg in 10 deg increments. As expected, an increase in the blade number increases both the y- and z-force magnitudes appearing as an asymptotic limit at 13 blades. As the blade skew angle increases, the y-forces increase and the direction of the force changes from negative to positive. Increased skew has negligible effect on the z-forces.

Figure 14 plots the mean y- and z-force coefficients for a constant skew of 30 deg and rakes ranging from 0.0 to $0.4*R_{\text{rotor}}$ in increments of 0.1. Again, increases in the blade number show an asymptotic increase in the force magnitude at a blade number of 13. Force magnitude appears to increase linearly with increased blade number. An increase in rake increases the y-force magnitude (increased force in the negative y-direction) but decreases the mean z-forces. Based on the MPUF runs, the maximum rotor forces are for the 30 deg skew and 0.4 rake propulsor. Here, the z-forces are in the opposite direction as the stator forces (0.02) and the y-forces are −0.024 (9–blade rotor). The magnitude of the resultant force vector is then 0.053.

Figure 15 plots the rms force magnitude coefficients $(=\sqrt{F_x'^2+F_y'^2+F_z'^2})$ for the range of blade skew angles (zero rake)

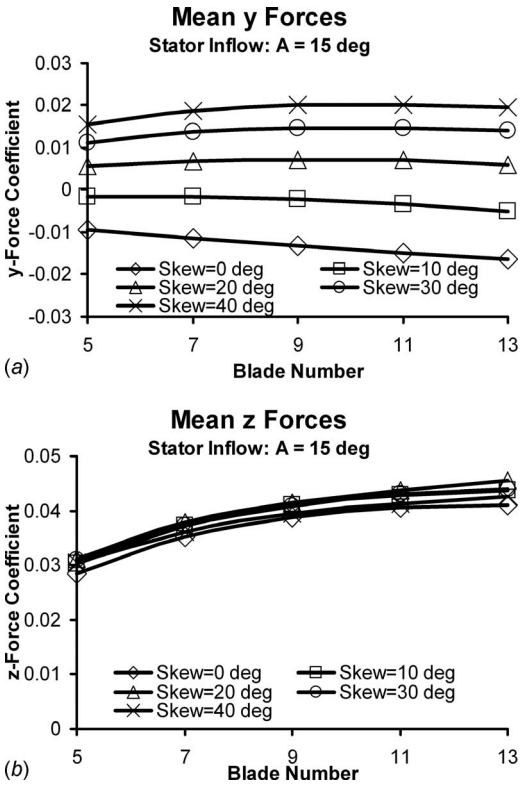

Fig. 13 Mean *y*- and *z*-force coefficients as a function of the blade number for the range of skews examined

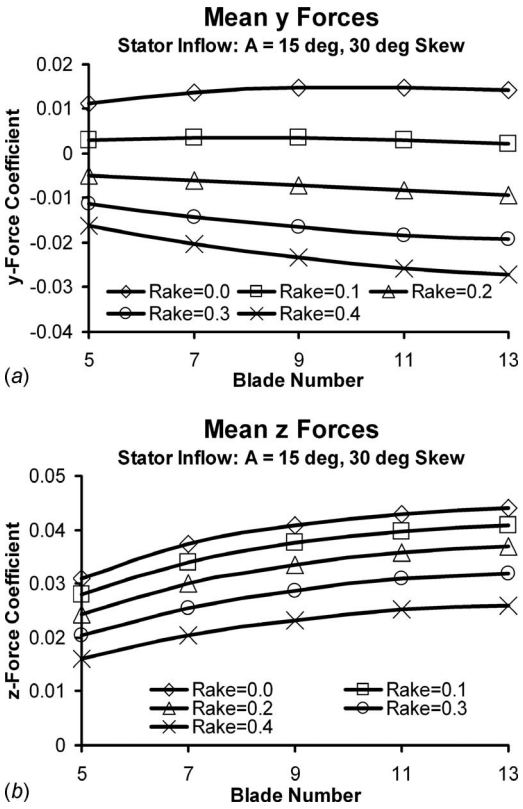

Fig. 14 Mean *y*- and *z*-force coefficients as a function of the blade number for a constant skew of 30 deg for rake values of 0.1, 0.2, 0.3, and 0.4

and for a range of rakes at a skew angle of 30 deg. As can be seen, the base blade (no rake or skew) resulted in significant unsteadiness, with peak values of 0.14 seen for 11 blades and minimum values of 0.027 for seven blades. As the skew angle was increased, the rms force magnitude coefficients were significantly decreased so that for a 30 deg skew, unsteady values of 0.03 were seen for nine and 13 blades. An increase in rake for a 30 deg skew also decreases the rms forces up to $c_{x\ \mathrm{total}}/R_{\mathrm{rotor}}=0.3$ after which the unsteadiness appears unaffected. The unsteadiness for nine and 11 blades was on the order of 0.02.

The desired rotor blade row would minimize the positive z-forces (since they oppose the negative z-forces produced by the stator), maximize the y-force magnitude, and minimize the unsteadiness. Based on these criteria, the nine-blade rotor with 30 deg skew and $0.4*R_{\mathrm{rotor}}$ rake demonstrated the optimum balance to maximize the mean forces and minimize the rms forces.

While MPUF is very useful in determining the optimal blade shapes and configurations as well as estimated unsteadiness, there are limitations in terms of fully quantifying the mean forces. These arise from the potential flow assumptions as well as the fact that MPUF was developed to examine propeller unsteady forces with minimal cross-flow effects. Since the rotor wakes are advected using a circumferentially averaged inflow, they cannot account for the strong cross-flow produced by the upstream stator row when it acts as a lifting surface. In addition, MPUF was not set up to predict the steady or unsteady hull and duct forces (although their influence on blade forces was modeled). Accordingly, FLUENT® was used to compute the quasi-steady forces for the 30 deg skew, $0.4*R_{\mathrm{rotor}}$ rake, nine-blade rotor case in order to get a more precise prediction of the steady forces. The numerical setup was similar to the FLUENT® computations for the upstream stator. The rotor blades were generated using an NACA 66-series airfoil section with 5% thickness. The hull and duct boundary layers were resolved to $y+=1.0$ and wall functions used for the rotor blades. To decrease the computational size of the problem, the FLUENT® solution for the $A=15$ deg stator case was used as inflow boundary conditions to the rotor problem. Velocities, turbulent kinetic energy (k) and dissipation (ε) were output from the stator solution on a plane immediately downstream of the stator blade row. The grid section defining the rotor was treated as a moving reference frame to simulate the blade rotation. The steady-state solution then effectively solved for the rotor, hull, and duct forces as though the rotor were frozen in time. Steady-state solutions were formed at rotor azimuthal positions of 0 deg, 5 deg, 10 deg, 15 deg, 20 deg, 25 deg, and 30 deg to simulate the variation in force as the rotor rotates. These computations were uncoupled with the stator flow (e.g., no propulsor force model was implemented into the stator flow solution).

The average stator and rotor force coefficients as computed using FLUENT® were constructed and the results were compared with the MPUF solutions in Table 1. The averages presented show the forces due to the blades alone as MPUF cannot model the hull and duct forces. Moment coefficients are defined as $C_m=M/(1/2\rho V^2\pi R_{\mathrm{prop}}^3)$. The moments were computed about the stator leading edge. As expected, the y-force coefficients generated by the stator blades are near zero with negative z-force coefficients produced. The MPUF solutions for the blade are approximately 30% less compared with the FLUENT® solution. Accordingly, the stator y-moments are less as well. Significant y-force coefficients were generated by the rotor blade in both cases with MPUF solutions slightly higher. The z-forces are significantly less for the MPUF solution. These comparisons reflect the limitations of the MPUF code in computing this complex problem stated above.

Table 2 summarizes the steady rotor and stator forces for the uncoupled solution. The stator, hull, and duct forces were computed on the upstream sections only and do not include the hull and duct sections used in the rotor computations. This way, the separate forces were isolated to provide a better indication of the

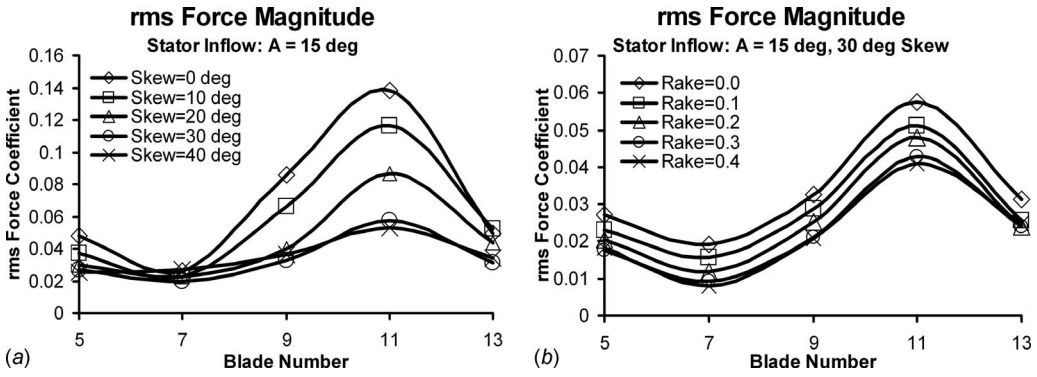

Fig. 15 Rms force magnitude coefficients as a function of blade number examining the effect of skew (zero rake, (*a*)) and rake (30 deg skew, (*b*))

total forces. As can be seen, the stators produced a force coefficient on the order of −0.371 exclusively in the *z*-direction. This resulted in a *y*-moment coefficient of 0.0349. The flow generated by the stator generates a responsive force by the hull and duct. After these effects were included, the *z*-force coefficients were diminished to −0.123, and the *y*-moment coefficient reduced to a value of 0.0166. As can be seen, the opposing hull/duct forces are significant.

Due to the rake and skew distribution, the rotor responds with forces in both the *y*- and *z*-directions with corresponding moments. There is a substantial effect due to the hull and duct that increase the *y*-force coefficient from −0.0195 (blades only) to 0.1036 for the total response. The *z*-forces act in a direction opposite to that generated by the stator. Still, the sum forces are substantial so that the magnitude of the force coefficient vector is 0.1091 and the moment vector is 0.0649. To put this number in perspective, this translates to force of 6.5 lbs (28.9 N) and moment about the stator leading edge of 12.9 ft lbs (17.5 N-m) for a 21″ (0.5334 m) vehicle traveling at 3 kn (1.54 m/s). To provide more perspective, maximum control surface forces for this same vehicle are on the order of 12 lbs (53.4 N). These values are approximately 50% of the maximum side forces produced by a UUV in a X-tail configuration.

As previously stated, the rotor was designed to produce zero thrust to minimize the coupling of the rotor on the stator flow. This assumption is only fully valid for minimal stator pitch amplitudes. As pitch amplitude is increased, significant drag is produced by the upstream stator row, which decelerates the axial velocity component. This velocity drop alters the rotor inflow so that the rotor will now produce thrust. As can be seen in Table 2, the stator *x*-force coefficient is 0.1055 for the blades alone ($A = 15$ deg) and is −0.1669 (thrust) for the rotor. When this occurs, the stator inflow velocity is increased, which further alters the stator wake velocities, which further influences the rotor response. Accordingly, a coupled flow situation is established, which was further investigated. To model this flow condition, the stator flow was computed with a momentum source distribution in the fluid

Table 1 Comparison of average stator and rotor forces

	Cfy	Cfz	Cmy	Cmz
Stator:				
Blades only, FLUENT®	−0.0001	−0.3710	0.0349	0.0000
Blades only, MPUF	−0.0003	−0.2673	0.0211	−0.0032
Rotor:				
Blade only, FLUENT®	−0.0195	0.0708	−0.0859	−0.0900
Blade only, MPUF	−0.0233	0.0232	−0.0089	−0.0567

Table 2 FLUENT® average stator and rotor forces (uncoupled solution)

	Cfx	Cfy	Cfz	Cmx	Cmy	Cmz
Stator:						
Blades only	0.1055	−0.0001	−0.3710	0.0007	0.0349	0.0000
With hull and duct (fore section)	0.1460	0.0005	−0.1230	0.0007	0.0166	−0.0004
Rotor:						
Blades only	−0.1669	−0.0195	0.0708	−0.1064	−0.0859	−0.0900
With hull and duct (aft section)	−0.0952	0.1036	0.0902	−0.1350	−0.0763	0.0257
Total	0.0508	0.1040	−0.0328	−0.1343	−0.0598	0.0253

Table 3 FLUENT® average stator and rotor forces (coupled solution)

	Cfx	Cfy	Cfz	Cmx	Cmy	Cmz
Stator:						
Blades only	0.1134	−0.0043	−0.4001	0.0021	0.0373	−0.0003
With hull and duct (fore section)	0.1542	0.0018	−0.1412	0.0021	0.0250	0.0001
Rotor:						
Blades only	−0.0686	−0.0248	0.0729	−0.0586	−0.0816	−0.1031
With hull and duct (aft section)	−0.0013	0.0950	0.0977	−0.0883	−0.0776	0.0012
Total	0.1529	0.0968	−0.0435	−0.0862	−0.0526	0.0013

volume occupied by the rotor. Force densities were computed based on the individual rotor blade forces and total rotor volume. The stator inflow was then computed and the stator wake velocities output to establish inflow boundary conditions to the rotor. An iterative process continued until the rotor and stator forces converged to within 1%.

The results are presented in Table 3. As can be seen there is a modest increase in stator blade drag forces compared with the uncoupled case (0.1134 versus 0.1055) but there is a significant reduction in the rotor thrust forces (−0.0686 versus −0.1669). The total *y*-forces are slightly decreased with the total *z*-force magnitudes increased (0.0435 versus 0.0328). Interestingly, the *z*-moment coefficient becomes very small. The force magnitude for the coupled case is very close with the uncoupled case (0.1061 versus 0.1091) with lesser moment about the stator leading edge (0.0526 versus 0.0649).

4 Conclusions

A methodology to generate propulsor side forces has been presented. The concept utilizes a preswirl propulsor configuration with the upstream stator blades situated at varying pitch angles to generate a circumferentially varying inflow. The variation in the stator blade pitch produces a side force and also introduces an effective downwash that is ingested into the downstream rotor. The rotor then produces a side force, whose magnitude and direction is dependent on the blade number, and rake and skew parameters. Computations were performed to characterize the stator induced flow for a sinusoidal variation in the blade pitch angles. The stator inflow was then used as the velocity boundary condition for the rotor model to examine design variables including the blade number, skew, rake, and a combination of the two using a potential flow method. Steady and unsteady forces were computed and used to determine optimal blade designs in terms of maximum mean forces and minimum unsteady forces.

Variation in the upstream stator configuration and pitch amplitude greatly affected the downstream flow characteristics. It was found that a stator blade row consisting of 12 blades generated a sufficiently smooth circumferential velocity variation. This number is considered workable for actual experimental designs. Computations focused on maintaining a zero mean blade pitch angle with maximum and minimum pitch angles at maximum and minimum *y*-locations. The induced stator side forces were exclusively in the negative *z*-direction. Increases in the pitch amplitude demonstrated increased the swirl velocity variation and increased the axial velocity differential from one side of the blade row to the other in response to the increased side forces generated by the stator blade row.

The downstream rotor blade response was highly dependent on the blade shape parameters. An increase in rake increased the steady *y*-forces while decreasing the steady *z*-forces with small reductions in the unsteady forces. Increasing the skew changed the direction of the *y*-force, but kept it small while showing little change in the *i*-force. The unsteady forces were decreased significantly. Odd blade numbers also resulted in smaller steady and unsteady forces. The design space study suggested that the optimal rotor configuration utilized nine blades, 30 deg skew, and a rake of $0.4 * R_{\text{rotor}}$. This particular case was examined using RANS with the 12-blade, 10 deg pitch amplitude stator configuration. Significant side forces were computed with a force coefficient magnitude of 0.1061 and a moment coefficient about the stator leading edge of 0.0526. These are equivalent to approximately half the maximum forces generated by conventional control surfaces for a 21 in. (0.5334 m) UUV traveling at 3 kn (1.54 m/s). Both coupled and uncoupled simulations were conducted and demonstrated that the resulting thrust characteristics of the rotor were altered with little change in the side forces produced.

This technique has shown the potential to generate significant side forces from the propulsor alone. Experiments are currently underway to validate the present computations as well as to further extend the actual capabilities.

Acknowledgment

This work was sponsored by the Naval Undersea Warfare Center, Internal Research Program, with Dr. Anthony Ruffa as the program manager and the Office of Naval Research University Laboratory Initiative Program under Contract No. N0001408WX20425, with Dr. Kam Ng as the program sponsor.

References

[1] Roddy, R. F., 2003, "Investigation of the Resistance, Propulsion, Stability and Control Characteristics of the NUWC/ARL UUV IMP from Captive Model Experiments," Naval Surface Warfare Center, Carderock Division, Report No. NSWCCD-50-TR-2003/010.

[2] Welch, J. R., 2007, "Design & Implementation of a SIMULINK Based Test Bed for Developing Prototype Algorithms for the Mid-Sized Autonomous Research Vehicle (MARV)," Naval Undersea Warfare Center, Report No. NUWC TR-11822.

[3] Haselton, F. R., 1969, "Tandem Propeller in Review," J. Hydronaut., **3**(4), pp. 161–167.

[4] Kerwin, J. E., and Lee, C. S., 1978, "Prediction of Steady and Unsteady Marine Propeller Performance by Numerical Lifting Surface Theory," Soc. Nav. Archit. Mar. Eng., Trans., **86**, pp. 218–253.

[5] Kerwin, J. E., 1986, "Marine Propellers," Annu. Rev. Fluid Mech., **18**, pp. 367–403.

[6] Huyer, S. A., and Snarski, S. R., 2002, "Unsteady Propulsor Force Prediction for Spatially and Temporally Varying Inflow," ASME Paper No. FEDSM2002-31346.

[7] Huyer, S. A., and Kuklinski, R., 2003, "Altering Propulsor Blade Force Response via Inflow Modulation," *Proceedings of the 2003 Undersea Defence Technology Europe*, Malmo, Sweden.

[8] Huyer, S. A., Henoch, C., Beal, D., James, R., Macumber, D., and Annaswamy, A., 2007, "Stator Wake Deficit Reduction via Trailing Edge Articulation and Associated Blade Force Response," *Proceedings of the Undersea Defence Technology Conference, Europe*, Naples, Italy.

[9] Huyer, S. A., and Beal, D., 2007, "A Turbulent Inflow Model Based on Velocity Modulation," J. Sound Vib., **308**, pp. 28–43.

[10] Fluent Inc., FLUENT® User's Guide.

Computational Investigation of a Race Car Wing With Vortex Generators in Ground Effect

Yuichi Kuya
e-mail: yuichi@soton.ac.uk

Kenji Takeda
Senior Lecturer
e-mail: ktakeda@soton.ac.uk

Xin Zhang
Professor
e-mail: x.zhang1@soton.ac.uk

School of Engineering Sciences,
University of Southampton,
Southampton SO17 1BJ, UK

Vortex generators can be applied to control separation in flows with adverse pressure gradients, such as wings. In this paper, a study using three-dimensional steady computations for an inverted wing with vortex generators in ground effect is described. The main aim is to provide understanding of the flow physics of the vortex generators, and how they affect the overall aerodynamic performance of the wing to complement previous experimental studies of the same configuration. Rectangular vane type sub-boundary layer and large-scale vortex generators are attached to the suction surface of the wing, including both counter-rotating and co-rotating configurations. In order to provide confidence, Reynolds-averaged Navier–Stokes simulations using the Spalart–Allmaras turbulence model are validated against the experimental results regarding force, pressure, and wake characteristics, with the validation exhibiting close agreement with the experimental results. The streamwise friction shows the downwash induced by the generated vortex acts to suppress flow separation. The flow field survey downstream of the vortex generators features breakdown and dominance of the generated vortex in the flow. The vortex generated by the counter-rotating sub-boundary layer vortex generator grows in size and breaks down as it develops downstream, while the vortex generated by the counter-rotating large-scale vortex generator shows high vorticity even further downstream, indicating the persistence of the vortex in the flow. The flow field behind the co-rotating sub-boundary layer vortex generator is dominated by a lateral flow, having the spanwise flow component rather than a swirling flow, and the vortex quickly dissipating as it develops downstream. The results from this paper complement previous experimental measurements by highlighting the flow physics of how vortex generators can help control flow separation for an inverted wing in ground effect, and how critical vortex generator type and size are for its effectiveness. [DOI: 10.1115/1.4000741]

1 Introduction

In open-wheel racing series, such as Formula 1 and Indy Racing, a front wing is inverted to produce downforce, that is, negative lift, leading to an enhancement of traction and cornering ability of cars. The front wing is operated in close proximity to a solid boundary, known as the ground effect regime, where different flow features are exhibited, compared with the freestream condition. Since aerodynamic performance plays a significant role in open-wheel race cars, investigations and testing are typically conducted via wind tunnel testing, computational simulations, and track-based testing [1]. Although wind tunnel testing remains a significant tool for aerodynamic development, computational fluid dynamics (CFD) plays an important role because of its efficient cost performance compared with wind tunnel testing, and the detailed flow information that is available.

The first computational investigations of an inverted wing in ground effect were performed by Katz [2] and Knowles et al. [3], using a potential flow-based panel method to simulate a single-element wing in ground effect. Katz [2] observed an enhancement of downforce as the wing is brought closer to the ground. Previously conducted experimental investigations [4–7] show downforce reduction below the height where the maximum downforce is produced due to flow separation and breakdown of edge vortices around end plates of a wing. No downforce reduction phenomenon, however, was observed even at excessively low ride height in the study of Katz [2]; viscous effects were not simulated, thus, no flow separation was captured. Zerihan and Zhang [8] performed a Reynolds-averaged Navier–Stokes (RANS) simulation for a two-dimensional single-element wing, using a fully structured grid with the Spalart–Allmaras (S-A) [9] and shear stress transport (SST) k-ω turbulence models. The computational results of pressure and velocity distributions were compared with their previously performed experiments [4,10]. The computations captured the trends of the pressure distributions at the center portion of the wing span, as well as wake characteristics. Mahon and Zhang [11] conducted a further computational analysis for the surface pressure and wake characteristics, using multiblock hybrid grids. Various types of turbulence models were compared with the results of the experiments [4,10]. The results of the SST k-ω model showed the most accurate prediction of the pressure distributions and force slope. For the wake flow, the realizable k-ϵ model showed the most accurate prediction. More recently, Kieffer et al. [12] examined effects of the incidence of a single-element wing, modeling a Formula Mazda wing. The turbulence was modeled by the standard k-ϵ model. The numerical results, however, were obtained by using a fixed ground boundary, and there was no experimental validation. In addition to the computational investigations of a single-element wing, some extended studies for an inverted wing in ground effect have been conducted, including studies of a double-element wing [3,13] and interactions between a wing and a rotating wheel [14,15].

In the current investigation, an inverted single-element wing with vortex generators (VGs) in ground effect is computed using RANS simulations. Kuya et al. [7,16] experimentally investigated the performance and characteristics of such configuration. In this paper, the computational approach is comprehensively validated with the experimental results. The computations are then used to

Contributed by the Fluids Engineering Division of ASME for publication in the JOURNAL OF FLUIDS ENGINEERING. Manuscript received September 14, 2009; final manuscript received November 20, 2009; published online February 3, 2010. Assoc. Editor: Zvi Rusak.

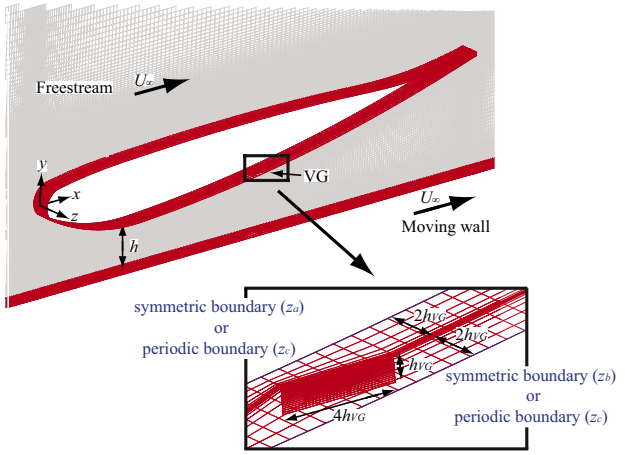

Fig. 1 Computational grid of inverted single-element wing and VG

examine the detailed flow physics of the VG separation control characteristics to support the experimental studies.

2 Computational Modeling

2.1 Governing Equations and Turbulence Modeling. The computations are performed by solving the three-dimensional steady RANS equations. A commercial RANS solver, FLUENT 6.2 [17], which uses the finite volume method, is used here. A second-order upwind scheme is used to interpolate values between computational nodes. The SIMPLEC pressure-velocity coupling algorithm [17] is employed.

Mahon and Zhang [11] compared various types of turbulence models using the same wing profile used here. In this study, the characteristics of an inverted wing is mainly examined at the wing ride height of $0.090c$, and Mahon and Zhang [11] showed that the SST k-ω model presents the best prediction at the ride height in pressure distributions and wake profiles. The S-A model, however, is employed here, since it has been found that the SST k-ω model is unstable at some ride heights examined, leading to unconverged computations. The S-A model exhibits the second best performance in the work of Mahon and Zhang [11], and is originally designed for wall-bounded aerodynamic flows. In addition, Zerihan and Zhang [8] also compared the S-A and SST k-ω models using the same wing profile used by Mahon and Zhang [11] and here, and showed a comparable performance of the two models. Although one-equation models may induce a larger numerical error than two-equation models, a careful validation study is performed here so as to provide sufficient confidence of the computations, and to estimate an amount of the errors.

2.2 Computational Geometries and Boundary Conditions. Figure 1 shows a schematic of an inverted single-element wing and its coordinate used in the computations, which has the same cross section profile as the wing used in the experimental study of Kuya et al. [7,16]. The wing profile is based on that of a NASA GA(W) profile, type LS(1)-0413, and has a chord c of 223.4 mm and a finite trailing edge of 1.65 mm. The origin of the coordinate system is set at the leading edge of the wing; the wing coordinates are given in the study of Zerihan [18]. The ride height h is defined as the distance from the lower boundary to the lowest point on the suction surface of the wing, and is varied between $0.067c$ and $0.448c$ in this study. The incidence α is measured relative to a line from the trailing edge to the most swelled point on the pressure surface, which corresponds to 2.6 deg relative to the chord line, and is fixed at 1 deg in this study, corresponding to the true incidence of 3.6 deg. A further description can be found in Refs. [7,16].

Rectangular vane type of sub-boundary layer vortex generators (SVGs) and large-scale vortex generators (LVGs) are studied here with a device height of 2 mm ($h_{VG}/c=0.009$) and 6 mm ($h_{VG}/c=0.027$), respectively. Figure 2 shows a schematic of VG configurations. The VGs attached on the suction side of the wing are oriented at 15 deg relative to the streamwise direction. The trailing edge of the VGs is set at $x=120$ mm, corresponding to $x/c=0.537$. The height and chord ratio of the VGs is fixed at 1:4, and the distance between the spanwise ends of the computational domain and the trailing edge of the VGs is fixed at $2h_{VG}$. Since the CtLVG configuration demands a grid three times wider than the other configurations in the spanwise direction, the CtLVG computational domain has additional cells along both the spanwise ends so that the grid expansion ratio from the VG is the same in both the computational domains. For the clean wing configuration, the same computational grid as the SVG configurations is used, where the computational cells for the VG are not set as a solid boundary. The computational VGs are modeled as a zero-thickness solid boundary because it is much simpler to generate, easier to modify, and can decrease the number of grid points significantly. Allan et al. [19] compared a simply modeled rectangular vane having zero thickness with a fully modeled trapezoidal vane with finite thickness. The comparison showed that the performance of the simply modeled rectangular vane is similar to that of the fully modeled trapezoidal vane, and hence, the simplified model is employed here.

A three-dimensional multiblock structured grid is used in this study. A grid generation package, Gridgen V15, is used to build the grid, and any special functions in the package are not used, although the functions may provide an optimized grid, leading to quicker convergence. The upstream boundary is modeled with a freestream velocity inlet of 30 m/s, corresponding to the Reynolds number of 450,000, based on the wing chord. The turbulent viscosity ratio of 8 is used as a result of preliminary studies to simulate previous experimental studies of the same configuration. For the downstream boundary, a condition of zero flux diffusion is applied, where the boundary plane is extrapolated from the downstream values and there is no gradient in the streamwise direction. A no-slip boundary condition is applied to the wall boundaries, which are the wing, VGs, and lower boundary. A moving wall condition is simulated at the lower boundary where a moving velocity is equal to the freestream. The initial cell spacing on the wall boundaries is fine enough to solve the viscous sublayer of the flow on the wall properly, maintaining y^+ of $O(1)$. The upper boundary is modeled with a symmetric condition. To simulate the counter-rotating VG configurations, both spanwise ends of the boundary are defined as symmetric conditions; meanwhile, periodic conditions are applied for the co-rotating VG configuration.

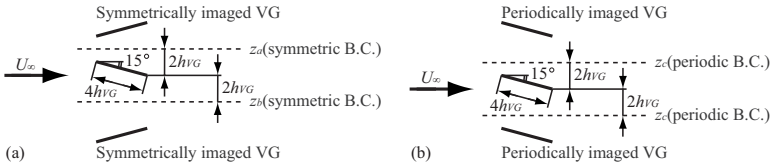

Fig. 2 Configurations of VGs on wing and boundary conditions at spanwise ends: (*a*) counter-rotating VGs and (*b*) co-rotating VGs

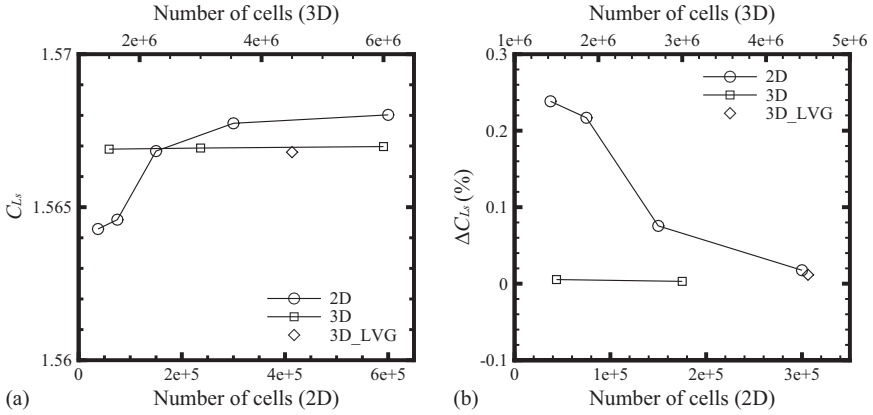

Fig. 3 Grid refinement study with clean wing configuration: (*a*) sectional downforce coefficient and (*b*) convergence ratio

As shown in Fig. 2, $z=-2h_{\mathrm{VG}}$ and $2h_{\mathrm{VG}}$ are referred to as z_a and z_b at the spanwise end boundaries for the counter-rotating VG configuration, respectively, and z_c for the co-rotating VG configuration.

The convergence criteria for all simulations are carefully monitored, allowing the numerical residuals to decrease by $O(10^{-4})$. Variations of downforce are lower than $O(10^{-6})$ for the final iterations. Both two-dimensional and three-dimensional grid refinement studies have been conducted with the clean wing configuration at the ride height of $0.179c$ regarding downforce. Figure 3 shows the grid convergence history with respect to the downforce coefficient. For the two-dimensional study, the number of cells is examined between 75,000 cells and 600,000 cells, and the grid of 150,000 cells is chosen; the difference between the finest and selected grids is less than 0.1%. The three-dimensional grid study has been conducted for a grid based on the two-dimensional grid of 150,000 cells. The number of cells examined is between 1,500,000 cells and 6,000,000 cells, and the grid of 3,000,000 cells is employed for the clean wing and SVG configurations; the difference between the finest and selected grids is less than 0.1%. As described above, for the CtLVG configuration, 1,500,000 cells are added to the grid of the clean and SVG configurations along the spanwise ends, resulting in a total of 4,500,000 cells. The grid for the CtLVG configuration also shows a small difference with respect to the finest grid, being less than 0.1%. The size of the computational domain has been also examined. The distances from the wing to the upstream and downstream boundaries are examined between $5c$ and $20c$, and are respectively set as $5c$ and $10c$ with differences from the largest grids of less than 0.01%. The distance between the upper and lower boundaries has been examined between $5c$ and $20c$, and is set as $10c$ with differences from the largest grid of less than 0.05%.

3 Results

To examine an application of RANS simulations to computations of an inverted wing with VGs in ground effect, validations of the computations against the experiments of Kuya et al. [7,16] are presented here. This is followed by the detailed investigations of the flow physics based on the computations.

3.1 Chordwise Surface Pressure Distributions. Figure 4 shows comparisons of chordwise pressure distributions of the computations and experiments on the wing of the four configurations at $h/c=0.090$. Note that the vertical lines in the figures represent the leading and trailing edges of the VGs, and the experimental results of the VG configurations are averaged in the spanwise direction. It should also be noted that the computational pressure of the counter-rotating VG configurations show distributions at two spanwise positions ($z=z_a$ and z_b).

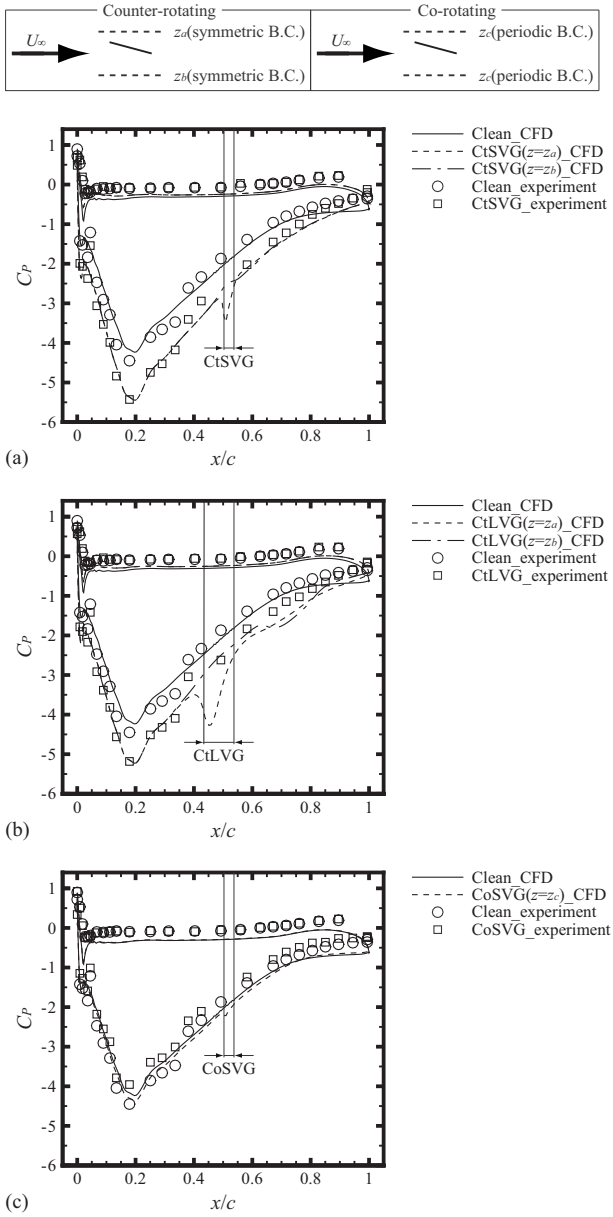

Fig. 4 Comparisons of computational and experimental chordwise surface pressure distributions on wing at $h/c=0.090$: (*a*) CtSVG, (*b*) CtLVG, and (*c*) CoSVG

Table 1 Sectional downforce at $h/c=0.090$

	Clean	CtSVG	CtLVG	CoSVG
$C_{L_{s\_\mathrm{CFD}}}$	1.63	2.29	2.25	1.70
$C_{L_{s\_\mathrm{experiment}}}$	1.91	2.46	2.37	1.68
ΔC_{L_s} (%)	−15	−7	−5	1

On the pressure surface, all the computations capture the general trend of the experimentally obtained distributions, while the computational values indicate underpredictions compared with the experiments. The computation of the clean wing shows flow separation at about 70% chord, characterized by a constant value region on the suction surface.

For the CtSVG configuration, the computation predicts the pressure distributions on the suction surface fairly well, including the gradient of the pressure recovery, in particular, the suction peak, while the experiments show somewhat less suction near the trailing edge. For both the counter-rotating configurations at $z=z_a$, a spike near the leading edge of the VG is noticeable in the computations. The size of the spike is more remarkable in the CtLVG configuration. The computation of the CtLVG configuration predicts the distribution upstream of the VG relatively well, including a prediction of the suction peak, while the computations show more suction near the trailing edge. The CtSVG configuration predicts more suction on the suction surface compared with the CtLVG configuration, which is in good agreement with the experiments. Of interest here is that both the counter-rotating VG configurations show a moderate pressure recovery slope toward the trailing edge and eliminate the constant value region, indicating the reduction in flow separation.

The computations of the clean wing and CoSVG configuration show apparently similar pressure distributions, indicating the flow separation region as featured by the experimental results. Therefore, there appears little or no effect of the CoSVGs in terms of the separation control. The spike near the leading edge of the CoSVGs is smaller than that of the counter-rotating VG configurations.

3.2 Sectional Force Characteristics. The wing used in the experiments has generic end plates at both spanwise ends of the wing, and the force characteristics are affected by the edge vortices induced around the end plates. Meanwhile, the computations are performed with symmetric or periodic boundary conditions at the spanwise ends of the computational domain. The end plates, therefore, are not simulated in the computations, so the computations correspond to a simulation around the center portion of the wing where there is no effect of the edge vortices. Accordingly, a comparison of the force values of downforce and drag between the experiments and computations is not sufficient. Alternatively, a comparison of sectional downforce is presented here. The experimental sectional downforce is calculated by integrating the pressure around the center portion of the wing performed in Ref. [7].

A validation for the sectional downforce is given in Table 1, presenting the sectional downforce of the computations, experiments, and differences between them at $h/c=0.090$. The computations of the three VG configurations show reasonable prediction compared with the experiments. Although the computation of the clean wing shows the highest deviation from the experimental result, the errors of VG configurations are less than 7%.

Figure 5 shows computationally calculated sectional downforce and drag of the four configurations at various ride heights. The experimental force characteristics for the full scale model are given in Ref. [7]. All the downforce curves feature the downforce enhancement phenomenon, as the ride height is decreased due to the Venturi effect. At much smaller ground clearances, the clean wing and CoSVG configuration exhibit the downforce reduction phenomenon. The CoSVG configuration produces similar or slightly higher downforce compared with the clean wing. The downforce reduction phenomenon is not observed in computations of the counter-rotating VG configurations, showing a continuous increase in downforce as the wing is brought closer to the ground. Both the counter-rotating VG configurations generate similar downforce. For the curves of the computational drag, all the computations indicate an increase in drag as the ride height decreases, as shown in the experiment [7]. The computations predict the same order of the degree of drag as the experiment with the CtLVG configuration producing the highest drag, and the clean wing producing the lowest drag.

3.3 Wake Velocity Profiles. Figure 6 shows comparisons of mean streamwise velocity profiles at $x/c=1.5$ of the four configurations at $h/c=0.090$, including the computational and experimental results. The thick and thin lines respectively indicate the computational and experimental results. The figure for the counter-rotating VG configurations shows profiles at two spanwise positions ($z=z_a$ and z_b).

All the computations overpredict in terms of the maximum velocity deficit of the wake. The boundary layer growth on the moving ground is captured well by all the computations. In the computations, the CtSVG configuration shows a larger velocity deficit compared with the clean wing and a small variance in the spanwise direction, which is in good agreement with the experimental results. The comparison between the clean wing and CtLVG configuration show that the computations can predict the general trend and correlation between the three profiles very well, showing a large variance in the spanwise direction. The computations of the CoSVG configuration shows a larger velocity deficit than the clean wing, as the experimental results show, while its difference is more apparent in the experimental results.

3.4 Streamwise Friction Distributions. Streamwise friction distributions on the suction surface of the four configurations at

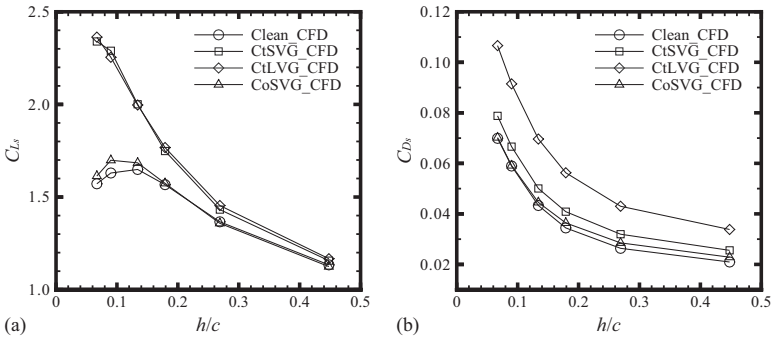

Fig. 5 Characteristics of computed sectional forces at various ride heights: (*a*) downforce and (*b*) drag

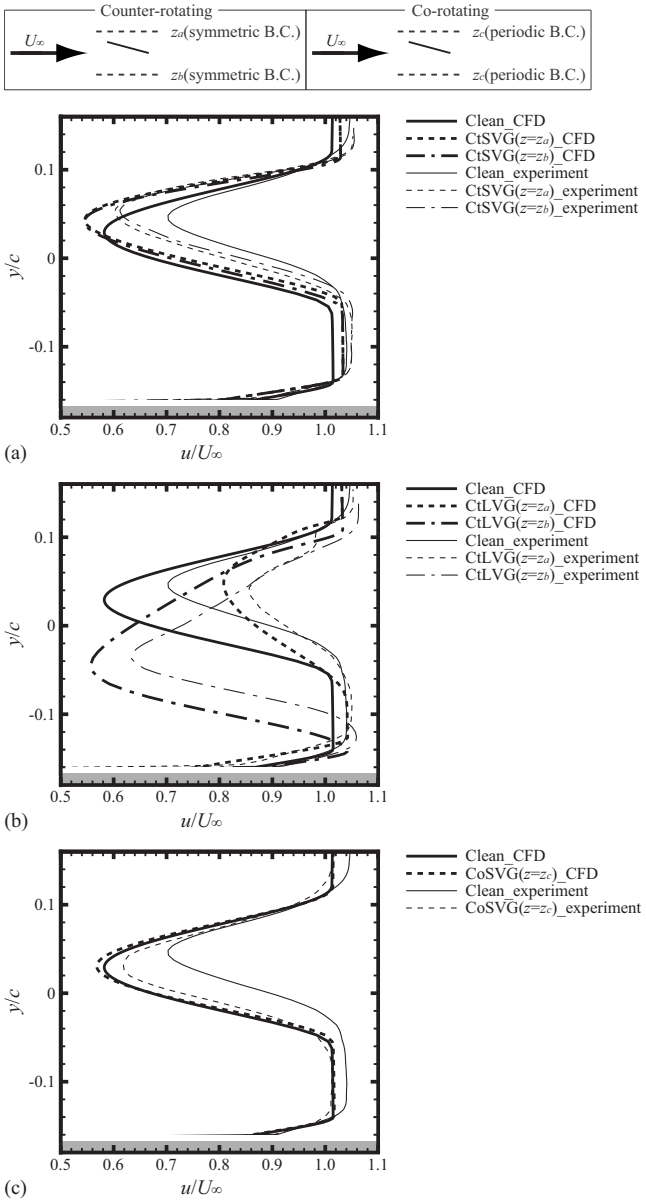

Fig. 6 Comparisons of computational and experimental streamwise velocity profiles of wake at $h/c=0.090$ at $x/c=1.5$: (*a*) CtSVG, (*b*) CtLVG, and (*c*) CoSVG

$h/c=0.090$ are shown in Fig. 7. Note that the vertical and horizontal lines in the figures represent the leading and trailing edges of the VGs, and the value of $C_{F_x}=0$, respectively.

The friction of the clean wing shows negative values downstream of 70% chord, corresponding to a region of the flow separation. The experimentally obtained separation point is at 65–80% chord of the clean wing; the wide range of the separation point is due to the strong three-dimensionality of the separated flow.

Both the counter-rotating VG configurations indicate higher values than the clean wing. This is because suction of both the counter-rotating VG configurations is stronger than that of the clean wing, and therefore, a larger amount of flow runs along the suction surface, resulting in the increase in the friction. A variance of the value in the spanwise direction is observed downstream of the VG, due to the secondary flow induced by the VG-generated vortex. The downwash toward the suction surface suppresses the flow separation, leading to higher values of the friction, as shown in the distributions at $z=z_a$.

The friction slope of the CtSVG configuration at $z=z_a$ indicates a spike around 60% chord, and decreases the value along the streamwise direction as the vortex becomes weaker downstream. Meanwhile, the upwash from the VG-generated vortex induces low friction, as indicated by the slope at $z=z_b$, indicating a small negative spike around 60% chord. Although the upwash weakens the friction, the value is positive at most of the regions, hence indicating a very small adverse effect.

For the CtLVG configuration, the friction is enhanced by the downwash at $z=z_a$ as with the CtSVG configuration. The reduced gradient of the slope downstream of 60% chord is less steep compared with the CtSVG configuration, indicating that the vortex is still dominant. The friction slope at $z=z_b$ shows a relatively wide range of a negative region between 60% and 87% chord, where the flow separation is enhanced by the upwash.

For the CoSVG configuration, a small variance is observed, compared with the clean wing. Although the CoSVG configuration shows the flow separation slightly further downstream compared with the clean wing, the effect for the separation control is apparently less than that of the CtSVG configuration. The separation point of the clean and CoSVG configuration is respectively observed at 70% and 75% chord.

3.5 Characteristics of VG-Generated Vortex. Figure 8 shows velocity vectors and streamwise vorticity contours at $x/c=0.63$, 0.72, and 0.81 of the CtSVG, CtLVG, and CoSVG configurations at $h/c=0.090$. Note that y_w in the figures denotes the normal distance from the wing surface, and hence, the upper edge of the figures corresponds to the suction surface of the wing. $z/c=0$ is the spanwise center of the computational domain. It should also be noted that the scale of the figures for the CtLVG configuration (Fig. 8(*b*)) is three times larger than the other configurations due to the size difference of the computational domain.

The results presented here feature breakdown and dominance of the VG-generated vortex in the flow. At $x/c=0.63$, the velocity vectors of the CtSVG configuration show the downwash to the suction surface at the left hand side of the contour; the downwash pumps the momentum into the boundary layer flow. The vortex center moves in the positive spanwise direction as it develops downstream, and the swirling motion mostly dissipates at $x/c=0.81$. Meanwhile, for the CtLVG configuration, the swirling motion of the velocity vectors can be observed even at $x/c=0.81$, indicating that the vortex is still dominant in the flow. The velocity vectors of the CoSVG configuration shows that the downwash to the suction surface is shown at $x/c=0.63$, however, the flow near the suction surface has a strong lateral component. Further downstream, the flow field is completely dominated by the lateral flow running in the positive spanwise direction. This is because the interaction between neighboring co-rotating vortices tends to cancel each other's downwash and upwash, and enhances the lateral component of the flow. Therefore, the lateral flow, rather than the swirling flow, becomes predominant.

For the streamwise vorticity contours, it is shown that the VG-generated vortex represented by negative vorticity induces the positive vorticity region on the suction surface. The vortex center of the CtLVG configuration is further from the wing surface than that of the CtSVG configuration, and the distance from the suction surface increases as the vortex develops downstream. Of great interest is that the vortex of the CtSVG grows and breaks down as it develops downstream, while the vortex of the CtLVG shows high vorticity values even further downstream, therefore indicating that the vortex of the CtLVG is still dominant in the flow, as also shown by the velocity vectors. For the CoSVG configuration, the vortex is likely to develop in the positive spanwise direction, and the second vortex is observed at $x/c=0.72$, which is generated by a neighboring VG and develops in the positive spanwise direction due to the lateral flow. The distance between the vortex and the suction surface increases as the vortex develops downstream,

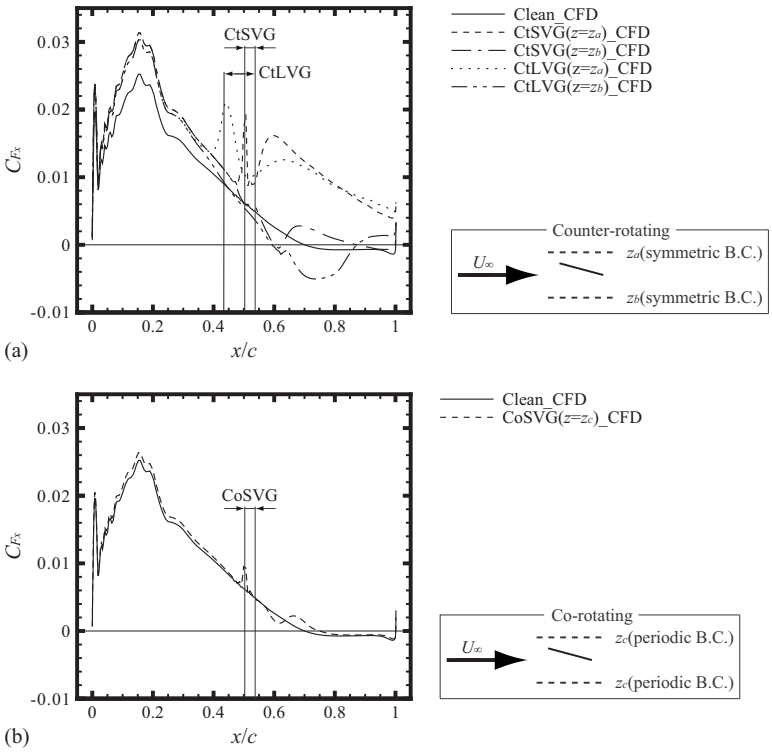

Fig. 7 Computational streamwise friction distributions on suction surface at *h*/*c*=0.090: (*a*) counter-rotating VG configurations and (*b*) co-rotating configuration

and it completely detaches from the suction surface at $x/c=0.81$. The vortex size of the CoSVG configuration at $x/c=0.63$ is smaller than the other configurations.

4 Discussion

The computations exhibit good agreement with the experiments [7,16] to simulate the flow around an inverted single-element wing with VGs in ground effect. Among the validated computations, the flow field surveys, including the streamwise friction distributions, velocity vectors, and streamwise vorticity contours, reveal the characteristics of the VG-generated vortex in the flow well. The computed force characteristics show that both the counter-rotating VG configurations can delay the onset of the downforce reduction phenomenon due to the suppression of flow separation, and produce higher downforce than the clean wing.

The vortex generated by the CtSVGs grows in size and breaks down as it develops downstream, reducing the swirling motion. This feature is in very good agreement with the result of the surface flow visualization in the experiment [16]. The computed streamwise friction also shows the decay of the vortex generated by the CtSVG in the streamwise direction. Lin [20] suggested that effective separation control is provided when VG-generated vortices are just strong enough to overcome separation, but are not so strong that they dominate in the flow further downstream, passing after an initial separation point. According to this criterion, the CtSVG configuration investigated here exhibits the best performance in terms of separation control. The computed streamwise friction provides further evidence of the advantage of the CtSVG. The downwash toward the suction surface induced by the VG-generated vortex increases the friction on the surface, helping to suppress the flow separation. Meanwhile, the upwash should have an adverse effect on the separation control. The friction distributions at $z=z_b$, however, indicates a very small region of negative friction, and therefore, the unfavorable effect of the CtSVG caused by the upwash is rather small.

The vortex generated by the CtLVG shows high vorticity even further downstream, indicating the dominance of the vortex. This strong vortex significantly affects the flow in the spanwise direction. The downwash induced by the CtLVG makes the flow attach on the suction surface at $z=z_a$, as with the CtSVG configuration, as observed in the result of the surface flow visualization in Ref. [16]. Indeed, the downwash induced by the CtLVGs might be more effective than that generated by the CtSVGs, but the unfavorable effect caused by the upwash induced by the CtLVGs at $z=z_b$ significantly reduces the wing performance due to the acceleration of flow separation on the suction surface. The friction distribution also shows the unfavorable effect of the upwash induced by the CtLVG configuration; a wider negative friction region with lower values compared with the clean wing at $z=z_b$. The greater strength of the vortex generated by the CtLVGs is also shown by the wake survey of the VGs, showing the dominance of the swirling flow downstream.

The flow field behind the CoSVG is dominated by the lateral flow component rather than the swirling flow, and the vortex quickly dissipates as it develops downstream. This lateral flow is identified in the result of the surface flow visualization in Ref. [16], where the spanwise flow pattern appeared. This is because the interaction between neighboring co-rotating vortices tends to cancel each other's downwash and upwash, accelerating the decay of the vortices and enhancing the lateral component of the flow. Therefore, the CoSVG configuration has a lesser effect on separation control than the counter-rotating configurations in the current investigation. The quicker decay of the vortices induced by the CoSVGs, compared with the CtSVGs captured here, is in good agreement with the investigation of Pauley and Eaton [21]. These results suggest that wider device spacing between each vane could induce more effective co-rotating vortices on the separation control, such that the interaction becomes less effective. In summary, the computational investigation reveals aerodynamic characteristics of an inverted single-element wing with VGs in ground effect,

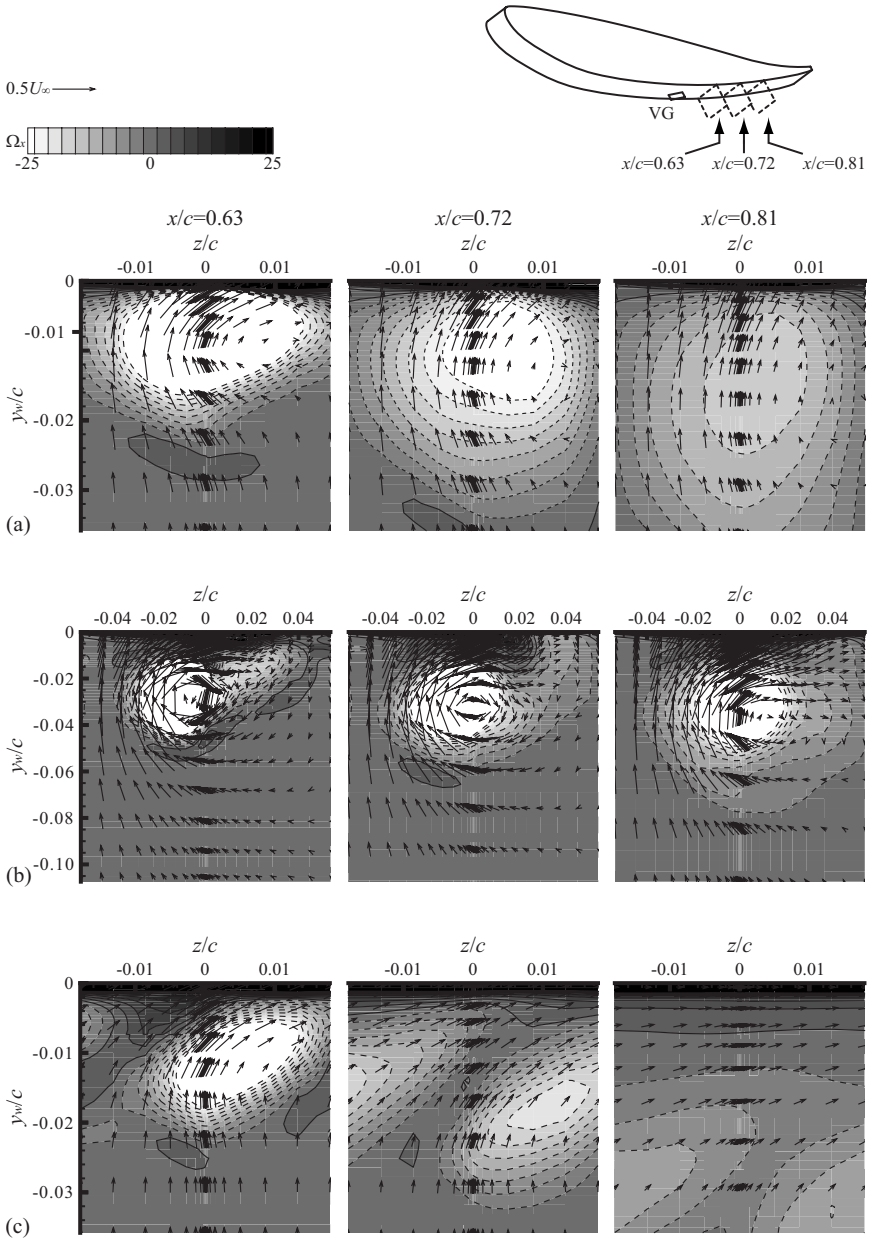

Fig. 8 Characteristics of VG-generated vortex in cross plane at $h/c=0.090$ at $x/c=0.63$, 0.72, and 0.81: (*a*) CtSVG, (*b*) CtLVG, and (*c*) CoSVG

and advantages of a use of the CtSVG configuration is presented for the separation control, supported by a number of detailed physical evidences.

5 Concluding Remarks

Three-dimensional computations of an inverted single-element wing with VGs in ground effect are performed by steady RANS simulations, and the following conclusions are drawn.

- Validation for the computations is demonstrated, regarding force, pressure, and wake characteristics compared with experiments. The computations show good agreement with the experimental results, confirming the applicability of the computational approach used.
- The clean wing shows flow separation downstream of 70% chord, represented by a constant pressure region on the suction surface. Both the counter-rotating VG configurations, however, show a moderate pressure recovery slope toward the trailing edge and eliminate the constant value region, indicating elimination or reduction in flow separation.
- The computed force characteristics at $\alpha=1$ deg show that both the counter-rotating VG configurations can delay the onset of the downforce reduction phenomenon due to the suppression of the flow separation, and produce higher downforce than the clean wing at low ride heights.
- Variances of the friction in the spanwise direction are observed downstream of the counter-rotating VGs due to the secondary flow induced by the VG-generated vortices. The downwash on the suction surface induces higher values of the friction suppressing the flow separation; meanwhile, the upwash induces low friction. The adverse effect of the upwash regarding the separation control is negligibly small in the CtSVG configuration; meanwhile, the upwash generated by the CtLVGs induces obvious unfavorable effects. The CoSVG configuration exhibits a very small difference of the friction distribution compared with the clean wing, however,

the CoSVG configuration shows the flow separation slightly further downstream.

- The flow field survey downstream of the VGs features the breakdown and dominance of the VG-generated vortex in the flow. The vortex generated by the CtSVGs grows in size and breaks down as it develops downstream, while the vortex generated by the CtLVGs shows high vorticity even further downstream, indicating the dominance of the vortex in the flow.
- The flow field behind the CoSVGs is dominated by a lateral flow, having the spanwise flow component rather than a swirling flow, and the vortex quickly dissipates as it develops downstream. This is because the interaction between neighboring co-rotating vortices is likely to enhance the lateral component of the flow. Due to this behavior of the vortex, the CoSVG configuration exhibits less effect in terms of the separation control than the other VG configurations in the current study.
- The computational investigation performed here reveals aerodynamic characteristics of an inverted single-element wing with VGs in ground effect, and highlights the advantages of using the CtSVG configuration for flow separation control.

Acknowledgment

Y. Kuya gratefully acknowledges the financial support of the Ministry of Education, Culture, Sports, Science and Technology of Japan and the School of Engineering Sciences, University of Southampton.

Nomenclature

Roman Symbols

C_{D_s} = sectional drag coefficient ($=2D_s/\rho U_\infty^2 c$)
C_{F_x} = streamwise friction coefficient ($=2\tau_x/\rho U_\infty^2$)
C_{L_s} = sectional downforce coefficient ($=2L_s/\rho U_\infty^2 c$)
C_P = pressure coefficient ($=2(p-p_\infty)/\rho U_\infty^2$)
c = wing chord
D_s = sectional drag
h = wing ride height
h_{VG} = device height of vortex generator
L_s = sectional downforce
p = pressure
p_∞ = freestream static pressure
U_∞ = freestream velocity
u_i = Cartesian components of velocity: streamwise, lateral, and spanwise directions ($=u,v,w$)
x_i = Cartesian tensor system: streamwise, lateral, and spanwise directions ($=x,y,z$)
y_w = distance from wall or wing surface
y^+ = normalized wall distance
z_a, z_b, z_c = spanwise ends of computational domain

Greek Symbols

α = wing incidence
ρ = density
τ_x = streamwise wall shear stress
Ω_x = nondimensional streamwise vorticity ($=(\partial w/\partial y - \partial v/\partial z)c/U_\infty$)

Glossary

CoSVG = co-rotating sub-boundary layer vortex generator
CtLVG = counter-rotating large-scale vortex generator
CtSVG = counter-rotating sub-boundary layer vortex generator
S-A = Spalart-Allmaras

References

[1] Zhang, X., Toet, W., and Zerihan, J., 2006, "Ground Effect Aerodynamics of Race Cars," Appl. Mech. Rev., **59**, pp. 33–49.
[2] Katz, J., 1985, "Calculation of the Aerodynamic Forces on Automotive Lifting Surfaces," ASME J. Fluids Eng., **107**, pp. 438–443.
[3] Knowles, K., Donoghue, D. T., and Finnis, M. V., 1994, "A Study of Wings in Ground Effect," *Proceedings of the Loughborough University Conference on Vehicle Aerodynamics*, Vol. 22, pp. 1–13.
[4] Zerihan, J., and Zhang, X., 2000, "Aerodynamics of a Single Element Wing in Ground Effect," J. Aircr., **37**(6), pp. 1058–1064.
[5] Zerihan, J., and Zhang, X., 2001, "Aerodynamics of Gurney Flaps on a Wing in Ground Effect," AIAA J., **39**(5), pp. 772–780.
[6] Soso, M. D., and Wilson, P. A., 2006, "Aerodynamics of a Wing in Ground Effect in Generic Racing Car Wake Flows," Proc. Inst. Mech. Eng., Part D (J. Automob. Eng.), **220**(1), pp. 1–13.
[7] Kuya, Y., Takeda, K., Zhang, X., Beeton, S., and Pandaleon, T., 2009, "Flow Separation Control on a Race Car Wing With Vortex Generators in Ground Effect," ASME J. Fluids Eng., **131**, p. 121102.
[8] Zerihan, J., and Zhang, X., 2001, "A Single Element Wing in Ground Effect—Comparisons of Experiments and Computation," AIAA Paper No. 2001-0423.
[9] Spalart, P. R., and Allmaras, S. R., 1992, "A One-Equation Turbulence Model for Aerodynamic Flows," AIAA Paper No. 1992-0439.
[10] Zhang, X., and Zerihan, J., 2003, "Off-Surface Aerodynamic Measurements of a Wing in Ground Effect," J. Aircr., **40**(4), pp. 716–725.
[11] Mahon, S., and Zhang, X., 2005, "Computational Analysis of Pressure and Wake Characteristics of an Aerofoil in Ground Effect," ASME J. Fluids Eng., **127**, pp. 290–298.
[12] Kieffer, W., Moujaes, S., and Armbya, N., 2006, "CFD Study of Section Characteristics of Formula Mazda Race Car Wings," Math. Comput. Model. Dyn. Syst., **43**, pp. 1275–1287.
[13] Mahon, S., and Zhang, X., 2006, "Computational Analysis of a Inverted Double-Element Airfoil in Ground Effect," ASME J. Fluids Eng., **128**, pp. 1172–1180.
[14] Diasinos, S., Barber, T. J., Leonardi, E., and Hall, S. D., 2004, "A Two-Dimensional Analysis of the Effect of a Rotating Cylinder on an Inverted Aerofoil in Ground Effect," *Proceedings of the 15th Australian Fluid Mechanics Conference*.
[15] Diasinos, S., Barber, T., Leonardi, E., and Gatto, A., 2006, "The Interaction of a Rotating Cylinder and an Inverted Aerofoil in Ground Effect: Validation and Verification," AIAA Paper No. 2006-3325.
[16] Kuya, Y., Takeda, K., Zhang, X., Beeton, S., and Pandaleon, T., 2009, "Flow Physics of a Race Car Wing With Vortex Generators in Ground Effect," ASME J. Fluids Eng., **131**, pp. 121103.
[17] FLUENT, 2005, *FLUENT 6.2 User's Guide*, ANSYS Inc., Southpointe, PA.
[18] Zerihan, J. D. C., 2001, "An Investigation Into the Aerodynamics of Wings in Ground Effect," Ph.D. thesis, University of Southampton, UK.
[19] Allan, B. G., Yao, C.-S., and Lin, J. C., 2002, "Simulation of Embedded Streamwise Vortices on a Flat Plate," NASA Technical Report No. CR-2002-211654, ICASE Report No. 2002-14.
[20] Lin, J. C., 1999, "Control of Turbulent Boundary-Layer Separation Using Micro-Vortex Generators," AIAA Paper No. 1999-3404.
[21] Pauley, W. R., and Eaton, J. K., 1988, "Experimental Study of the Development of Longitudinal Vortex Pairs Embedded in a Turbulent Boundary Layer," AIAA J., **26**(7), pp. 816–823.

Comparison of Experiments and Simulation of Joule Heating in ac Electrokinetic Chips

Stuart J. Williams
Department of Mechanical Engineering,
University of Louisville,
Louisville, KY 40292
e-mail: stuart.williams@louisville.edu

Pramod Chamarthy
General Electric,
Niskayuna, NY 12309
e-mail: pramodchamarthy@yahoo.com

Steven T. Wereley
Mechanical Engineering,
Purdue University,
West Lafayette, IN 47907
e-mail: wereley@purdue.edu

ac electrokinetic manipulations of particles and fluids are important techniques in the development of lab-on-a-chip technologies. Most of these systems involve planar microelectrode geometries, generating high strength electric fields. When these fields are applied to a dielectric medium, Joule heating occurs. Understanding electrothermal heating and monitoring the temperature in these environments are critical for temperature-sensitive investigations including biological applications. Additionally, significant changes in fluid temperature when subjected to an electric field will induce electrohydrodynamic flows, potentially disrupting the intended microfluidic profile. This work investigates heat generated from the interaction of ac electric fields and water at various electrical conductivities (from 0.92 mS/m to 390 mS/m). The electrode geometry is an indium tin oxide (ITO) electrode strip 20 μm wide and a grounded, planar ITO substrate separated by a 50 μm spacer with microfluidic features. Laser-induced fluorescence is used to measure the experimental changes in temperature. A normalization procedure that requires a single temperature-sensitive dye, Rhodamine B (RhB), is used to reduce uncertainty. The experimental electrothermal results are compared with theory and computer simulations. [DOI: 10.1115/1.4000740]

1 Introduction

Micro-electrode structures are used in ac electrokinetics to generate strong electric fields for manipulating suspended micro- and nanoparticles as well as fluids in lab-on-a-chip systems. One such electrokinetic technique, dielectrophoresis (DEP), is used as a noninvasive means to selectively manipulate and capture suspended particles in microfluidic devices [1]. When conductive, electrically neutral particles are subjected to an electric field, they will polarize, inducing applied moments on the particle. If the electric field is nonuniform, there will be an imbalance of moments, resulting in DEP and particle translation. The strength and direction of the DEP forces are dependent on the dielectric properties of the particle and fluid, as well as on the electric field strength. DEP has been used to manipulate micro- and nanometer-sized particles [2,3] as well as DNA [4], viruses [5], and bacteria [6]. ac electroosmosis (ACEO) is another electrokinetic technique referring to the electrokinetic pumping of ionic fluids using ac signals [7,8]. The tangential component of the electric field near the electrode interface acts upon charges in the double layer, resulting in fluid motion. Fluid velocities in the order of mm/s can be achieved with an applied potential of a few V [8].

The strong electric fields necessary for DEP and ACEO are typically generated with fabricated, micrometer-sized electrodes and with an applied ac signal using commercially available benchtop signal generators. Various electrode geometries are used for DEP and ACEO, including interdigitated, comblike structures [6,7,9] for fluid and particle manipulation and single-particle DEP trapping arrangements such as point-and-lid [10], quadruple [11], and octopole [12,13] electrodes. The applied ac signals for DEP and ACEO are typically 0–20 V and frequencies typically between 1 kHz and 10 MHz. The dielectric properties of the fluid medium are dependent on the specific application. Electrical conductivities of the fluid range from deionized (DI) water ($\sim$5.0 μS/m) to biological growth media ($>$1 S/m). DEP experiments incorporating low-conductivity growth media and bacteria have also been reported [14].

These strong electric fields will act on the conducting fluid medium, resulting in Joule heating. This could harm temperature-sensitive biological samples. In addition, the heating changes the conductivity and permittivity of the fluid—the applied electric field will act on these dielectric gradients resulting in electrothermal fluid motion [15–18]. Both Joule heating and electrothermal fluid pumping could be unwanted effects for electrokinetic lab-on-a-chip systems.

It is important to monitor the effects of Joule heating in electrokinetic microsystems. There are a variety of temperature measuring techniques that have been incorporated at this scale [19]. Thermocouples can be incorporated into the microchannel [20] or can be fabricated on the channel surface [21,22]. Similarly, resistance temperature detectors have been used to monitor heat transfer, with their resistive elements fabricated along the microchannel surface [23,24]. Each of these techniques, however, requires precisely controlled fabrication. Thermochromic liquid crystals (TLCs) have also been used for temperature measurements due to their unique, temperature-dependent optical properties. TLC slurries and paints can achieve measurement resolution to approximately 1 μm [25] while encapsulated crystals have been used for simultaneous velocity and temperature measurements [26] as well as transient temperature measurements [27,28]. Infrared thermography has been used to measure the boiling characteristics in microchannels [29,30]. However, infrared thermography can only be used to measure surface temperatures.

Particles exhibit random movement due to their interaction with liquid molecules, a phenomenon called Brownian motion. The suspended particle's displacement due to Brownian motion is proportional to temperature. Both microscale particle tracking and particle image velocimetry thermometry techniques have been adapted in order to measure Brownian motion and determine temperature [31–34]. However, these techniques were not implemented for our experiments as the translation of the tracer particles was affected by DEP and electrokinetic hydrodynamics. Due to these hindrances, an alternate nonintrusive temperature measurement method that did not use tracer particles was chosen.

Contributed by the Fluids Engineering Division of ASME for publication in the JOURNAL OF FLUIDS ENGINEERING. Manuscript received May 27, 2009; final manuscript received October 22, 2009; published online February 4, 2010. Assoc. Editor: Pavlos P. Vlachos.

Among the various methods available, laser-induced fluorescence (LIF) is capable of making nonintrusive temperature measurements within a volume of liquid. For LIF thermometry, the temperature-dependent fluorescent intensity of dyes is utilized to measure temperature. LIF has been used at the microscale previously [35–37]. Two dyes can be used to eliminate uncertainty due to nonuniform illumination [38–40], where the temperature-insensitive dye is used to normalize the intensity of the temperature-sensitive dye. In general, Rhodamine B (RhB) and Rhodamine 110 (Rh110) are used as the temperature-dependent and temperature-independent dyes, respectively. This normalized technique is referred to as the ratiometric laser-induced fluorescence thermometry (R-LIFT) method or the dual emission laser-induced fluorescence (DELIF) method. We have used the R-LIFT method previously for microscale fluid investigations [41]. Here, a normalization procedure that requires a single dye, first used by Ross et al. [37] to measure Joule heating for electroosmotic flow, was applied. What differentiates the present investigation from previous work [37] is the comparison of temperature measurements to numerical simulations for Joule heating in ac electrokinetic chips.

2 Electrothermal Theory

In order to estimate the temperature rise due to Joule heating the energy balance equation needs to be solved [17,18] as follows:

$$\rho_m c_p(\partial T/\partial t + (v \cdot \nabla)T) = k\nabla^2 T + \langle \sigma |\boldsymbol{E}|^2 \rangle + Q \tag{1}$$

where ρ_m is mass density, c_p is the heat capacity, T is temperature, v is velocity, k is thermal conductivity, σ is the electrical conductivity of the liquid, E is the electric field, and Q is a heat source. This equation can be simplified for ac electrokinetic microsystems. The applied ac electric field produces an oscillating temperature component. Scaling analysis by Ramos et al. [17] demonstrated that for a characteristic length scale of 20 μm (the width of electrodes used herein) thermal equilibrium is established within 1 ms of applying the electric field. Therefore, the oscillating temperature component can be neglected for frequencies greater than 1 kHz. Heat convection is negligible when compared with heat conduction as shown with a dimensional analysis of the second term in Eq. (1),

$$|\rho_m c_p (v \cdot \nabla)T|/|k\nabla^2 T| \approx \rho_m c_p v l/k \leq 0.07 \tag{2}$$

where l is the characteristic length of the system ($l < 100$ μm) and the variables are $c_p = 4.18 \times 10^3$ J kg^{-1} K^{-1}, $k = 0.6$ J m^{-1} s^{-1} K^{-1}, $\rho_m = 1000$ kg m^{-3}, and $v < 100$ μm/s [17,18]. This ratio of convective to conductive heat transfer is a form of the Nusselt number. Further, if we assume that the electric field is the only source of generated heat ($Q=0$), then Eq. (1) simplifies to

$$k\nabla^2 T + \langle \sigma |\boldsymbol{E}|^2 \rangle = 0 \tag{3}$$

This equation is used in numerical models to calculate Joule heating for the microsystem.

A similar nondimensional analysis can be applied to the above expression [17],

$$k\Delta T/l^2 \approx \sigma V_{\text{rms}}^2/l^2 \rightarrow \Delta T \approx \sigma V_{\text{rms}}^2/k \tag{4}$$

The above analysis shows that the change in temperature is proportional to the conductivity of the fluid medium (σ) and proportional to voltage squared (V^2). These electrothermal trends will be compared with the results from numerical simulations and experiments.

3 Theory of LIF Thermometry

For laser-induced fluorescence, the dependence of fluorescence radiation I_f on the concentration of the dye C can be expressed with

$$I_f = \beta_c \phi I_0 (1 - e^{-\varepsilon b C}) \tag{5}$$

where β_c, ϕ, I_0, ε, and b are the collection efficiency, quantum efficiency, incident irradiation, molar absorptivity, and absorption path length, respectively. Equation (5) can be simplified at low concentrations of the dye, when less than 5% of the incident irradiation is absorbed,

$$I_f = \beta_c \phi I_0 \varepsilon b C \tag{6}$$

Factors such as photobleaching, nonuniform illumination, nonuniform dye concentration, and fluctuations of light can all affect LIF measurements. Uncertainty due to illumination variations can be minimized using the two-color LIF method and ratiometric normalization methods. Typically RhB is the temperature-sensitive dye and Rh110 is the temperature-insensitive dye. However, Rh110 is, in fact, temperature-dependent ($\sim 0.1\%$ K^{-1}), just not as strongly as RhB ($\sim 2.0\%$ K^{-1}) [39]. The ratio of their fluorescent intensities can be written as

$$I_{\text{RhB}}/I_{\text{Rh110}} = \frac{\beta_{\text{CRhB}} \phi_{\text{RhB}} \varepsilon_{\text{RhB}} C_{\text{RhB}}}{\beta_{\text{CRh110}} \phi_{\text{Rh110}} \varepsilon_{\text{Rh110}} C_{\text{Rh110}}} \tag{7}$$

This expression is independent of incident irradiation (I_0) and absorption path length (b). The absorption spectral intensity ratio and the molar absorptivity ratio are nearly temperature-independent while the quantum efficiency ratio depends on temperature. If the fluorescence of the dyes does not depend on the pH of the solution, then this intensity ratio is only dependent on temperature for a fixed concentration ratio [42]. Proper R-LIFT measurements require careful calibration to correlate the fluorescence intensity ratio of the dyes to the temperature of the fluid.

The calculated normalized image $I_{\text{NR-LIFT}}$ for the R-LIFT can be expressed as

$$I_{\text{NR-LIFT}} = \frac{I_{\text{RhB}}/I_{\text{Rh110}}}{I_{0\text{–RhB}}/I_{0\text{–Rh110}}} \tag{8}$$

where $I_{0\text{–Rhb}}$ and $I_{0\text{–Rh110}}$ denote images for the two dyes at the reference temperature, and I_{Rhb} and I_{Rh110} are images for the two dyes at the measurement temperature. Assuming Rh110 is temperature-independent the image at the reference temperature $I_{0\text{–Rh100}}$ will be identical with the image at the measurement temperature I_{Rh100}. Equation (8) can be simplified to

$$I_{\text{N-LIFT}} = I_{\text{RhB}}/I_{0\text{–RhB}} \tag{9}$$

where a single image for the temperature-dependent dye at a reference temperature can be used to account for the nonuniform illumination as well as the normalization process. This normalization process, first utilized by Ross et al. [37], will be called N-LIFT to differentiate it from the NR-LIFT method. Since a single reference image is sufficient for all measurements, this method can be used to make instantaneous measurements with a single camera. The measurement region in the reference image needs to be identical to that in the measurement region. Also, if the optical path length changes during the experiment, this method cannot be used. The N-LIFT method is used here to determine the temperature of the fluid in a microsystem due to Joule heating in an ac electrokinetic chip.

4 Experimental

Experiments were conducted in a standard microparticle image velocimetry (μPIV) setup, as illustrated in Fig. 1. It consists of an upright microscope (Nikon Eclipse, ME600), an interline transfer charge coupled device (CCD) camera (Roper Scientific Photometrics, CoolSNAP HQ), and a Nikon mercury-arc lamp was used as the illumination source. Images were acquired with METAMORPH imaging software. Laser grade RhB (Acros Organics, Geel, Belgium) was dissolved in different conductivities of water. The dye was mixed in 1 ml of methanol beforehand to increase its solubility in water. The fluid samples were further prepared by dissolving

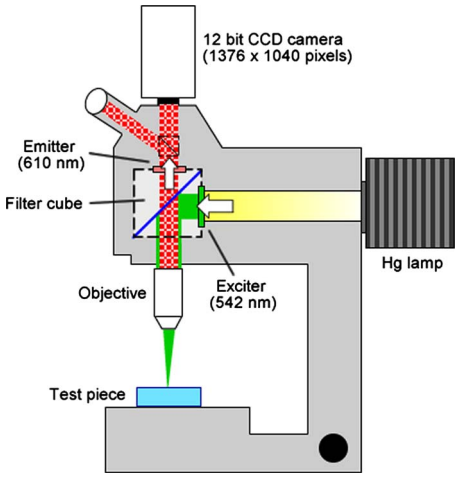

Fig. 1 LIF thermometry experimental setup

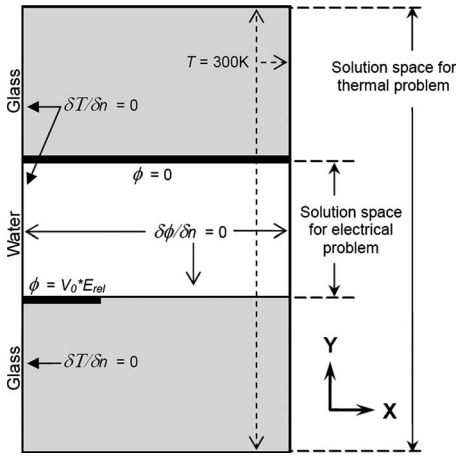

Fig. 3 Schematic of the electrical and thermal problem space and boundary conditions for the numerical model

different amounts of sodium chloride (NaCl) to change its electrical conductivity. Five samples were prepared (one without NaCl) and their conductivity was measured with a bench-top conductivity meter (Denver Instruments, Model 220). The RhB dye was excited with a filter ($\lambda \sim 542$ nm) attached to the front of the mercury-arc lamp.

The calibration experiments were conducted in a 400 μm square glass microchannel (Vitrocom, Inc., Mountain Lakes, NJ) submerged in a well machined from an aluminum block. The capillary was filled with the dye solution, sealed on both ends, and placed in the well. DI water filled the well and was sealed on top with an acrylic plate. The aluminum block was heated using a thermofoil resistance heater (Minco Products, Inc., Minneapolis, MN) and was enclosed in an insulating material. The temperature of the water bath (24–68 °C) was measured with a thermal couple at temperature intervals of 2 °C. The setup reached equilibrium temperature in approximately 10–15 min, at which the thermocouple showed a steady temperature reading.

The test chip is illustrated in Fig. 2. The top substrate is a transparent, electrically conductive indium tin oxide (ITO) coated glass substrate (0.71 mm thick) with fluidic ports manually drilled. The opposite substrate consists of four independently addressable ITO micro-electrode strips 20 μm wide, 3 mm long, and spaced by 20 μm. These ITO microband chips were commercially available (ABTECH Scientific Inc., Richmond, VA). The sheet resistance (R_s) of the ITO was specified by the manufacturer to be 10 Ω/sq. A microchannel was cut into a double-sided adhesive tape (Adhesives Research Inc., Glen Rock, PA) and provided a 50 μm spacer between the ITO substrates. The microchannel was approximately 1 mm wide and ran perpendicular to the length of the electrode strips. An ac signal (0–25 V_{pp}, 1.0 MHz) was applied across one electrode strip to a grounded ITO plane. The applied frequency of 1.0 MHz was chosen to prevent electrolysis that might otherwise have occurred at lower frequencies for our experiments [18].

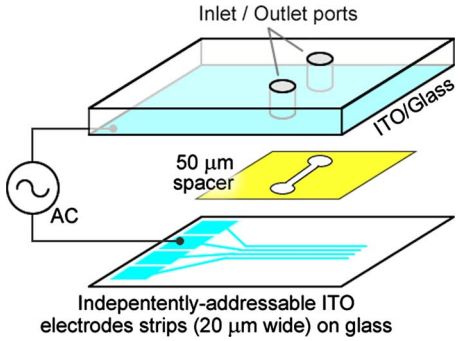

Fig. 2 ac electrokinetic chip for N-LIFT experiments

The temperature of the fluid medium was measured using a thermocouple and this value was used as the reference temperature. The fluid was manually injected into the chip and then adjusted until no bulk fluid motion was observed. At this time a reference temperature image ($I_{0-\mathrm{RhB}}$) was acquired. An ac signal was applied and, after a 1 min delay, five images were acquired within a 1 s time period. The fluorescent intensity of these images was averaged for a single temperature image (I_{RhB}). The signal was turned off and fresh solution was injected for the next trial. This process was repeated for each fluid conductivity sample ($\sigma = 0.918, 104, 200, 319, 390$ mS/m) and each applied voltage ($V_0 = 5, 10, 15, 20, 25$ V_{pp}).

5 Numerical Model

COMSOL MULTIPHYSICS was used for numerical modeling of the electrokinetic chip and simulate Joule heating. The problem space and boundary conditions for the electrical and thermal problems are modeled similarly to the work by Green et al. [16], and is shown schematically in Fig. 3. The thickness of the glass layers is 0.71 mm and fluid-filled spacing is 50 μm. Due to symmetry, the simulation is half of the electrokinetic chip, with only 10 μm of the electrode strip used. The width (x-direction) of the simulation space is extended until minimal changes in the numerical results were noticed (>1.0 mm).

The thermal and electrical problems are decoupled since induced fluid convection does not contribute to the thermal problem. The electrical problem is bounded to within the fluid medium. The Laplace equation for a potential (ϕ) in a homogeneous medium is first solved with [16]

$$\nabla^2 \phi = 0, \quad \boldsymbol{E} = -\nabla \phi \tag{10}$$

The boundary condition for the electrode strip V_0 refers to the rms value of the applied potential.

The ITO traces of the experimental chip cause a loss in the applied electric field. Electrical resistance of the ITO will reduce the applied potential (V_o) by a factor (E_{rel}). The geometry of the independently addressable ITO electrodes was incorporated into a computer model to determine this loss. This model included the ITO-coated glass and the liquid medium between the substrates.

For medium conductivities 0.918 mS/m, 104 mS/m, 200 mS/m, 319 mS/m, 390 mS/m, and 1 S/m, the calculated values of E_{rel} were 0.99, 0.92, 0.86, 0.81, 0.78, and 0.64, respectively. E_{rel} decreased with increasing fluid conductivity. This trend was ex-

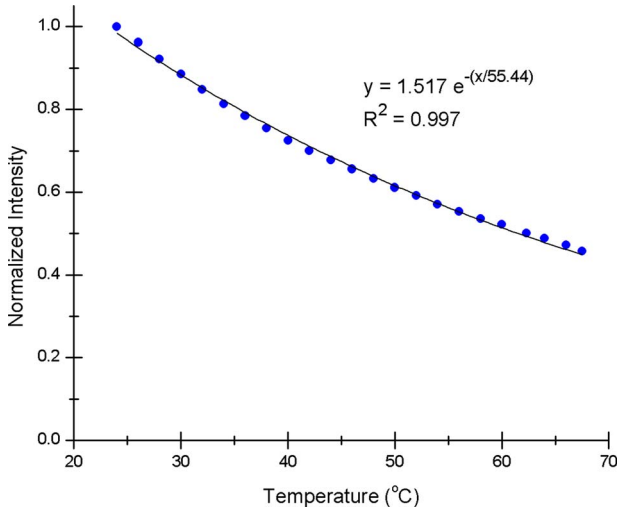

Fig. 4 Normalized fluorescence intensity for RhB

pected as the resistance across the medium decreases with larger fluid conductivities, resulting in a reduced value of the potential applied across the liquid. From Eq. (4) it is expected that the increase in temperature is proportional to the conductivity of the fluid; however, incorporation of E_{rel} will result in a nonlinear relationship. The manufactured ITO had a sheet resistance of 10 Ω/sq; if gold or a more conductive material was used for the electrodes there would be less electrical loss, leading to increased E_{rel} values.

The applied voltage in the numerical model was multiplied by this factor ($\phi = E_{rel}V_0$). After solving for the electric field, this value was used to solve the thermal problem in Eq. (3) with the values of the thermal conductivity (k) of water and glass being set at 0.6 J m^{-1} s^{-1} K^{-1} and 1.0 J m^{-1} s^{-1} K^{-1}, respectively.

6 Results and Discussion

The fluorescent intensity of the calibration images was normalized with the image acquired at room temperature (24°C, arbitrarily chosen) and shown in Fig. 4. The calibration data were

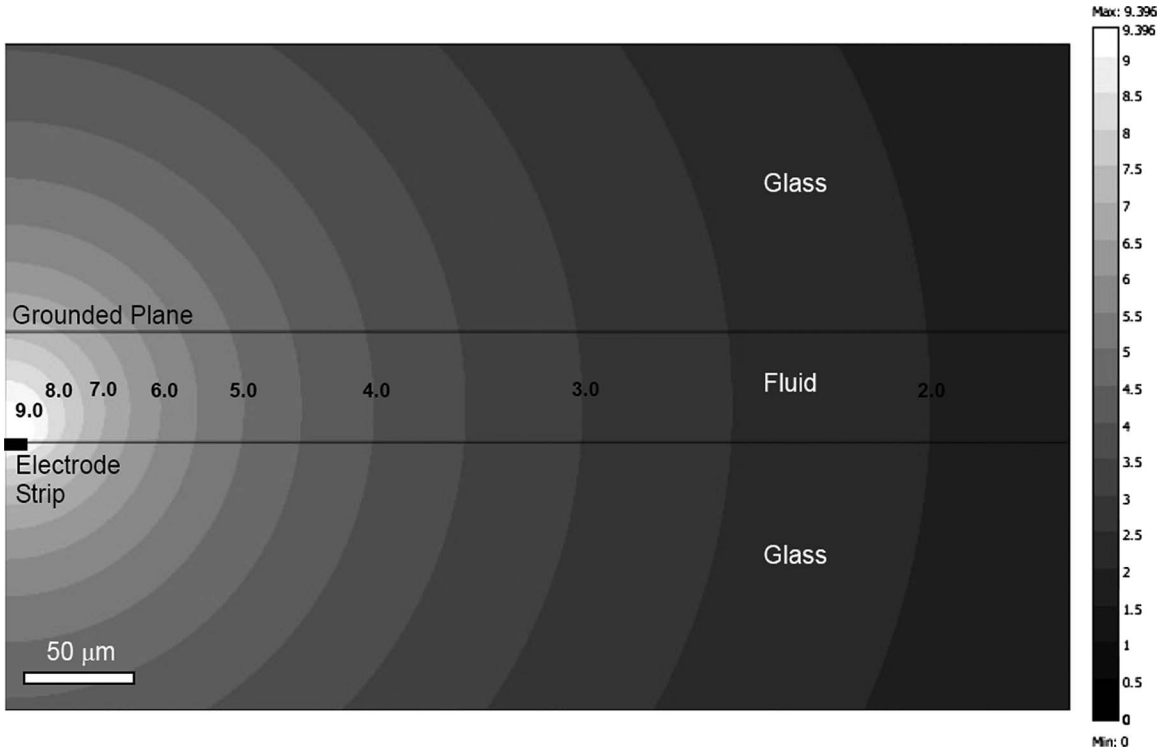

Fig. 5 A portion of the numerical simulation showing the increase in temperature due to Joule heating for a fluid sample with conductivity $\sigma = 200$ mS/m and applied voltage $V = 20$ V_{pp}

Table 1 Maximum temperature change from numerical simulations and experiments

Conductivity (mS/m)	Change in temperature									
	Simulations ($T_0 = 300$ K)					Experiment				
	Applied voltage (V_{pp})					Applied voltage (V_{pp})				
	5	10	15	20	25	5	10	15	20	25
0.918[a]	0.004	0.015	0.035	0.061	0.096	0.3	−0.4	−0.5	3.3	0.8
104	0.37	1.47	3.31	5.89	9.20	0.4	2.2	4.3	6.1	10.5
200	0.62	2.49	5.61	9.97	15.57	1.1	1.3	4.6	9.6	14.1
319	0.87	3.47	7.82	13.9	21.7	0.3	2.3	6.4	12.1	19.7
390	0.99	3.97	8.93	15.9	24.8	1.8	3.9	10.0	17.2	26.6
1000	1.70	6.81	15.3	27.2	42.6					

[a]No NaCl was added to the RhB solution.

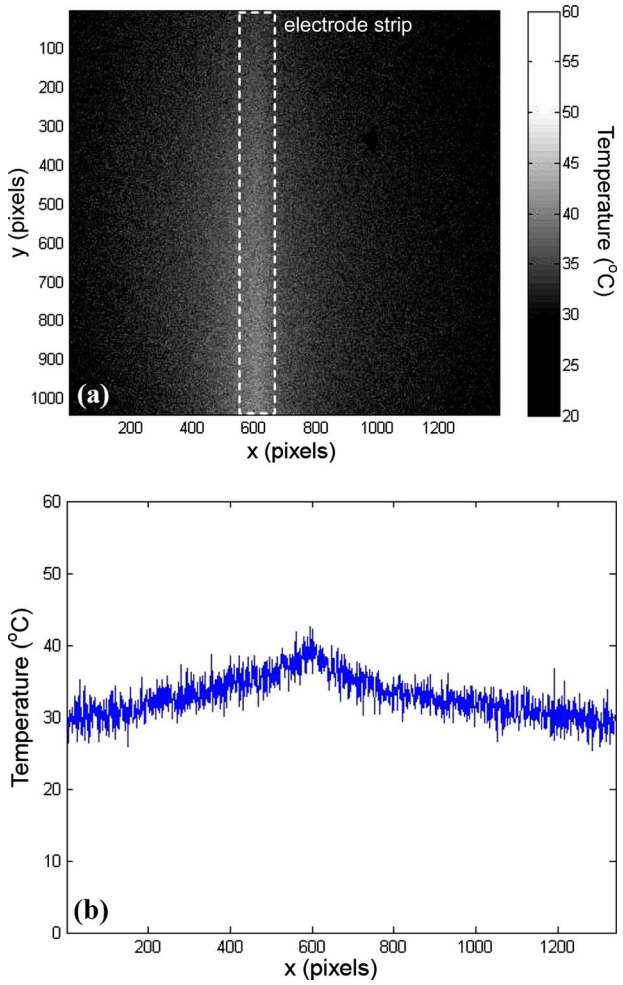

Fig. 6 (*a*) N-LIFT results showing the temperature increase in the medium (σ=200 mS/m) above the electrode strip at 25 V_{pp}. (*b*) Averaged temperature values across the strip.

fitted to an exponential decay, and this curve was used to determine the measured temperature from acquired images.

Numerical simulations were conducted for each of the five experimental fluid conductivities and five applied voltages. A zoomed-in plot for one of the simulations (200 mS/m, 20 V_{pp}) is shown in Fig. 5. The maximum temperature increase occurs at the interface of the electrode strip. The maximum value for the temperature increase from numerical simulations was recorded and compared with the maximum value obtained from experimental measurements (Table 1).

Figure 6(*a*) shows a normalized image obtained from N-LIFT (top-view) with the electrode strip running vertically along the length of the image for σ=200 mS/m and V=25 V_{pp}. The temperature values perpendicular to the electrode strip were averaged, Figure 6(*b*) shows the resulting temperature profile. The maximum temperature increase was recorded and compared with numerical simulations (Table 1).

Table 1 shows the maximum temperature change from both numerical simulations and experiments. To illustrate the Joule heating trends of these obtained values, Fig. 7 shows the temperature increase plotted against voltage squared (V_{pp}^2) for each conductivity, and Fig. 8 has temperature increase versus medium conductivity. Experimental measurements are shown with points while numerical simulation values are shown with a solid line and labeled with parentheses.

The experimental data follow the expected trend that temperature is proportional to the square of the applied voltage (V^2).

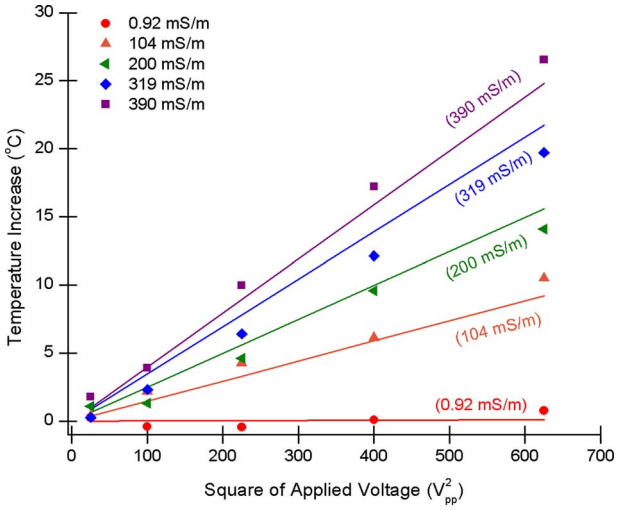

Fig. 7 Obtained maximum change in temperature values versus voltage squared obtained from N-LIFT experiments (data points) and numerical simulations (lines)

Theory also states that temperature change is proportional to fluid conductivity; however, the resulting curve (Fig. 8) is nonlinear due to the loss of the applied field to the ITO traces. The loss in electric field increased with greater fluid conductivity. Joule heating is negligible for the fluid sample with conductivity 0.918 mS/m, and trends could not be identified with LIF thermometry. In addition, simulations calculated the expected increase in temperature for this low conductive solution at 25 V_{pp} was less than 0.1°C. The maximum measured temperature change of 26.6°C occurred with the 390 mS/m fluid sample at 25 V_{pp}. However, typical biological growth media have conductivities greater than 1 S/m. For example, phosphate-buffered saline (PBS) and Dulbecco's modified eagle medium (DMEM) each have an electrical conductivity greater than 1 S/m [43]. Numerical simulations calculated a temperature increase of almost 1.7°C for a 1 S/m sample at 5 V_{pp} and over 42°C at 25 V_{pp} (Table 1). Therefore any temperature-sensitive electrokinetic microsystem with biological growth media or other high-conductivity fluid needs to be carefully monitored for Joule heating.

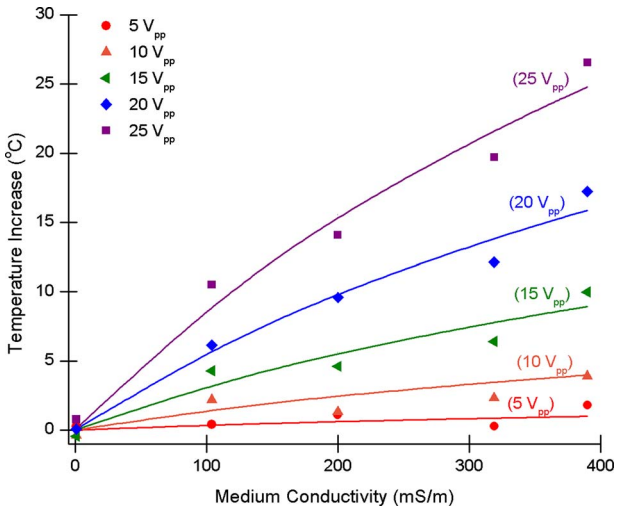

Fig. 8 Obtained maximum change in temperature values versus conductivity obtained from N-LIFT experimental measurements (data points) and numerical simulations (lines)

Electrokinetically induced fluid flow was readily observed visually for all but the least conductive fluid sample with applied voltages of 20 V_{pp} and 25 V_{pp}. This fluid flow is a combination of electrothermal hydrodynamics and ACEO. Microfluidic measurement techniques such as μPIV could be utilized to quantify and characterize this electrokinetic fluid velocity. The aim of future experiments will investigate the impact of Joule heating on electrokinetically induced flow. This flow can disrupt any intended fluid flow in microfluidic systems, especially at high applied voltages.

The thermal noise present in the camera and the uncertainty involved in the calibration curve are the two main sources of error in this technique. The uncertainty involved in the calibration curve represents the accuracy of the method while the thermal noise represents the variation in the measurements. The error involved in the measurement of temperature e_T can be expressed as

$$e_T = \pm \{(e_C)^2 + (e_N)^2\}^{1/2} \tag{11}$$

where e_C is the error involved in the calibration curve and e_N is error due to thermal noise. The error due to the thermal noise e_N, defined as the standard deviation of the single-pixel measurement, was $\pm 1.1\,^{\circ}$C for the N-LIFT method. The uncertainty involved in the calibration curve depends on the difference between the normalization temperature and the measured temperature increases. The mean uncertainty involved in the calibration curve e_C was measured to be $\pm 0.6\,^{\circ}$C. The total error in the measurement of temperature was estimated to be $\pm 1.25\,^{\circ}$C for the N-LIFT method. This uncertainty is less than measurements with a similar, two-color normalization method (NR-LIFT) under similar experimental conditions. Additional error is introduced with the NR-LIFT method from single-pixel measurements of both dyes, as opposed to one dye in the method described herein. In addition, Rh110 is slightly temperature-dependent ($\sim 0.2\%/\,^{\circ}$C), introducing additional error, especially at higher temperatures. Therefore, the N-LIFT method has less uncertainty than the NR-LIFT method. However, one drawback is the introduction of uncertainties when comparing the acquired image to only one reference image at a known temperature, especially at measured temperatures much greater than the reference temperature.

These uncertainties are for single-pixel measurements. The error due to the thermal noise can be reduced by averaging over larger areas. For the recorded temperatures (Table 1), e_N can be effectively neglected as it was averaged over a large number of pixels. Hence, the uncertainty involved in the N-LIFT measurements will be e_C, $\pm 0.6\,^{\circ}$C.

ac electrokinetic techniques such as DEP and ACEO are utilized for lab-on-a-chip microsystems due to their inherently strong electric fields; however, these electric fields heat the fluid sample. Monitoring Joule heating effects is especially important for temperature-sensitive experiments and biological samples. LIF thermometry utilizing the N-LIFT method is a simple procedure to noninvasively measure Joule heating effects. In addition, numerical simulations can assist in designing proper electrokinetic chips to minimize unwanted Joule heating.

7 Conclusions

A LIF normalization procedure that requires a single dye [37] was used to determine Joule heating in a simple ac electrokinetic chip. Fluid samples of various conductivities (0.918 mS/m, 104 mS/m, 200 mS/m, 314 mS/m, and 390 mS/m) were subjected to electric potentials from 5 V_{pp} to 25 V_{pp} at 1 MHz. Numerical simulations were in good agreement with experimental measurements. Further, experimental data verified expected theoretical trends that temperature is proportional to the square of the applied voltage squared (V^2).

Acknowledgment

S.J.W. acknowledges support under a National Science Foundation Graduate Research Fellowship and a Purdue University's Laura Winkelman Fellowship for Doctoral Studies in the School of Mechanical Engineering.

References

[1] Pohl, H. A., 1978, *Dielectrophoresis: The Behavior of Neutral Matter in Nonuniform Electric Fields*, Cambridge University Press, Cambridge.

[2] Müller, T., Gerardino, A., Schnelle, T., Shirley, S. G., Bordoni, F., De Gasperis, G., Leoni, R., and Fuhr, G., 1996, "Trapping of Micrometre and Sub-Micrometre Particles by High-Frequency Electric Fields and Hydrodynamic Forces," J. Phys. D: Appl. Phys., **29**, pp. 340–349.

[3] Schnelle, T., Muller, T., Gradl, G., Shirley, S. G., and Fuhr, G., 2000, "Dielectrophoretic Manipulation of Suspended Submicron Particles," Electrophoresis, **21**, pp. 66–73.

[4] Holzel, R., Gajovic-Eichelmann, N., and Bier, F. F., 2003, "Oriented and Vectorial Immobilization of Linear M13 dsDNA Between Interdigitated Electrodes—Towards Single Molecule DNA Nanostructures," Biosens. Bioelectron., **18**, pp. 555–564.

[5] Morgan, H., Hughes, M. P., and Green, N. G., 1999, "Separation of Submicron Bioparticles by Dielectrophoresis," Biophys. J., **77**, pp. 516–525.

[6] Li, H. B., Zheng, Y. N., Akin, D., and Bashir, R., 2005, "Characterization and Modeling of a Microfluidic Dielectrophoresis Filter for Biological Species," J. Microelectromech. Syst., **14**, pp. 103–112.

[7] Ajdari, A., 2000, "Pumping Liquids Using Asymmetric Electrode Arrays," Phys. Rev. E, **61**, pp. R45–R48.

[8] Studer, V., Pepin, A., Chen, Y., and Ajdari, A., 2004, "An Integrated AC Electrokinetic Pump in a Microfluidic Loop for Fast and Tunable Flow Control," Analyst (Cambridge, U.K.), **129**, pp. 944–949.

[9] Suehiro, J., and Pethig, R., 1998, "The Dielectrophoretic Movement and Positioning of a Biological Cell Using a Three-Dimensional Grid Electrode System," J. Phys. D: Appl. Phys., **31**, pp. 3298–3305.

[10] Gray, D. S., Tan, J. L., Voldman, J., and Chen, C. S., 2004, "Dielectrophoretic Registration of Living Cells to a Microelectrode Array," Biosens. Bioelectron., **19**, pp. 771–780.

[11] Huang, Y., and Pethig, R., 1991, "Electrode Design for Negative Dielectrophoresis," Meas. Sci. Technol., **2**, pp. 1142–1146.

[12] Schnelle, T., Muller, T., and Fuhr, G., 2000, "Trapping in AC Octode Field Cages," J. Electrost., **50**, pp. 17–29.

[13] Schnelle, T., Hagedorn, R., Fuhr, G., Fiedler, S., and Muller, T., 1993, "Three-Dimensional Electric-Field Traps for Manipulation of Cells—Calculation and Experimental-Verification," Biochim. Biophys. Acta, **1157**, pp. 127–140.

[14] Yang, L., Banada, P. P., Bhunia, A. K., and Bashir, R., 2008, "Effects of Dielectrophoresis on Growth, Viability and Immuno-Reactivity of *Listeria Monocytogenes*," Journal of Biological Engineering, 2:6.10.1186/1754-1611-2-6

[15] Green, N. G., Ramos, A., Gonzalez, A., Castellanos, A., and Morgan, H., 2000, "Electric Field Induced Fluid Flow on Microelectrodes: The Effect of Illumination," J. Phys. D: Appl. Phys., **33**, pp. L13–L17.

[16] Green, N. G., Ramos, A., Gonzalez, A., Castellanos, A., and Morgan, H., 2001, "Electrothermally Induced Fluid Flow on Microelectrodes," J. Electrost., **53**, pp. 71–87.

[17] Ramos, A., Morgan, H., Green, N. G., and Castellanos, A., 1998, "Ac Electrokinetics: A Review of Forces in Microelectrode Structures," J. Phys. D: Appl. Phys., **31**, pp. 2338–2353.

[18] Castellanos, A., Ramos, A., Gonzalez, A., Green, N. G., and Morgan, H., 2003, "Electrohydrodynamics and Dielectrophoresis in Microsystems: Scaling Laws," J. Phys. D: Appl. Phys., **36**, pp. 2584–2597.

[19] Jaeger, M. S., Mueller, T., and Schnelle, T., 2007, "Thermometry in Dielectrophoresis Chips for Contact-Free Cell Handling," J. Phys. D: Appl. Phys., **40**, pp. 95–105.

[20] Lee, P. S., Garimella, S. V., and Liu, D., 2005, "Investigation of Heat Transfer in Rectangular Microchannels," Int. J. Heat Mass Transfer, **48**, pp. 1688–1704.

[21] Chen, T. L., and Garimella, S. V., 2006, "Measurements and High-Speed Visualizations of Flow Boiling of a Dielectric Fluid in a Silicon Microchannel Heat Sink," Int. J. Multiphase Flow, **32**, pp. 957–971.

[22] Jang, S. P., Kim, S. J., and Paik, K. W., 2003, "Experimental Investigation of Thermal Characteristics for a Microchannel Heat Sink Subject to an Impinging Jet, Using a Micro-Thermal Sensor Array," Sens. Actuators, A, **105**, pp. 211–224.

[23] Jiang, L. N., Wang, Y. L., Wong, M., and Zohar, Y., 1999, "Fabrication and Characterization of a Microsystem for a Micro-Scale Heat Transfer Study," J. Micromech. Microeng., **9**, pp. 422–428.

[24] Sammarco, T. S., and Burns, M. A., 1999, "Thermocapillary Pumping of Discrete Drops in Microfabricated Analysis Devices," AIChE J., **45**, pp. 350–366.

[25] Höhmann, C., and Stephan, P., 2002, "Microscale Temperature Measurement at an Evaporating Liquid Meniscus," Exp. Therm. Fluid Sci., **26**, pp. 157–162.

[26] Fujisawa, N., Funatani, S., and Katoh, N., 2005, "Scanning Liquid-Crystal Thermometry and Stereo Velocimetry for Simultaneous Three-Dimensional Measurement of Temperature and Velocity Field in a Turbulent Rayleigh-Bérnard Convection," Exp. Fluids, **38**, pp. 291–303.

[27] Nozaki, T., Mochizuki, T., Kaji, N., and Mori, Y. H., 1995, "Application of

Liquid-Crystal Thermometry to Drop Temperature-Measurements," Exp. Fluids, **18**, pp. 137–144.
[28] Richards, C. D., and Richards, R. F., 1998, "Transient Temperature Measurements in a Convectively Cooled Droplet," Exp. Fluids, **25**, pp. 392–400.
[29] Hetsroni, G., Gurevich, M., Mosyak, A., Pogrebnyak, E., Rozenblit, R., and Yarin, L. P., 2003, "Boiling in Capillary Tubes," Int. J. Multiphase Flow, **29**, pp. 1551–1563.
[30] Hetsroni, G., Mosyak, A., and Segal, Z., 2001, "Nonuniform Temperature Distribution in Electronic Devices Cooled by Flow in Parallel Microchannels," IEEE Trans. Compon. Packag. Technol., **24**, pp. 16–23.
[31] Chamarthy, P., Garimella, S. V., and Wereley, S. T., 2009, "Non-Intrusive Temperature Measurement Using Microscale Visualization Techniques," Exp. Fluids, **47**, pp. 159–170.
[32] Hohreiter, V., Wereley, S. T., Olesen, M. G., and Chung, J. N., 2002, "Cross-Correlation Analysis for Temperature Measurement," Meas. Sci. Technol., **13**, pp. 1072–1078.
[33] Olsen, M. G., and Adrian, R. J., 2000, "Brownian Motion and Correlation in Particle Image Velocimetry," Opt. Laser Technol., **32**, pp. 621–627.
[34] Park, J. S., Choi, C. K., and Kihm, K. D., 2005, "Temperature Measurement for Nanoparticle Suspension by Detecting the Brownian Motion Using Optical Serial Sectioning Microscopy (OSSM)," Meas. Sci. Technol., **16**, pp. 1418–1429.
[35] Kim, H. J., and Kihm, K. D., 2002, "Two-Color (Rh-B & Rh-110) Laser Induced Fluorescence (LIF) Thermometry With Sub-Millimeter Measurement Resolution," ASME J. Heat Transfer, **124**, p. 596.
[36] Kim, H. J., Kihm, K. D., and Allen, J. S., 2003, "Examination of Ratiometric Laser Induced Fluorescence Thermometry for Microscale Spatial Measurement Resolution," Int. J. Heat Mass Transfer, **46**, pp. 3967–3974.
[37] Ross, D., Gaitan, M., and Locascio, L. E., 2001, "Temperature Measurement in Microfluidic Systems Using a Temperature-Dependent Fluorescent Dye," Anal. Chem., **73**, pp. 4117–4123.
[38] Coolen, M. C. J., Kieft, R. N., Rindt, C. C. M., and van Steenhoven, A. A., 1999, "Application of 2-D LIF Temperature Measurements in Water Using a Nd: YAG laser," Exp. Fluids, **27**, pp. 420–426.
[39] Sakakibara, J., and Adrian, R. J., 1999, "Whole Field Measurement of Temperature in Water Using Two-Color Laser Induced Fluorescence," Exp. Fluids, **26**, pp. 7–15.
[40] Natrajan, V. K., and Christensen, K. T., 2009, "Two-Color Laser-Induced Fluorescent Thermometry for Microfluidic Systems," Meas. Sci. Technol., **20**, 015401.
[41] Pramod, C., Wereley, S. T., and Garimella, S. V., 2007, "Microscale Laser-Induced Fluorescence Method for Non-Intrusive Temperature Measurement," ASME International Mechanical Engineering Congress and Exposition, Seattle, WA.
[42] Guilbault, G. G., 1973, *Practical Fluorescence; Theory, Methods, and Techniques*, Dekker, New York.
[43] Fuhr, G., Mueller, T., Baukloh, V., and Lucas, K., 1998, "High-Frequency Electric Field Trapping of Individual Human Spermatozoa," Hum. Reprod., **13**, pp. 136–141.

C. G. Giannopapa
e-mail: c.g.giannopapa@tue.nl

J. M. B. Kroot

A. S. Tijsseling

Department of Mathematics and Computer Science,
Eindhoven University of Technology,
P.O. Box 513,
5600 MB Eindhoven, The Netherlands

M. C. M. Rutten

F. N. van de Vosse

Department of Biomedical Engineering,
Eindhoven University of Technology,
P.O. Box 513,
5600 MB Eindhoven, The Netherlands

Wave Propagation in Thin-Walled Aortic Analogues

Research on wave propagation in liquid filled vessels is often motivated by the need to understand arterial blood flows. Theoretical and experimental investigation of the propagation of waves in flexible tubes has been studied by many researchers. The analytical one-dimensional frequency domain wave theory has a great advantage of providing accurate results without the additional computational cost related to the modern time domain simulation models. For assessing the validity of analytical and numerical models, well defined in vitro experiments are of great importance. The objective of this paper is to present a frequency domain analytical model based on the one-dimensional wave propagation theory and validate it against experimental data obtained for aortic analogs. The elastic and viscoelastic properties of the wall are included in the analytical model. The pressure, volumetric flow rate, and wall distention obtained from the analytical model are compared with experimental data in two straight tubes with aortic relevance. The analytical results and the experimental measurements were found to be in good agreement when the viscoelastic properties of the wall are taken into account.
[DOI: 10.1115/1.4000792]

Keywords: artery, viscoelastic, wave propagation, analytical method, frequency domain, in vitro experiments

1 Introduction

Wave propagation in liquid filled vessels was studied for over 200 years, and one motivation is to understand arterial blood flows [1–3]. Other studies involve applications in civil, biomedical, and mechanical engineering.

The firm basis of the theoretical investigation of wave propagation in tubes is related to the work of Womersley [4], even though Young [5] was one of the first investigators interested in understanding the transient motion of fluids in pipes, elastic tubes, conical vessels, and blood circulation; see also Ref. [6]. During the 1960s, there was a large activity in the scientific communities related to analytical solutions of the equations of motion of viscous, incompressible fluids in the frequency domain. This work is summarized by Cox [7]. A lot of questions related to the physiological fluid dynamics were addressed by the work of Lighthill [8].

In the last 4 decades, with the advancement of scientific computing, the interest of the scientific community has shifted toward a more complicated two-dimensional and three-dimensional computer simulation time domain models, solved using finite elements or finite volumes [9–16]. The major drawback of these methods is increased computational time, compared with one-dimensional domain analytical models. In Ref. [16], a time domain based one-dimensional model was presented to be used to provide boundary conditions for fully three-dimensional computations.

Experimental measurements have been performed to better understand wave propagation phenomena and to validate analytical and numerical models. An extensive review of the work in the field is by Tijsseling [17]. von Kries [18] was one of the first investigators to perform wave propagation experiments in rubber hoses. The work of Klip [19] was the first attempt to validate the Womersley theory. Up until the work of Gerrard [20], the Womersley theory [4] had only been tested for tethered tubes. Gerrard was interested in determining the behavior of long tubes where the longitudinal motion was present. In the work of Giannopapa [21], a complete experimental data set measured in aortic analogs was presented.

Most of the experimental work on wave propagation in liquid filled tubes does not consider vessels with wall thickness less than 1 mm as aortic analogs. This is due to the fact that such tubes, which can produce wave speeds as low as those in the aorta, are not commercially available and need specific manufacturing. However, measurements in thinner wall tubes can provide relevant validation data for computational and analytical methods where the wall thickness to diameter ratio reduces significantly. In Ref. [21], tubes with relevant aortic dimensions, as provided by Westerhof et al. [22], were manufactured and used in order to obtain pressure, pressure gradient, volumetric flow rate, and wall distention measurements.

Predicting and understanding pressure and flows in aortic analogs are of significant importance because they are often used for medical diagnostics related to the cardiovascular system. As the heart beats, a pressure wave is initiated due to the injection of a volume of blood into the arterial system. The arteries distend to accommodate the change in volume, and the wave propagates along the aorta into the main arteries.

The aim of this paper is to present a one-dimensional analytical method for predicting pressure, volumetric flow rate, and wall distention, and compare it with in vitro experiments in liquid filled viscoelastic tubes of aortic relevance. The analytical model presented in this paper is based on the one-dimensional linear theory in the frequency domain for wave propagation in elastic and viscoelastic vessels. The experimental measurements are performed in elastic tubes that have the same dimensions as the aorta, but yet without tapering. The wave speed of the traveling wave is of the same order as the one in the aorta. The measured quantities are pressure, volumetric flow rate, and wall distention.

2 Mathematical Formulation

The theory related to propagation of pressure disturbances in distensible vessels for a circular uniform tube is often referred to as the Womersley theory or linear theory, and is outlined below.

Contributed by the Fluids Engineering Division of ASME for publication in the JOURNAL OF FLUIDS ENGINEERING. Manuscript received June 23, 2008; final manuscript received December 7, 2009; published online February 4, 2010. Assoc. Editor: Dimitris Drikakis.

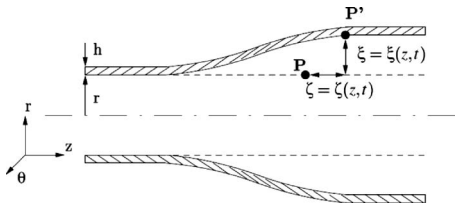

Fig. 1 Tube motion variables. Point $P(z,r)$ on the surface of the wall at rest displaces to position $P'(z+\zeta, r+\xi)$.

2.1 Linear Theory of Wave Propagation in Flexible Vessels. Consider a flexible tube filled with water; see Fig. 1. A disturbance in a fluid filled tube propagates as a wave. The wave speed in the fluid is given by the Moens–Korteweg equation [23]

$$c = \sqrt{\frac{K}{\rho_f}\left(1 + \psi\frac{2r_0}{h}\frac{K}{E}\right)^{-1}} \tag{1}$$

where K is the bulk modulus, ρ_f is the mass density of the fluid, r_0 is the initial radius of the tube, h is the wall thickness, E is the Young's modulus, and ψ is a coefficient that accounts for different longitudinal support conditions for thin-walled and thick-walled tubes. The thin-wall assumption holds when the wall thickness over the inner diameter is less than 1/20. In the case were the tube wall is very flexible $K \gg E$, Eq. (1) reduces to

$$c_0 = \sqrt{\psi^{-1}\frac{Eh}{2r_0\rho_f}} \tag{2}$$

The momentum equation and the continuity equation for incompressible Newtonian fluids in a uniform elastic tube under the assumption that the flow is axisymmetric, and neglecting body forces can be solved in the frequency domain after linearization. Note that possible developing boundary layers are not considered because the 1D calculations are already in good agreement with the measurements, as shown later on.

Momentum equation

$$\rho\left(\frac{\partial \mathbf{U}}{\partial t} + \nabla(\mathbf{U}\mathbf{U})\right) = \nabla \cdot \boldsymbol{\sigma} \tag{3}$$

Continuity equation or mass conservation

$$\nabla \cdot \mathbf{U} = 0 \tag{4}$$

Here, $\mathbf{U}$ stands for the velocity field and $\boldsymbol{\sigma}$ for the stress tensor. These equations form the basis, from which Womersley [4] derives his linear theory.

For Newtonian fluids, the constitutive equation for the stress tensor $\boldsymbol{\sigma}$ is given by

$$\boldsymbol{\sigma} = 2\eta\,\mathrm{dev}(\dot{\boldsymbol{\varepsilon}}) - p\mathbf{I} = \eta(\nabla\mathbf{U} + \nabla\mathbf{U}^T) - p\mathbf{I} \tag{5}$$

where η is the dynamic viscosity, $\dot{\boldsymbol{\varepsilon}}$ is the strain rate tensor, p is the pressure, and dev(.) is the deviatoric part of the tensor. Substituting Eq. (5) into Eq. (3), the momentum equation can be rewritten as

$$\rho\frac{\partial \mathbf{U}}{\partial t} = \nabla \cdot \eta(\nabla\mathbf{U} + \nabla\mathbf{U}^T) - \rho\,\nabla(\mathbf{U}\mathbf{U}) - \nabla p \tag{6}$$

The wavelength λ ($\lambda = 2\pi c/\omega$) of the disturbance of interest is assumed to be long, compared with the diameter $2r_0$ of the tube ($\lambda/(2r_0) \gg 1$). It is convenient to make the Navier–Stokes equations nondimensional. Therefore, consider U_z^* and U_r^* as typical velocities in the axial (z) and radial (r) direction, respectively. The ratio between the two velocities is defined by $u^* = U_r^*/U_z^*$, and in the following treatment, u^* is considered to be small. Provided that $|U_r^*/c| \ll 1$ and $|U_z^*/c| \ll 1$, the convective terms plus all velocity derivatives in the z-direction in the momentum equation can be neglected. The nonlinear form of the Navier–Stokes equation (6) in cylindrical coordinates under axisymmetric conditions (θ-direction neglected) can therefore be reduced to

$$\rho\frac{\partial U_r}{\partial t} + \frac{\partial p}{\partial r} = \eta\left[\frac{\partial^2 U_r}{\partial r^2} + \frac{1}{r}\frac{\partial U_r}{\partial r} - \frac{U_r}{r^2}\right] \tag{7}$$

$$\rho\frac{\partial U_z}{\partial t} + \frac{\partial p}{\partial z} = \eta\left[\frac{\partial^2 U_z}{\partial r^2} + \frac{1}{r}\frac{\partial U_z}{\partial r}\right] \tag{8}$$

The continuity equation in an incompressible fluid reads

$$\frac{1}{r}\frac{\partial (rU_r)}{\partial r} + \frac{\partial U_z}{\partial z} = 0 \tag{9}$$

To be able to integrate over a tube's cross section, appropriate boundary conditions must be specified. At the wall at r_0, the no-slip and no-leak conditions apply. It is assumed that there is no boundary layer effect (negligible in the sizes used) and no axial movement; a hypothesis, which also has an in-vivo relevance in blood flow [24]. Thus

$$U_z|_{r_0} = 0 \tag{10}$$

Axisymmetry requires

$$U_r|_{r=0} = \left.\frac{\partial U_z}{\partial r}\right|_{r=0} = 0 \tag{11}$$

In linear theory, the wave solution can be expressed as a combination of harmonics with angular frequency ω and wave number k. Therefore, each harmonic φ (where φ can be p, U_r, U_z) is of the form

$$\varphi = \hat{\varphi} e^{i(\omega t - kz)} \tag{12}$$

In an elastic tube, the propagation constants are functions of the nondimensional frequency. This nondimensional frequency is called the Womersley number α, which is also known as the Stokes number; see, e.g., Ref. [25]. It is defined as

$$\alpha = r_0\sqrt{\frac{\omega\rho}{\eta}} \tag{13}$$

The combination of the Navier–Stokes equations for the fluid and the equation of motion for the solid, including its constitutive equations, gives a dispersion equation otherwise called frequency equation; see also Ref. [4]. The solution of the frequency equation determines the wave number of propagation k as a function of the mechanical and geometrical properties of the tube, the density and the viscosity of the fluid, and the Womersley number α

$$k(\omega) = \pm\frac{\omega}{c_0}\sqrt{\frac{1}{1 - F_{10}}} \tag{14}$$

where c_0 is the wave speed and F_{10} is a function of the Womersley parameter α

$$F_{10} = \frac{2J_1(\alpha i^{3/2})}{\alpha i^{3/2} J_0(\alpha i^{3/2})} \tag{15}$$

with J_0 and J_1 as the Bessel functions of the first kind of order 0 and 1, respectively. The two roots given by Eq. (14) are complex numbers, and therefore, the propagation coefficient k can be expressed as $k = \Re(k) + i\Im(k)$, where the root is chosen, such that $\Re(k) > 0$. Using this expression for the wave number, the wave speed c and the attenuation constant γ are functions of the classical Moens–Korteweg wave speed c_0 and the real part of the propagation coefficient, namely

$$c = \frac{c_0}{\Re(k)} \tag{16}$$

and the attenuation constant given by

Fig. 2 Schematic of axial positions of a tube with closed ends, used in the 1D model

$$\gamma = \frac{-2\pi\Im(k)}{\Re(k)} \tag{17}$$

2.2 Wave Reflections at Closed Ends. Section 2.1 describes the transmission of a wave in a cylindrical infinitely long tube filled with a fluid with uniform properties. In practice however, a tube has two ends and a finite length. At the ends, the waves will be reflected. This section describes how the reflecting waves can be determined.

A tube of length L is considered starting at $z=-L_0$ and ending at $z=L_1$ (i.e., $L=L_0+L_1$), as shown in Fig. 2. If an input pressure p_i is applied at $z=0$ in the positive direction, then a wave will travel through the tube and will be reflected at $z=L_1$. A continuous harmonic pressure excitation with frequency ω is assumed.

The first time this wave arrives at $z=z_1$, the pressure is the real part of

$$p(\omega,z_1,t) = p_i(\omega,0)e^{i(\omega t-kz_1)} \tag{18}$$

Note that the notation of taking the real part is omitted in this equation, as well as in all of the following equations, for the sake of readability. At $z=L_1$, the pressure due to the wave is

$$p(\omega,L_1,t) = p_i(\omega,0)e^{i(\omega t-kL_1)} \tag{19}$$

The wave is reflected at the distal closed end. Let the reflection parameter be denoted by Γ_1. The reflected wave travels in the negative direction, and at $z=z_1$, the pressure is

$$p(\omega,z_1,t) = p_i(\omega,0)\Gamma_1 e^{i(\omega t-k(2L_1-z_1))} \tag{20}$$

When this wave reaches $z=-L_0$, the pressure is

$$p(\omega,-L_0,t) = p_i(\omega,0)\Gamma_1 e^{i(\omega t-k(2L-L_0))} \tag{21}$$

and the wave gets reflected again due to the proximal closed end. Let the reflection parameter be denoted by Γ_0. When the reflected wave reaches $z=z_1$ for the third time, the pressure is

$$p(\omega,z_1,t) = p_i(\omega,0)\Gamma_0\Gamma_1 e^{i(\omega t-k(2L+z_1))} \tag{22}$$

This process continues. The pressure perturbation in the tube is the sum of all reflected waves

$$p(\omega,z_1,t) = p_i(\omega,0)e^{i(\omega t-kz_1)}[1+\Gamma_1 e^{-2ik(L-L_0-z_1)}+\Gamma_0\Gamma_1 e^{-2ikL} + \Gamma_0\Gamma_1^2 e^{-2ik(2L-L_0-z_1)}+\ldots] \tag{23}$$

or, for recursive purposes

$$p(\omega,z_1,t) = p_i(\omega,0)e^{i(\omega t-kz_1)}[1+\Gamma_1 e^{-2ik(L_1-z_1)} \times(1+\Gamma_0 e^{-2ik(L_0+z_1)}(1+\Gamma_1 e^{-2ik(L_1-z_1)}(\ldots)))] \tag{24}$$

Assembling the terms that represent waves in the positive direction and, separately, those representing waves in the negative direction, the expression for pressure can be written as

$$p(\omega,z_1,t) = p_i(\omega,0)e^{i(\omega t-kz_1)}\frac{1+\Gamma_1 e^{-2ik(L_1-z_1)}}{1-\Gamma_0\Gamma_1 e^{-2ikL}} \tag{25}$$

Here, the geometric series expansion of $1/(1-x)$ is used. This is a general result. For the special case of total reflection at the two ends, $\Gamma_0=\Gamma_1=1$ holds and

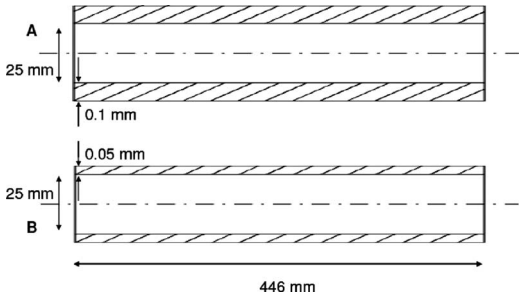

Fig. 3 Polyurethane vessels

$$p(\omega,z_1,t) = p_i(\omega,0)e^{i(\omega t+kL_0)}\frac{\cos k(L_1-z_1)}{i\sin kL} \tag{26}$$

The volumetric flow rate $\dot{Q}$ follows directly from Eq. (23) by taking into account the direction of the propagation

$$\dot{Q}(\omega,z_1,t) = \dot{Q}_i(\omega,0)e^{i(\omega t-kz_1)}[1-\Gamma_1 e^{-2ik(L-L_0-z_1)}+\Gamma_0\Gamma_1 e^{-2ikL} - \Gamma_0\Gamma_1^2 e^{-2ik(2L-L_0-z_1)}+\ldots] \tag{27}$$

Here, $\dot{Q}_i(\omega,0)$ represents the input volumetric flow rate. For the special case of total reflection, this yields

$$\dot{Q}(\omega,z_1,t) = \dot{Q}_i(\omega,0)e^{i(\omega t+kL_0)}\frac{\sin k(L_1-z_1)}{\sin kL} \tag{28}$$

Using a linear elastic material law based on the thin walled cylinder theory, the cross-sectional area changes according to

$$\frac{\partial A}{\partial t} = C_0\frac{\partial p}{\partial t} \tag{29}$$

with C_0 as the compliance per unit of length of the vessel

$$C_0 = \frac{2\pi(1-\nu^2)r^3}{hE} \tag{30}$$

and ν as the Poisson ratio. Thus, the cross-sectional area can be derived from the pressure by

$$A(\omega,z_1,t) = A_0(\omega,z_1)+C_0(p(\omega,z_1,t)-p_0(\omega,z_1)) \tag{31}$$

with a subscript denoting the initial state, and herewith also the wall distension.

3 Physical Experiments

3.1 Vessels Design and Specifications. The vessels were designed to be analogs of the human aorta. One of the most referenced sources for arterial dimensions is that of Westerhof et al. [22]. According to their measurements in the human aorta, the ratio of Young's modulus multiplied by the thickness of the arterial wall over the arterial lumen diameter was used. For this paper, two straight vessels were manufactured, of which the dimensions can be seen in Fig. 3.

The vessels were manufactured by spin coating using a solution of polyurethane (PU, Desmopan 588, Bayer, Germany) dissolved in tetrahydrofurane (THF, BASF, Germany). To measure the material properties of the vessels, relaxation tests were performed. The stress versus the dimensionless time is shown in Fig. 4.

The complex viscoelastic modulus of the material can be written as a function of the angular frequency

$$\hat{E}(\omega) = \tilde{c}\Gamma(1-n)\omega^n e^{n\pi i/2} \tag{32}$$

where Γ is the gamma function and the values of $\tilde{c}$ and n are obtained by fitting a power law model with the relaxation data, and are found to be 1.3 $(\mathrm{Pa/s}^n)$ and 0.065, respectively.

3.2 Experimental Setup. A schematic diagram of the experimental setup that used to carry out the wave propagation experiments in flexible vessels is shown in Fig. 5. The apparatus consists

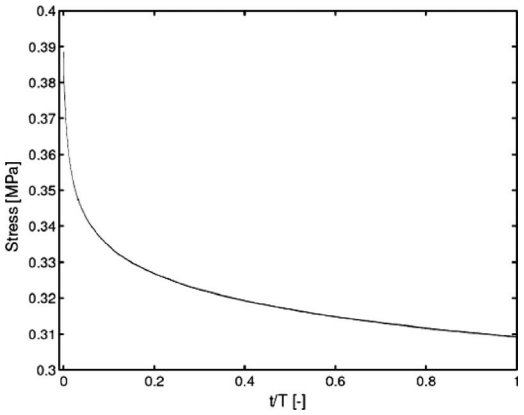

Fig. 4 Relaxation test (3% elongation)

of: open container filled with water (E); closed container at constant pressure, 1 bar (C); open container (D); two-way manually operated solenoid valve (A); three-way PC operated solenoid valve (B); and a vessel (F). The vessel is placed in horizontal position inside container E. The water column above the vessel prescribes the static pressure outside the vessel. The vessel is prestrained axially to 3%. The vessel is fixed on both sides against axial movement, whereas it can freely expand in the radial direction. The vessel is connected on one side via the three-way solenoid valve, either to container C or D. When the solenoid valve is not engaged, the vessel is connected to the open tank (D), which prescribes the initial pressure inside the vessel. By engaging the solenoid valve, it opens for 50 ms and generates a pulse by introducing a propagating pressure wave. The sensors used are typical for in-vivo clinical measurements. The pressure inside the vessel is measured simultaneously by two pressure sensors (Radi Medical Systems 12000XT), 17 mm apart. By using two simultaneous pressure measurements, the pressure gradient is obtained. The volumetric flow rate is measured using a perivascular flow rate sensor (MC28AX, Transonic, The Netherlands). The wall motion is measured using an ultrasound wall tracking system [26].

4 Results

The vessels are preloaded at 2.94 kPa, relative to the pressure outside the vessel, and during measurement, the two-way solenoid valve is kept closed to preserve the volume of water induced in the vessel by the 50 ms opening of the valve. To ensure that the vessel undergoes small deformations, it was inflated by inducing known amounts of fluid, and with diameter static pressure measurements, it was concluded that the corresponding strains are less than 3% and consequently may be considered as small.

Measurements of pressure, volumetric flow rate, and wall distention were performed at ten locations along the vessel $z=[0.03,0.05,0.1,0.15,0.2,0.25,0.3,0.35,0.4,0.45]$ m. Every measurement was repeated 16 times for statistical evaluation of the reliability and reproducibility of the measured data. The standard deviation was determined and it was found to be of the order of the signal to noise ratio. The volume increase in the vessel by the engagement of the solenoid valve was 2.57 ml.

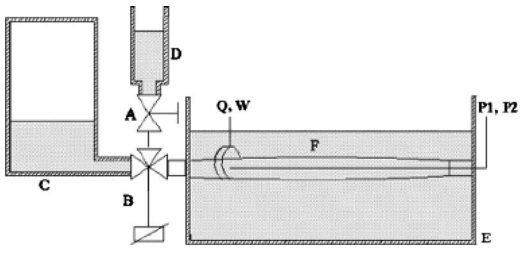

Fig. 5 Experimental setup

The anchoring of the tubes is throughout against axial movement so $\psi=1-\nu^2$, where ν is the Poisson ratio, and for vessels A and B, it is assumed that $\nu=0.5$. The wave velocities in tubes A and B are $c_0\approx 9$ m/s and 6 m/s, respectively. The analytical results were obtained using the fluid parameters $\rho=998$ kg/m^3 and $\eta=1.04\cdot 10^{-3}$ kg/ms. The initial 3% axial prestrain is taken into account in the analytical model.

Figures 6 and 7 show the experimental results obtained from the measurements for vessel A against the analytical results. Vessel A has a wall thickness of 0.1 mm and wave velocity of $c_0\approx 9$ m/s. This velocity has been verified by the measurements, after determining the axial distance traveled by the pulse per second. The experimental results are the same in both figures. The difference is in the analytical model: Fig. 6 represents an elastic wall, whereas Fig. 7 represents a viscoelastic wall. The measurements of the pressure sensors, volumetric flow rate meter, and ultrasound wall distention for 0.5 s are shown for each of the ten locations z along the tube. The viscoelasticity of the wall is evident in the measurements by the attenuation of the waves. The propagation of pressure, volumetric flow rate, and wall expansion for the accommodation of the traveling wave through the vessel can be identified by the time difference between the pulse arrival at $z=0.03$ m and at $z=0.45$ m. At location $z=0.45$ m, the amplitude of the pressure pulse has almost doubled because of the interference of the forward and the backward traveling wave. Nine reflections in 0.5 s can be clearly identified. The direction of the flow alters every time the wave is reflected at one of the ends, and it is indicated by the positive and the negative sign in the flow measurements. The pressure signal is at all times positive due to the full reflection at the closed ends. The wall distention signal follows the pressure signal. It is also at all times positive as the wall expands from its original position, driven by the pressure.

In Fig. 6, the analytical theory of an elastic vessel of the same dimensions as vessel A, with Young's modulus 17.2 MPa, is compared with the experimental data. If an elastic wall is considered, the analytical theory is not sufficient to predict the propagating wave. This is expected due to the fact that the amplitude of the waves is damped significantly in the experimental measurements, mainly due to the vessel's viscoelasticity. The analytical results of the elastic wall help to clearly identify the forward and the backward traveling waves during multiple reflections.

In Fig. 7, the results of the analytical theory for a viscoelastic vessel are presented, with material properties as obtained by the relaxation test using the complex Young's modulus (32) and the same dimensions as vessel A. The results are compared with the experimental data for vessel A and show to be in close agreement. Small deviations between experimental and analytical data can be related to the accuracy of the fitting of the material properties of the wall. Pressure is shown in Fig. 7(*a*), volumetric flow rate in Fig. 7(*b*), and the wall distention in Fig. 7(*c*).

In Fig. 8 the comparison between the analytical solution and the experimental measurements obtained from viscoelastic vessel B is obtained. Vessel B has a wall thickness of 0.05 mm and wave velocity $c_0\approx 6$ m/s, which has also been verified by the measurements. The pressure, volumetric flow rate, and wall distention are shown in Figs. 8(*a*)–8(*c*), respectively. The comparison between the analytical solution and the experimental data is in close agreement. The agreement between the analytical solution and the measurements is better for the thinner vessel B, as the influence of the error related to the material properties is smaller.

5 Conclusions

In this paper, a frequency domain analytical model, based on the one-dimensional wave propagation theory, was presented and compared with experimental measurements. The analytical model is able to predict pressure waves, volumetric flow rate, and wall distention. New experimental measurements of pressure, volumet-

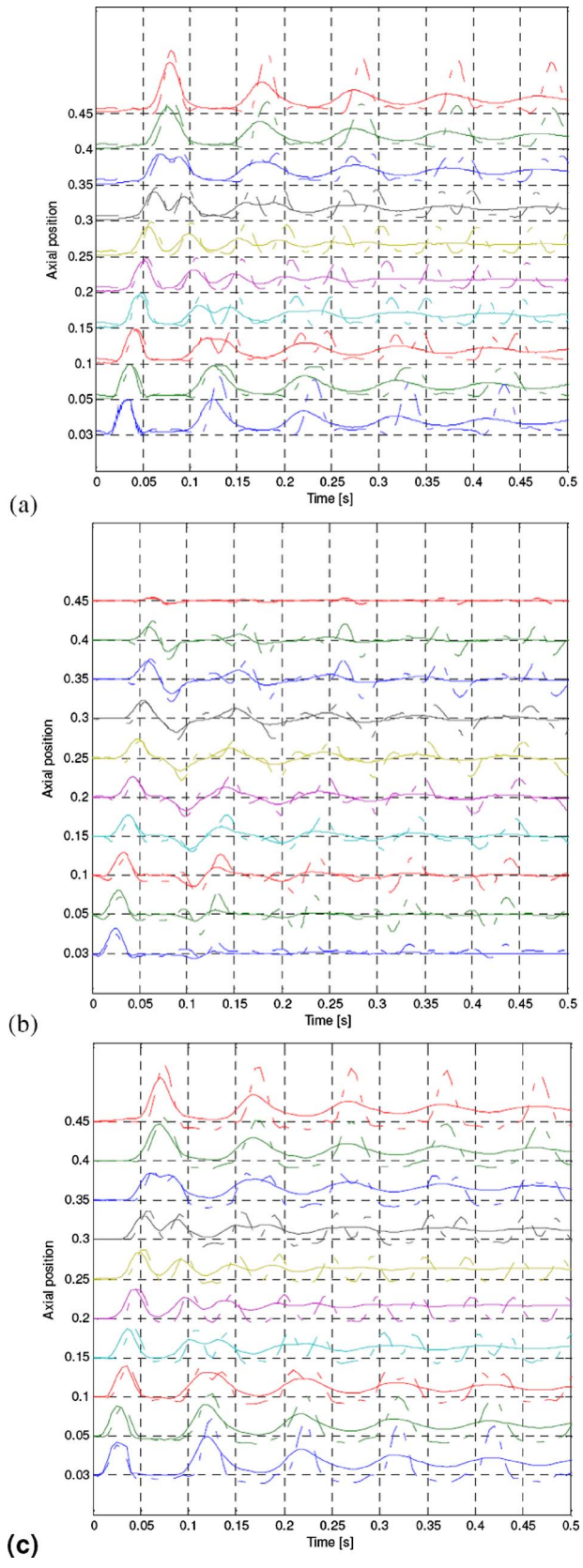

Fig. 6 Vessel A. Solid line experimental data, dashed line analytical solution for elastic wall. (*a*) pressure (Pa), (*b*) flow rate (m^3/s), and (*c*) wall distention (μm).

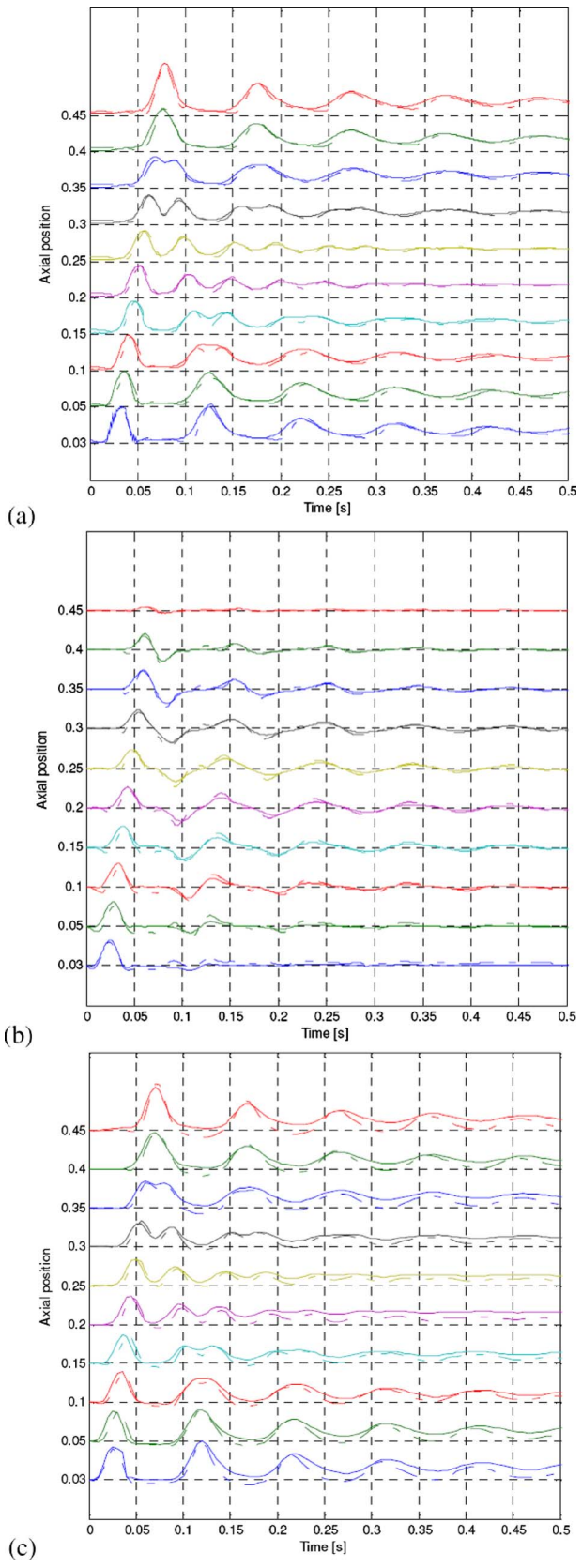

Fig. 7 Vessel A. Solid line experimental data, dashed line analytical solution for viscoelastic wall. (*a*) pressure (Pa), (*b*) flow rate (m^3/s), and (*c*) wall distention (μm).

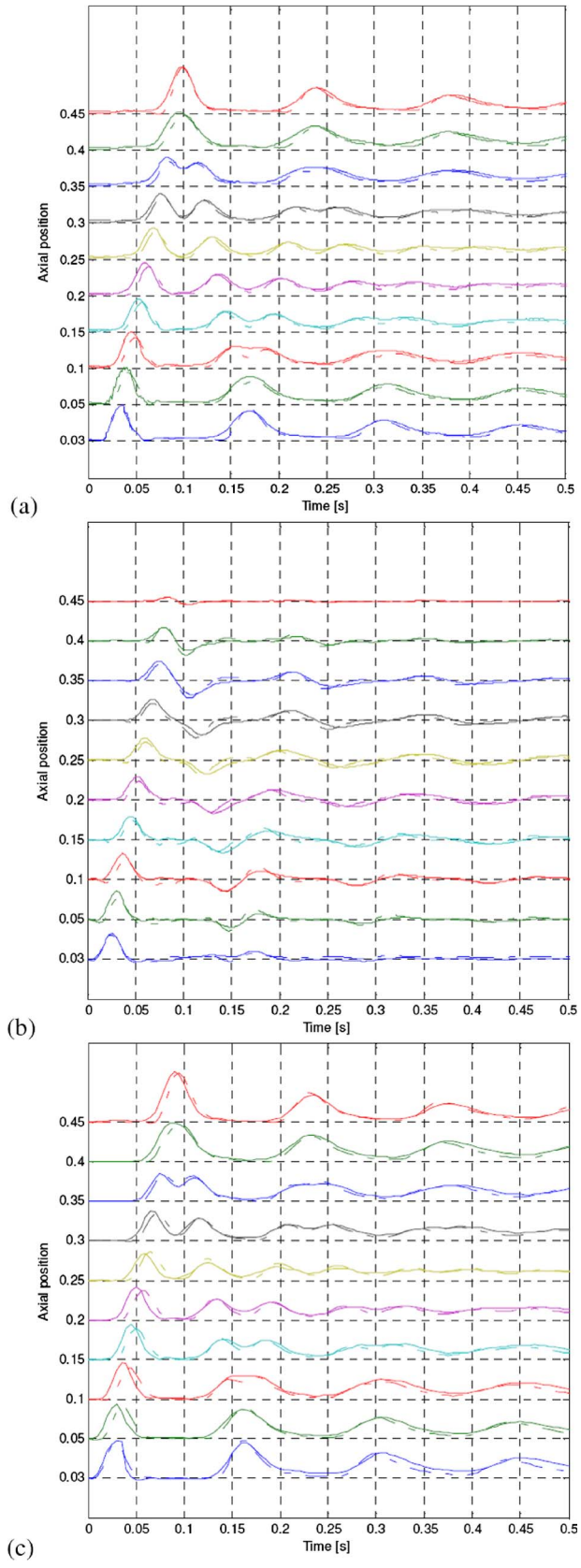

Fig. 8 Vessel B. Solid line experimental data, dashed line analytical solution for viscoelastic wall. (*a*) Pressure (Pa), (*b*) Flow rate (m^3/s), and (*c*) wall distention (μm).

ric flow rate, and wall distention were performed in very thin-wall vessels that are aortic analogs having wave speeds similar to those found in the human aorta. The predictions of the one-dimensional analytical model were in good agreement with the experimental measurements giving confidence that it can be used for predicting waves in blood flow research. Moreover, the experiments are new and useful to others.

Acknowledgment

The authors would like to thank Marie Curie Research Training Networks Fellowships, European Commission, and EPSRC, UK for partially funding this project.

References

[1] Lighthill, J., 1978, *Waves in Fluids*, Cambridge University Press, Cambridge, UK.
[2] Fung, Y. C., 1984, *Biodynamics: Circulation*, Springer, New York.
[3] Fung, Y. C., 1997, *Biomechanics: Circulation*, Springer, New York.
[4] Womersley, J. R., 1957, "An Elastic Tube Theory of Pulse Transmission and Oscillatory Flow in Mammalian Arteries," Technical Report No. WADC-TR-56-614, Wright Air Development Center, Dayton, OH.
[5] Young, T., 1808, "Hydraulic Investigations, Subservient to an Intended Croonian Lecture of the Motion of Blood," Philos. Trans. R. Soc. London, **98**, pp. 164–186.
[6] Tijsseling, A.S., and Anderson, A., 2008, "Thomas Young's Research on Fluid Transients: 200 Years on," *Proceedings of the BHR Group 2008 on Pressure Surges*, pp. 21–33.
[7] Cox, R., 1968, "Wave Propagation Through a Newtonian Fluid Contained Within a Thick-Walled Viscoelastic Tube," Biophys. J., **8**, pp. 691–709.
[8] Lighthill, M. J., 1972, "Physiological Fluid Dynamics: A Survey," J. Fluid Mech., **52**, pp. 475–497.
[9] Giannopapa, C. G., 2007, "Indicative Results and Progress on the Development of the Unified Single Solutions Method for Fluid-Structure Interaction Problems," Proceedings 2007 ASME Pressure Vessels and Piping Division Conference, San Antonio, Texas, July 22–26, pp. PVP 2007-026420.
[10] Heil, M., 1998, "Stokes Flow in an Elastic Tube—A Large Displacement Fluid-Structure Interaction Problem," Int. J. Numer. Methods Fluids, **28**, pp. 243–265.
[11] Perktold, K., and Rappitsch, G., 1995, "Computer Simulation of Local Blood Flow and Vessel Mechanics in a Compliant Carotid Artery Bifurcation Model," J. Biomech., **28**(7), pp. 845–856.
[12] Taylor, C. A., Hughes, T. R., and Zarins, C. K., 1998, "Finite Element Modeling of Blood Flow in Arteries," Comput. Methods Appl. Mech. Eng., **158**, pp. 155–196.
[13] Wan, J., Steele, B., Spicer, S. A., Strohband, S., Feeijoo, C. R., and Hughes, T. R., 2002, "A One-Dimensional Finite Element Method for Simulation Based Medical Planning for Cardiovascular Disease," Comput. Methods Biomech. Biomed. Eng., **5**(3), pp. 195–206.
[14] Vignon-Clementel, I. E., Figueroa, C. A., Jansen, K. E., and Taylor, C. A., 2006, "Outflow Boundary Conditions for Three-Dimensional Finite Element Modeling of Blood Flow and Pressure in Arteries," Comput. Methods Appl. Mech. Eng., **195**, pp. 3776–3796.
[15] Johnston, B. M., Johnston, P. R., Corney, S., and Kilpatrick, D., 2004, "Non-Newtonian Blood Flow in Human Right Coronary Arteries: Steady State Simulations," J. Biomech., **37**, pp. 709–720.
[16] Bessems, D., Giannopapa, C., Rutten, M. C. M, and van der Vosse, F. N., 2007, "Experimental Validation of a Time-Domain-Based Wave Propagation Model of Blood Flow in Viscoelastic Vessels."
[17] Tijsseling, A. S., 1996, "Fluid-Structure Interaction in Liquid Filled Pipe Systems: A Review," J. Fluids Struct., **10**, pp. 109–146.
[18] von Kries, J., 1892, *Studien zur Pulslehre. Akademische Verlagsbuchhandlung von JCB Mohr*, Paul Siebeck, Freiburg, Germany.
[19] Klip, W., 1962, *Velocity and Damping of Pulse Waves*, Martinus Nijhoff, The Hague, The Netherlands.
[20] Gerrard, J. H., 1985, "An Experimental Test of the Theory of Waves in Fluid-Filled Deformable Tubes," J. Fluid Mech., **156**, pp. 321–347.
[21] Giannopapa, C. G., 2004, "Fluid-Structure Interaction in Flexible Vessels," Ph.D. thesis, University of London, UK.
[22] Westerhof, N., Bosman, F., Vries, C. J. D., and Noordergraaf, A., 1969, "Analogue Studies of the Human Systematic Arterial Tree," J. Biomech., **2**, pp. 121–143.
[23] Korteweg, D. J., 1878, "Uber die Fortpflanzungs geschwindigkeit des Schalles in elastischen Rohren," Ann. Phys. Chem., **241**, pp. 525–542.
[24] Pedley, T. J., 1980, *The Fluid Mechanics of Large Blood Vessels*, Cambridge University Press, Cambridge, England.
[25] Sarpkaya, T., 2005, "On the Parameter β=Re/KC=$D^2/\upsilon T$," J. Fluids Struct., **21**, pp. 435–440.
[26] Brands, P. J., Hoeks, A. P. G., Willigers, J., and Willekes, C., 1999, "An Integrated System for the Non-Invasive Assessment of Vessel Wall and Homodynamic Properties of Large Arteries by Means of Ultrasound," Eur. J. Ultrasound, **9**, pp. 257–266.

Large Eddy Simulation of Turbulent Axial Flow Along an Array of Rods

F. Abbasian
e-mail: fabbasia@ryerson.ca

S. D. Yu
Professor
Mem. ASME
e-mail: syu@ryerson.ca

J. Cao
Associate Professor
e-mail: jcao@ryerson.ca

Department of Mechanical and Industrial Engineering,
Ryerson University,
350 Victoria Street,
Toronto, ON M5B 2K3, Canada

Large eddy simulation (LES) is employed in this paper to model the axial flow along a circular array of rods with a focus on anisotropic large-scale turbulence. The circular array consists of four whole rods and eight half rods, with a pitch-to-diameter ratio of 1.08. A dynamic Smagorinsky model with SIMPLE coupling method and a bounded central difference scheme are used to reduce numerical errors. The high demands for computations of the three-dimensional turbulent flows are afforded through parallel processing and utilization of 20 processors. The numerical results obtained using LES are compared with independent experimental data available in the literature; good agreement is achieved. The LES model was developed to accurately predict (i) the dependence of turbulence intensity and dominant frequency on the gap size and (ii) the turbulence structure in different directions. [DOI: 10.1115/1.4000574]

Keywords: complex flow, large eddy simulation, turbulence

1 Introduction

In nuclear reactors, the fluid-solid interaction between the coolant and fuel bundles is an important source of excitations for vibrations. These excitations are dominantly produced by the local turbulence in axial flows. Paidoussis [1] in a recent paper pointed out the significance of the turbulence effects induced by the core plates in a boiling water reactor. For complex cross sectional geometries of nuclear fuel bundles, the turbulent axial flow can induce a significant unsteady side force, which in turn causes the rod bundle structure to vibrate in a CANDU®[1] reactor channel [2]. Excessive bundle vibrations can potentially cause damage to the supporting tube. In this paper, large eddy simulation (LES) is used to simulate the turbulent axial flow in a circular subchannel consisting of four whole rods and eight half rods, as illustrated in Fig. 1. This problem was first studied experimentally by Curling and Paidoussis [3,4].

Experimental studies of turbulent flows along a rod bundle structure have been conducted by many researchers. The nugget of all these studies was the dependence of turbulence intensity and frequency on the cross sectional geometry and flow velocity. Rowe et al. [5] performed a thorough investigation on turbulence structure through laser Doppler velocimetry and showed that turbulence intensity increases as the gap size decreases. They found that the turbulence intensity in the azimuthal direction is smaller than that in the axial direction, and attributed this phenomenon to the intensity distortion caused by the secondary flows. From an autocorrelation analysis, they obtained the periodicity of the turbulence in the gap regions, and concluded that the dependence of the turbulence intensity on the Reynolds number is insignificant. Moller [6] showed that the azimuthal turbulence intensity has a dominant frequency in near-wall regions, and the axial turbulence intensity exhibits a stronger periodic pattern with a dominant frequency away from the wall surfaces. Rehme [7] confirmed the dependence of the turbulence intensity on the gap size, and showed that the turbulence mixing factor decreases with gap size. Besides the geometry dependence and anisotropic nature of the turbulence, the formation of axial vortices and secondary flows also drew attention from some researchers. The magnitude of the secondary flow velocity is very small compared to that of the axial bulk flow velocity. Hooper and Wood [8] did not capture the secondary flow velocities with their apparatus, and concluded that they were less than 1% of the bulk flow velocity. Vonka [9] found that the secondary flow velocity is only 0.1% of the bulk flow velocity.

A review of the literature reveals that little work has been done in axial flow simulations compared to cross-flow. Because of high costs associated with instrumentation for turbulence measurements and challenges in placing sensors in certain flow regions, the need for numerical simulations is pronounced more than ever. The Reynolds-averaged Navier–Stokes (RANS) models [10,11] were employed in many of the earlier turbulent flow simulations. The main drawback of such an averaging approach is their failure to accurately model the large-scale gap mixing for nongradient type turbulence and predict turbulence driven secondary flows. LES is an alternative approach that benefits from the accuracy of the direct numerical simulation (DNS) and shortens simulation time through filtering the NS equations. In LES, the filtered NS equations are solved in such a way that large-scale turbulence is directly resolved while small-scale turbulence is modeled implicitly. The size of the filter is usually the size of the volume cell. Ikeno et al. [12] used LES to study the effect of mixing-vane arrangements in pressurized water reactors. Kim and No [13] used the pressure fluctuations predicted by LES to perform spectral analyses in bundle flows.

In this paper, the dynamic Smagorinsky model (DSM) is adopted in simulating the turbulent axial flow along an array of rods. The main purpose of the present work is to evaluate the capability of DSM as a subgrid-scale model in predicting turbulence in a densely packed bundle geometry ($P/d=1.08$). The dependence of turbulence on the geometry is studied and validated using the experimental results. The coherent structures inside the bundle geometry are studied, and the effect of lateral and near-wall mesh resolution on the eddy formation and resolved turbulence is investigated. The LES model presented in this paper proved to be promising and produced the simulation results that are in good agreement with the experimental results [3,4]. With the successful application of LES reported in this paper, turbulent axial flows along an actual nuclear fuel bundle can be simulated for desired operating conditions.

[1]CANadian Deuterium and Uranium is a registered trademark of the Atomic Energy of Canada Limited (AECL).

Contributed by the Fluids Engineering Division of ASME for publication in the JOURNAL OF FLUIDS ENGINEERING. Manuscript received August 11, 2008; final manuscript received September 26, 2009; published online February 16, 2010. Assoc. Editor: Ugo Piomelli.

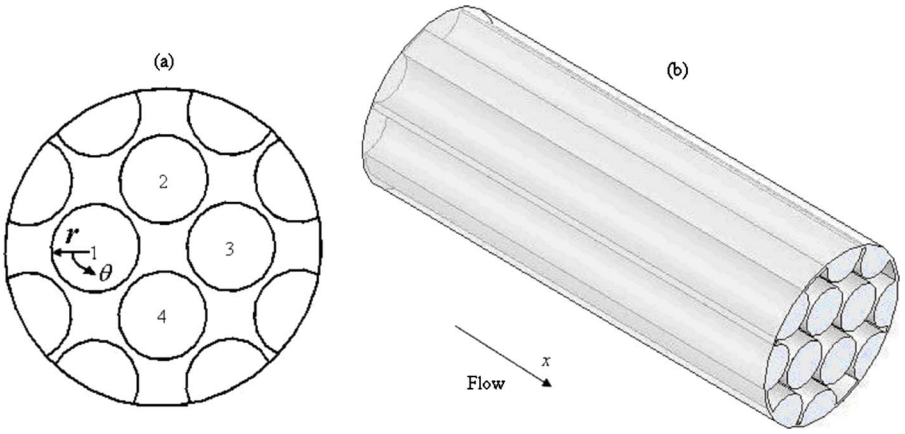

Fig. 1 The geometry of the simulation bundle used in the experiment by Curling and Paidoussis in Refs. [3,4]: (*a*) the cross section view and the coordinate system, and (*b*) isometric view of the bundle and flow direction

2 Numerical Scheme and Computational Model

The physical model, as shown in Fig. 1, consists of a circular flow channel, four whole rods, and eight half rods. All rods are of identical diameter of 5.715 cm. The circular flow channel diameter is 20.48 cm with a length of 55.24 cm. Various locations on the surface of cylinder 1 and the subchannel areas associated with it are identified for direct comparisons of computed turbulent pressures with the measurements at the corresponding locations reported in Refs. [3,4]. Table 1 presents the flow characteristics and hydraulic diameter.

Adopting the DSM, three-dimensional filtered unsteady NS equations governing axial flow along an eight-rod bundle are solved using the finite volume discretization. An implicit SIMPLE velocity-pressure coupling method is employed in conjunction with LES with adequate time step size. The filtered continuity and momentum equations for an incompressible fluid flow in the absence of body forces can be written in the following form:

$$\frac{\partial \bar{u}_i}{\partial x_i} = 0, \quad \frac{\partial \bar{u}_i}{\partial t} + \frac{\partial \bar{u}_i \bar{u}_j}{\partial x_j} = -\frac{1}{\rho}\frac{\partial \bar{p}}{\partial x_i} + \nu \frac{\partial^2 \bar{u}_i}{\partial x_j \partial x_j} - \frac{\partial \tau_{ij}}{\partial x_j} \tag{1}$$

where the overbar denotes filtered quantity, τ_{ij} is the subgrid-scale (SGS) stress tensor modeled using turbulent viscosity μ_t, which is defined by Smagorinsky [14] as

$$\mu_t = \rho (C_s \bar{\Delta})^2 |\bar{S}| \tag{2}$$

where $|\bar{S}| = \sqrt{2\bar{S}_{ij}\bar{S}_{ij}}$, $C_s\bar{\Delta}$ is the mixing length, C_s is the Smagorinsky constant and is 0.17 for homogeneous isotropic turbulence, and $\bar{\Delta}$ is the cubic root of cell volume. The Smagorinsky model offers a universal model parameter, which is considered a shortcoming for this method. It is well known that adopting a universal constant C_s requires the use of additional wall functions in order to damp SGS viscosity near the solid boundaries. In order to resolve this problem, the DSM [15] is used, where the model parameter is dynamically calculated based on the resolved scales. In short, the DSM obviates the need for defining a constant model parameter and wall function, and improves the accuracy of the model by having correct near-wall behavior. In the DSM, the model parameter varies with space and time, and is computed by sequentially applying grid and test filters.

Differencing scheme used in LES is normally challenging as numerical errors may be introduced. A blend of second order central differencing along with a second order upwind scheme is written as $\Phi_f = \Phi_{f,\mathrm{UP}} + (\Phi_{f,\mathrm{CD}} - \Phi_{f,\mathrm{UP}})$, where Φ_f is the face value, UP denotes the upwind, and CD denotes the central differencing. The upwind part of the scheme is treated implicitly and the central differencing part is treated explicitly. Using this method, the numerical dissipation is significantly reduced. However, there are some unphysical oscillations added to the solution. In order to prevent this problem, the bounded central differencing scheme is used in the present study, where a blend of central differencing, and second and first order upwind schemes are used based on the normalized variable diagram (NVD) [16] and the convection boundedness criterion (CBC). The first order scheme is used in case CBC is violated. As reported by Abbasian et al. [17], the under-relaxation factor (URF) of 0.6–0.8 accelerates computations in solving an unsteady RANS problem for high-frequency fluctuating pressures. Here, the URF has been conservatively chosen between 0.5 and 0.7 to ensure numerical stability.

Three different meshes with quadrilateral volume cells were tested in the simulation procedure. The meshes were gradually coarsened in the axial, radial, and azimuthal directions. The parameters describing meshes and time steps employed in this study are grouped in Table 2. The mesh used to produce simulation

Table 1 Flow velocities and Reynolds numbers used in the experiment and simulation

Mean axial flow velocity U (m/s)	Hydraulic diameter D_h (m)	Reynolds number Re	Reynolds number based on friction velocity Re_τ	P/d
0.253	0.0273	7000	438	1.08
0.759	0.0273	21,000	1177	1.08
1.27	0.0273	35,000	1864	1.08
1.77	0.0273	49,000	2524	1.08
3.54	0.0273	98,000	5048	1.08

Table 2 Specifications for space and time discretizations

Mesh	I	II	III
Grid size	253×10^3	430×10^3	1310×10^3
y^+	4.35	2.7	1
Δr ($\times10^{-3}$ m)	0.15–2	0.1–1.4	0.044–0.8
r^+	6.5–87	4.5–63	2–34
$r\Delta\theta$ ($\times10^{-3}$ m)	2–2.2	1.4–1.6	0.8–0.84
$(r\theta)^+$	87–96	63–72	34–36
Δx ($\times10^{-3}$ m)	5.9	2.5	2.5
x^+	252	107	107
δ ($\times10^{-3}$ m)	0.5	1.25	1.12
LETOT (s)	0.01	0.01	0.01
Δt (s)	0.001	0.0001	0.0001

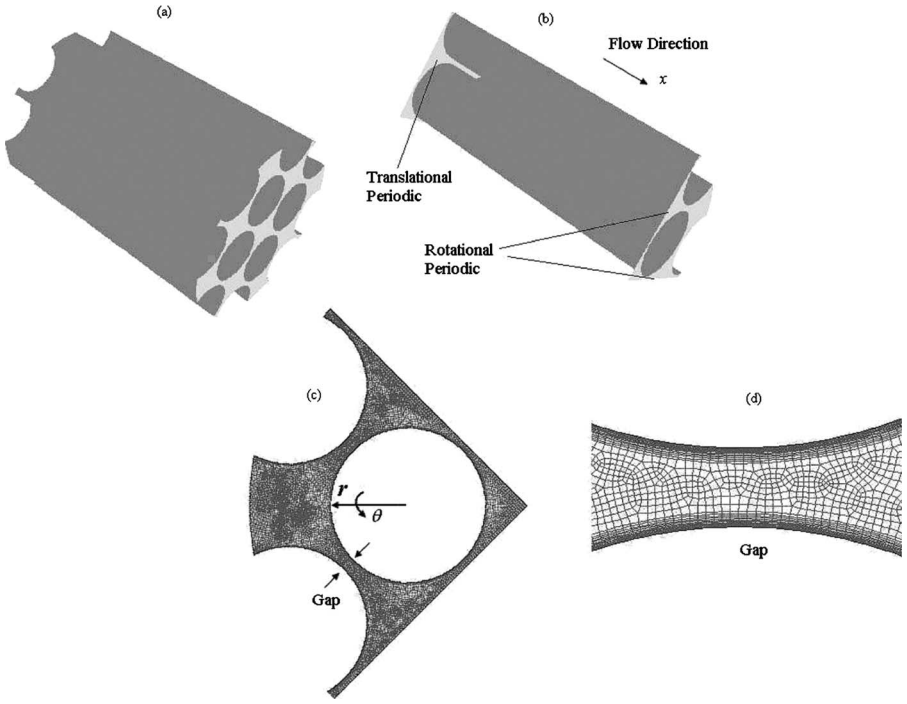

Fig. 2 The computational domain: (*a*) the eight-rod model, (*b*) the quarter model and the position of translational and rotational periodic boundaries, (*c*) the quadrilateral mesh of a quarter of the cross section, and (*d*) the mesh of a zoomed gap region with boundary layers

results reported in this paper is mesh III with $y^+=1$ on the wall, dimensionless mesh size $\Delta^+<34$ in the radial direction, $\Delta^+<36$ in the azimuthal direction, and $\Delta^+<107$ in the axial direction. The boundary layer consists of 15 layers with a magnifying ratio of 1.15 as it moves away from the wall. The time step has been calculated based on the large eddy turnover time (LETOT) or l/u, where l and u are the length and velocity scales, equal to $0.05D_h$ and $0.2U$, respectively. In the present study, a uniform time step of 0.01 times LETOT is used. The computational domain along with the meshed cross section and boundary layers in the gap region are given in Fig. 2. Due to symmetry, only a quarter of the system is modelled. The planes of symmetry are considered to be the translational and rotational periodic boundaries, which are suitable for modelling fully developed turbulent flows. The length of the computational domain (x-direction) is $11D_h$, where D_h is the hydraulic diameter. Among the three meshes examined in the simulation (Table 2), mesh III provided reasonable agreement with the experimental results (Fig. 3) and was used in the simulation. The solution converged in about 10,000 time steps with different elapsed time for the meshes, which are gathered in Table 3.

3 Results and Discussion

3.1 Spectral Analysis. A cell-centered finite volume scheme is employed and the solution is obtained for each variable in the filtered NS equations over the computational domain. In a cell-based solver, the face value of a variable is determined by averaging the variable over the two neighboring cells. The value of a variable at a node is determined by averaging the values of the variable over all of its surrounding cells, and the weighting factor used for a surrounding cell is inversely proportional to the distance between the node and the centroid of the cell. For the locations that are neither cell centroid nor node, interpolation is used to provide the data based on the solution.

The pressure differences between the two diametral points on the cylinder surface, normalized with respect to $1/2\rho U^2$, are shown in Fig. 4 for three different Reynolds numbers. The general trend traced in this figure is that the amplitude of the normalized pressure grows in the gap region and the frequency increases with the mean axial flow velocity. It is also observed that the normalized pressures decrease with the mean flow velocity.

The power spectral densities (PSDs) obtained from the numerical simulation are compared with those reported in Ref. [3] and

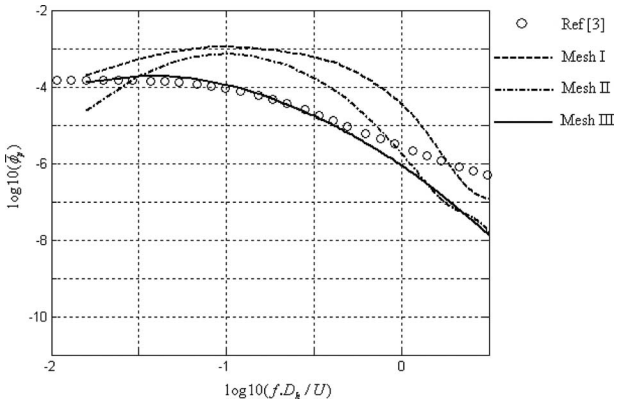

Fig. 3 PSDs of wall pressures for the different meshes used in the simulation

Table 3 Convergence elapsed time for different meshes

Meshes	Number of volume cells	Convergence time[a] (h)
I	253,000	12
II	430,000	35
III	1,310,000	96

[a]On a cluster of 20 processors (SunFire E2900, 20×1.8 GHz UltraSPARC-IV+, 192 Gbyte RAM).

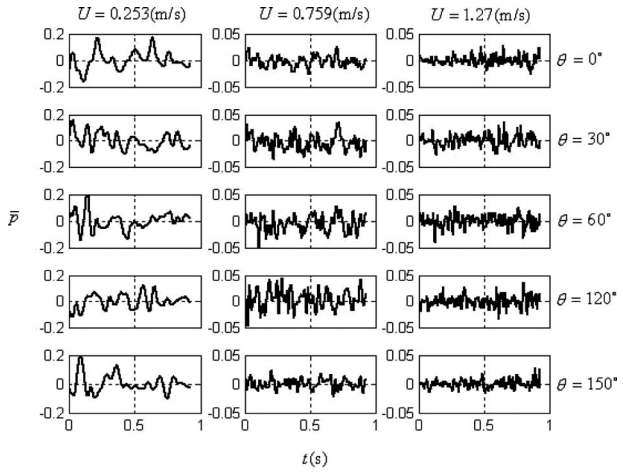

Fig. 4 Normalized pressures $\bar{p}=p/(1/2\rho U^2)$ in different azimuthal locations for different flow velocities (all the amounts are differential pressures, which are the difference between the pressure values at two diametral locations, e.g., 0 deg, 180 deg, etc.)

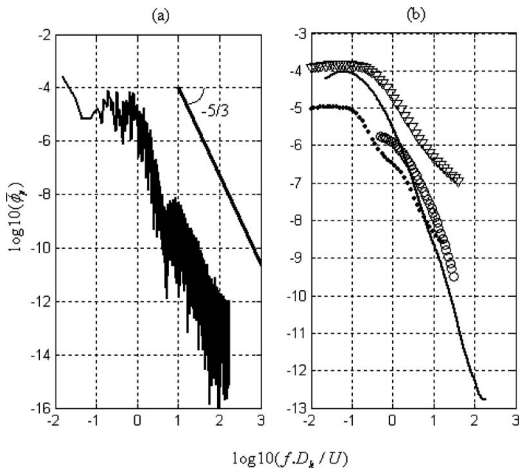

Fig. 6 (*a*) The original PSD of wall pressures (LES present); (*b*) smoothened PSD of the present numerical results and other experimental results from different resources (where ○ denotes results from Ref. [22], • denotes results from Ref. [23], ▽ denotes results from Ref. [3], and — denotes LES present results)

are shown in Fig. 5. The PSDs are obtained using $\phi = H(f)\cdot \mathrm{Conj}(H(f))/n\cdot f$ where "Conj" is the conjugate operator, $H(f)$ is the discrete Fourier transform of the time domain signal, n is the data record length, and f is the sampling frequency. In simulations, a time step of 0.0001 s, which is equivalent to 10 kHz sampling frequency, is used. In the simulation runs, the data length is 10,000 or 1 s. All PSDs in this paper are one-sided spectrum within the frequency range between 0 kHz and 5 kHz. The frequency range between 10 Hz and 50 Hz was windowed, following the experimental procedure as extraneous low-frequency noises normally affect the results. Intriguingly, numerical errors may also affect the pressures. The erroneous nature of these low-frequency signals were identified based on the fact that they randomly emerged in the low-frequency regions. The experimental dominant frequencies for flow velocities of 0.759 m/s and 1.27 m/s were 20 Hz and 35 Hz, respectively. From the present numerical results, the corresponding frequencies are 18.4 Hz and 34 Hz, respectively. There is also good agreement for the PSD amplitudes at different azimuthal locations. The trend confirmed in the experimental procedure [3] was that the PSD amplitude increases in the gap regions, and this trend is shown again in Fig. 5 for both numerical and experimental results. The PSD amplitude grows from 0 deg to 30 deg and 60 deg, and similarly for 120 deg and 150 deg as they mirror the points at acute angles (i.e. 30 deg$=\pi-150$ deg and 60 deg$=\pi-120$ deg). The PSDs are not completely the same for the symmetrical locations in the experimental approach because of geometry imperfections, or in the numerical approach because of the random nature of the flow. The normalized PSD results are also compared with other experimental data. The PSD is directly plotted in Fig. 6(*a*), and is smoothened with a quadratic averaging filter in Fig. 6(*b*). A typical wall pressure spectrum comprises the ascending low-frequency portion up to the peak. The peak of the curve is referred to as the convective ridge and represents the dominant frequency with maximum turbulent energy and pressure fluctuations. Beyond the dominant frequency, the large-scale turbulence scatters to smaller scales with energy cascade. While the spectrum in the low wave numbers is geometry dependent, the trend in the high wave numbers represents the viscous dissipation and is universal. The low-frequency range is especially more important when studying the fluid forces spectra in the problem of fluid-induced vibration in nuclear fuel bundles. The predicted PSD amplitude and dominant frequency perfectly match with the experimental result [3]. The trends K^2 and $K^{-5/3}$ for the low and high wave numbers (K) reported in Refs. [18–21] are observed in the predicted spectrum. This confirms the capability of the DSM and the bounded central differencing scheme to predict the PSD and dominant frequency. However, Fig. 6(*b*) also shows that the PSD slope for the high wave numbers predicted by LES is higher than the experimental

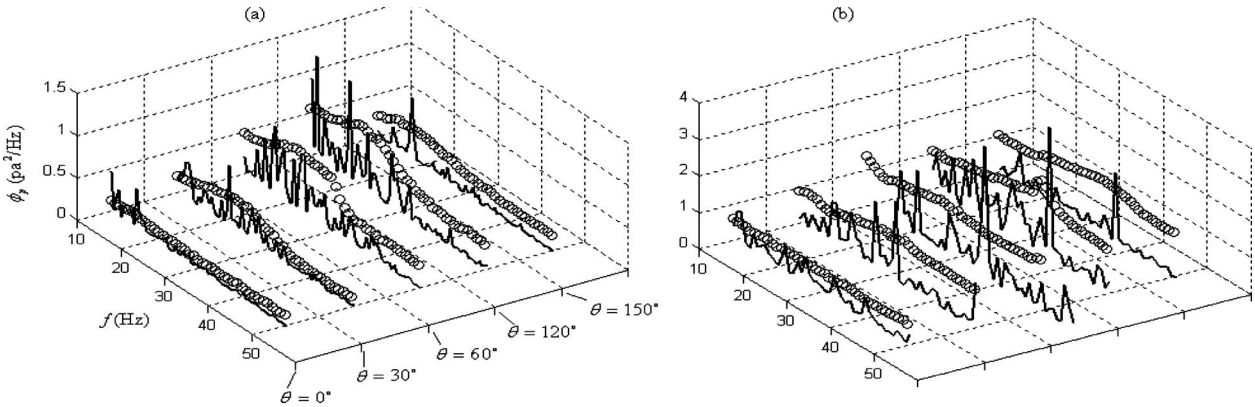

Fig. 5 PSDs of wall pressures in various azimuthal directions at $x/D_h=10.01$ (where ○ denotes the experimental results [3] and — denotes the LES present results): (*a*) $U=0.759$ m/s and (*b*) $U=1.27$ m/s

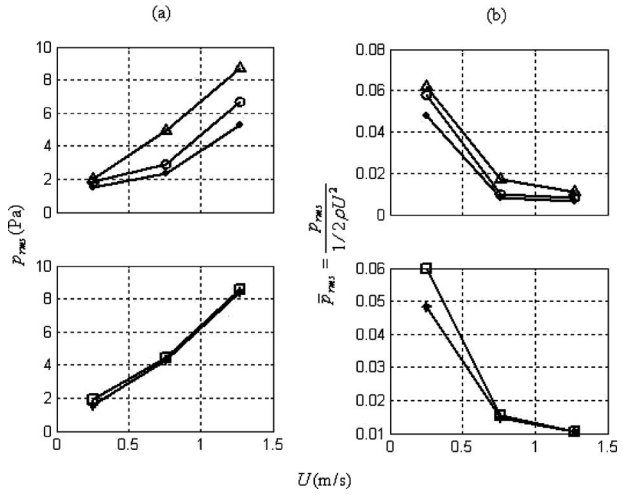

Fig. 7 Mean value of the pressures: (*a*) rms of pressures at different locations for different flow velocities and (*b*) rms of normalized pressures (—•— (θ=0 deg), —○— (θ=30 deg), —△— (θ=60 deg), —□— (θ=120 deg), and —✦— (θ=150 deg))

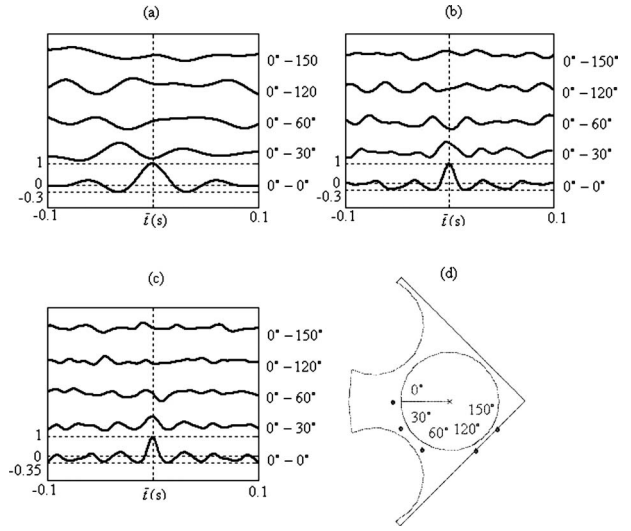

Fig. 8 Cross-correlation coefficients between the azimuthal velocity fluctuations at different locations: (*a*) *U*=0.253 m/s, (*b*) *U*=0.759 m/s, (*c*) *U*=1.27 m/s, and (*d*) data point locations. Each curve is shifted upwards by a different distance

results [3], and is closer to Refs. [22,23] for the case of pipe and annular flows. This indicates that the bounded central differencing scheme may still contribute to the numerical dissipation. It should be noted that in the experimental procedures, a cut-off frequency is normally applied to the signal to eliminate the low-frequency noises, which may affect the ascending portion of the spectrum.

3.2 Coherent Structure Analysis. The root mean square (rms) values of the pressures at different azimuthal locations in 1 s duration are presented in Fig. 7(*a*) for three different flow velocities. The rms of pressures are normalized by the dynamic pressure and are shown in Fig. 7(*b*). Clinch [22] reported that the rms value of the pressure signal is approximately equal to 0.007 $\times(1/2\rho U^2)$ for the case of pipe flow. The results shown in Fig. 7 are consistent with the experimental results in Ref. [4], where the direct variation in rms pressures with the square of velocity is more pronounced for the higher velocities (i.e., 0.759 m/s and 1.27 m/s).

The near periodicity of the coherence structures formation is investigated using the correlation analysis. The autocorrelation of a random signal exhibits periodicity with the same frequency as the dominant frequency of the original signal, and exponentially decays with time. The cross-correlation coefficients of the azimuthal velocity fluctuations are shown in Fig. 8. The autocorrelation of the velocity fluctuations in the wide-gap region (θ =0 deg) and cross-correlations between the velocities at θ =0 deg and other locations are shown. Using the flow velocities and time scale, the streamwise wavelength of the autocorrelations at all velocities is approximately equal to $2D_h$, which can be regarded as the space between the two consecutive coherent structures. The strongest correlation of the velocity fluctuations occurs between the two adjacent points, and decreases with separation distance as shown in Fig. 8 and as reported in Ref. [4]. The weakest correlation occurs between velocities at θ=0 deg and θ =150 deg, which are two furthest-apart locations. In the present analysis, there are also time delays appearing on the cross-correlation coefficients. In the experimental work [4], although the cross-correlations in the axial direction showed time delays, the correlations for the same streamwise and different azimuthal locations generally centered with no time delay as there was no lateral convection for pressure. In the present model, the time delay in the lateral velocity fluctuations at different azimuthal locations is the result of the vortices around the rod surface. The coherence structure is caused by these vortices forming at different steamwise locations and propagating along the axial direction for a given azimuthal location in the cross section, which causes time delay in the cross-correlation curves.

3.3 Turbulence Intensity and Mean Flow Analysis. In this section, turbulence intensities in different directions and mean flow characteristics are investigated. The simulation results are compared with a new set of experimental results, as turbulence intensity and mean flow velocity are not discussed in Refs. [3,4]. The experimental approaches given in this section are used for qualitative comparisons of turbulence intensity and mean flow velocity in the cross section of a bundle geometry. The mean flow results are obtained using data sampling and time averaging of instantaneous values over a 1 s period of time. The normalized PSDs of flow velocity components in the narrow-gap and wide-gap locations are given in Fig. 9. The narrow-gap location is at

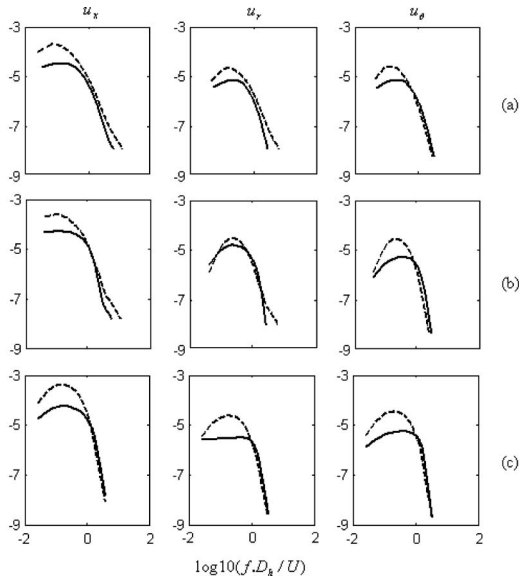

Fig. 9 Smoothened PSDs of velocity fluctuations for different velocity components (where — denotes the wide-gap location and ---- denotes the narrow-gap location): (*a*) *U*=0.253 m/s, (*b*) *U*=0.759 m/s, and (*c*) *U*=1.27 (m/s)

Table 4 Turbulence intensities for the wide-gap (subchannel center) and narrow-gap locations

Present	Rowe et al. [5]
$P/d=1.08$, $\mathrm{Re}=4.9\times10^4$	$P/d=1.25$, $\mathrm{Re}=10^5$
Subchannel center	
$I_x=4\%$	$I_x=4.1\%$
$I_r=2.5\%$	$I_r=2.9\%$
Narrow-gap	
$I_x=8.1\%$	$I_x=5.2\%$
$I_r=4.1\%$	$I_r=3.1\%$

Note: I_x is the axial intensity and I_r is the radial intensity.

halfway between two adjacent cylinders such as cylinders 1 and 2. The wide-gap location lies between two nonadjacent cylinders such as cylinders 1 and 3 (see Fig. 1). The results show that the PSD amplitude of the axial velocity fluctuations is higher than that of lateral velocities. In almost all of the curves, the spectra in the narrow-gap regions have higher PSD amplitudes, and exhibit more periodic pattern with a distinguishable convective ridge compared to the wide-gap regions [5–8].

The axial I_x and radial I_r turbulence intensities are compared with the experimental results in Table 4. The numerical and experimental results are consistent with each other in the wide-gap regions. The computed turbulence intensities in the narrow-gap region are higher than the experimental data. As shown in Table 4, the experiments of Rowe et al. [5] were performed for a pitch to diameter ratio of 1.25 and a Reynolds number nearly twice as much as the present Reynolds number. The present pitch-to-diameter ratio of 1.08 may be the cause of higher intensities in the narrow-gap region. The time-averaged axial and radial flow velocities normalized by the mean axial velocity are compared to the experimental results obtained by Moller [6] for $P/d=1.072$ and a Reynolds number of 8.5×10^4 and are given in Table 5. The velocity contours are also shown in Fig. 10. The normalized axial flow velocity varies between $0.8U$ in the gaps and $1.23U$ in the subchannel centers, while the normalized radial velocity has a maximum time-averaged value of $0.13U$. The cross-flow vectors on a cross section plane are given in Fig. 11. The time-averaged vectors show two single symmetric vortices. The velocities associated with the secondary flows increase from zero at the center of the swirl to the maximum value away from the center, and have a plane-averaged value of $0.002U$. The time-averaged turbulent kinetic energy is shown in Fig. 12. The kinetic energy is per unit mass and is normalized by the square of the mean axial velocity. The minimal energy value in the center of subchannels is evident,

Table 5 Time-averaged velocity magnitude normalized by the mean axial velocity

	Present	Moller [6]
	$P/d=1.08$, $\mathrm{Re}=4.9\times10^4$	$P/d=1.072$, $\mathrm{Re}=8.5\times10^4$
Center	1.23	1.1
Near-wall	0.82	0.7

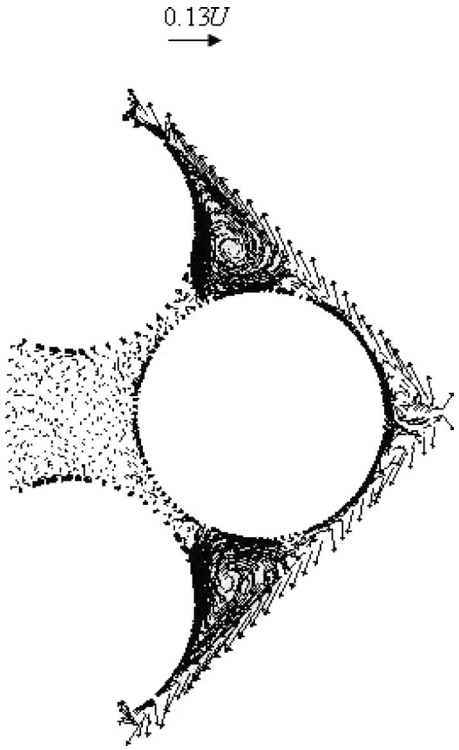

Fig. 11 Time-averaged cross-flow vectors for $U=1.77$ m/s

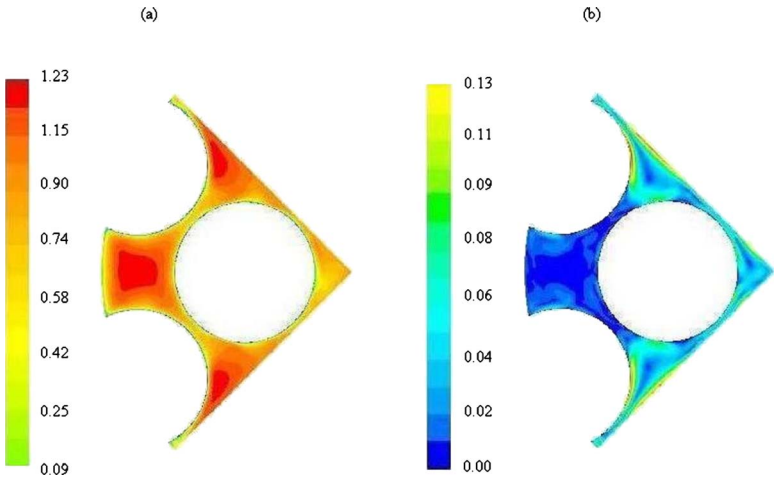

Fig. 10 Contours of the time-averaged flow velocity normalized by the mean axial velocity for $U=1.77$ m/s: (*a*) axial u_x and (*b*) radial u_r velocities

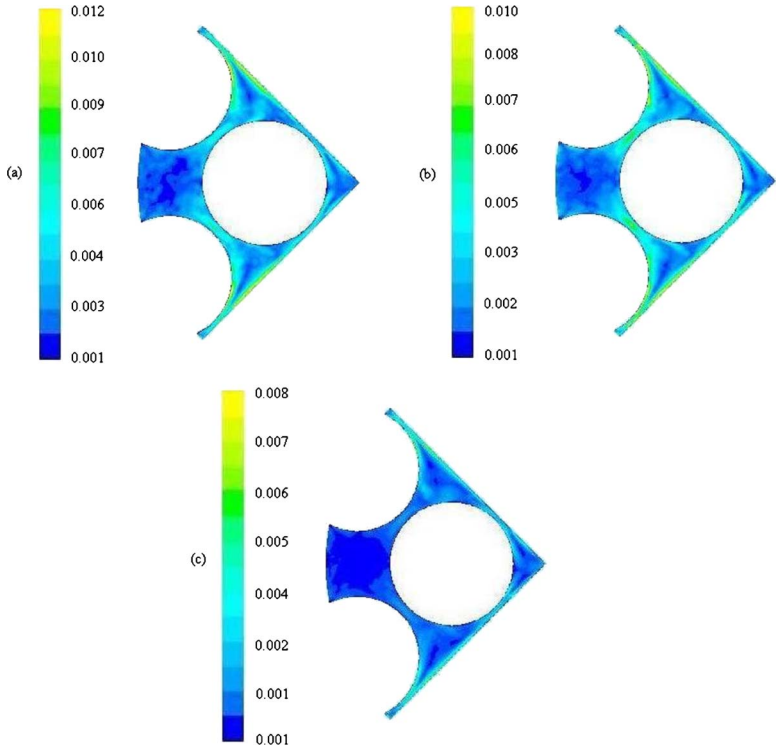

Fig. 12 Time-averaged resolved turbulent kinetic energy per unit mass normalized by the square of mean axial velocity (k/U^2): (*a*) U=0.253 m/s, (*b*) U=0.759 m/s, and (*c*) U=1.27 m/s

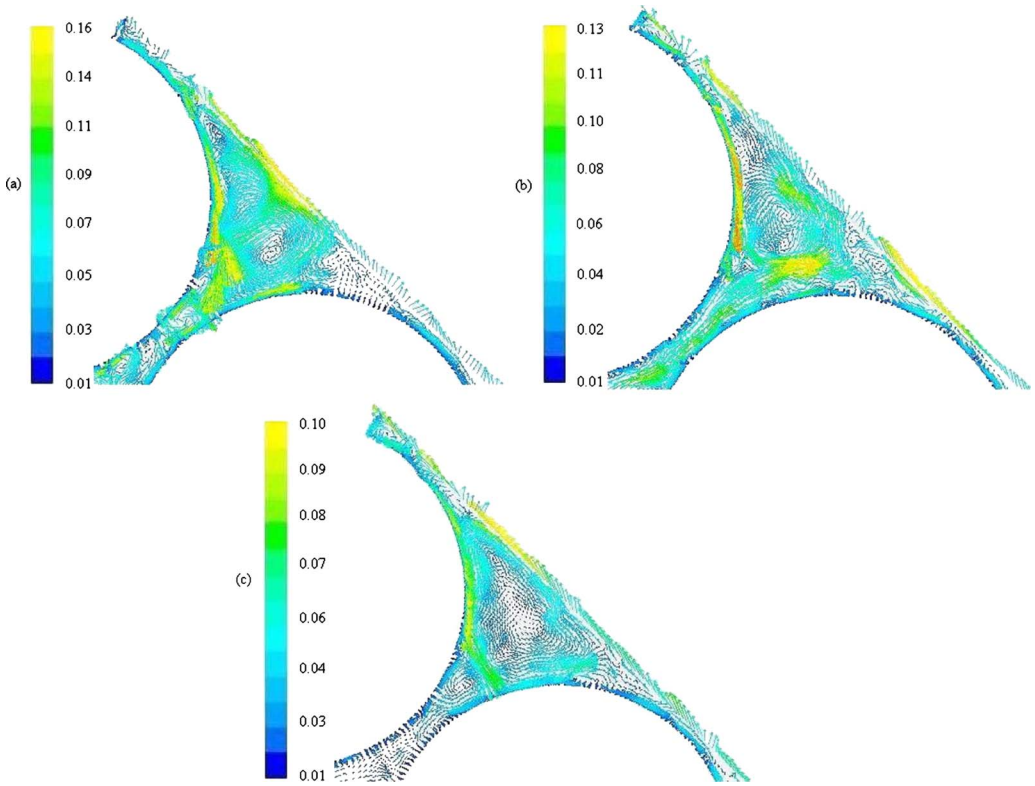

Fig. 13 Instantaneous cross-flow velocity vectors normalized by the mean axial flow velocity: (*a*) U=0.759 m/s, (*b*) U=1.77 m/s, and (*c*) U=3.54 m/s

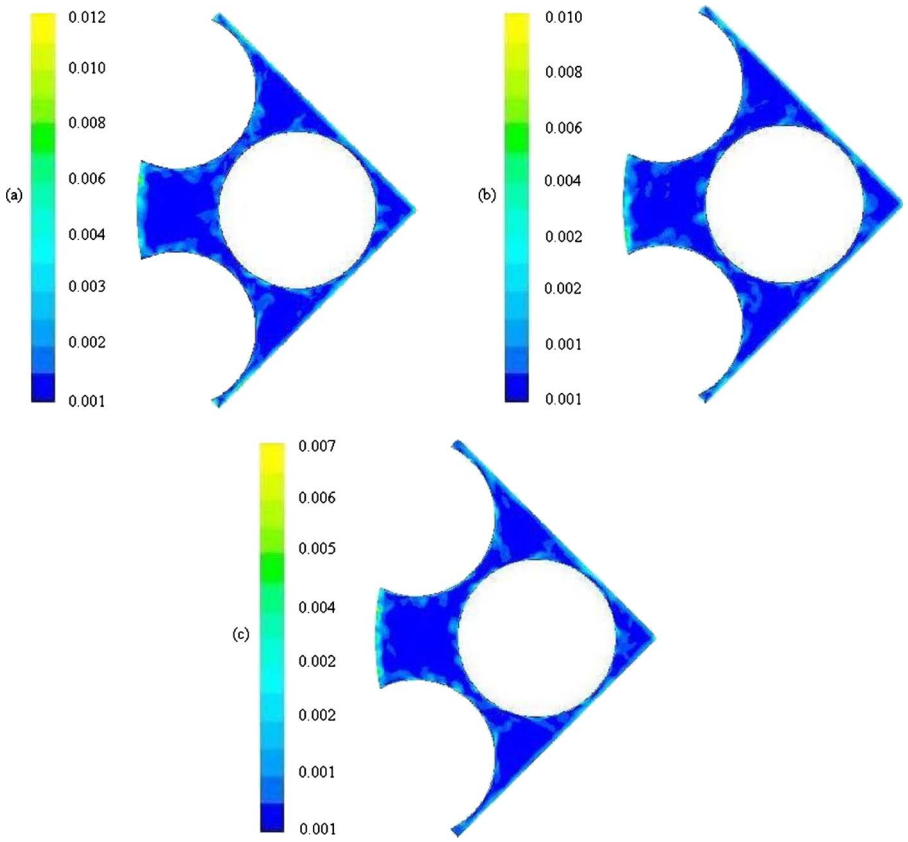

Fig. 14 Instantaneous subgrid-scale turbulent kinetic energy per unit mass normalized by the square of mean axial velocity (k_s/U^2): (*a*) U=0.759 m/s, (*b*) U=1.77 m/s, and (*c*) U=3.54 m/s

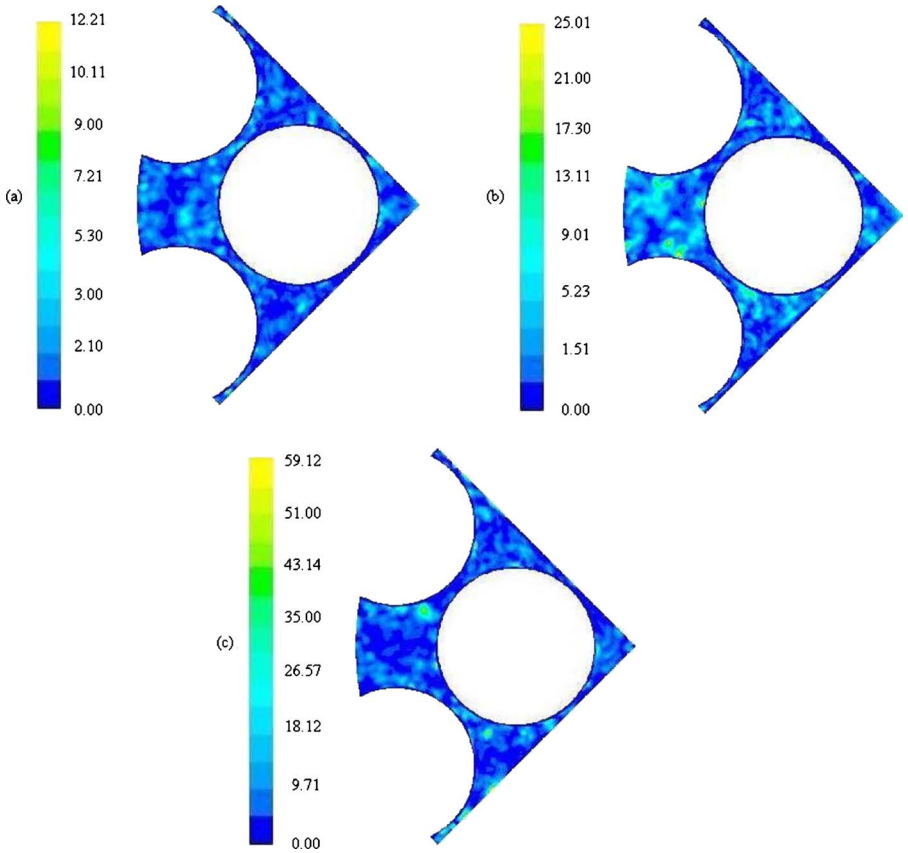

Fig. 15 Instantaneous subgrid-scale viscosity ratio (ν_t/ν): (*a*) U=0.759 m/s, (*b*) U=1.77 m/s, and (*c*) U=3.54 m/s

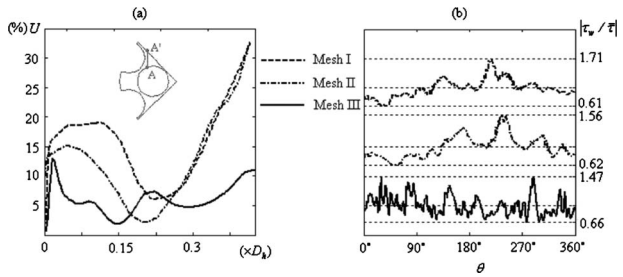

Fig. 16 (*a*) Instantaneous radial flow velocities normalized by the mean axial flow velocity on the line *AA′*; (*b*) instantaneous wall shear stress normalized by the circumferentially averaged shear stress ($\bar{\tau}$). Each curve of (*b*) is shifted upward by different distances.

which is caused by the minimal resolved Reynolds stresses in those areas. The maximal energy, as expected, appears in the vicinity of the eddies and the gap regions.

3.4 Instantaneous Flow Analysis. The instantaneous cross-flow vectors are shown in Fig. 13 for three different flow velocities. A broader range of Reynolds numbers is used in this subsection for the instantaneous flow analysis. The maximum magnitudes of velocity vectors are between 0.10 and 0.16 times the mean axial flow velocity. Eddies are formed in different locations in the subchannels. The coherent structures are a network of such eddies and are normally characterized when the second invariant of the velocity gradient is positive with the vorticity stronger than the strain. The centers of eddies are associated with positive second velocity invariant and have minimal energy dissipation, while the maximal energy dissipation occurs at the vicinity of eddies. The subgrid-scale turbulent kinetic energy is shown in Fig. 14. The contours are for the unit mass of the flow and are normalized by the mean axial flow velocity. The contours for all velocities show maximal values near the wall boundaries, and a rapid decrease at the subchannel center. Conversely, for the viscosity ratio contours shown in Fig. 15, the turbulent viscosity is damped on the solid boundaries and increases with the distance from the walls.

3.5 Grid Resolution. As shown in Fig. 3, grid resolution has significant effect on the result predicted by LES. Meshes I and II provided higher dissipation rate as indicated by the steeper PSD curve for the high wave numbers as compared to mesh III and the experimental results [3]. The main difference between meshes II and III is the finer lateral mesh and improved boundary layer mesh with $y^+=1$ for mesh III. Moreover, meshes I and II significantly overpredict PSD amplitude. In Fig. 16(*a*), instantaneous normalized radial flow velocity has been plotted on the line *AA′* that passes through the center of axial vortices. The curves understandably show decay in the middle as a result of minimal radial velocity magnitude at the center of vortices. While the curves for the coarse meshes (I and II) represent a single eddy, the curve for mesh III shows more oscillatory pattern that signifies the development of flow separation and formation of eddies. Similarly in Fig. 16(*b*), where the instantaneous wall shear stress is normalized by the circumferentially averaged shear stress, same comparison may be made. Mesh III exhibits more oscillatory behavior as a result of more localized eddy formation. The more detailed flow separation and eddy formation captured by mesh III can enhance

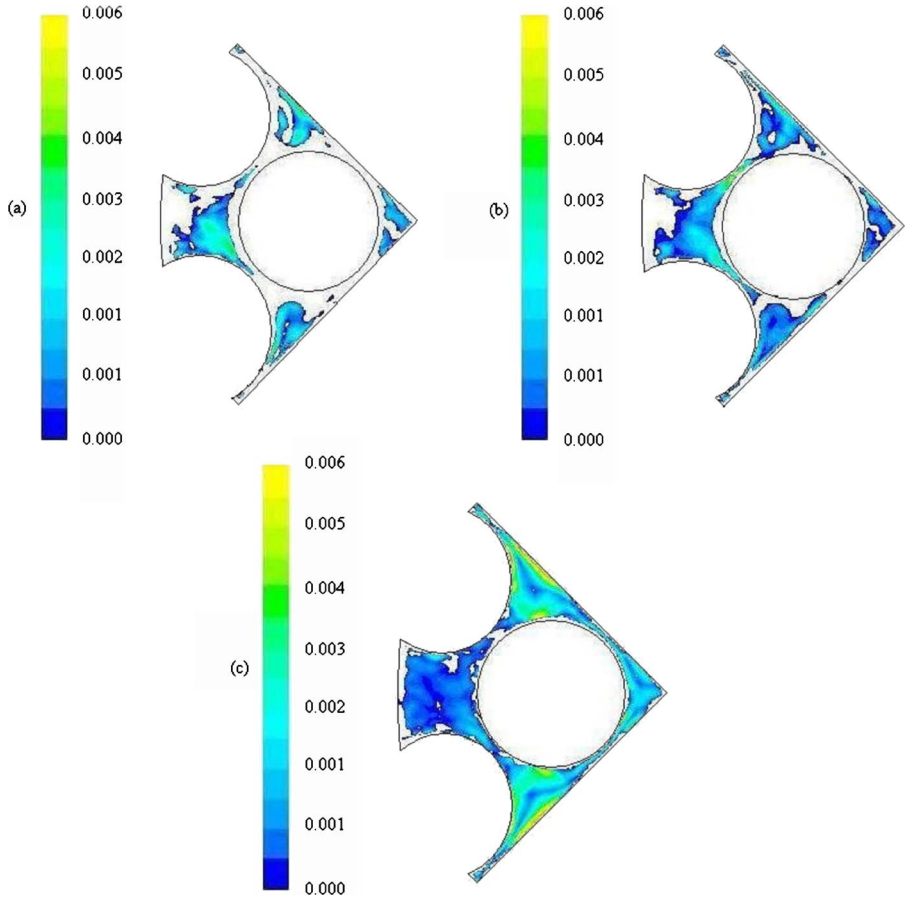

Fig. 17 Cross section areas associated with $(k-k_s)/U^2>0$: (*a*) mesh I, (*b*) mesh II, and (*c*) mesh III

the turbulent stresses resolved by LES and widen the LES region. It should be noted that the results shown in Fig. 16 are referenced by the mean value. The magnitudes of the wall stresses are higher for the coarse meshes because of the higher velocity gradients. The effect of mesh resolution on the resolved turbulence is further investigated by comparing the resolved and modeled kinetic energy in Fig. 17. The areas with a resolved kinetic energy higher than the modeled one are shown for the three meshes. The resolved kinetic energy (k) is time-averaged and the subgrid-scale turbulent energy (k_s) is instantaneous. The empty portions of the contours represent $k_s > k$. While there is no major difference between meshes I and II, a significant change can be seen for mesh III. According to the figure, larger area of higher resolved turbulent energy is shown for mesh III. For the coarse meshes I and II, a large portion of the contours near and away from the walls and even some areas in subchannel centers have higher modeled turbulent energy, while in the case of mesh III, only near-wall regions are emptied and the larger part of the cross section is filled with the higher resolved eddies and represents the LES region.

4 Conclusion

LES with DSM is employed in this paper to simulate turbulent axial flow along an array of rods. The spectral and mean flow analyses delivered results consistent with those experimentally obtained for the same geometry; however, some discrepancy is observed in the pressure spectrum for the higher wave numbers. Although a bounded central differencing scheme, which is competitive in terms of minimizing the numerical errors, is used, the effect of unphysical ripples and numerical dissipation on the pressure spectrum cannot be completely ruled out. The developed LES approach is successful in confirming the findings about coherent structures, geometry dependence, and turbulence characteristics in the bundle flows previously reported by the experimentalists in the literature. The mesh resolution and its effect on the eddy formation and development of the LES regions are also examined in this paper. It is found that proper lateral mesh resolution can significantly contribute to the eddy formation, and consequently, a more realistic simulation result of turbulent stresses. LES is an efficient tool in predicting unsteady flow characteristics in a fuel assembly. The capability of the model is attractive to the nuclear industry in predicting unsteady side forces induced by the turbulent flows through subchannels of a fuel bundle.

Acknowledgment

The authors would like to thank the National Science and Engineering Research Council of Canada (NSERC) for its financial support, and Dr. H. Schmider and Dr. G. Liu of HPCVL, Queen's University, Canada, for their technical support in parallel processing.

Nomenclature

C_s = Smagorinsky constant
D_h = hydraulic diameter (m)
d = cylinder diameter (m)
f = turbulence frequency (1/s)
k = resolved turbulent kinetic energy per unit mass, $1/2(u_x'^2+u_r'^2+u_\theta'^2)$ (m^2/s^2)
k_s = subgrid-scale turbulent kinetic energy per unit mass (m^2/s^2)
P = pitch (center-to-center distance) (m)
p = pressure (Pa)
$\bar{p}$ = normalized pressure, $p/1/2\rho U^2$
Re = Reynolds number
Re_τ = Reynolds number based on friction velocity
r = radial coordinate
r^+ = dimensionless mesh size in the radial direction
$S_{i,j}$ = strain rate tensor (1/s)
$|S|$ = filtered strain rate magnitude (1/s)
St = Strouhal number, $f \cdot D_h / U$
t = simulation time (s)
$\bar{t}$ = time delay (s)
$u_{x,r,\theta}$ = velocity tensor (m/s)
u_τ = friction velocity $(\tau_w/\rho)^{1/2}$ (m/s)
$u'_{x,r,\theta}$ = fluctuating velocity components (m/s)
U = mean axial flow velocity (m/s)
$U_{x,r,\theta}$ = time-averaged flow velocity (m/s)
$\bar{U}_{x,r,\theta}$ = time-averaged flow velocity normalized by the mean axial velocity
x^+ = dimensionless mesh size in the axial direction
y^+ = dimensionless cell distance from the wall, $u_\tau y/\nu$
δ = boundary layer thickness (m)
Δ = filter length, differential operator (m)
Δ^+ = dimensionless mesh size
ϕ_p = PSD of pressures (Pa^2/Hz)
$\bar{\phi}_p$ = normalized PSD, $\phi_p/\rho^2 U^3 D_h$
μ_t = turbulent viscosity ($kg\ m^{-1}\ s^{-1}$)
ν = kinematic molecular viscosity ($m^2\ s^{-1}$)
ν_t = kinematic turbulent viscosity ($m^2\ s^{-1}$)
θ = azimuthal coordinate
ρ = density ($kg\ m^{-3}$)
$\tau_{i,j}$ = subgrid-scale stress tensor ($kg\ m^{-1}\ s^{-2}$)
τ_w = wall shear stress ($kg\ m^{-1}\ s^{-2}$)

References

[1] Paidoussis, M. P., 2006, "Real-Life Experience With Flow-Induced Vibration," J. Fluids Struct., **22**, pp. 741–755.
[2] Norsworthy, A. G., Field, G. J., Meysner, A., Dalton, K., and Crandell, A., 1994, " Fuel Bundle to Pressure Tube Fretting in Bruce and Darlington Reactors," Proceedings of the 15th Canadian Nuclear Society Annual Conference, Montreal, Canada, Jun. 5–8.
[3] Curling, L. R., and Paidoussis, M. P., 1992, "Measurements and Characterization of Wall-Pressure Fluctuations on Cylinders in a Bundle in Turbulent Axial Flow; Part 1: Spectral Characteristics," J. Sound Vib., **157**(3), pp. 405–433.
[4] Curling, L. R., and Paidoussis, M. P., 1992, "Measurements and Characterization of Wall-Pressure Fluctuations on Cylinders in a Bundle in Turbulent Axial Flow; Part 2: Temporal Characteristics," J. Sound Vib., **157**(3), pp. 435–449.
[5] Rowe, D. S., Johnson, B. M., and Kundsen, J. G., 1974, "Implications Concerning Rod Bundle Cross Flow Mixing Based on Measurements of Turbulent Flow Structure," Int. J. Heat Mass Transfer, **17**, pp. 407–419.
[6] Moller, S. V., 1991, "On Phenomena of Turbulent Flow Through Rod Bundles," Exp. Therm. Fluid Sci., **4**, pp. 25–35.
[7] Rehme, K., 1992, "The Structure of Turbulence in Rod Bundles and the Implications on Natural Mixing Between the Subchannels," Int. J. Heat Mass Transfer, **35**(2), pp. 567–581.
[8] Hooper, J. D., and Wood, D. H., 1984, "Fully Developed Rod Bundle Flow Over a Large Range of Reynolds Number," Nucl. Eng. Des., **83**, pp. 31–46.
[9] Vonka, V., 1988, "Measurements of Secondary Flow Vortices in a Rod Bundle," Nucl. Eng. Des., **106**, pp. 191–207.
[10] Lee, K. B., and Jang, H. C., 1997, "A Numerical Prediction on the Turbulent Flow in Closely Spaced Bare Rod Arrays by a Nonlinear κ-ε Model," Nucl. Eng. Des., **172**, pp. 351–357.
[11] In, W. K., Shin, C. H., Oh, D. S., and Chun, T. H., 2004, "CFD Simulation of the Turbulent Flow and Heat Transfer in a Bare Rod Bundle," Proceedings of the ICAPP '04, Pittsburgh, PA, Jun. 13–17, Paper No. 4179, pp. 1544–1551.
[12] Ikeno, T., Kajishima, T., and Murata, T., 2006, "The Effect of Mixing-Vane Arrangements in a Subchannel Turbulent Flow," J. Nucl. Sci. Technol., **43**(10), pp. 1194–1205.
[13] Kim, H. M., and No, H. C., 2004, "Analysis of Power Spectrum Density in the PWR Fuel Assembly Using the 3-D LES Turbulent Model of FLUENT 6," Proceedings of the 12th ASME International Conference on Nuclear Engineering (ICONE12), Arlington, VA, Apr. 25–29, 2004, pp. 295–303.
[14] Smagorinsky, J. S., 1963, "General Circulation Experiments With the Primitive Equations, Part I: The Basic Experiment," Mon. Weather Rev., **91**, pp. 99–152.
[15] Germano, M., Piomelli, U., Moin, P., and Cabot, W. H., 1991, "A Dynamic Subgrid-Scale Eddy Viscosity Model," Phys. Fluids A, **3**(7), pp. 1760–1765.
[16] Leonard, B. P., 1991, "The ULTIMATE Conservative Difference Scheme Applied to Unsteady One-Dimensional Advection," Comput. Methods Appl. Mech. Eng., **88**, pp. 17–74.
[17] Abbasian, F., Cao, J., and Yu, S. D., 2008, "Numerical and Experimental Studies of Oscillatory Airflows Induced by Rotation of a Grass-Cutting Blade," ASME J. Fluids Eng., **130**(3), p. 031104.

[18] Kraichnan, R. H., 1956, "Pressure Fluctuations in Turbulent Flow Over a Flat Plate," J. Acoust. Soc. Am., **28**(3), pp. 378–390.
[19] Farabee, T. M., and Casarella, M. J., 1991, "Spectral Features of Wall Pressure Fluctuations Beneath Turbulent Boundary Layers," Phys. Fluids A, **3**(10), pp. 2410–2420.
[20] Addad, Y., Laurence, D., Talotte, C., and Jacob, M. C., 2003, "Large Eddy Simulation of a Forward-Backward Facing Step for Acoustic Source Identification," Int. J. Heat Fluid Flow, **24**, pp. 562–571.
[21] Abbasian, F., Cao, J., and Yu, S. D., 2008, "Measurements of Turbulent Pressures of Flow in a Water-Conveying Pipe Containing a Simulation Fuel Bundle," Proceedings of the 2008 Canadian Nuclear Society Annual Conference, Toronto, Canada.
[22] Clinch, J. M., 1969, "Measurements of the Wall Pressure Field at the Surface of a Smooth-Walled Pipe Containing Turbulent Water Flow," J. Sound Vib., **9**, pp. 398–419.
[23] Mulcahy, T. M., Wambsganss, M. W., Lin, W. H., Yeh, T. T., and Lawrence, W. P., 1981, "Measurements of Wall Pressure Fluctuations on a Cylinder in Annular Water Flow With Upstream Disturbances, Part I: No Flow Spoilers," General Electric Co., Nuclear Engineering Division, San Jose, CA, Report No. GEAP-24310.

Mihael Sekavčnik
Department of Energy Engineering,
Faculty of Mechanical Engineering,
University of Ljubljana,
Aškerčeva 6,
SI-1000 Ljubljana, Slovenia
e-mail: mihael.sekavcnik@fs.uni-lj.si

Tine Gantar
Envita d.o.o.,
Trzaska 132,
SI-1000 Ljubljana, Slovenia
e-mail: tine.gantar@envita.si

Mitja Mori
Department of Energy Engineering,
Faculty of Mechanical Engineering,
University of Ljubljana,
Aškerčeva 6,
SI-1000 Ljubljana, Slovenia
e-mail: mitja.mori@fs.uni-lj.si

A Single-Stage Centripetal Pump—Design Features and an Investigation of the Operating Characteristics

In this paper, we present an experimental and numerical investigation of a single-stage centripetal pump (SSCP). This SSCP is designed to operate in the pump regime, while forcing the working media through impeller-stator flow channels in the radial inward direction. The measured performance curves are characterized by a hysteresis, since the throttle-closing performance curves do not correspond to the throttle-opening performance curves throughout the whole operating range. A computational fluid dynamics (CFD) model was developed to establish these throttle-closing and throttle-opening performance curves. The flow conditions obtained with the CFD simulations confirm that the hydraulic behavior of the SSCP is influenced by the partial circumferential stall that occurs in the impeller-stator flow channels. It was shown that the inflow conditions to the impeller-stator assembly considerably influence the flow rate of the stall cessation, the size of the hysteresis, and the head generated during part-load operations.
[DOI: 10.1115/1.4000846]

Keywords: single-stage centripetal pump, measurements, CFD analysis, performance curves, hysteresis, stall

1 Introduction

Regarding the basic flow direction and the transfer of energy between an impeller and a fluid, radial turbomachinery can be divided into four types: centrifugal pumps, centripetal pumps, centripetal turbines, and centrifugal turbines. These are presented in a four-quadrant chart describing the particular turbomachine type, Fig. 1. The typical geometry of each type of radial turbomachinery is shown in the meridional and cascade plane (the impeller, stator, and guide vanes are designated by I, S, and GV, respectively).

Centrifugal pumps, as power-absorbing machines (Fig. 1, quadrant I), and centripetal turbines, as power-producing machines (Fig. 1, quadrant III), represent the conventional forms of radial turbomachinery. These are machines with a defined form, an optimized design for different standard applications, and a known range of operation. The flow and energy characteristics of conventional radial turbomachinery are, to a large extent, known and widely discussed. In contrast, the amount of research conducted on unconventional radial turbomachinery, whose main feature is a change in the basic flow direction, is far from extensive. An experimental and numerical investigation of the flow and energy characteristics of a centrifugal turbine was performed by Sekavčnik et al. [1–4]. Good agreement between the measured and calculated energy characteristics was obtained. Restrictions regarding the impeller design were given. The effect of the Coriolis force on the energy characteristics was explained. The position in the Cordier diagram was determined according to the measured energy maps.

The initial investigations on centripetal pumps were made by Petermann [5] and Pfleiderer [6]. Petermann proved experimentally that a radial pump with the appropriate geometrical and operating parameters could operate in the pump regime while forcing the fluid in the centripetal direction. This pump regime operation is determined by the transfer of energy from the pump's impeller blades to the fluid, which is forced through the impeller cascade, receiving a certain head rise along the streamline at the flow rate determined by the intersection of the pump and system head-capacity curves. The first guidelines for the design of a centripetal radial pump presented in Ref. [5] state that the following—a small value for the impeller radius ratio R_2/R_1, an appropriate impeller-blade geometry, an appointed direction for the impeller rotation, and the installation of an appropriate stator on the inner impeller radius—are essential to obtain a centripetal flow direction in the pump regime. The centripetal pump can be, in general, utilized in applications where the working media flows radially inward and a total head rise is required. Petermann [5], e.g., suggested that a centripetal pump stage could be used to ensure a total pressure rise in the return channels of multistage centrifugal pumps.

Some time later, Gantar and Sekavčnik [7–9] focused their research on the hydraulic behavior of radial pump stages (RPS) and the requirements that have to be fulfilled in order to achieve centripetal pumping. The influence of the RPS geometry and the operating conditions on the basic flow direction in the pump regime were studied systematically using analytical and numerical tools. The results of the research were given in terms of the flow and energy characteristics, as well as the four-quadrant charts showing all the operating regimes of the RPS. The four-quadrant chart—also known as the "circle diagram"—is a standard method (used by several authors: Knapp [10,11], Stepanoff [12], Karassik et al. [13], and Guelich [14]) for the presentation of possible operating regimes (modes) and the complete energy characteristics of a pump.

Based on RPS research, Gantar et al. [15] designed a flange-to-flange single-stage centripetal pump (SSCP) using computer-aided design (CAD) and CFD tools, measured the performance curves of the SSCP in a test facility with water as the working medium, and compared the calculated and measured results. The measured performance curves of the SSCP are characterized by a hysteresis,

Contributed by the Fluids Engineering Division of ASME for publication in the JOURNAL OF FLUIDS ENGINEERING. Manuscript received May 27, 2009; final manuscript received December 11, 2009; published online February 16, 2010. Assoc. Editor: Edward M. Bennett.

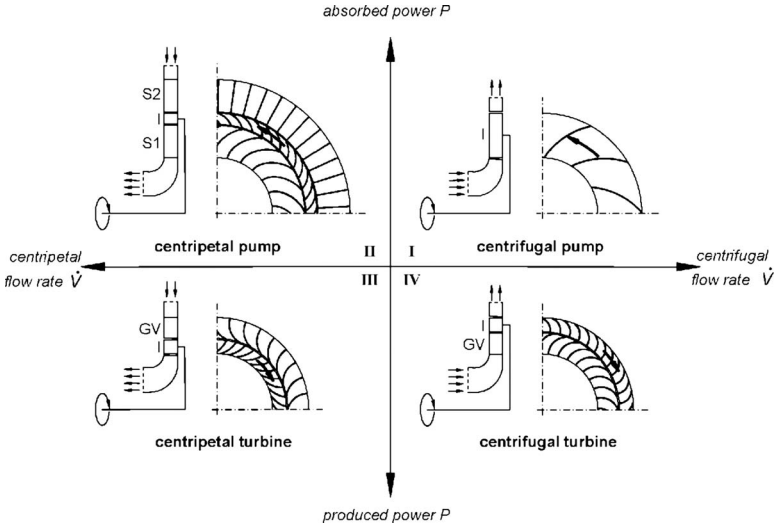

Fig. 1 Basic division of radial turbomachinery

where the performance curves differ, depending on whether the measurement points were obtained during a flow rate reduction (throttle-closing performance curves) or during a flow rate increase (throttle-opening performance curves). The delivery head and the efficiency of the SSCP are abruptly decreased when reducing the flow rate from the point of the maximum head. The calculated head-capacity and efficiency-capacity performance curves have a similar curve shape to the measured throttle-closing curves. However, using the applied CFD approach, the measured throttle-opening curve in the hysteresis could not be established.

In the present paper, further research on the SSCP is presented, focusing on:

- a prediction of throttle-closing and throttle-opening performance curves using CFD tools;
- an analysis of the fluid flow conditions along both performance curves;
- an analysis of the stall phenomenon occurring in the SSCP; and
- a prediction of the effect of the impeller-stator inflow conditions on the performance of the SSCP.

2 Single-Stage Centripetal Pump Design

The main hydraulic elements of the SSCP are the volute casing V, the impeller I, the stator on the outer impeller diameter S2, and the stator on the inner impeller diameter S1. The geometry of the SSCP in the cascade plane is shown in Fig. 2. The volute is a welded sheet-metal piece. The impeller and both stators were manufactured using the selective laser sintering process, and the PA3200GF Polyamide material was used. The surface roughness of the impeller and both stators was reduced, performing the surface-smoothing treatment (Step 1: treatment with small metal balls, Step 2: grinding and painting). The SSCP is equipped with a Plexiglas window, enabling optical access to the impeller-stator assembly.

The stator S2 was designed to deliver some prerotation of the flow approaching the impeller inlet. The impeller geometry is very similar to the one investigated in Refs. [7–9] as a part of the unconventional radial pump stage. The size of the impeller is smaller and the blades are relatively thicker due to the smaller impeller size when compared with the impeller discussed in Refs. [7–9]. The stator S1 was designed to reduce the peripheral velocity component of the flow exiting the impeller and to ensure a flow without rotation at the discharge flange.

The impeller is rotationally fixed to the shaft and rotates with the rotational speed n in the direction depicted in Fig. 3. The main geometrical parameters of the SSCP are given in Table 1. The direction of the flow through the SSCP is shown by the arrows in Fig. 3.

3 Measurements

The performance of the SSCP was tested in a rig, shown schematically in Fig. 4. The working medium was water. The tank and the pump were connected with the suction and discharge pipelines, with both pipelines equipped with butterfly valves located close to the tank. The butterfly valve 1 was used for the flow rate variation. The pump was driven by an eight-pole three-phase asynchronous motor with a nominal power of $P_n=0.55$ kW, governed by means of a variable-frequency drive, allowing the adjustment of the motor's rotational speed. The pump's performance was measured at a rotational speed of $n \cong 600$ min^{-1}.

The flow rate was measured with an orifice plate connected to a differential pressure sensor. The orifice plate was manufactured and integrated into the test rig according to Ref. [16]. The static pressure rise/drop $\Delta p_{p-\mathrm{st}}$ from the pump's suction flange to the pump's discharge flange was obtained using a differential pressure transducer. The rotational speed n was determined by an optical proximity sensor. To calculate the torque M, the motor was doubly embedded and equipped with a fixed arm pressing onto the dyna-

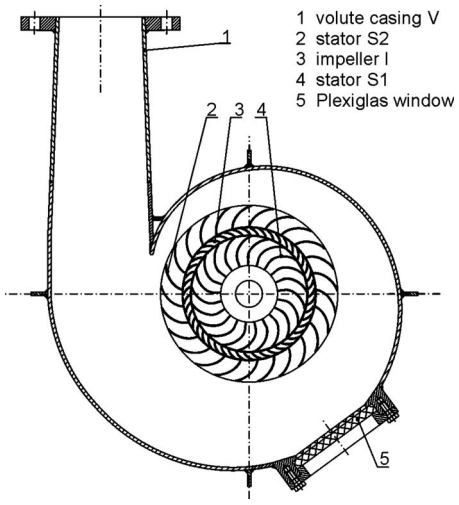

Fig. 2 SSCP in cascade plane section

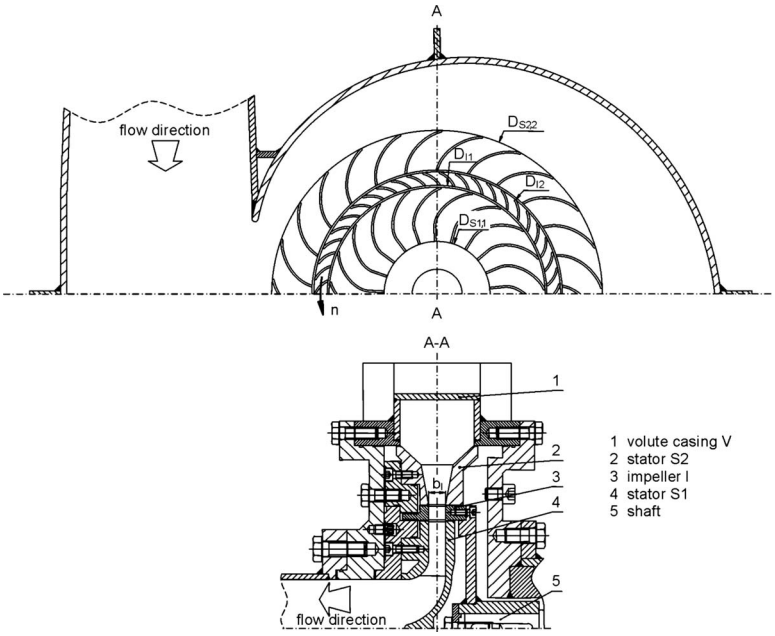

Fig. 3 Cross section of the SSCP in cascade and meridional plane

mometer. The water temperature T_w was measured using a Pt100 resistance temperature detector. A personal computer equipped with a multichannel card was used for the data acquisition and the postprocessing of the data.

Due to a slight variation in the rotational speed (± 5 min^{-1}) during the measurement of the pump's performance curves, the measured operating points were recalculated according to the hydraulic affinity laws for turbomachinery to a constant rotational speed of $n=600$ min^{-1}. Water temperature was $T_w \approx 25\,^{\circ}$C. The Reynolds number, based on the outer impeller diameter D_2, the impeller circumferential velocity u_2, and the kinematic viscosity of water at 25°C, is $\mathrm{Re}_u=(u_2 \cdot D_2)/\nu=1.42\times 10^6$.

Table 1 Main geometrical parameters of the SSCP

Geometrical parameter	Impeller	Stator S2	Stator S1
Outer diameter	$D_{I2}=200$ mm	$D_{S2,2}=268$ mm	$D_{S1,2}=172$ mm
Inner diameter	$D_{I1}=175$ mm	$D_{S2,1}=203$ mm	$D_{S1,1}=86$ mm
Width	$b_I=14$ mm	-	-
Blade number	$Z_I=47$	$Z_{S2}=26$	$Z_{S1}=21$
Outer blade angle	$\beta_{I2}=20$ deg	$\alpha_{S2,2}=20$ deg	$\alpha_{S1,2}=20$ deg
Inner blade angle	$\beta_{I1}=60$ deg	$\alpha_{S2,1}=70$ deg	$\beta_{S1,1}=90$ deg

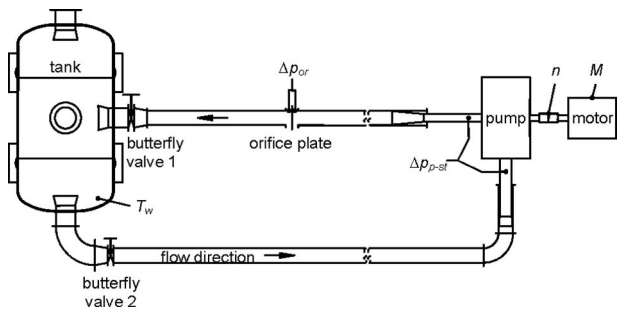

Fig. 4 Ground plan of the test rig

4 CFD Analysis

Steady-state CFD simulations are widely used in the field of turbomachinery for studying three-dimensional turbulent flow during both design and off-design conditions. Good agreement between the calculated results and those obtained with measurements was proven by several authors [17–20]. Muggli et al. [17] used CFD tools to investigate the mixed-flow pump's characteristics between 20% and 100% of the flow rate at the best-efficiency point (BEP). The calculated energy characteristics (stage total head, static pressure rise in the impeller and static pressure difference in the diffuser) of the investigated pump are in better agreement with the measured ones in the region of the BEP than in the region of the part-load. The level of the simulation accuracy determining the stage total head around the BEP is in the range of $\pm 5\%$; although it is increased to $\pm 10\%$ when the flow rate is reduced toward shutoff (the level of the simulation accuracy refers to the percentage deviation of the calculated value with respect to the measured one). Similar findings were also established in Refs. [18,19]. Gugau [18] investigated three centrifugal pumps: pump *nq* 28 with a vaneless diffuser, and also pumps *nq* 20 and *nq* 26, both with a volute casing. A broad series of numerical simulations were undertaken, investigating the influence of the frame-change model and turbulence models on the calculated energy characteristics, mainly in the region between 50% and 120% of the flow rate at the BEP. Regarding the agreement between the calculated and measured energy characteristics, it can be concluded that the use of the mixing plane interface generally leads to better agreement with the measured results, while the influence of the turbulence model on the energy characteristics is not particularly noticeable. The level of the simulation accuracy, when using the mixing plane interface, is below $\pm 10\%$ for the investigated flow rate region. Adami et al. [19] performed a CFD analysis of two vertical multistage pumps (*nq* 33 and *nq* 39) designed according to API 610. The authors confirmed that secondary flow effects, such as leakage flows, disk-friction losses, and wall friction, should not be neglected if the aim is to reach a high level of numerical simulation accuracy. When the flow through the pump's side chambers and the balancing holes were included in the CFD analysis, the calculated energy characteristics in the region be-

Table 2 Main properties of the calculated variations

Approach	Grid (number of elements/nodes)	Relative average element size h^*	Designation
Segmental	Coarse (160,000/55,000)	1.64	Seg_grid3_$k\omega$
Segmental	Medium (340,000/115,000)	1.27	Seg_grid2_$k\omega$
Segmental	Fine (700,000/235,000)	1.00	Seg_grid1_$k\omega$
Full pitch-360 deg	Coarse (4,350,000/1,460,000)	1.64	360 deg_grid3_$k\omega$

$h^*=h/h_{\text{fine}}$.

tween 60% and 120% of the BEP flow rate fit to the experimental data with a level of accuracy better than ±5%. Braun et al. [20] proved that the CFD tools are also suitable for a flow simulation of turbomachinery with unstable energy characteristics. It was confirmed that the flow conditions and the energy characteristics obtained with a steady-state numerical flow analysis of the pump-turbine working in the pump mode correspond very well to the experimental data. The recirculation onset within the guide vanes of the pump-turbine leading to an unstable energy characteristic was shown by means of CFD tools.

In the case of the present research, the steady-state three-dimensional turbulent flow of a viscous fluid was modeled by the Reynolds averaged Navier–Stokes (RANS) equations applied on a finite-volume discretization scheme. The two-equation k-ω turbulence model was applied in the calculations. An unstructured tetrahedral grid with prismatic layers on all the walls was created for every computational domain, and the grid-size optimization process was performed. The grids of different domains were connected using the general grid interface (GGI) method. All the walls were considered to be hydraulically smooth with no slip influence on the flow. An automatic wall function was used. The second-order advection scheme was used for the analysis of the near-BEP operating points; however, for part-load operating points, a specified blend factor with a value 0.75 was used for the advection scheme due to an insufficient convergence behavior during full second-order accuracy. The residual convergence criterion for the rms mass-momentum and turbulence equations was set to 5×10^{-5}. The interfaces between the stationary and rotating domains were set as a frozen rotor. The two frames of reference were connected in such a way that they had a fixed relative position throughout the calculation, but with the appropriate frame transformation occurring across the interface [21]. A commercial software package—ANSYS CFX 10.0 with ANSYS ICEM CFD 10.0—was used to provide the discretization (grids), the interface, boundary and parameter definition, and finally, the calculations.

The hydraulic behavior of the SSCP was analyzed at a constant rotational speed of the impeller $n=600$ min^{-1}. The analyzed fluid was water at 25°C. The Reynolds number Re_u is the same as in the measurements ($\text{Re}_u=1.42\times10^6$).

The hydraulic behavior of the SSCP was analyzed using two different CFD approaches.

4.1 Segmental. In the first calculation step, the flow domain was composed of the suction pipe, the volute, and the stator S2. The inflow was set at the position of the suction pipe inlet located upstream of the suction flange. The computed velocity distributions at the domain interface between the volute and the stator S2 were exported, averaged, and finally used as the inlet boundary conditions for the second step of the segmental approach. In the second step, the computational domain consisted of the stator S2, the impeller I, the stator S1, the bend that directs the fluid flow axially, and the discharge pipe. Here, a rotational periodic interface was used for all the computational domains: The impeller grid consisted of two blades and both stators grids consisted of one blade each ($Z_I=47, Z_{S1}=21, Z_{S2}=26$). The corresponding pitch angles are: $\theta_I=15.3$ deg, $\theta_{S1}=17.1$ deg, and $\theta_{S2}=13.8$ deg. When combining the partial results of both steps, the hydraulic characteristics from the suction to the discharge flange of the SSCP were obtained. It should be noted that the CFD calculations were carried out at four different relative angular settings of the impeller blades against the stator blades for each flow rate. The results of the numerical investigations, given in Sec. 5, represent the average values of the four different relative impeller-stator positions.

4.2 Full Pitch-360 deg. In the full pitch-360 deg approach, the flow in the SSCP—from the suction to the discharge flange—was analyzed in the joint grid assembly that consisted of the suction pipe grid, the volute grid, the 360 deg grids of the stator S2, the impeller, the stator S1, the bend and the axial pipe with the discharge flange, and the discharge pipe grid. It was found that in the full pitch-360 deg approach, the influence of the impeller angular location on the flow conditions and SSCP performance curves is negligible. This was confirmed by two sets of full pitch-360 deg calculations: four different angular settings of the impeller were analyzed at two flow rates ($\varphi=0.17$ and $\varphi=0.26$).

Four numerical models were investigated: three different refinement levels on the segmental approach and one on the full pitch-360 deg approach. The refinement factor in the average cell size, as well as in the essential boundary layer cell thickness was approximately 1.3 (see Table 2, where relative average cell size is given for all grid variations). The full pitch-360 deg calculation was carried out only for the coarse grid due to limitations in the available computational capacities.

5 Results

5.1 Definition of the Dimensionless Coefficients. The calculated and measured characteristics of the analyzed SSCP are presented by means of the dimensionless coefficients defined in Eqs. (1)–(4).

Flow coefficient φ

$$\varphi=\frac{2\dot{V}}{\pi D_2^2 b\omega} \tag{1}$$

Head coefficient ψ ($\Delta p_{p-\text{tot}}$ stands for the total pressure rise from the pump's suction flange to the pump's discharge flange)

$$\psi=\frac{8\Delta p_{p-\text{tot}}}{\rho D_2^2\omega^2} \tag{2}$$

Power coefficient λ

$$\lambda=\frac{M}{\rho D_2^5\omega^2} \tag{3}$$

Efficiency η

$$\eta=\frac{\dot{V}\Delta p_{p-\text{tot}}}{M\omega} \tag{4}$$

5.2 Error Analysis. The application of the measurement-uncertainty analysis to the SSCP best-efficiency point according to Ref. [22] gives a relative uncertainty U, where P stands for the precision limit and B for the bias limit, Eq. (5). Table 3 gives the relative uncertainty of the main measured parameters at the experimenter's 95% confidence estimate. It should be noted that the

Table 3 Measurement uncertainty at the best-efficiency point

Parameter	Relative uncertainty U (%)
Flow coefficient φ	1.07
Head coefficient ψ	1.61
Power coefficient λ	0.90
Efficiency η	1.98

uncertainty for each variable was calculated, taking into account the sensor uncertainty and the analog-to-digital conversion uncertainty

$$U = \sqrt{P^2 + B^2} \tag{5}$$

The discretization error in the performed CFD calculations was estimated according to Ref. [23]. In Table 4, the grid-refinement factor r, the solution values ϕ, the extrapolated solution value ϕ_{ext}^{21}, the approximate relative error e_a^{21}, the extrapolated relative error e_{ext}^{21}, and the fine-grid convergence index $\text{GCI}_{\text{fine}}^{21}$ are given on the basis of the calculated head coefficient ψ and the efficiency η at three flow rate coefficients φ. The extrapolated relative error e_{ext}^{21} is below 1% at the best-efficiency point for both the head coefficient ψ and the efficiency η. At a reduced flow rate $\varphi = 0.17$, the extrapolated relative error e_{ext}^{21} increases to about 2.5% and to not more than 1.7% at the flow rate coefficient of $\varphi = 0.34$. The fine-grid convergence index $\text{GCI}_{\text{fine}}^{21}$ is estimated to be below 3.5% in the region $0.17 < \varphi < 0.34$ (see also Figs. 6, 10, and 11).

5.3 Performance Characteristics of the SSCP. The energy transferred from the SSCP to the working medium is not increasing continuously toward shutoff. Such a pump is prone to lead to unstable system operations. The resulting $\psi-\varphi$ curve is referred to as unstable and includes a large hysteresis since the throttle-closing $\psi-\varphi$ curve does not correspond to the throttle-opening $\psi-\varphi$ curve throughout the whole operating range (see Fig. 5). When the flow rate is reduced from its maximum value (A), the pump head rises to (B) and due to the unstable nature of the flow at (B), the flow pattern is changed at the same butterfly valve throttling rate (constant loss coefficient) leading to the operating point (C), determined with a markedly reduced pump flow rate and head with regard to the pump's performance at (B). It should be emphasized that a stationary operation on the curve section between (B) and (C) cannot be established since the transition from operating point (B) to (C) occurs suddenly. A further reduction in the flow rate from (C) to shutoff (D) leads to a moderate drop of the pump head. When the flow rate is increased from the point of shutoff, the measured $\psi-\varphi$ curve corresponds to the one obtained at the flow rate reduction up to the operating point (C). A

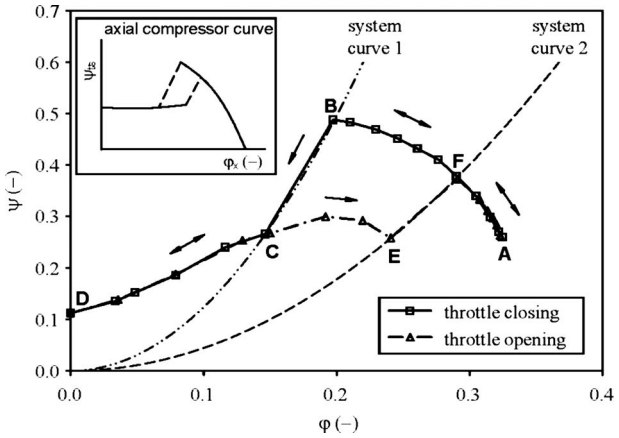

Fig. 5 Measured $\psi-\varphi$ curves of the SSCP

further increase in the flow rate from operating point (C) leads to pump head values that are considerably lower than in the case of the flow rate reduction, i.e., section (C) to (E). The throttle-opening $\psi-\varphi$ curve meets the throttle-closing $\psi-\varphi$ curve at (F) after a steep and sudden rise from operating point (E) to (F), marked with a higher head and flow rate. The operation at (E) is unstable and the transition from operating point (E) to (F) occurs at a constant butterfly valve opening (constant loss coefficient). In the region between (F) and (A), the throttle-opening $\psi-\varphi$ curve corresponds to the throttle-closing $\psi-\varphi$ curve.

The following findings are important.

- If the flow rate is reduced from (A) over (F) to (B) and then increased toward (A), the operating points lie on the (A)-(F)-(B) $\psi-\varphi$ curve.
- The pump has to operate between (A) and (F) on the $\psi-\varphi$ curve before the operating points between (F) and (B) can be achieved.

The described hydraulic behavior is similar to that observed in axial-flow compressors, resulting from the rotating-stall phenomenon. The axial-flow compressor performance in the rotating stall was investigated in Refs. [24–27]. When the flow rate through an axial compressor is reduced from the design value, the flow at a certain operating point becomes unstable, resulting in the onset of the rotating-stall phenomenon. With such operating behavior, the compressor annulus is partially blocked with retarded flow regions rotating around the compressor axis. The consequences of the rotating stall can be a significant reduction in the flow rate, the delivery pressure, and the efficiency. The occurrence of the hysteresis in the performance curves between the stall onset and the

Table 4 Discretization error estimation

	At $\varphi=0.17$		At $\varphi=0.26$		At $\varphi=0.34$	
	$\phi=\psi$	$\phi=\eta$	$\phi=\psi$	$\phi=\eta$	$\phi=\psi$	$\phi=\eta$
r_{21}	1.27	1.27	1.27	1.27	1.27	1.27
r_{32}	1.29	1.29	1.29	1.29	1.29	1.29
ϕ_1	0.366	0.321	0.591	0.580	0.372	0.454
ϕ_2	0.353	0.312	0.579	0.579	0.348	0.432
ϕ_3	0.319	0.292	0.540	0.552	0.223	0.302
ϕ_{ext}^{21}	0.375	0.329	0.597	0.580	0.378	0.459
e_a^{21} (%)	3.55	2.80	2.03	0.17	6.45	4.85
e_{ext}^{21} (%)	2.39	2.51	0.99	0.01	1.68	1.09
$\text{GCI}_{\text{fine}}^{21}$ (%)	3.06	3.21	1.25	0.01	2.13	1.38

Sub- or superscripts 1, 2, and 3 relate to grids 1, 2, and 3, respectively.

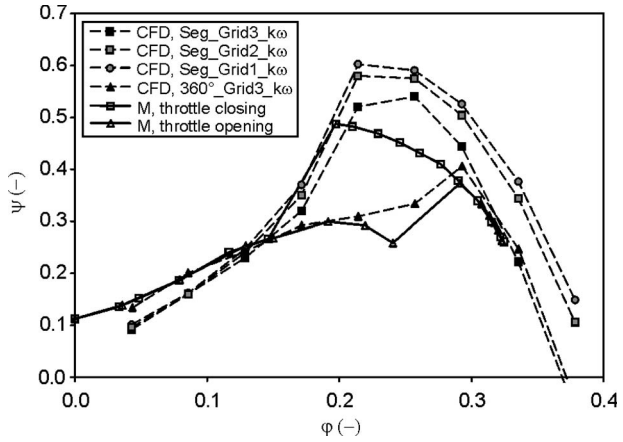

Fig. 6 Comparison of measured and calculated $\psi-\varphi$ curves of the SSCP

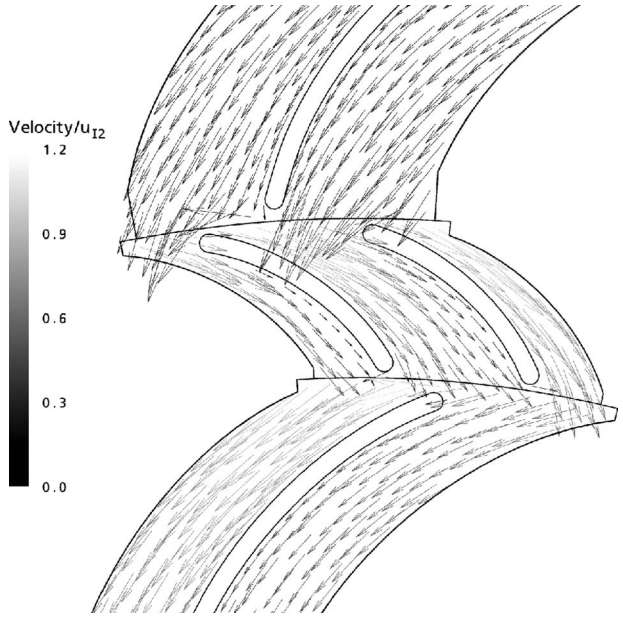

Fig. 7 Velocity vectors, midchannel, segmental approach, $\varphi=0.26$

stall cessation is typical for axial-flow compressors. In the top-left corner of Fig. 5, the dimensionless pressure-capacity curve of a typical axial-flow compressor undergoing a full-span stall is shown.

The study of the hydraulic behavior of the SSCP was carried out using CFD tools according to the described segmental and full pitch-360 deg approaches. The $\psi-\varphi$ curve acquired using the segmental approach corresponds to the measured throttle-closing $\psi-\varphi$ curve; however, there are quite large discrepancies between the two curves, see Fig. 6. The calculated $\psi-\varphi$ curve is considerably higher than the measured $\psi-\varphi$ curve in the flow region $\varphi>0.15$. This discrepancy can be explained by the significant difference in the surface roughness present during the performed calculations, and that of the real surface roughness of the impeller and both stators installed in the measured pump. All the walls were considered to be hydraulically smooth in the case of the numerical analyses; however, the actual surface roughness of the impeller and both stators installed in the measured pump was far from being hydraulically smooth. The selective laser sintering method yielded rough surfaces for the manufactured impeller and both stators. The surface roughness was reduced; however, the surfaces of the impeller and both stators were still rather rough in the regions of small channel cross sections (e.g., throughout the impeller cascade), where the surface-smoothing treatment was imperfect. Certainly, making the surfaces of the impeller and both stators almost hydraulically smooth would contribute to a better agreement between the calculated and measured $\psi-\varphi$ curves in the flow region $\varphi>0.15$. A marked impact of surface roughness on the $\psi-\varphi$ curve was proven with measurements. The impeller and both stators were installed in the pump after the surface-smoothing treatment with small metal balls, but without being ground and painted. The deterioration of the head and efficiency was considerable when compared with the ground and painted impeller-stator assembly. The not-ground and not-painted impeller-stator assembly led to a 70% decrease in the shutoff head and a 30% decrease in the maximal head, if compared with the ground and painted impeller-stator assembly. Such a marked influence of the surface roughness on the performance curves is mainly caused by a high number of blades and small channel cross sections, especially in the impeller and the stator S1.

The lower branch of the hysteresis in the head-capacity characteristic of the SSCP could not be established using the segmental approach since the performed steady-state numerical analyses delivered practically the same result at a certain flow rate, regardless of the initial simulation conditions.

In contrast, the $\psi-\varphi$ curve that was obtained using the full pitch-360 deg approach corresponds to the measured throttle-opening $\psi-\varphi$ curve. If it is compared with the $\psi-\varphi$ curve obtained using the segmental approach with the corresponding grid quality, it can be concluded that in the flow rate regions of $\varphi>0.3$ and $\varphi<0.15$, both the calculated $\psi-\varphi$ curves are very similar. In contrast, there is an evident distinction between the curves in the flow rate region $0.15<\varphi<0.3$. In this flow rate region, the calculated full pitch-360 deg $\psi-\varphi$ curve suits the lower branch of the measured $\psi-\varphi$ curve, while the calculated segmental $\psi-\varphi$ curve corresponds to the upper branch of the measured $\psi-\varphi$ curve. The size and location of the $\psi-\varphi$ curve hysteresis is predicted well by combining both calculation approaches. However, the upper branch of the hysteresis in the head-capacity curve of the SSCP could not be established using the full pitch-360 deg approach since, like the segmental approach, the performed steady-state numerical analyses delivered practically the same result at a certain flow rate, regardless of the initial conditions of the simulation.

It has to be mentioned that the calculated characteristics were shifted to lower flow rates for the amount of volumetric losses calculated according to Ref. [28]. For calculation of volumetric losses, the static pressure difference between both sides of the impeller obtained with CFD analysis (segmental approach, grid 1) was used. The level of volumetric losses is very small (although the diameter where the leakage occurs are quite large) due to: small static pressure difference between both sides of the impeller, double labyrinth sealing, small clearances, and rough sealing surfaces. Calculated volumetric losses are $\varphi_{vol}<0.004$ throughout the whole operating range ($\varphi_{opt}=0.26$). Volumetric efficiency at the best-efficiency point is above 98%.

The differences in the flow conditions on both branches of the hysteresis are shown at the same flow rate coefficient $\varphi=0.26$ in Figs. 7–9. The velocity vectors in the impeller and both stators are shown in the relative (rotating) and absolute (stationary) frames, respectively. Regarding the number and the density distribution of the computational grids, the velocity vectors presented in Figs. 7–9 are shown in a reduced number and equally spaced manner to provide a clearer representation of the flow conditions.

At the flow rate coefficient of $\varphi=0.26$, the segmental calculation resulted in favorable flow conditions in the impeller and both stators, leading to a maximum efficiency (see Fig. 7). In contrast, at the same flow rate coefficient of $\varphi=0.26$, the flow conditions obtained with the full pitch-360 deg calculations are characterized

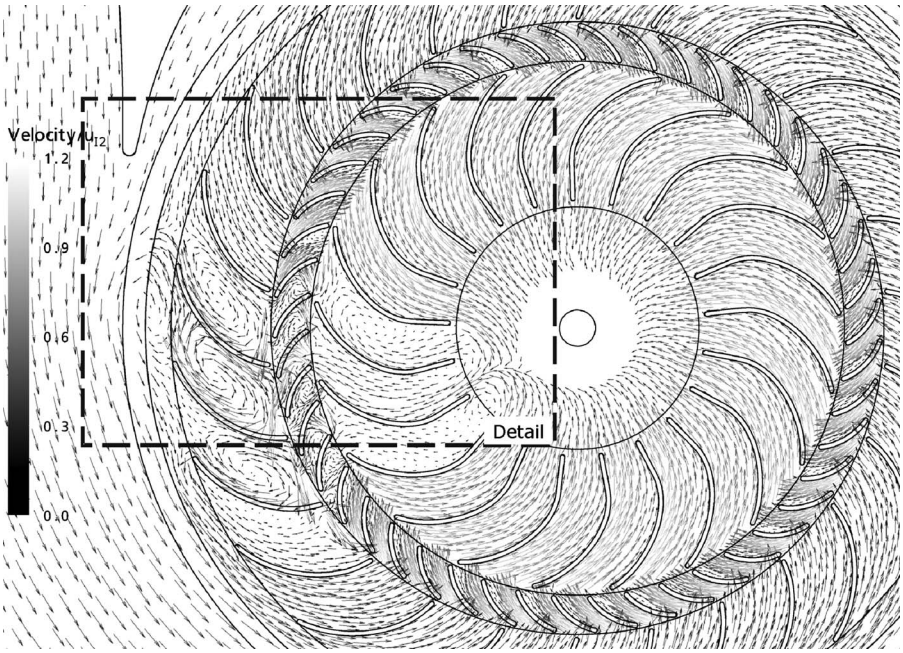

Fig. 8 Velocity vectors, midchannel, full pitch-360 deg approach, φ=0.26

by a highly separated flow, occurring at about 14% of the impeller-stator circumference (see Figs. 8 and 9) and with favorable flow conditions in the remaining portion of the impeller-stator circumference (such a flow pattern is characteristic of the stall phenomenon). With this type of operating behavior, the SSCP impeller-stator assembly is partially blocked with retarded flow sections, which results in a lower head and efficiency, compared with the upper branch of the hysteresis established with the segmental approach. It is clear that the development of completely different flow patterns determines the differences in the hydraulic characteristics on both branches of the hysteresis.

In the case of the segmental calculations, the flow tends to separate toward the impeller outlet at operating points away from the optimal flow rate (at lower flow rates near the suction side of the blade outlet; at higher flow rates near the pressure side of the blade outlet) due to a rather diverging impeller cascade. If the flow rate is reduced from the point of the maximum head, the flow conditions in the impeller become instantly, highly unfavorable with large areas of highly separated flow, leading to an abrupt deterioration of the head and the efficiency.

In the case of the full pitch-360 deg calculations, the flow at $\varphi > 0.29$ is generally favorable with a limited flow separation at the impeller-blade pressure side, but most importantly, the flow conditions are axisymmetric. With the flow rate reduction, the portion of the impeller-stator circumference characterized by the

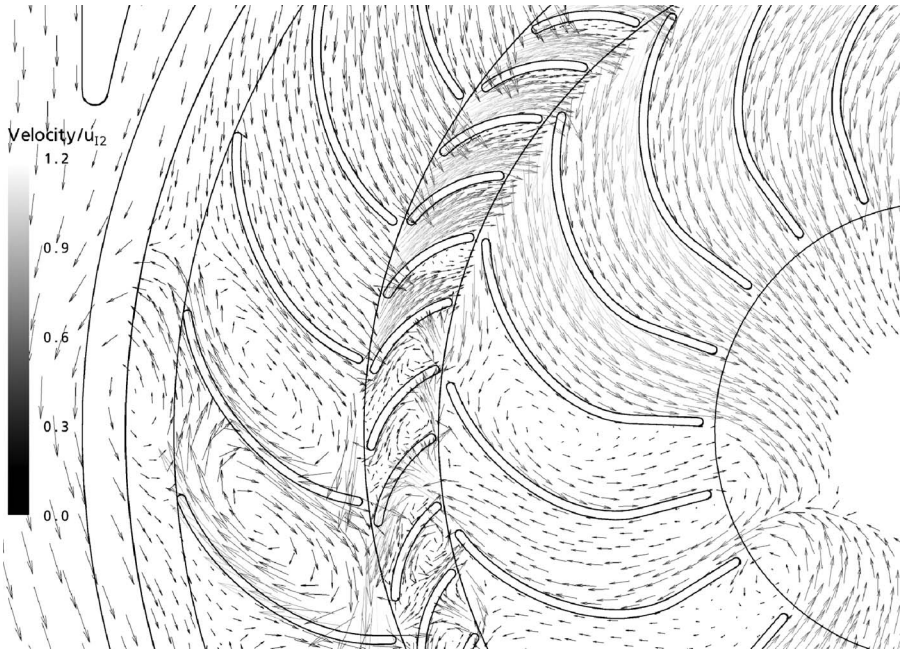

Fig. 9 Velocity vectors, midchannel detail, full pitch-360 deg approach, φ=0.26

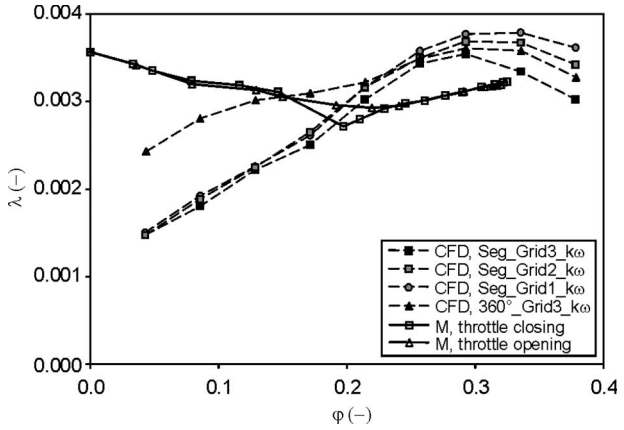

Fig. 10 Comparison of measured and calculated $\lambda-\varphi$ curves of the SSCP

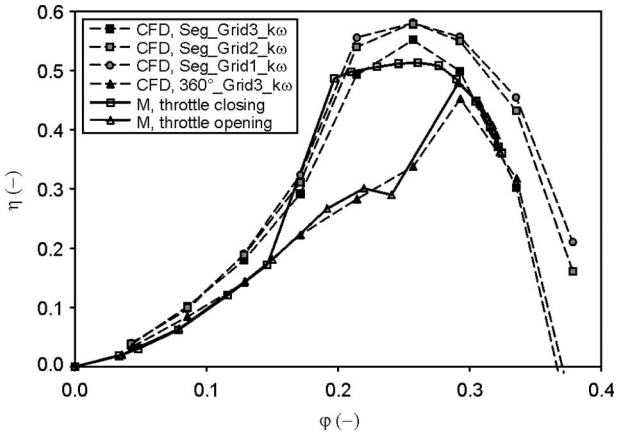

Fig. 11 Comparison of measured and calculated $\eta-\varphi$ curves of the SSCP

highly separated (stalled) flow increases at the expense of the portion of the impeller-stator circumference with generally favorable flow conditions. Although no unsteady-flow simulations were performed, it can be stated—based on the flow pattern in the full pitch-360 deg calculations, the hysteresis in the $\psi-\varphi$ curve, and other similarities with the axial compressors (i.e., a large number of short impeller blades, a small or negligible difference in the peripheral velocity component of the flow entering, and later leaving the impeller)—that the hydraulic behavior of the SSCP is influenced by the rotating-stall phenomenon occurring in the impeller-stator assembly.

The measured power-capacity curve of the analyzed SSCP, shown in Fig. 10, includes a hysteresis as well. The $\lambda-\varphi$ curve slightly decreases with the flow rate reduction from the point of the maximum flow rate to the saddle at the point of the maximum delivery head. After the saddle, the $\lambda-\varphi$ curve increases toward shutoff. The throttle-opening $\lambda-\varphi$ curve corresponds completely to the throttle-closing $\lambda-\varphi$ curve, except in the region of the curves' saddle where the throttle-opening $\lambda-\varphi$ curve lies above the throttle-closing $\lambda-\varphi$ curve. The power-capacity curve hysteresis is considerably smaller than the one present in the head-capacity curve. The power values shown in Fig. 10 were calculated as the measured shaft power reduced by the sum of the disk-friction losses, the volumetric losses, and the mechanical losses present at each operating point. The disk-friction losses and the volumetric losses were calculated according to Refs. [14,28], respectively. The size of the mechanical losses was measured.

The calculated power-capacity curves are compared with the measured one in Fig. 10. The shape of the calculated and measured $\lambda-\varphi$ curves is similar in the region between the maximum flow rate and the measured curve saddle; however, the discrepancy is relatively large. The calculated and measured power-capacity curves meet at the measured curve saddle. Decreasing the flow rate from the measured curve saddle leads to a larger discrepancy between the calculated and the measured $\lambda-\varphi$ curves. The measured $\lambda-\varphi$ curve rises toward shutoff, while the calculated $\lambda-\varphi$ curve drops toward shutoff. As indicated by the significant discrepancy between the calculated and measured power-capacity curves in the region from the curves' saddle toward shutoff, the used CFD approach showed weakness in predicting extensively separated flow conditions during the part-load operation (calculated and measured curves even have opposite inclination). Additionally, the calculated curve obtained by the segmental approach diverges (in direction toward shutoff) from the curve obtained by the full pitch-360 deg approach. As a result, the small hysteresis in the measured power-capacity characteristic cannot be predicted with the used CFD method. Anyway, it was observed that part-load operation of the SSCP was still better predicted by the full pitch-360 deg simulation than the segmental one. The full pitch-360 deg calculation is able to simulate the partial circumferential blockage of the impeller-stator channels as they occur during the stall phenomenon (with an angular share of blocked channels and an angular share of channels with generally favorable flow conditions), which cannot be achieved with the segmental approach that uses the periodic boundary condition.

The hydraulic efficiency of the SSCP versus the dimensionless flow rate coefficient is shown in Fig. 11. The measured hydraulic efficiency was calculated from the measured hydraulic power, divided by the measured shaft power reduced by the disk-friction, volumetric, and mechanical losses. The measured $\eta-\varphi$ curve is also characterized by a wide hysteresis. The throttle-closing $\eta-\varphi$ curve differs considerably from the throttle-opening $\eta-\varphi$ curve in the region of hysteresis. The efficiency decreases abruptly when the flow rate is reduced below $\varphi=0.2$.

The calculated $\eta-\varphi$ curve obtained with the segmental approach has a similar curve shape to the measured throttle-closing $\eta-\varphi$ curve. The measured throttle-opening $\eta-\varphi$ curve was established using the full pitch-360 deg calculations. The discrepancy between the measured $\eta-\varphi$ curves and the calculated $\eta-\varphi$ curves is, in the region $\varphi>0.2$, smaller than in the case of the head-capacity or power-capacity curves (the calculated power-capacity curve compensates for the amount of discrepancy present at the head-capacity curve).

The maximum measured hydraulic efficiency of $\eta_{opt}=0.52$ is achieved at a flow rate coefficient of $\varphi_{opt}=0.26$; however, it can only be achieved along the throttle-closing curve, which means that the best-efficiency point lies in the region of hysteresis. According to measurements, there is a wide operating region between $0.19<\varphi<0.30$, with the hydraulic efficiency not being remarkably lower that the optimum one.

The peak efficiency of the SSCP is rather low. One important reason for the low peak hydraulic efficiency of the measured SSCP is the rough surface of the impeller and both stators. However, there are also some general design weaknesses of the SSCP in comparison with single-stage centrifugal pumps:

- The number of the impeller-stator blades is rather large;
- The diverging impeller cascade;
- The circumferential component of the flow with high velocities exiting the impeller is reduced to zero in the narrow passages of the stator S1 (at the best-efficiency point the hydraulic losses in the stator S1 and the bend leading toward the discharge flange represent around 25% of the head generated in the impeller);
- The favorable flow conditions occur at rather large flow rates due to the pump's hydraulic design (the impeller inlet area is large).

Table 5 Influence of turbulence model on the calculated energy characteristics

	φ	ψ	λ	η	φ/φ_A	ψ/ψ_A	λ/λ_A	η/η_A
A.	0.09	0.16	0.0019	0.10	1	1	1	1
Turbulence model k-ω	0.17	0.37	0.0026	0.32	1	1	1	1
	0.26	0.59	0.0036	0.58	1	1	1	1
B.	0.09	0.09	0.0014	0.08	1	0.57	0.73	0.79
Turbulence model k-ε	0.17	0.29	0.0021	0.32	1	0.79	0.82	1.00
	0.26	0.55	0.0033	0.59	1	0.94	0.93	1.01

The specific speed nq, calculated according to Eq. (6), of the SSCP at the best-efficiency point has (according to the performed measurements) the value $nq=80$ due to the large impeller inlet area and low delivery head values ψ, which are mainly caused by the high level of hydraulic losses in the stator S1 and by the marked surface roughness

$$nq = n \cdot \frac{\dot{V}_{\text{opt}}^{1/2}}{H_{\text{opt}}^{3/4}} \tag{6}$$

5.4 Variation in Turbulence Model. The influence of the turbulence models on the calculated energy characteristics was studied using the fine-grid and segmental approach. The k-ε turbulence model leads to smaller head and power coefficients, while, in contrast, the efficiency values are more similar—especially near the best-efficiency point. Some results are summarized in Table 5, representing the main performance values for three different flow rates. The main weakness of the k-ε turbulence model is poor prediction of flow conditions in the part-load region. The performance characteristics were also calculated using the SST turbulence model; however, the results are not shown in Table 5 due to an unsatisfactory solver convergence when applying the SST turbulence model to the flow simulation throughout the part-load region.

5.5 Influence of Inflow Conditions on the SSCP Performance Characteristics. According to the flow pattern analysis of the full pitch-360 deg calculations, the cessation of the last stalled flow section always occurs near the volute tongue (see also Figs. 8 and 9). Obviously, the effect of the nonaxisymmetric shape of the volute influences the inflow conditions to the impeller-stator assembly, especially near the volute tongue, and this consequently increases the flow rate of the stall cessation. To determine the effect of the impeller-stator inflow conditions on the performance of the SSCP, a set of CFD calculations was performed without the volute (for axisymmetric inflow conditions to the impeller-stator assembly). The $\psi-\varphi$ curves for the CFD calculations performed (a) *with the volute* and (b) *with the axisymmetric inflow* are shown in Fig. 12. In the case of the axisymmetric inflow to the impeller-stator assembly, the stalling ceases at approximately $\Delta\varphi=0.065$ lower flow coefficient than in the case with the volute, which makes the size of the hysteresis in the performance curves considerably smaller. Furthermore, the part-load head is markedly higher at the axisymmetric inflow than in the case with the volute. It can be concluded that at centripetal pumping the presence of axisymmetric inflow conditions is essential for obtaining a lower flow rate of stall cessation, a smaller size of the hysteresis in the performance curves, and a higher head at the part-load.

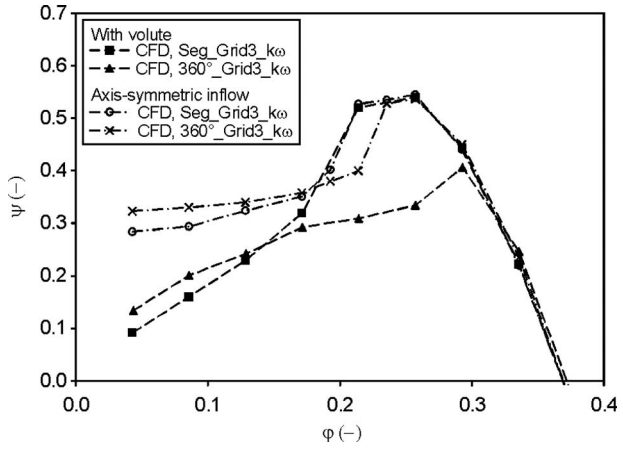

Fig. 12 Influence of inflow conditions on the $\psi-\varphi$ curves of the SSCP

6 Conclusions

In the present paper, a numerical and experimental investigation of a SSCP is presented. Based on the obtained results, the following can be concluded.

- The $\psi-\varphi$ and $\eta-\varphi$ curves acquired using the segmental CFD approach predict operating points along the measured throttle-closing $\psi-\varphi$ and $\eta-\varphi$ curves. The measured throttle-opening $\psi-\varphi$ and $\eta-\varphi$ curves correspond to the calculated $\psi-\varphi$ and $\eta-\varphi$ curves obtained using the full pitch-360 deg CFD approach. Combining both CFD approaches, the size and location of the hysteresis in the $\psi-\varphi$ and $\eta-\varphi$ curves of the SSCP was established.
- The concluding proposal for an efficient prediction of both branches of the hysteresis is: use the full pitch-360 deg approach to estimate the lower branch of the hysteresis; if interested in an estimate of the upper branch of the hysteresis, use the segmental model.
- The flow conditions obtained using the full pitch-360 deg calculations confirmed that the hydraulic behavior of the SSCP is influenced by the partial circumferential stall occurring in the impeller-stator assembly.
- The volute of the SSCP causes nonaxisymmetry of the inflow conditions to the impeller-stator assembly and increases the extent of the stall, influencing the operation of the SSCP.
- When the inflow conditions applied to the impeller-stator assembly are axisymmetric, a lower flow rate of stall cessation, a smaller size of the hysteresis, and a higher head at part-load were obtained.
- The developed CFD approach combination can be used for the prediction of the hysteresis in the performance curves of other turbomachinery undergoing stall, e.g., axial-flow compressors.

Nomenclature

B = bias limit (%)
D = diameter (m)
$\text{GCI}_{\text{fine}}^{21}$ = fine-grid convergence index (%)
H = total head rise (m)
M = torque (kg m^2 s^{-2})
P = power (W)

P = precision limit (%)
Re = Reynolds number
T = temperature (°C)
$\dot{V}$ = volume flow rate ($m^3\ s^{-1}$)
U = uncertainty (%)
Z = blade number
b = width (m)
c = velocity ($m\ s^{-1}$)
e_a^{21} = approximate relative error (%)
e_{ext}^{21} = extrapolated relative error (%)
g = acceleration due to gravity ($m\ s^{-2}$)
h = element size (m)
n = rotational speed (s^{-1}, min^{-1})
nq = pump's specific speed
p = pressure $kg\ m^{-1}\ s^{-2}$
r = grid-refinement factor
u = circumferential velocity ($m\ s^{-1}$)
u_{I2} = circumferential velocity at impeller outer diameter ($m\ s^{-1}$)

Greek Letters

α = stator blade angle (deg)
β = impeller-blade angle (deg)
Δp = pressure difference ($kg\ m^{-1}\ s^{-2}$)
η = efficiency
θ = pitch angle (deg)
λ = power coefficient
ν = kinematic viscosity ($m^2\ s^{-1}$)
π = Ludolf's number
ρ = fluid density (kg/m^3)
ϕ = solution value
ϕ_{ext}^{21} = extrapolated solution value
φ = flow coefficient
ψ = head coefficient
ω = angular velocity (s^{-1})

Subscripts

1 = inner, grid number 1
2 = outer, grid number 2
3 = grid number 3
in = inflow
opt = optimum
or = orifice plate
out = outflow
n = nominal
p = pump
u = circumferential
I = impeller
S1 = stator S1
S2 = stator S2
st = static
tot = total
ts = total to static
vol = volumetric
x = axial
w = water

References

[1] Sekavčnik, M., 1998, "Radial Turbine for Smaller Power," Ph.D. thesis, Faculty of Mechanical Engineering, University of Ljubljana, Slovenia.
[2] Sekavčnik, M., Tuma, M., and Florjančič, D., 1998, "Characteristics of One Stage Radial Centrifugal Turbine," Proceedings of the ASME 1998 International Gas Turbine and Aeroengine Congress & Exhibition, Stockholm, Sweden.
[3] Sekavčnik, M., Tuma, M., and Florjančič, D., 1999, "Messtechnische Untersuchungen einer einstufigen Radialturbine," Forsch. Ingenieurwes., **65**(1), pp. 13–19.
[4] Sekavčnik, M., Drobnic, B., and Tuma, M., 2002, "Numerical Investigation of Single Stage Radial Centrifugal Turbine," Proceedings of the First International Conference on Heat Transfer, Fluid Mechanics, and Thermodynamics, Kruger Park, South Africa.
[5] Petermann, H., 1951, "Untersuchungen am Zentripetalrad fuer Kreiselverdichter," Forsch. Geb. Ingenieurwes., **17**(2), pp. 51–59.
[6] Pfleiderer, C., 1961, "Die Kreiselpumpen fuer Fluessigketen und Gase," *5. Auflage*, Springer-Verlag, Berlin, pp. 235–236.
[7] Gantar, T., and Sekavčnik, M., 2007, "Operating Regimes of an Unconventional Radial Pump Stage," Forsch. Ingenieurwes., **71**(2), pp. 89–97.
[8] Gantar, T., and Sekavčnik, M., 2008, "Hydraulic Behaviour of Unconventional Radial Pump Stages," Trans. Can. Soc. Mech. Eng., **32**(2), pp. 155–179.
[9] Gantar, T., 2008, "Energy Characteristics of Radial Turbomachinery With Unconventional Flow Direction," Ph.D. thesis, Faculty of Mechanical Engineering, University of Ljubljana, Slovenia.
[10] Knapp, R. T., 1937, "Complete Characteristics of Centrifugal Pumps and Their Use in the Prediction of Transient Behavior," Mech. Eng. (Am. Soc. Mech. Eng.), **59**(8), pp. 683–689.
[11] Knapp, R. T., 1938, "Complete Characteristics of Centrifugal Pumps and Their Use in the Prediction of Transient Behavior," Mech. Eng. (Am. Soc. Mech. Eng.), **60**(8), pp. 676–680.
[12] Stepanoff, A. J., 1957, *Centrifugal and Axial Flow Pumps*, 2nd ed., Wiley, New York, pp. 269–285.
[13] Karassik, I. J., Messina, J. P., Cooper, P., and Heald, C. C., 2001, *Pump Handbook*, 3rd ed., McGraw-Hill, New York, pp. 2.376–2.382.
[14] Guelich, J. F., 1999, *Kreiselpumpen, Ein Handbuch fuer Entwicklung, Anlageplanung und Betrieb, 1*, Springer, Berlin, pp. 54–112.
[15] Gantar, T., Sekavčnik, M., and Mori, M., 2008, "Numerical and Experimental Investigation of a Single Stage Centripetal Pump," Forsch. Ingenieurwes., **72**(1), pp. 53–65.
[16] 1991, "Measurement of Fluid Flow by Means of Pressure Differential Devices—Part 1: Orifice Plates, Nozzles and Venturi Tubes Inserted in Circular Cross-Section Conduits Running Full," ISO 5167, 1st ed.
[17] Muggli, F. A., Holbein, P., and Dupont, P., 2002, "CFD Calculation of a Mixed Flow Pump Characteristic From Shutoff to Maximum Flow," ASME J. Fluids Eng., **124**(3), pp. 798–802.
[18] Gugau, M., 2004, "Ein Beitrag zur Validierung der numerischen Berechnung von Kreiselpumpen," Ph.D. thesis, Techische Universitaet Darmstadt, Deutschland.
[19] Adami, P., Della Gatta, S., Martelli, F., Bertolazzi, L., Maestri, D., Marenco, G., and Piva, A., 2005, "Multistage Centrifugal Pumps: Assessment of a Mixing Plane Method for CFD Analysis," *60°Congresso Nazionale ATI*, Rome, Italy.
[20] Braun, O., Kueny, J. L., and Avellan, F., 2005, "Numerical Analysis of Flow Phenomena Related to the Unstable Energy-Discharge Characteristic of a Pump-Turbine in Pump Mode," ASME Fluids Engineering Division Summer Meeting, Houston, TX.
[21] ANSYS CFX Help, 2005, *ANSYS CFX-Solver, Release 10.0: Modelling*, ANSYS Europe Ltd., Waterloo, Ontario, Canada, pp. 136–137.
[22] 1999, "Rotodynamic Pumps—Hydraulic Performance acceptance Tests—Grades 1 and 2," ISO 9906.
[23] Celik, B. I., Ghia, U., Roache, P. J., and Freitas, C. J., "Procedure for Estimation and Reporting of Uncertainty Due to Discretization in CFD Applications," Journal of Fluids Engineering Editorial Policy Statement on the Control of Numerical Accuracy, www.asme.org
[24] Day, I. J., 2004, "Stall and Surge," *Cambridge Turbomachinery Course*, University of Cambridge, Cambridge, England.
[25] Day, I. J., Greitzer, E. M., and Cunpsty, N. A., 1978, "Prediction of Compressor Performance in Rotating Stall," ASME J. Eng. Power, **100**(1), pp. 1–14.
[26] Greitzer, E. M., 1978, "Surge and Rotating Stall in Axial Flow Compressors, Part I: Theoretical Compression System Model," ASME J. Eng. Power, **98**(2), pp. 190–198.
[27] Greitzer, E. M., 1978, "Surge and Rotating Stall in Axial Flow Compressors, Part II: Experimental Results and Comparison With Theory," ASME J. Eng. Power, **98**(2), pp. 199–217.
[28] Idelchik, I. E., 1986, *Handbook of Hydraulic Resistance*, 2nd ed., Hemisphere, WA, pp. 425–459.

On the Relationships Among Strouhal Number, Pressure Drag, and Separation Pressure for Blocked Bluff-Body Flow

W. W. H. Yeung
Yeung's Consultancy,
#04-352 Blk 281,
Choa Chua Kang Avenue 3,
Singapore 680281, Singapore
e-mail: wwhyeung@yahoo.com.sg

Strouhal number, pressure drag, and separation pressure are some of the intrinsic parameters for investigating the flow around a bluff-body. An attempt is made to formulate a relationship involving these quantities for flow around a two-dimensional bluff section of various shapes in a confined environment such as a wind tunnel. It includes (a) establishing a relation between the Strouhal number and a modified Strouhal number by a theoretical wake width and (b) incorporating this wake width into a momentum equation to determine the pressure drag. Comparisons have been made with the experimental data, a theoretical prediction (for unconfined flow), and an empirical proposal in literature to indicate that the present methodology is appropriate. Together with its extension to axisymmetric bodies, the current method is able to provide proper limits to the experimental data for a rectangular flat-plate of various width-to-span ratios. In addition, if the separation pressure is given, then the Strouhal number is inversely proportional to the drag coefficient, being comparable to a proposal based on statistical results. Finally, through an example, it is also demonstrated how one of these three parameters may be reasonably estimated from the measured values of the other two.
[DOI: 10.1115/1.4000575]

1 Introduction

Periodic shedding of vortices with alternating circulation is a typical phenomenon observed in the wake of a bluff-body when the Reynolds number $\mathrm{Re}=\rho Uh/\mu$ is sufficiently large. Here, U is the freestream velocity, h is the lateral dimension of the body, ρ is the fluid density, and μ is the dynamic viscosity of the fluid. The phenomenon of vortex-shedding is often quantified by the conventional Strouhal number $S=fh/U$ with f being the frequency of vortex-shedding. For unconfined flow, von Kármán and Rubach [1] described the two-dimensional vortex street by an idealized potential-flow model of two rows of staggered point vortices of opposite strength. Deduced from the consideration of momentum (see, e.g., Lamb [2]), the drag F_d arising from the vortex street is a function of the velocities and spacing dimensions of the vortex street.

Roshko [3] investigated the nature of the wake structures behind bluff sections by measuring the shedding frequencies in the wake of three different cylindrical shapes at a negligibly small blockage ratio z (which is the ratio of reference area of the model to the cross-sectional area of the enclosure) of 2.2% in a wind tunnel. In passing, owing to the constraint from the tunnel walls on the lateral displacement of streamlines, wind-tunnel measurements must be properly corrected if they are used as data for unconfined flow. The bluff sections tested include a circular cylinder, a 90 deg wedge and a flat-plate normal to freestream. While S is approximately constant for each shape over the subcritical range of Reynolds number, it is distinctly different for various sections, as listed in Table 1, in the order of increasingly bluff. By realizing the similarity in the wake structures, he demonstrated how a dimensional analysis led to a universal Strouhal number $S^*=fd'/U_S$ where the characteristic velocity is $U_S=kU$ (which is the velocity on the free streamline at separation, see Fig. 2) and the characteristic length d' is the distance between free streamlines from his "notched-hodograph" theory. k was termed the base-pressure parameter, even though it was actually found from $k=\sqrt{1-c_{ps}}$, where $c_{ps}=2(p_s-p_\infty)/(\rho U^2)$. p_s is the pressure at flow separation and p_∞ is the freestream pressure. Using the measurements of base-pressure and taking d' to be the wake width, Roshko found that $S^*=0.164$, being independent of the body shape as well as the Reynolds number. By further assuming the width of the vortex street to be d', and by choosing $k=1.4$ as the mean value from his measurements, the predicted values of drag coefficient $c_d=2F_d/(\rho U^2 h)$ from the Kármán drag formula are in accord with measurements.

For each value of the velocity of vortices, the drag is insensitive to changes in the spacing ratio of the vortices in the Kármán drag formula, as demonstrated by Kronauer [4]. From an analysis based on the Kronauer's minimum drag criterion, Bearman [5] evaluated the lateral displacement between the vortex rows and equated it to the wake width to arrive at $S^*=0.181$ for a variety of blunt-based bodies and wake interference configurations. Besides, he arrived at a unique relationship between the product of Strouhal number and drag coefficient Sc_d and k

$$Sc_d = F(k) \tag{1}$$

where F is a function of k given in Appendix. Equation (1) was formulated with a general collapse of data of various two-dimensional bluff-body shapes with splitter plates and base bleed. Additional evidence is also provided by Bearman [6] containing the data for the smooth and turbulent flows past a circular cylinder in the critical Reynolds number regime. Particular features of Eq. (1), as shown in Fig. 1(*a*), include (i) Sc_d being positive when $k \geq 1$, (ii) Sc_d attaining its maximum value of about 0.27 at $k \approx 1.55$, and (iii) Sc_d asymptotically approaching 0.16 as $k \to \infty$. The relationship between k and the spacing ratio of vortices is given in Appendix. With a relationship such as Eq. (1) available,

Contributed by the Fluids Engineering Division of ASME for publication in the JOURNAL OF FLUIDS ENGINEERING. Manuscript received November 24, 2008; final manuscript received October 13, 2009; published online February 3, 2010. Assoc. Editor: James A. Liburdy.

Table 1 Measured Strouhal number S and drag coefficient c_d from Roshko [3]

	S	c_d
Circular cylinder ($\mathrm{Re}=1.45\times10^4$)	0.198	1.15
90 deg wedge ($4\times10^3<\mathrm{Re}<2.4\times10^4$)	0.178	1.30
Flat-plate ($4\times10^3<\mathrm{Re}<2.4\times10^4$)	0.135	1.80

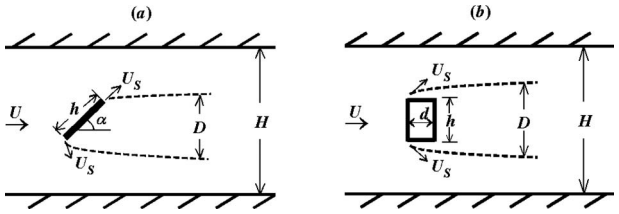

Fig. 2 Definition sketch for (*a*) an inclined flat-plate and (*b*) rectangular section in a wind tunnel.

one of S, c_d, and k may be estimated from the measured values of the other two.

Simmons [7] and Griffin [8] independently proposed the use of a wake width d' at the end of the vortex formation region, "where a vortex is fully formed, is shed and then moves away from the base region." Using a least-square fit of experimental data ranging from stationary to vibrating structures, [8] proposed

$$Sc_d = -0.48 + 0.5k \tag{2}$$

It was further suggested that

$$\frac{Sc_d}{k^3} = 0.073 \pm 0.005 \tag{3}$$

for the data of S^* vary from 0.12 to 0.18 over a range of $\mathrm{Re}^*=\mathrm{Re}(kd'/h)$ between 100 and 10^7. Similar to Eq. (1), Sc_d is positive from Eqs. (2) and (3) when $k\geq1$, see Fig. 1(*a*). Nevertheless, note that Sc_d from Eq. (2) is linear in k while that from Eq. (3) is cubic. Over the range where $1.1\leq k\leq1.5$, the values of Sc_d from the three equations agree well with each other. When $k>1.5$, Eqs. (2) and (3) exhibit an upswing trend, which is different from that of Eq. (1).

As later noticed by Bearman and Trueman [9], their data of Sc_d and k for rectangular cylinders of various depth-to-width ratios did not fall onto the curve of Eq. (1). Also found by Simmons [7] was that his set of experimental data $(S,c_d,c_{pb})=(0.21,1.35,-1.34)$ for a 60 deg wedge (at a negligibly small blockage ratio of 3.5%) produced a value of Sc_d greater than the maximum value of Eq. (1) unless the data were corrected for the blockage-effect by the method of Maskell [10]. This method has been widely accepted as a suitable means of correcting wind-tunnel data for the blockage-effect on bluff-bodies created by rigid walls. A similar anomaly was also found when using the data (already corrected for the blockage-effect) of Twigge-Molecey and Baines [11] for a 60 deg wedge. Subsequently, Griffin [8] pointed out that the measurements by Modi and El-Sherbiny [12] of vortex-shedding from a circular cylinder at a blockage ratio of 36% led to $Sc_d=0.51$ at $k=1.95$, being also beyond the theoretical prediction of Eq. (1) but still within the curve-fitting prediction of Eq. (2).

For three-dimensional bluff-bodies, Calvert [13,14] measured the Strouhal number and the base-pressure of cones of various apex angles as well as a disk at different inclinations. When the wake width was taken to be the distance between two major peaks of the turbulence profile at a stream wise location where the static pressure reaches a minimum, $S^*=0.20$ was found. In addition, with a square plate inclined about an axis parallel to two of its sides, the variation in Strouhal number with incidence was observed to be nearly the same as that of the disk, when the Strouhal number was based on an equivalent diameter $2L/\sqrt{\pi}$, where L is the length of the side of the plate. The wake Strouhal number of a sphere within the range where $2\times10^4<\mathrm{Re}<6\times10^4$ measured by Calvert [15] was about 0.19. However, the equation linking S, c_d, and c_{ps} in the three-dimensional case has seldom been mentioned in literature perhaps because the theoretical formulation is more involved in comparison to the two-dimensional situation.

In a recent study, Yeung [16] investigated the blockage-effect on drag and base-pressure of a bluff-body. By incorporating a potential-flow model for unconfined flow and the theoretical wake width into the momentum equation for the confined flow, the predicted drag, and the base-pressure are in reasonable agreement with experimental data.

The objectives and motivation of this paper are to

(i) provide (with a sound theoretical background) a relationship among Sc_d, k and blockage ratio z for two-dimensional bluff sections,
(ii) extend it to axisymmetric bluff-bodies without involving the discrete vortices directly,
(iii) offer a relation between S and c_d, comparable to the empirical formula by Hoerner [17].

It is emphasized that the pressure distribution downstream of separation on a bluff-body such as a circular cylinder is not always constant but varies with its location. Different definitions of the base-pressure therefore exist in literature. To avoid ambiguity, the separation pressure (instead of the base-pressure) is utilized throughout the present study and k is called separation-pressure parameter.

2 Inclined Flat-Plate and Rectangular Sections

Consider a flat-plate at inclination α situated in the middle of a wind tunnel, as shown in Fig. 2(*a*). In the presence of freestream of speed U, a wake having a characteristic width D behind the

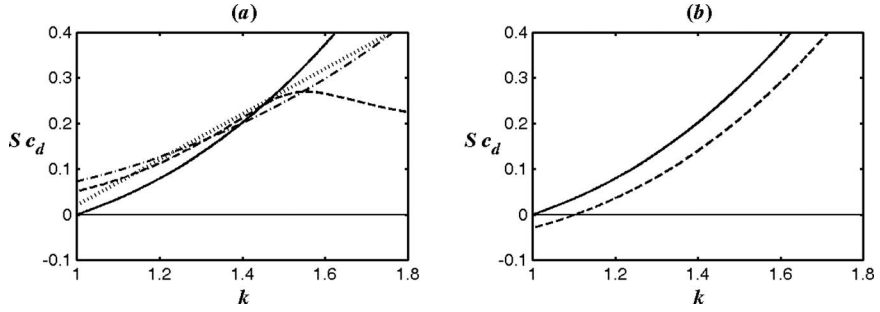

Fig. 1 Relationships of Sc_d, k, and z. (*a*) $z=0$: — —: Eq. (1); ···: Eq. (2); –•–: Eq. (3); ——: Eq. (8). (*b*) $S^{**}=0.15$: — —: Eq. (7) with $z=25\%$ and $\alpha=90$ deg; and ——: Eq. (8).

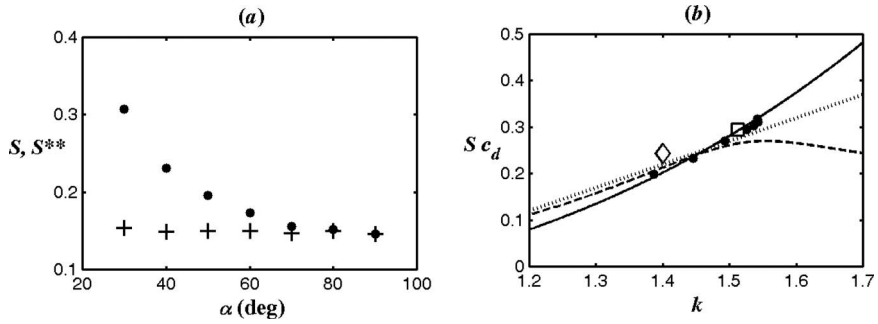

Fig. 3 Variations in (*a*) Strouhal numbers with angle of incidence and (*b*) Sc_d with k for flat-plate in unconfined flow. (*a*) ●: S from Fage and Johansen [19]; +: S^{**} from Eq. (4) with $z=0$. (*b*) ●: from Fage and Johansen [19], ◇: from Roshko [3]; □: from Bearman and Trueman [9]; — —: Eq. (1); ···: Eq. (2); and ——: Eq. (8).

plate is formed. Continuity is applied to deduce the important parameter $(1-z)$ for the blocked flow, where the blockage ratio is defined as $z=h \sin \alpha/H$ with h being the plate width and H being the tunnel width. A theoretical wake width was found by Yeung [18] as

$$D^* = hk(1-z)^{3/2}\sin \alpha \tag{4}$$

such that the modified Strouhal number $S^{**}=fD^*/(kU)$ is independent of α and z (see for example Fig. 3(*a*) as a typical case). The values of D^* are in fact in good agreement with the measurements quoted in Ref. [18]. Therefore, D^* is considered as a suitable choice of the characteristic wake width without resorting to experiments. Surprisingly, the relationship between S and S^{**}

$$S^{**} = S(1-z)^{3/2}\sin \alpha \approx 0.15 \tag{5}$$

is merely geometrical as the separation-pressure coefficient c_{ps} $(=1-k^2)$ is not involved.

The momentum equation from Maskell [10] for a two-dimensional bluff section is

$$c_d = k^2\frac{D}{h} - \frac{D}{h}\left(1-\frac{D}{h}z\right)^{-1} \tag{6}$$

By equating D to D^* and by combining Eq. (5) with Eq. (6), it is readily derived that

$$Sc_d = k^3 S^{**} - \frac{kS^{**}}{1-k(1-z)^{3/2}z\sin \alpha} \tag{7}$$

In the limit that $z \to 0$ (i.e., unconfined flow), Eq. (7) is simplified to

$$Sc_d = k^3 S^{**} - kS^{**} \tag{8}$$

which is independent of the angle of inclination. Note that Maskell's method used in Simmons [7] is based on a first-order approximation of Eq. (6); that is $(1-Dz/h)^{-1} \approx 1+Dz/h$, and through the same order of approximation, the wake width is related to the drag and the separation-pressure coefficients without resorting to the wake dynamics, which is characterized by vortex-shedding. Such an approximation is well justified because the experimental data quoted in Ref. [10] to validate the method are of low blockage ratio (i.e., $z<8\%$). But this approximation is considered not necessary here and Eq. (6) is utilized in the present form with the wake width deduced from the Strouhal number, which is closely linked to the physics of the wake dynamics.

As displayed in Fig. 1(*b*), Sc_d from Eq. (8) (i) passes through $(k,Sc_d)=(1,0)$, (ii) increases monotonically without any maximum value when $k \geq 1$, and (iii) is cubic in k so it is different from Eq. (2) but resembles Eq. (3). Furthermore, for an inclined plate (i.e., $\alpha>0$) with nonzero blockage ratio (i.e., $0<z<1$), it can be shown by simple calculations that $0<1-k(1-z)^{3/2}z \sin \alpha<1$ over the range $1<k<2$. In other words, the value of Sc_d from Eq. (7) is always less than that from Eq. (8) for a given k in this range. This result is illustrated graphically in Fig. 1(*b*), where the curve of Eq. (7) (with $z=25\%$ and $\alpha=90$ deg) lies on the right of Eq. (8) because of the blockage-effect. While Sc_d from Eq. (8) is always positive for $k \geq 1$, Sc_d is negative from Eq. (7) over the range $1<k<k^*$, where k^* satisfies the condition that $(k^*)^3 z(1-z)^{3/2}\sin \alpha-(k^*)^2+1=0$. For instance, it is displayed in Fig. 1(*b*) that $k^* \approx 1.10$.

At $\alpha=90$ deg, the blockage ratio of the flat-plate used in Fage and Johansen [19] is 1/14 or 7.2% and its maximum depth-to-width ratio d/h as shown in Fig. 2(*b*) is 0.03. In Yeung and Parkinson [20], it was elaborated how the effects of blockage and clearance between the plate and tunnel walls compensated for each other such that the data may be considered as blockage-effect free, (i.e., $z=0$). The modified Strouhal number S^{**}, which was obtained by applying Eq. (4) to the experimental data of S from Ref. [19] for 30 deg $\leq \alpha \leq$ 90 deg in Fig. 3(*a*), is independent of inclination α giving a mean value of approximately 0.15. The experimental data from Ref. [3] (see Table 1) and Ref. [19] are compared with curves of Eqs. (1), (2), and (8) in Fig. 3(*b*). Additionally, the data points $(S,c_d,c_{ps})=(0.14,2.07,-1.29)$ from Ref. [9] corresponding to a thin rectangular section with $d/h=0.2$ and $\alpha=90$ deg is also included. Some of the data points lie within the portion where the three curves are close to each other. However, those corresponding to larger values of k tend to follow the trend of Eq. (8).

Awbi [21] studied the wind-tunnel constraint on two-dimensional rectangular prisms (see Fig. 2(*b*)) normal to the freestream. His data are chosen in this study because the blockage ratio was varied by employing movable side-walls in a wind tunnel without affecting the aspect ratio (which is the ratio of width to span) of the prism. The variations in Strouhal number with the blockage ratio $(5\% \leq z \leq 25\%)$ for prisms at $d/h=0.2$, 0.5, 1.0, and 1.5 are depicted in Fig. 4(*a*), while values of S^{**} obtained from Eq. (5) (with $\alpha=90$ deg) are shown in Fig. 4(*b*). S^{**} is approximately independent of z but varies linearly with d/h, as reflected in Fig. 4(*c*) (where the data points for $d/h=0.03$ from Ref. [19] are also included). The data corresponding to $d/h=0.2$, 0.5, and 1.0 at $z=5\%$ and 25%, respectively, are compared with Eqs. (1), (2), and (7) in Fig. 5, where the value of S^{**} in Eq. (7) is suitably taken from Fig. 4(*c*). The data points at $z=5\%$ lie closely to all these curves but those at $z=25\%$ are closer to Eq. (7). In particular, $(k,Sc_d)=(2.43,1.04)$ in Fig. 5(*b*) (i.e., $d/h=0.5$ and $z=25\%$) is beyond the largest k value, namely, $(k,Sc_d)=(1.95,0.51)$ from Ref. [12] for a circular cylinder at a blockage ratio of 36%, as quoted in Ref. [8].

3 Wedge

Okamoto et al. [22] studied the flow past a symmetrical wedge of base width h and apex angle δ (see Fig. 6(*a*)) at $\mathrm{Re}=9\times10^4$

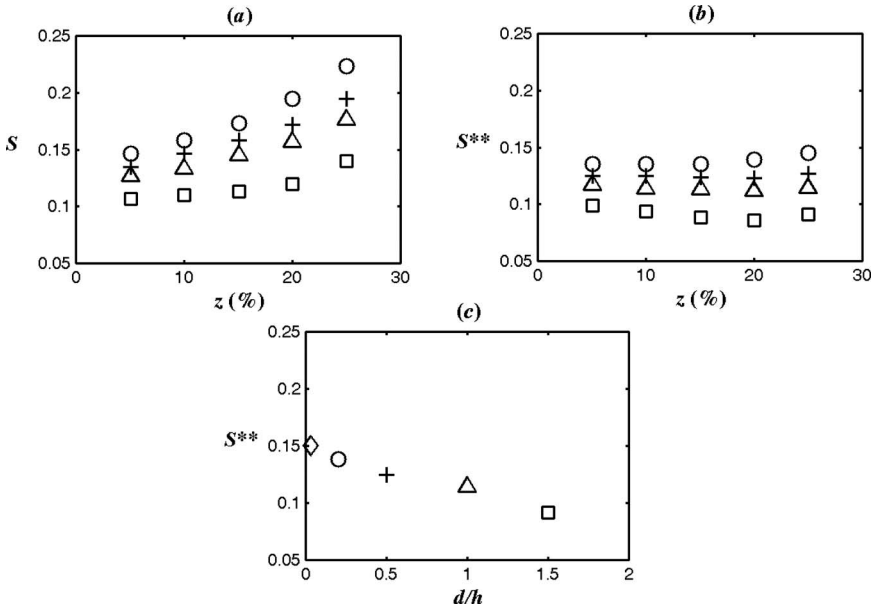

Fig. 4 Variations in Strouhal numbers for a rectangular section with blockage ratio in (*a*) and (*b*) and with *d*/*h* in (*c*). (*a*) *S* from Awbi [21]. (*b*) and (c) S^{**} from Eq. (5) with α=90 deg; ○: *d*/*h*=0.2, +: 0.5, △: 1.0, □: 1.5; and ◇: *d*/*h*=0.03 from Fage and Johansen [19].

(based on h) and a negligibly small blockage ratio of 2.5%. The vortex-shedding frequency in the form of Strouhal number as a function of the apex angle in the range 15 deg$\leq\delta\leq$180 deg is displayed in Fig. 6(*b*) with modified Strouhal number S^{**} based on kU and

$$D^* = hk(1 - 0.2 - 0.2\sin(\delta + 90\ \text{deg})) \tag{9}$$

The measurement from Ref. [7] for δ=60 deg is included in Fig. 6(*b*) for comparison. As shown,

$$S^{**} = S(1 - 0.2 - 0.2\sin(\delta + 90\ \text{deg})) \approx 0.148 \tag{10}$$

which is consistent with those for a flat-plate and rectangular sections, as discussed in Sec. 2.

Ramamurthy and Ng [23] investigated the blockage-effect on the Strouhal number in the wake of a symmetrical wedge with δ =60 deg over 7.1%$\leq z\leq$42.3% and found a distinct increase in Strouhal number with z. It should be noted that their width of the

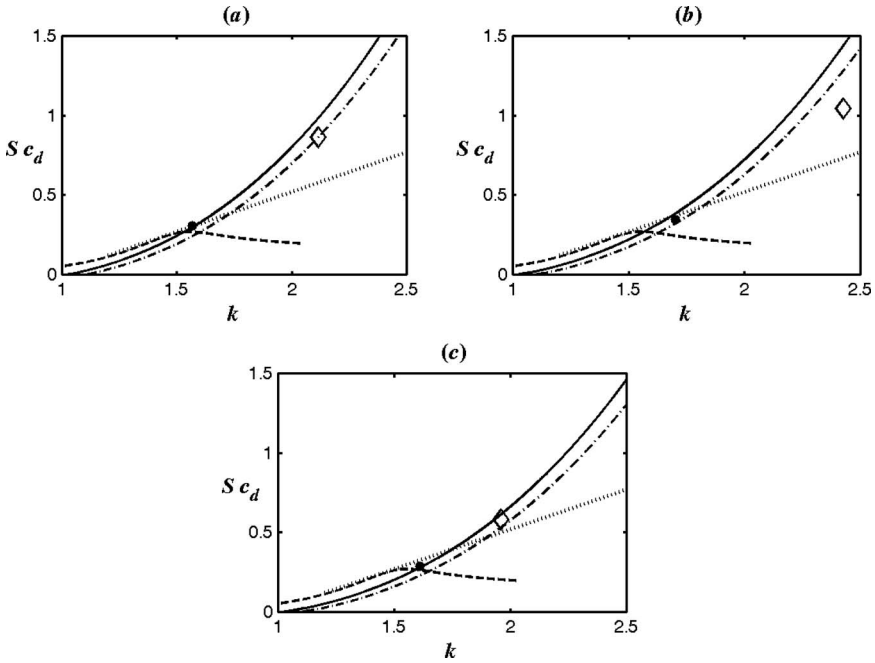

Fig. 5 Variation in Sc_d with *k* for a rectangular prism in confined flow from Awbi [21]. (*a*) *d*/*h*=0.2, (*b*) 0.5, and (*c*) 1.0; ●: *z*=5%, ◇: *z*=25%; — —: Eq. (1); ···: Eq. (2); –•– : Eq. (7); and ——: Eq. (8).

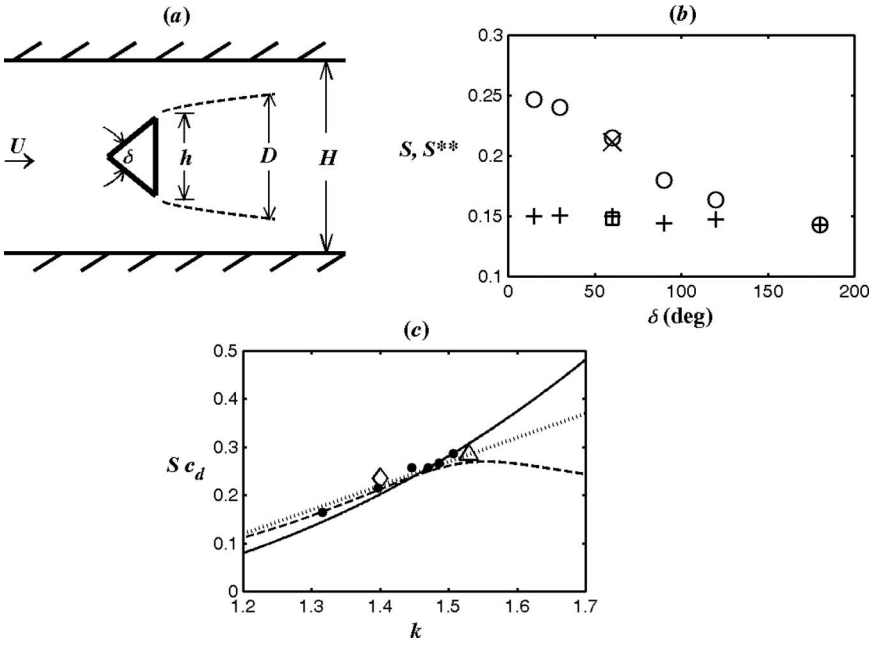

Fig. 6 Flow around a symmetrical wedge in a wind tunnel. (*a*) Definition sketch. (*b*) Variations in Strouhal numbers with apex angle. ○: *S* from Okamoto et al. [22], +: S^{**} from Eq. (10); ×: *S* from Simmons [7], and □: S^{**} from Eq. (10). (*c*) Variation in Sc_d with *k*. ● [22]: with 15 deg≤ δ≤180 deg; △ [7]: with δ=60 deg; ◇: Roshko [3] with δ=90 deg; — —:Eq. (1); ···: Eq. (2); and ——: Eq. (8).

models was changed to simulate the blockage-effect in the wind tunnel with fixed walls. As such, the aspect ratio of the models did not remain constant. Based on

$$D^* = hk(1-z)(1-0.2-0.2\sin(\delta+90\ \text{deg})) \tag{11}$$

and kU, the modified Strouhal number S^{**} as depicted in Fig. 7(*a*) is independent of z and related to S as

$$S^{**} = S(1-z)(1-0.2-0.2\sin(\delta+90\ \text{deg})) \approx 0.146 \tag{12}$$

Following the method in Sec. 2, it can be derived that

$$Sc_d = k^3 S^{**} - \frac{kS^{**}}{1-k(1-z)z(1-0.2-0.2\sin(\delta+90\ \text{deg}))} \tag{13}$$

with Eq. (8) remaining as the expression for unconfined flow. While the data points from Refs. [3,7,22] are near the curves of Eqs. (1), (2), and (8) with z=0 in Fig. 6(*c*), the data from Ref. [23] and Ramamurthy and Lee [24] with z=14% and 28% follow the trend of Eq. (13) in Fig. 7(*b*).

4 Circular Cylinder at Subcritical Reynolds Numbers

It is well known that the Strouhal number, the separation pressure, the drag, and the location of flow separation on a circular cylinder change with the Reynolds number. In the present study, the regime of subcritical Reynolds numbers is of concern. The surface pressure distributions on a circular cylinder at 8.3%≤z≤33.3% and Re=10^5 (based on diameter h in Fig. 8(*a*)) plotted in Fig. 8(*b*) are from Parkinson and Hameury [25], indicating that

(i) within this range of blockage ratio z, the angle of flow separation is approximately at $\beta=\beta_s=80$ deg, where β is measured from the frontal stagnation point,
(ii) the pressure at separation c_{ps} is different from the pressure at $\beta=180$ deg,
(iii) the magnitudes of c_{ps} and c_d increase with increasing z.

The variation in Strouhal number over the same range of block-

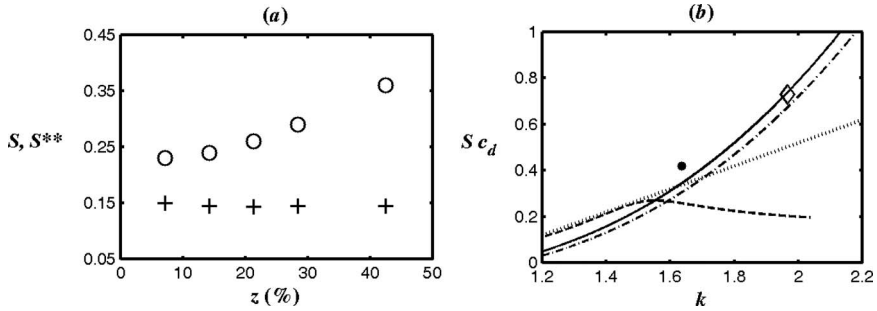

Fig. 7 Variations in (*a*) Strouhal numbers with blockage ratio, (*b*) Sc_d with *k* for a 60 deg wedge in confined flow from Ramamurthy and Ng [23]. (*a*) ○: *S*, +: S^{**} from Eq. (12) with β=60 deg. (*b*) ●: z=14%; ◇: z=28%; — —: Eq. (1); ···: Eq. (2); ——: Eq. (13) with z=14%; and –•– : Eq. (13) with z=28%.

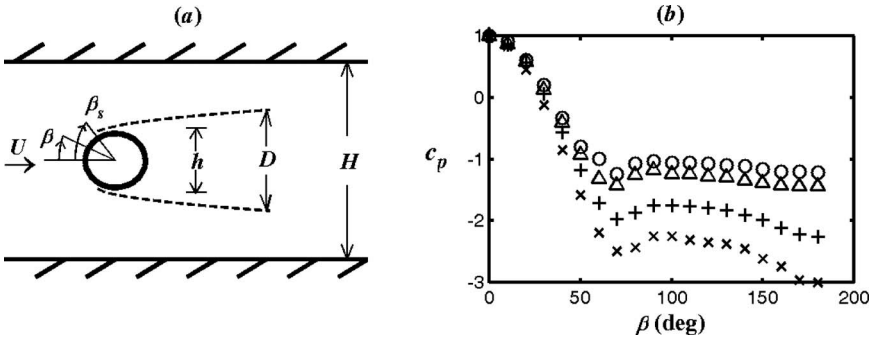

Fig. 8 Flow past a circular cylinder in confinement. (*a*) Definition sketch. (*b*) Pressure distributions from Parkinson and Hameury [25]. ○: *z*=8.3%, △: 13.8%, +: 25%, and ×: 33.3%.

age ratio and at the same Reynolds number, as reported in Kong et al. [26], is shown in Fig. 9(*a*). If the modified Strouhal number is based on kU and D^*, where

$$D^* = hk(1-z)^{1/2}\sin\beta_s \tag{14}$$

then

$$S^{**} = S(1-z)^{1/2}\sin\beta_s \approx 0.185 \tag{15}$$

By substituting D^* into D in Eq. (5) and combining it with Eq. (4), it is found that

$$Sc_d = 0.185k^3 - \frac{0.185k}{1-k(1-z)^{1/2}z\sin\beta_s} \tag{16}$$

By letting $z=0$ (i.e., unconfined flow), Eq. (16) is reduced to Eq. (7) with $S^{**}=0.185$ and is plotted in Fig. 9(*b*) to compare with Eqs. (1) and (2) and data from Ref. [3] at $\mathrm{Re}=1.45\times10^4$ and $z=2.2\%$. Interestingly, the data from other Reynolds number ranges such as Norberg [27] (where $(S,c_d,c_{ps})=(0.21,0.89,-0.75)$ and $z=1.6\%$) at $\mathrm{Re}=1.5\times10^3$, Bearman [6] (where $(S,c_d,c_{ps})=(0.32,0.33,-0.34)$, corrected for blockage) at $\mathrm{Re}=2.13\times10^5$ and Roshko [28] (where $(S,c_d,c_{ps})=(0.27,0.7,-0.86)$ corrected for blockage) at $\mathrm{Re}=8.4\times10^6$ are also close to the three curves. Fig. 9(*c*) shows that the experimental data from Ref. [25] at $z=8.3\%$ is near the curves of Eqs. (1), (2), and (16). Nevertheless, the data point at $z=33.3\%$ seems to agree well with Eq. (16).

5 Axisymmetric Bluff-Bodies

Equation (1) is for two-dimensional bluff sections in unconfined flow. To establish the corresponding expression for three-dimensional bluff-bodies in confined flow, rectilinear vortices in the wake, as in Ref. [1], are to be replaced by vortex loops and their stability has to be analyzed. An attempt is made here to demonstrate how such an expression can be derived from the present methodology for blocked flow without involving the discrete vortices directly.

Consider a disk of diameter h normal to the freestream as defined in Fig. 10(*a*), where the blockage ratio is $z=A/A_t$ with $A=\pi h^2/4$ being the disk area and A_t being the cross-sectional area

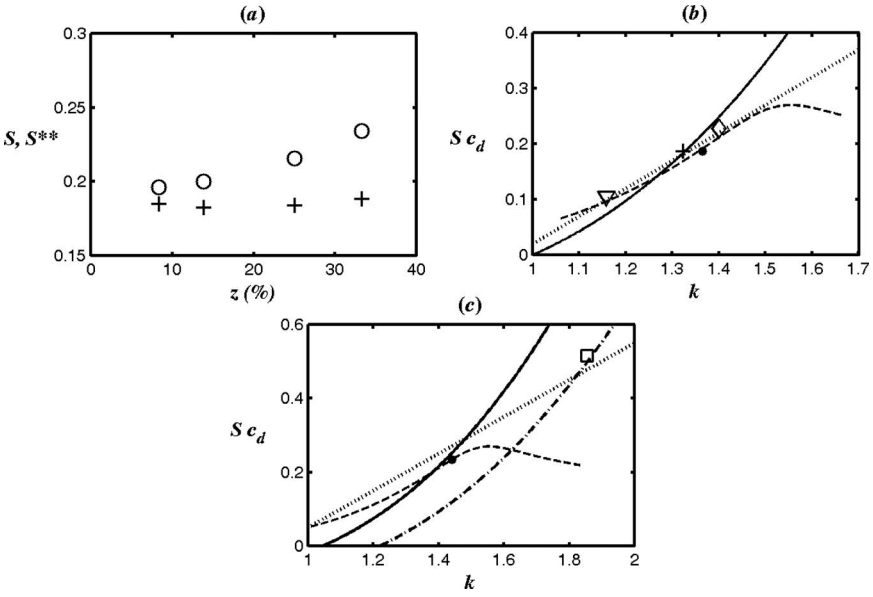

Fig. 9 Variations in (*a*) Strouhal numbers with blockage ratio, (*b*) and (*c*) Sc_d with k for a circular cylinder. — —: Eq. (1); ···: Eq. (2). (*a*) ○: S from Kong et al. [26], +: S^{**} from Eq. (15) with β_s=80 deg. (*b*) ◇: Roshko [3], ●: Roshko [28], +: Norberg [27], ▽: Bearman [6], and ——: Eq. (8). (*c*) ●: *z*=8.3%, □: *z*=33.3% from Parkinson and Hameury [25] and Kong et al. [26], ——: Eq. (16) with β_s=80 deg and *z*=8.3%, and –•–: Eq. (16) with β_s=80 deg and *z*=33.3%.

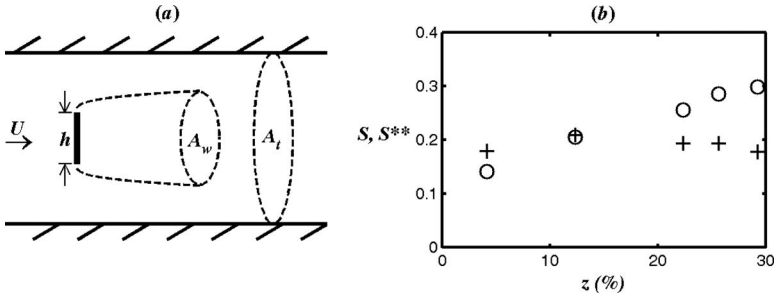

Fig. 10 Flow past a normal disk in confinement. (*a*) Definition sketch. (*b*) Variations in Strouhal numbers with blockage ratio *z*. ○: *S* from Miau and Liu [29], +: S^{**} from Eq. (19).

of the tunnel. The momentum equation from Ref. [10] for a three-dimensional bluff-body with an effective wake of cross-sectional area A_w is

$$c_d = k^2\frac{A_w}{A} - \frac{A_w}{A}\left(1 - \frac{A_w}{A}z\right)^{-1} \tag{17}$$

Miau and Lin [29] employed a laser velocimeter to measure Strouhal number in the wake behind a disk over $4.1\% < z < 29.2\%$. Their data over $1\times10^3 < \mathrm{Re} < 3\times10^4$ as shown in Fig. 10(*b*) are almost independent of the blockage ratio when expressed in terms of $S^{**} = fD^*/(kU)$ with the theoretical wake width defined as

$$D^* = hk\sqrt{2}(1-z)^{5/2} \tag{18}$$

and

$$S^{**} = S\sqrt{2}(1-z)^{5/2} \approx 0.191 \tag{19}$$

It is interesting to note that S^{**} is about the same as S^* found by Calvert [13,14]. By substituting $A_w/A = (D^*/h)^2$ into Eq. (17) and combining it with Eq. (19)

$$Sc_d = 0.191\sqrt{2}k^4(1-z)^{5/2} - \frac{0.191\sqrt{2}k^2(1-z)^{5/2}}{(1-2k^2(1-z)^5 z)} \tag{20}$$

If $z=0$, then Eq. (20) is reduced to

$$Sc_d = 0.191\sqrt{2}(k^2-1)k^2 \tag{21}$$

which is quartic in k, as compared to being cubic as in Eq. (8). It can be shown by simple calculations that $0 < 1-2k^2(1-z)^5 z < 1$, if $0 < z < 1$ and $1 < k < 2$. Therefore, similar to the inclined flat-plate as discussed in Sec. 2, Equation (20) is to the right of Eq. (21), as depicted in Fig. 11(*b*).

As for a sphere of diameter h in Fig. 11(*a*), it is proposed that the unconfined flow at subcritical Reynolds numbers around it is similar to that around a circular cylinder. Based on Eq. (14),

$$D^* = hk\sin\beta_s \tag{22}$$

which leads to the modified Strouhal number

$$S^{**} = S\sin\beta_s = 0.188\sin 80\ \deg = 0.185 \tag{23}$$

being reasonably consistent with the wake Strouhal number of 0.19 from the measurements in Ref. [15], as stated in Sec. 1. With $A_w = \pi(hk\sin\beta_s)^2/4$, $z=0$, and $D=D^*$, Eqs. (17), (22), and (23) can be combined to give

$$Sc_d = 0.185(k^2-1)k^2 \tag{24}$$

Fig. 11(*b*) shows the variations in Eqs. (21) and (24) being quite different from that of Eq. (1) for two-dimensional flow. One data point for the disk in Fig. 11(*b*) is from Fail et al. [30] and the other is from Ref. [14] where only S and k are measured (so $c_d = 1.17$ is taken from Ref. [17], see pp. 3–16 and 3–17). As shown, these two data points are closer to the variation in Eq. (21). Another two data point for the sphere are, respectively, from Achenbach [31,32] at $\mathrm{Re} = 1.62\times10^5$, and Kim and Durbin [33] at $\mathrm{Re} = 4200$, being reasonably close to Eq. (24).

6 Discussion

For unconfined flow with suitable values of S^{**}, Sc_d is related to k through Eq. (8), which is applicable to a variety of two-dimensional sections considered here. For the flat-plate and the wedge, $S^{**} = 0.15$. However, the value of S^{**} for a rectangular prism increases from 0.092 with $d/h = 1.5$ to 0.138 when $d/h = 0.2$ and it is as high as 0.185 for a circular cylinder at subcritical Reynolds numbers. The variations indicate that the size and shape

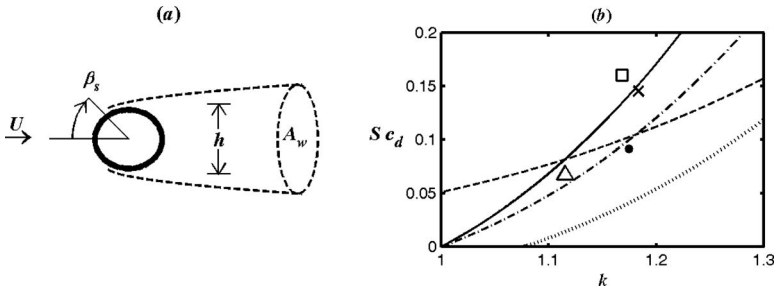

Fig. 11 Unconfined flow past an axisymmetric bluff-body. (*a*) Definition sketch of the flow past a sphere. (*b*) Variations in product of Sc_d with *k*. Disk: × from Fail et al. [30], □ from Calvert [14] and Hoerner [17], ···: Eq. (20) with *z*=10%; ——: Eq. (21); sphere: △ from Kim and Durbin [33], ● from Achenbach [31,32], –•–: Eq. (24); and — —: Eq. (1).

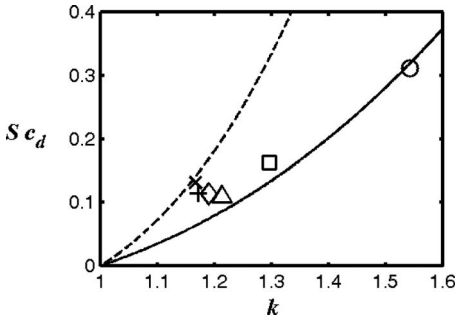

Fig. 12 Sc_d versus k for unconfined flow past a rectangular flat-plate of various aspect ratios. ×: aspect ratio=1, +: 2, ◇: 5, △: 10, □: 20, from Fail et al. [30], ○: two-dimensional from Fage and Johansen [19], ——: Eq. (8), and — —: Eq. (21).

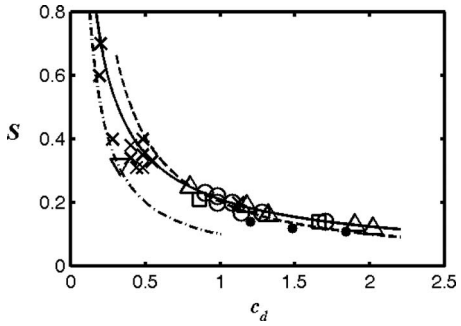

Fig. 13 Variation in Strouhal number with drag coefficient of different two-dimensional bluff-bodies. ×: supercritical blunt bodies, △ : structural shapes, □, ○: circular cylinder and plate, ●: stalled RAE airfoil from Hoerner [17], ▽: circular cylinder at Re=2.13×10^5 from Bearman [6], ——: Eq. (25), — —: Eq. (26), –•–: Eq. (27).

of the aft body may significantly influence the vortex formation region. Therefore, the similarity in the wake structure of different bluff-bodies, as originally proposed by Roshko [3], may require careful consideration. If the blockage ratio is not zero, then additional parameters such as the angle of attack, apex angle, and angle of flow separation are involved so that Eqs. (7), (13), and (16) are needed to demonstrate the appropriate trends. That may explain the scatter of experimental data quoted in Ref. [8].

With the variations in Strouhal number for a square plate and an inclined disk being almost the same as what was found experimentally in Ref. [14], the variation in Eq. (8) for a normal flat-plate is compared with that of Eq. (21) for a disk in Fig. 12. It demonstrates that the two curves provide proper limits for experimental data from Ref. [19] for a two-dimensional flat-plate and that from Ref. [30] for a rectangular plate (with aspect ratio varying from 1 to 20), lending further support to the present finding.

Based on the statistical results of experimental data for a variety of two-dimensional bluff sections such as plates, airfoils, blunt bodies, and cylinders at $\mathrm{Re} > 10^3$, Hoerner [17] proposed a relationship between Strouhal number and drag coefficient, namely,

$$S = 0.21/c_d^{3/4} \tag{25}$$

From the theoretical analysis in Ref. [5], the proposal in Ref. [8] and the present study (including the experimental data quoted herein), it is obvious that S, c_d, and k are coupled. Therefore, if k takes a mean value of 1.4 for flow around a bluff-body (such as a flat-plate, a circular cylinder, and a wedge at $4\times10^3 < \mathrm{Re} < 2.4\times10^4$ as in Ref. [3], see Sec. 1), and if $S^{**}=0.15$ (from the flat-plate and wedge data considered in Sec. 2) is selected, then Eq. (7) is reduced to

$$S = 0.20/c_d \tag{26}$$

which is comparable to Eq. (25). Indeed, the variations in Eqs. (25) and (26) agree in the region of high c_d and low S in Fig. 13, where the data for structural shapes, circular cylinder and plate, and stalled airfoil are located. For flow past a circular cylinder at supercritical Reynolds number regime (see Fig. 2 on p. 3-3 of Ref. [17] where $2\times10^5 < \mathrm{Re} < 4\times10^5$), $k \approx \sqrt{1-(-0.45)}$ can be estimated from Fage and Falkner [34]. If $S^{**}=0.185$ is still suitable for this Reynolds number range (as deduced from Fig. 9(*b*)), then Eq. (8) becomes

$$S = 0.10/c_d \tag{27}$$

Fig. 13 confirms that Eq. (27) can represent the trend of the data in the supercritical range where c_d is low and S is high. The extra data point $(S, c_d)=(0.32, 0.33)$ at $\mathrm{Re}=2.13\times10^5$ from Bearman [6] is also consistent with Eq. (27).

Finally, an application of the present study is demonstrated through an example of estimating the Strouhal number, when the measured values of pressure drag and separation pressure are available. Fig. 14(*a*) displays the variations in c_d and $-c_{ps}$ of a circular disk over blockage ratio $z=1\%$, 2%, 5%, 10%, 15%, and 20% from Melbourne [35]. By substituting them into Eq. (20), the values of S as a function of z are found to be reasonably close to the experimental data from Ref. [29] in Fig. 14(*b*).

7 Conclusion

A methodology is presented in this study to couple Strouhal number, drag coefficient and separation pressure parameter of a two-dimensional bluff section immersed in a blocked flow. In the limit of vanishingly small blockage ratio, consistent results are found in comparison with experimental data from literature, a theoretical equation from Ref. [5] and a proposal from Ref. [8] based on curve-fitting. The present relationship is suitable to depict the trend of the experimental data such as a rectangular section, a wedge and a circular cylinder at subcritical Reynolds numbers in confined flow. Its counterpart for the axisymmetric bluff-bodies has also been derived. The validity of these two relationships are confirmed by comparing them with experimental data for the rectangular flat-plate of various aspect ratios. When the separation-pressure is fixed, the Strouhal number is inversely proportional to the drag coefficient, a relationship similar to the empirical one proposed in Ref. [17]. It is also demonstrated how one of S, c_d, and k may be estimated from the measured values of the other two.

Nomenclature

A = reference area for a 2D section or an axisymmetric body
A_t = cross-sectional area of wind tunnel defined in Fig. 10
A_w = cross-sectional area of characteristic wake behind an axisymmetric body, $\pi(D^*)^2/4$
c_d = drag coefficient, $2F_d/(\rho U^2 h)$ for a 2D section and $2F_d/(\rho U^2 A)$ for a 3D body
c_p = pressure coefficient, $2(p-p_\infty)/\rho U^2$
c_{ps} = separation pressure coefficient, $2(p_s-p_\infty)/\rho U^2$
D = experimental wake width
D^* = theoretical wake width
d = depth of rectangular section defined in Fig. 2(*b*)
d' = wake width for universal Strouhal number
F_d = drag force
f = frequency of vortex-shedding
h = lateral dimension of a bluff-body
H = width of wind tunnel
k = separation-pressure parameter, $\sqrt{1-c_{ps}}$

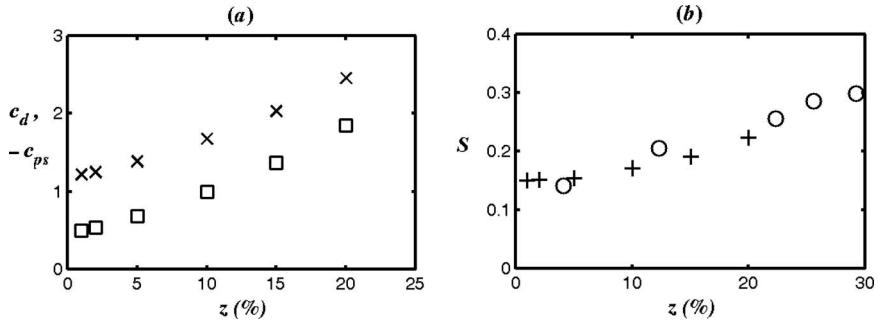

Fig. 14 Prediction of Strouhal number from pressure drag and separation pressure for a circular disk at various blockage ratios. (*a*) ×: c_d, □: $-c_{ps}$ from Melbourne [35] and (*b*) ○: *S* from Miau and Liu [29]; +: from Eq. (20).

p_s = separation pressure
p_∞ = freestream pressure
Re = Reynolds number, $\rho Uh/\mu$
S = conventional Strouhal number, fh/U
S^* = universal Strouhal number, fd'/U_s
S^{**} = modified Strouhal number, fD^*/U_s
U = freestream velocity
x, y = coordinates
z = blockage ratio, A/A_t
α = angle of inclination defined in Fig. 2(*a*)
β = angle measured from frontal stagnation point defined in Fig. 8
β_s = angular location of flow separation
δ = apex angle of wedge in Fig. 6(*a*)
μ = dynamic viscosity of fluid
ρ = fluid density

Appendix

This Appendix provides some details of the right-hand side of Eq. (1). According to Bearman [5], the product of Strouhal number S and drag coefficient c_d is given by

$$Sc_d = \frac{U_N}{U}\frac{4}{\pi}\left(1-\frac{U_N}{U}\right)^2\left[\coth^2\frac{\pi b}{a}+\left(\frac{1}{1-U_N/U}-2\right)\frac{\pi b}{a}\coth\frac{\pi b}{a}\right] \tag{A1}$$

where

$$2\cosh\frac{\pi b}{a}=\left(\frac{1}{1-U_N/U}-2\right)\sinh\frac{\pi b}{a}\left(\cosh\frac{\pi b}{a}\sinh\frac{\pi b}{a}-\frac{\pi b}{a}\right) \tag{A2}$$

and

$$\frac{U_N}{U}\frac{b}{a}\frac{1}{k}=0.181 \tag{A3}$$

where U is the freestream velocity, U_N is the velocity of the vortices relative to the body, k is base-pressure parameter, and a and b are, respectively, the longitudinal spacing and the lateral spacing between vortices. For a given value of b/a, use Eq. (A2) to find U_N/U and then Eq. (A3) to calculate k. The corresponding value of Sc_d can be determined by substituting these values of b/a and k into Eq. (A1). The curve of Eq. (1) in Fig. 1(*a*) is plotted by repeating the aforementioned calculation for $0.15<b/a<0.5$. For instance, the maximum value of Sc_d occurs at $b/a\approx 0.408$ (corresponding to $k\approx 1.55$ and $U_N/U\approx 0.688$), which is much larger than 0.281 as found by Kármán. In addition, by letting $b/a\to\infty$, it is noted that $U_N/U\to 0.5$ from Eq. (A2). Therefore, $k\approx 2.762b/a$ from Eq. (A3), indicating that $k\to\infty$ as well.

References

[1] von Kármán, T., and Rubach, H., 1912, "Über den Mechanismus des Flüssigkeits- und Uftwiderstandes," Phys. Z., **8**, pp. 49–59.
[2] Lamb, H., 1932, *Hydrodynamics*, Dover, New York.
[3] Roshko, A., 1954, "On the Drag and Shedding Frequency of Two-Dimensional Bluff Bodies," NACA TN 3169.
[4] Kronauer, R. E., 1964, "Predicting Eddy Frequency in Separated Wakes," IUTAM Symposium on Concentrated Vortex Motions in Fluids, Ann Arbor, MI.
[5] Bearman, P. W., 1967, "On Vortex Street Wakes," J. Fluid Mech., **28**, pp. 625–641.
[6] Bearman, P.W., 1968, "The Flow Around a Circular Cylinder in the Critical Reynolds Number Régime," NPL Aero Report No. 1257.
[7] Simmons, J. E. L., 1977, "Similarities Between Two-Dimensional and Axisymmetric Vortex Wakes," Aeronaut. Q., **26**, pp. 15–20.
[8] Griffin, O. M., 1981, "Universal Similarity in the Wakes of Stationary and Vibrating Bluff Structures. Trans," ASME J. Fluids Eng., **103**, pp. 52–58.
[9] Bearman, P. W., and Trueman, D. M., 1972, "An Investigation of the Flow Around Rectangular Cylinders," Aeronaut. Q., **23**, pp. 229–237.
[10] Maskell, E.C., 1963, "Theory of the Blockage Effects on Bluff Bodies and Stalled Wings in a Closed Wind Tunnel," Report No. ARC/R&M-3400.
[11] Twigge-Molecey, C. F. M., and Baines, W. D., 1973, "Aerodynamic Forces on a Triangular Cylinder," J. Engrg. Mech. Div. ASCE, **99**, pp. 803–818.
[12] Modi, V. J., and El-Sherbiny, S. E., 1977, "A Free Streamline Model for Bluff Bodies in Confined Flow," ASME J. Fluids Eng., **99**, pp. 585–592.
[13] Calvert, J. R., 1967, "Experiments on the Low-Speed Flow Past Cones," J. Fluid Mech., **27**, pp. 273–289.
[14] Calvert, J. R., 1967, "Experiments on the Flow Past an Inclined Disk," J. Fluid Mech., **29**, pp. 691–703.
[15] Calvert, J. R., 1972, "Some Experiments on the Flow Past a Sphere," Aeronaut. J., April, pp. 248–250.
[16] Yeung, W. W. H., 2009, "On Pressure Invariance, Wake Width and Drag Prediction of a Bluff Body in Confined Flow," J. Fluid Mech., **622**, pp. 321–344.
[17] Hoerner, S. F., 1965, *Fluid-Dynamic Drag*, Hoerner Fluid Dynamics, Bricktown, New Jersey.
[18] Yeung, W. W. H., 2008, "Self-Similarity of Confined Flow Past a Bluff Body," J. Wind Eng. Ind. Aerodyn., **96**, pp. 369–388.
[19] Fage, A., and Johansen, F. C., 1927, "On the Flow of Air Behind an Inclined Flat Plate of Infinite Span," Proc. R. Soc. London, Ser. A, **116**, pp. 170–196.
[20] Yeung, W. W. H., and Parkinson, G. V., 2000, "Base Pressure Prediction in Bluff-Body Potential-Flow Models," J. Fluid Mech., **423**, pp. 381–394.
[21] Awbi, H. B., 1978, "Wind-Tunnel-Wall Constraint on Two-Dimensional Rectangular-Section Prisms," J. Wind Eng. Ind. Aerodyn., **3**, pp. 285–306.
[22] Okamoto, T., Yagita, M., and Ohtsuka, K., 1977, "Experimental Investigation of the Wake of a Wedge," Bull. JSME, **20**, pp. 323–328.
[23] Ramamurthy, A. S., and Ng, C. P., 1973, "Effects of Blockage on Steady Force Coefficients," J. Engrg. Mech. Div. ASCE, **99**, pp. 755–772.
[24] Ramamurthy, A. S., and Lee, P. M., 1973, "Wall Effects on Flow Past Bluff Bodies," J. Sound Vib., **31**, pp. 443–451.
[25] Parkinson, G. V., and Hameury, M., 1990, "Performance of the Tolerant Tunnel for Bluff Body Testing," J. Wind Eng. Ind. Aerodyn., **33**, pp. 35–42.
[26] Kong, L., Hameury, M., and Parkinson, G. V., 1998, "Unsteady-Flow Testing in a Low Correction Wind Tunnel," J. Fluids Struct., **12**, pp. 33–45.
[27] Norberg, C., 1994, "An Experimental Investigation of the Flow Around a Circular Cylinder: Influence of Aspect Ratio," J. Fluid Mech., **258**, pp. 287–316.
[28] Roshko, A., 1961, "Experiments on the Flow Past a Circular Cylinder at Very High Reynolds Number," J. Fluid Mech., **10**, pp. 345.
[29] Miau, J. J., and Liu, T. W., 1990, "Vortex Flowmeter Designed With Wall Pressure Measurement," Rev. Sci. Instrum., **61**(10), pp. 2676–2681.
[30] Fail, R., Lawford, J.A., Eyre, R.C. W., 1957, "Low-Speed Experiments on the Wake Characteristics of Flat Plates Normal to an Air Stream," Report No. ARC/R&M-3120.

[31] Achenbach, E., 1972, "Experiments on the Flow Past Spheres at Very High Reynolds Numbers," J. Fluid Mech., **54**, pp. 565–575.
[32] Achenbach, E., 1974, "The Effects of Surface Roughness and Tunnel Blockage on the Flow Past Spheres," J. Fluid Mech., **65**, pp. 113–125.
[33] Kim, H. J., and Durbin, P. A., 1988, "Observations of the Frequencies in a Sphere Wake and of Drag Increase by Acoustic Excitation," Phys. Fluids, **31**(11), pp. 3260–3265.
[34] Fage, A., Falkner, V. M., 1931, "Further Experiments on the Flow Around a Circular Cylinder," ARC/R&M Report No. 1369 (Also in Hoerner, S. F., 1965, *Fluid-Dynamic Drag*. Hoerner Fluid Dynamics).
[35] Melbourne, W. H., 1982, "Wind Tunnel Blockage Effects and Corrections," *Proceedings of the International Workshop on Wind tunnel Modeling Criteria and Techniques in Civil Engineering Applications*.

On the Streamwise Development of Density Jumps

A. Regev

S. Hassid
e-mail: cvrhasd@tx.technion.ac.il

Department of Civil and Environmental Engineering,
Technion—Israel Institute of Technology,
Haifa 32000, Israel

The analysis of density jumps in two-layer channel flows of miscible fluids controlled by a downstream obstruction, in which one of the layers is infinitely deep and at rest, is extended to consider the dependence of its features on its streamwise dimension. The momentum conservation equation in the entrainment and roller regions, and the energy conservation equation after the jump are corrected to account for friction. The streamwise coordinate is related to the increase in the density layer height through a linear expression derived from CFD calculations. Three regimes are distinguished: (1) for short distances from the origin to the obstruction, only an entrainment region exists; (2) for medium distances, two regions can be distinguished, i.e., the entrainment region, and the roller region, in which no entrainment is assumed; and (3) for long distances, three regions can be distinguished—the entrainment, the roller, and the postjump regions, characterized by approximate energy conservation. It is shown that initially the dimensionless total entrainment ratio increases as the distance to the obstruction increases, until a roller region appears. A further increase in distance to the obstruction does not have a significant effect on the total entrainment, until the appearance of a postjump region, resulting in a gradual decrease in the total entrainment. These results are supported by numerical calculations using the FLUENT CFD software package, which are in good agreement with experimental results. [DOI: 10.1115/1.4000794]

Keywords: density jump, entrainment, stratified flow

1 Introduction

The present work focuses on the streamwise development of density jumps, i.e., hydraulic jumps in a horizontally flowing layer bounded by a wall, and an infinitely deep layer of stagnant fluid with a slightly different density. As shown in a previous publication [1], density jumps are characterized by a considerable entrainment of fluid from the stagnant environment into the flowing layer that changes the density across such jumps. Examples of such flows are air entrainment into smoke and other atmospheric flows on one hand, and fresh water entrainment into salted water (such as in the cooling system of a power station) and other maritime and oceanic flows on the other.

Density jumps were studied theoretically and experimentally by Wilkinson and Wood [2], Wood and Simpson [3], Baddour and Abbink [4], Baddour [5], Hassid et. al [6] and other investigators. These researchers agree that the flow can be divided into two regions: an entrainment region, in which entrainment occurs but the flow remains supercritical, and a roller region, in which there is no entrainment and the transfer from supercritical to subcritical flow takes place (see Fig. 1). They also agree that, contrary to the case of an internal hydraulic jump with no entrainment, the governing equations for the density jump yields a range of solutions and, thus, one needs an additional boundary condition to fully solve the problem, which can be given by the height of a weir downstream of the jump.

In all those works, however, the horizontal extent of the density jump was not considered. The solutions, based on the momentum and mass integral equations, assume that the regions delineated have enough space to develop in the streamwise direction. In the work of Baddour [7], the friction in the part of the flow downstream of the jump, which in the absence of obstruction or narrowing of the channel controls the flow, is taken into account—in flows in which the postjump streamwise dimension is much larger than the one of the jump. Even in this case, the streamwise development of the density jump is not considered.

In this work, it is proposed to analyze the streamwise development of a density jump and consider whether the simple models shown in the previous works can be extended to include the streamwise features of a density jump.

1.1 One-Dimensional Analysis of the Density Jump. The methodology used in the present analysis is based on the work of Regev et al. [1], in which the density jump is treated on the basis of the mass, momentum, and thermal energy (or salinity) conservation, assuming uniform velocity and density profiles. This results in an equation relating the ratio between the flow heights before and after the jump h_2/h_1, with the upstream Froude number $\mathrm{Fr}_1 \equiv q/\{g(\Delta\rho/\rho)h_1^3\}^{1/2}$, and the final dimensionless entrainment ε_f, i.e., the ratio between the mass flow rates after and before the jump minus 1

$$\left(\frac{h_2}{h_1}\right)^3 - \left(\frac{h_2}{h_1}\right)(1+2\mathrm{Fr}_1^2)(1+\varepsilon_f) + 2\mathrm{Fr}_1^2(1+\varepsilon_f)^3 = 0 \qquad (1)$$

In place of the entrainment ε_f, some researchers [4,5] prefer to use the dilution $(s_f = 1+\varepsilon_f)$.

The cubic Eq. (1) admits two physical solutions, one at the end of the entrainment region h'_1, and one at the end of the roller region h_2

$$\frac{h'_1}{h_1} = 2\sqrt{M}\cos\{(2\pi-\theta)/3\} \quad \text{and} \quad \frac{h_2}{h_1} = 2\sqrt{M}\cos(\theta/3) \qquad (2)$$

where

$$\cos\theta = R/M^{3/2}, \quad R = -\mathrm{Fr}_1^2(1+\varepsilon_f)^3, \quad M = \frac{(1+2\mathrm{Fr}_1^2)(1+\varepsilon_f)}{3} \qquad (3)$$

Note that Eq. (2) can be shown also in terms of other dimensionless heights and entrainments H''_2, H''_1 and $(1+\varepsilon_f)''$

Contributed by the Fluids Engineering Division of ASME for publication in the JOURNAL OF FLUIDS ENGINEERING. Manuscript received March 29, 2009; final manuscript received November 25, 2009; published online February 17, 2010. Assoc. Editor: Meng Wang.

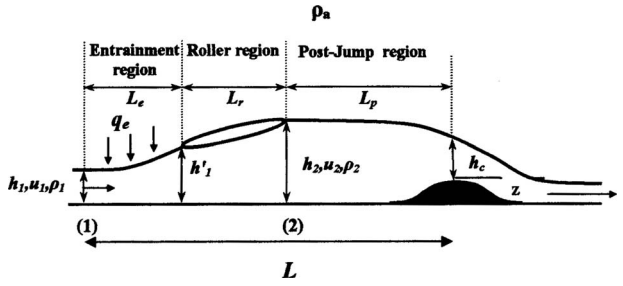

Fig. 1 Density jump in a two-layer flow controlled by a weir

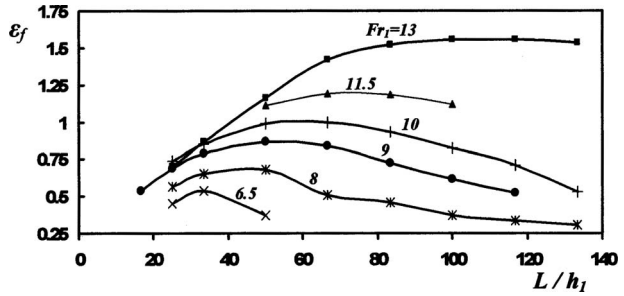

Fig. 2 Dependence of the dimensionless entrainment on the dimensionless distance of the obstruction from the origin—for $Z/h_1=3.33$ (calculated using FLUENT)

$$H''_1 = 2\sqrt{(1+\varepsilon_f)''}\cos\{(2\pi-\theta)/3\} \quad \text{and}$$
$$H''_2 = 2\sqrt{(1+\varepsilon_f)''}\cos(\theta/3) \tag{4}$$

with

$$H''_1 = \frac{h'_1}{h_1}\frac{3\mathrm{Fr}_1^{2/3}}{1+2\mathrm{Fr}_1^2}, \quad H_2'' = \frac{h_2}{h_1}\frac{3\mathrm{Fr}_1^{2/3}}{1+2\mathrm{Fr}_1^2} \tag{5}$$

and

$$s''_f = (1+\varepsilon_f)'' = (1+\varepsilon_f)\frac{3\mathrm{Fr}_1^{4/3}}{1+2\mathrm{Fr}_1^2} \tag{6}$$

$$\cos(\theta) = -(1+\varepsilon_f)''^{3/2} \tag{7}$$

Expressions relating ε_f to the upstream and downstream conditions are given in Ref. [1]. The advantage of Eqs. (4) and (7) over Eqs. (2) and (3) is that one obtains a single relationship for the height ratios, with the dependence on the Froude number implicit.

1.2 The Density Jump Analyzed Using a Computational Fluid Dynamics (CFD) Package. The FLUENT [8] CFD package version 6.2.16 was used to simulate the flow. FLUENT is a very widely-used commercial CFD package and is based on the control volume approach. The calculation is based on the *k-e* turbulent energy-dissipation model. Note that the *k-e* model, modified to account for the buoyancy-induced anisotropy, was used by Leschziner [9] to simulate a density jump and reproduce the results of Wilkinson and Wood [2]. Later, McGuirk and Papadimitriou [10] used a *k-e* model and the Reynolds stress model to simulate an uprising plume, and the jump created by the turning of the plume. They showed that the difference in the predicted entrainment between these two turbulent models is relatively small. Note that both in FLUENT and in the previous two references [9,10] the influence of stratification on the turbulent energy (k) equation is expressed through a negative production term, which does not appear in the dissipation (e) equation.

In the present computations, the grid consists of 15,000 to 200,000 triangular elements, depending on the distance to the obstruction. To check grid dependence and convergence, several cases were calculated using different numbers of elements (18,000, 73,000, and 294,000). The difference in the total entrainment between the denser grid (294,000) and the least dense grid (18,000) was less than 2%. The downstream and upper boundary conditions were of the pressure outlet type with adiabatic temperature and pressure distributions for reverse flow. The downstream boundary was sufficiently downstream from the obstruction and the upper boundary was sufficiently above the entrance so that the boundary conditions can be considered as having no influence on the results. The upstream side consists of a wall with an opening at the bottom, through which a constant velocity and density stream flows. This velocity and density were used to determine the upstream Froude number Fr_1. The lower boundary was a wall. The discretization for momentum and energy equations was second order upwind, and pressure staggering option (PRESTO) for the pressure equation (connected to the continuity one). The pressure velocity coupling was through the semi-implicit method for pressure-linked equations-consistent (SIMPLEC) algorithm (see Ref. [8]). Two criteria were used to check for the convergence of the solution, as follows: (1) a constant integral flux at a cross section downstream of the obstruction (relative change of 10^{-6} between subsequent iterations), and (2) mass flow unbalance less than 10^{-5} of the total mass flow ((total mass flow in-total mass flow out) over all fluid boundaries).

Different upstream Froude numbers were used ranging from 6.5 to 13, as well as different distances (normalized with the initial flow depth) to the obstruction from 16.6 to 133.33, and normalized obstruction heights of 0, 2, and 3.33.

The dependence of the dimensionless total entrainment ratio ε_f on the dimensionless distance of the obstruction from the origin L/h_1, as calculated numerically using Fluent, is exemplified in Fig. 2. The jump is controlled by an obstruction with $Z/h_1=3.33$ and upstream Froude numbers ranging from 6.5 to 13. Lower Froude numbers for this value of Z/h_1 result in submerged jumps, defined by the existence of a layer above the entrance, in which the density is higher than in the ambient fluid but there is no velocity. It can be seen that whereas for small distances, the entrainment ratio increases with L/h_1—for larger values of L/h_1, it reaches a maximum and then decreases.

This behavior is illustrated in Fig. 3, in which the streamlines (lines) and equal-density contours (colored area) of the developing density layer for $\mathrm{Fr}_1=9$ and $Z/h_1=3.33$ are shown (the case $L/h_1=66.67$ is shown twice because of the two different scales in the horizontal direction). For these cases, the one-dimensional analysis of Eqs. (1)–(3) and Ref. [1] should show no difference, since the upstream Froude number, as well as the dimensionless obstruction height are the same, leading to the same entrainment and postjump height, which do not depend on L/h_1; and yet, one can see that there is a large difference between the cases. In the upper cases, with a relatively short nondimensional distance to the downstream obstruction ($L/h_1=25$ and 33), there is no roller region, and the entrainment region extends all the way to the obstruction. In the middle cases, for a nondimensional distance of the downstream obstruction of $L/h_1=50$ and 66.67, there is a rather short roller, partly extending over the obstruction. For $L/h_1=83.33$, 100, and 116.67, there is a fully developed roller region and an extended postroller region without entrainment, which is described using the energy conservation equation in a one-dimensional analysis. In addition, there are large differences in the dimensionless entrainment, as follows: 0.688, 0.87, and 0.721 for $L/h_1=25$, 50, and 83.3 respectively, calculated using $(\psi_{\max}-\psi_{\mathrm{init}})/\psi_{\mathrm{init}}$, where $\psi_{\max}$ is the stream function inside the roller region, and ψ_{init} is the value of the stream function at the entrance wall. For comparison, the dimensionless entrainment calculated using the one-dimensional simplified method without accounting for friction is 1.175.

A better insight can be achieved if one observes the streamwise development of the entrainment $\varepsilon(x)$, calculated on the basis of

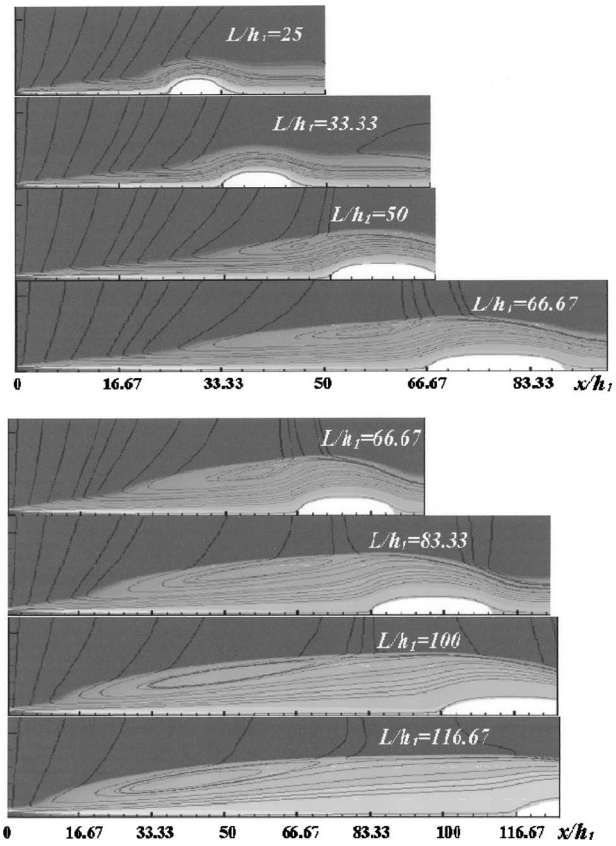

Fig. 3 Development of the density jump for $Fr_1=9$ and $Z/h_1=3.33$ for different values of L/h_1 (25, 33.3, 50, 66.7, 83.33, 100, and 116.7)

difference in stream function, as shown in Fig. 4 for the same cases as in Fig. 3. One can see that for high values of x/h_1 the entrainment is shown to reach a constant value, but contrary to the calculations using the 1D theory, this happens gradually. For high values of x/h_1 there is a region of detrainment, due to the definition of the stream function in the closed roller region. Note that the exact point of transition from the entrainment region to the roller region cannot be seen precisely from Fig. 3. There is a region in which the streamlines have a sharp bend, characterizing the beginning of the roller region, but at the same time, the entrainment of ambient fluid into the stream continues.

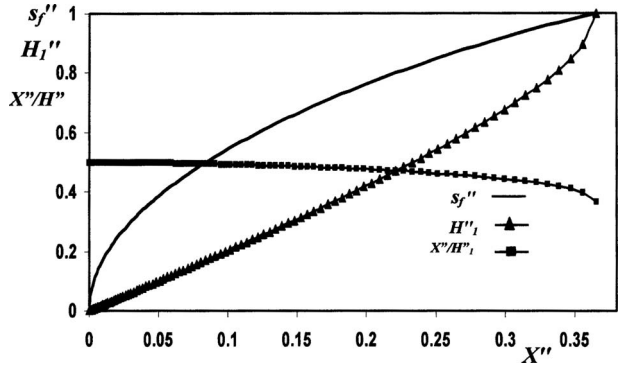

Fig. 5 Normalized height H''_1 (Eq. (4)) and dilution s_f'' (Eq. (6)) versus normalized streamwise coordinate X''

1.3 Extension of the 1D Theory to Include Streamwise Development. The equation for mass conservation, in terms of the volume flux q_e and local cumulative entrainment $\varepsilon(x)$, defined as the ratio of the increase in the volume flow rate at a certain x to the initial flow rate, is

$$\frac{dq_e(x)}{dx} = u_1 h_1 \frac{d\varepsilon(x)}{dx} = v(x) \tag{8}$$

where $v(x)$ is the cross-stream velocity at the upper edge of the density layer, which from the integrated continuity equation is equal to the rate of increase in the flow rate through the density layer.

A reasonable first-order assumption for $v(x)$ is that it is proportional to the mean velocity in the density layer at the same value of x

$$\frac{v(x)}{u(x)} = \xi = \frac{v(x)}{q(x)/h(x)} = \frac{v(x)h(x)}{u_1 h_1 (1+\varepsilon(x))} \tag{9}$$

$$\frac{x}{h_1}\xi = \int_0^{\varepsilon} \frac{h'_1}{h_1}\frac{d\varepsilon'}{1+\varepsilon'} \tag{10}$$

or

$$X'' \equiv \frac{x+x_0}{h_1}\xi\frac{3\mathrm{Fr}_1^{2/3}}{2\mathrm{Fr}_1^{2}+1} = \int_0^{s''_f} H_1''\frac{ds''}{s''} \tag{11}$$

Figure 5 shows the dependence of H''_1 and s_f'' in terms of X''. Integration from a virtual origin, where $s_f''=0$, makes it possible

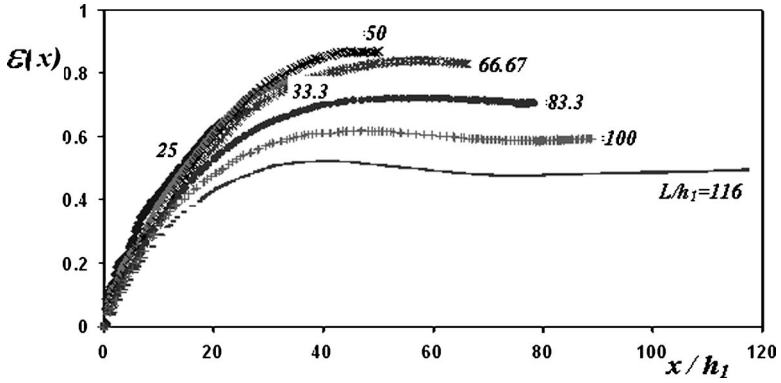

Fig. 4 Development of entrainment $\varepsilon(x)$ in a density jump for $Fr_1=9$ and $Z/h_1=3.33$ for different values of L/h_1 as calculated by FLUENT. (Detrainment for L/h_1 higher than 50 due to including the closed roller region in the calculated entrainment.) Cases are shown in Fig. 3. Maximum entrainment calculated by 1D theory is 1.175.

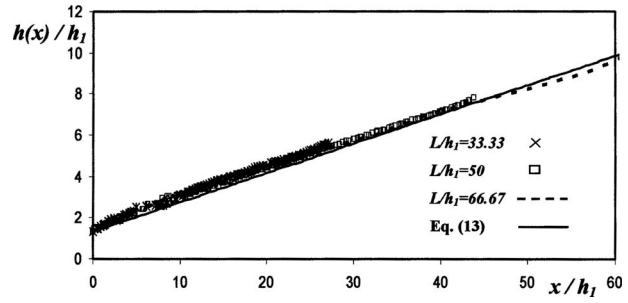

Fig. 6 Dimensionless density layer height versus dimensionless streamwise coordinate in the entrainment region for $Fr_1=10$, $Z/h_1=3.33$, and different values of the distance of the obstruction from the origin

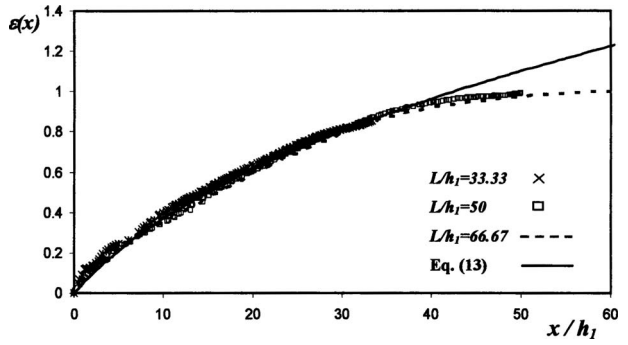

Fig. 7 Dimensionless entrainment in the jump versus normalized streamwise coordinate for $Fr_1=10$, $Z/h_1=3.33$, and different values of the distance of the obstruction from the origin

to collapse the dependence into a single curve, independent of Fr_1. In the same figure one can see that the ratio X'' to H''_1 (or $(x+x_0)/h'_1$) is almost constant for a large part of the range, implying a linear variation in $h'_1(x)$ with x.

Although it is evident that both v and u decrease with the streamwise coordinate x, the assumption of a constant vertical to mean horizontal velocity ratio is obviously in need of justification. One may expect that the vertical velocity and the entrainment should depend on the local Froude number. It can, however, be argued that where the local Froude number is higher than one, as is the case in the entrainment region, the inertial forces are dominant and the gravitational ones are secondary. In such cases one can ignore the gravitational forces influence on entrainment and relate entrainment to the inertial forces and, therefore, make them, to a first approximation, proportional to the local mean velocity in the density layer. The value of the constant v/u ratio chosen will have to be justified on the basis of computational results obtained, using the CFD package FLUENT, which was described in Sec. 1.2.

Figure 6 presents the value of the density layer nondimensional height $h(x)/h_1$ as a function of x/h_1 calculated using FLUENT, for $Fr_1=10$ and $Z/h_1=3.33$ for several distances of the obstruction from the origin. Only the values inside the entrainment region are presented. It can be seen that the computed relationship of $h(x)/h_1$ on x/h_1 is essentially linear and independent of the distance of the obstruction from the origin, which is consistent with the analysis in Eqs. (9)–(11) (X''/H''_1 almost constant over the range of X''), thus giving an aposteriori justification of using the constant v/u assumption. Different upstream Froude numbers result in similar curves with a slightly different slope. Thus, an explicit equation for the dependence of h'_1/h_1 on x/h_1 can be used

$$\frac{h'_1}{h_1}=1+a\frac{x}{h_1} \tag{12}$$

consistent with a local entrainment $\varepsilon(x)$

$$\varepsilon(x)=\left(1+a\frac{x}{h_1}\right)^{\xi/a}-1 \tag{13}$$

Figure 7 shows the dependence of $\varepsilon(x)$ on x/h_1 obtained from the CFD calculations (same cases as in Fig. 6). This dependence is also described by Eq. (13) with $a=0.146$ and $\xi/a=1/3$. The CFD calculations show that the value of a varies between 0.125 and 0.15 for different Froude numbers, and the value of ξ varies between 0.04 and 0.055, whereas $\xi/a=1/3$ remains almost constant [11]. Note that although the entrainment region for $L/h_1=33.33$ and $L/h_1=50$ ends at $x/h_1=27$ and 43, respectively, a small entrainment still takes place in the transition zone. This case is similar to $L/h_1=25$ and 33.33 for $Fr_1=9$, as shown in the upper part of Fig. 3.

1.4 Streamwise Development of the Roller Region. Many works have dealt with the length of the hydraulic jump and its slope, which is similar to the roller region of the density jump. Engelund [12], for example, suggested that the roller has a slope α of 10 deg. Valiani [13] divided the jump into two regions: the first one with $\alpha_1=5.5$ deg and the second with $\alpha_2=10$ deg, then proceeded to calculate the total length of the jump

$$\frac{L_r}{h'_1}=\frac{1}{\tan(\alpha_1)}\frac{2}{3}\frac{\left(\frac{h_2}{h'_1}\right)^3-1}{\frac{h_2}{h'_1}\left(\frac{h_2}{h'_1}+1\right)} \tag{14}$$

Another set of data was collected by the U.S. Bureau of Reclamation (USBR) [14] (see also Ref. [15]). Although a density jump is different from a hydraulic jump, there are various similarities between the hydraulic jump and the roller region, and in particular, the conjugate depth equation is similar [1]. There are, however, differences, the main one being that in the density jump the Froude number at the beginning of the roller region is relatively small, reduced due to the entrainment. This results in a higher flow rate, combined with an increase in the flow depth. Numerical simulations using the FLUENT [8] package show that the slope of depth growth within the roller region is very close to the corresponding one at the end of the entrainment region [11]. For Froude numbers at the end of the entrainment region ($Fr'_1=1-4$), the slope varies from 0.125 to 0.15, corresponding to angles between 7 deg and 8 deg, approximately, suggesting a linear relationship between the stream height change across the roller region and its length

$$L_r=\frac{1}{\tan(\alpha)}(h_2-h'_1) \tag{15}$$

The length of the roller region, nondimensionalized using the postjump depth, of Eq. (14) [13], the USBR data, and the simplified model Eq. (15) ($\alpha=7.5$ deg), as a function of the Froude number at the beginning of the roller region Fr'_1, is shown in Fig. 8. One can see that the values are virtually the same up to $Fr'_1=5$; higher Froude numbers at the beginning of the roller region are not expected in density jumps. The coefficient $1/\tan(\alpha)$ of Eq. (15) is very close to the value of a in Eq. (13)—and it might be said that in most cases, the development of the density layer height in the roller region continues almost as a direct continuation as in the entrainment region.

1.5 The Influence of the Distance of the Obstruction From the Origin. The classical solution [1] assumes that the distance from the origin to the obstruction L is sufficient for the jump to develop. When this assumption is justified, it is possible to divide the jump into three regions:

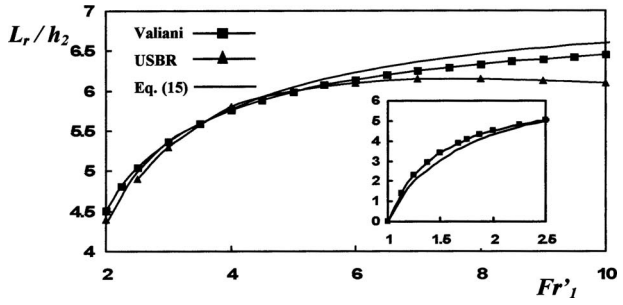

Fig. 8 The roller length divided by the downstream flow depth as a function of the Froude number at the beginning of the roller region. Comparison between data from Refs. [14,13], and Eq. (15) suggested for the density jump.

(a) the entrainment region, for which the momentum equation with entrainment is valid, modified to account for friction

$$\left(\frac{h'_1}{h_1}\right)^3 - \left(\frac{h'_1}{h_1}\right)\left(1 + \left(2 - f\frac{L_e}{h_1}\left(1 + \left(\frac{1+\varepsilon_f}{h'_1/h_1}\right)^2\right)\right)\mathrm{Fr}_1^{\,2}\right) \times (1+\varepsilon_f) + 2\mathrm{Fr}_1^{\,2}(1+\varepsilon_f)^3 = 0 \tag{16}$$

where f is the Fanning friction factor and

$$\frac{L_e}{h_1} = \frac{(h'_1 - h_1)}{a h_1} \tag{17}$$

(b) the roller region, in which the momentum equation is valid, but there is no entrainment. Here, the classical expression for the hydraulic jump modified to account for friction, can be used

$$\frac{h_2}{h'_1} = \frac{1}{2}\left(-1 + \sqrt{1 + \mathrm{Fr}'^2_1\left[8 - 2\left(\frac{h_2}{h'_1} + \frac{h'_1}{h_2}\right)f\frac{L_r}{(h_2 - h'_1)}\right]}\right) \tag{18}$$

where

$$\mathrm{Fr}_1' = \mathrm{Fr}_1\left(\frac{1+\varepsilon_f}{h'_1/h_1}\right)^{3/2} \tag{19}$$

The extent of this region is calculated using Eq. (15)

$$\frac{L_r}{h_1} = \frac{h_2 - h'_1}{0.125 h_1} \tag{20}$$

(c) the postroller region (not a part of the jump), in which the assumptions of no entrainment and an approximate energy balance equation can be made, taking into account energy loss due to friction

$$\frac{h_2}{h_1} + \frac{\mathrm{Fr}_1^{\,2}(1+\varepsilon_f)^3}{2(h_2/h_1)^2}\left[1 - f\frac{L_p}{h_1}\right] = \frac{3}{2}\mathrm{Fr}_1^{\,2/3}(1+\varepsilon_f) + \frac{Z}{h_1} \tag{21}$$

with L_p being the streamwise dimension of the postjump region, from the end of the roller region to the obstruction. This can be calculated from the total distance L, the length of the entrainment region L_e, and the roller region L_r

$$\frac{L_p}{h_1} = \frac{L - L_r - L_e}{h_1} \tag{22}$$

On the basis of the dimensionless distance from the origin, three regimes can be distinguished on the basis of the CFD results (Fig. 3)

1. The three-region regime for sufficiently large dimensionless distance L/h_1. In this case, increased friction in the postjump region results in decreased entrainment, and consequently moving "back" of the roller region toward the x-coordinate origin.
2. As the distance of the obstruction from the origin is decreased, a point comes so that $L_p=0$. Beyond this distance, there is a roller region with a smaller streamwise extent, determined by

$$\frac{L_r}{h_1} = \frac{L - L_e}{h_1} \tag{23}$$

At this regime, h_2/h_1 and ε_f are determined from Eq. (21) with $L_p=0$, together with the equations relevant for the entrainment and roller regions (Eqs. (16)–(19)). The length of the entrainment region L_e is determined from Eq. (17). For the two-region regime, the h_2/h_1 dependence inside the roller region results in a steeper dependence of h_2/h_1 on x/h_1 than is consistent with Eq. (20). This is confirmed by calculations with FLUENT.

3. As the distance between the obstruction and the origin is further decreased, a point comes that there is no more roller region—in this case there is only an entrainment region in which h_1'/h_1 can be calculated using Eq. (17) and the entrainment using Eq. (16), or using Eq. (13). In this regime the super-critical flow continues after the obstruction. Note that in this case no flow is possible beyond a certain value of Z/h_1:

$$\frac{Z_{\max}}{h_1} + \frac{3}{2}\frac{h_c}{h_1} = \frac{h'_1}{h_1} + \frac{q^2(1+\varepsilon_f)^2}{2g h'^2_1} \rightarrow \frac{Z}{h_1} \le 1 + a\frac{L}{h_1} + \frac{\mathrm{Fr}_1^{\,2}}{2}\left(1 + a\frac{L}{h_1}\right)^{2a/\xi - 2} - \frac{3}{2}\left[\left(1 + a\frac{L}{h_1}\right)^{2a/\xi}\mathrm{Fr}_1^{\,2}\right]^{1/3} \tag{24}$$

Figure 9 illustrates the influence of the distance of the obstruction from the origin on the total entrainment (Fig. 9(*a*)), and the height at the end of the entrainment region (Fig. 9(*b*)) for several values of the obstruction height ($Z/h_1=0$ to 2) for $\mathrm{Fr}_1=5$, as calculated using the simplified 1D model. (Notice that the case of $Z/h_1=0$ case is a limit to which the flow tends as the obstruction tends to zero, but the flow is assumed to remain critical at the control section $x=L$.)

Figure 10 presents several Froude numbers (from 6.5 to 13) for $Z/h_1=3.3$. The assumed value of a—consistent with the results from FLUENT—is 0.125, and the assumed value of the friction factor is 0.005, corresponding to a Reynolds number of 13,000 approximately. The entrainment and height are calculated using the one-dimensional equations. For high values of L/h_1, consistent with the existence of a postentrainment region, an increase in the distance of the obstruction of the origin results in a decreased extent of the entrainment region, due to the slight decrease in entrainment.

These results are qualitatively similar to those obtained by FLUENT, as shown in Fig. 2, although in the CFD results there is a rather more gradual transition between the three regimes. In all cases, the value of the maximum entrainment possible (not the maximum entrainment consistent with momentum balance, as in Eqs. (1) and (4)) is less than what would be obtained without considering friction. These figures exemplify the influence of friction and the distance of the obstruction and point to significant

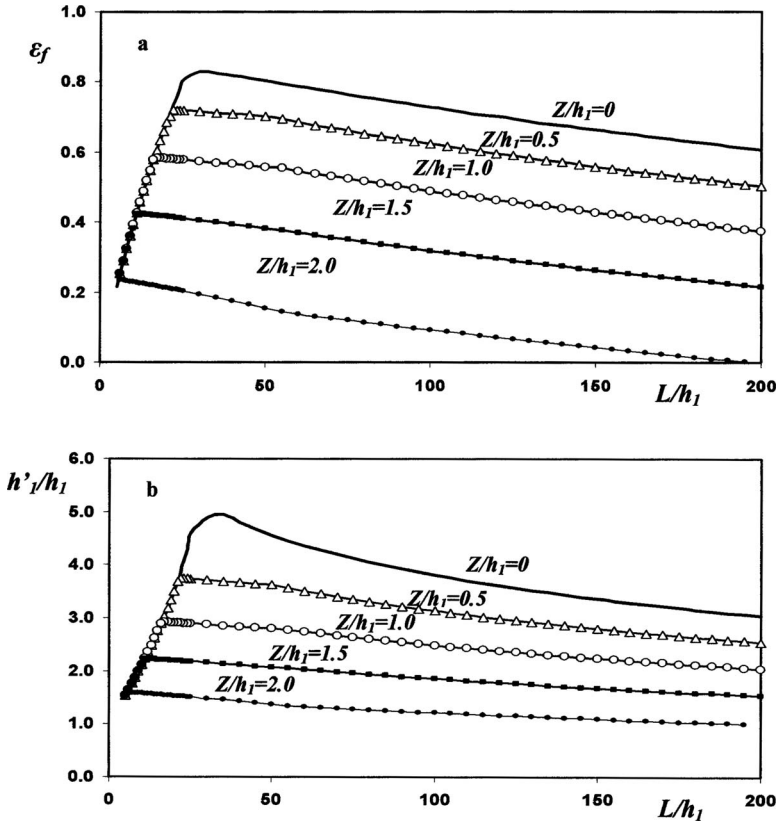

Fig. 9 (*a*) Final entrainment and (*b*) nondimensional density layer thickness at the end of entrainment region calculated from simplified model in an obstruction-controlled density jump as a function of the distance of the obstruction from the origin for $Fr_1=5$. If friction is neglected, the value of ε_f is 0.99, 0.84, 0.69, 0.510, and 0.29 for $Z/h_1=0$, 0.5, 1, 1.5, and 2, respectively.

deviations from expressions based exclusively on the conservation laws without accounting for friction.

2 Experimental Results

To test the computational results for the entrainment in density jumps, a series of flow visualization experiments using smoke were conducted in a physical model schematically described in Fig. 11. The channel is open on the lower side to allow entrainment. Entrainment was measured using two Venturi devices, i.e., one in the entrance and one in the exit.

The flow is along a 4.0 m long and 1.0 m wide inverted channel. At the beginning of the channel the flow is supercritical and uniform. At the end of the channel an obstruction was created by gradually lowering the roof into the channel to create an obstruction, as can be shown in Fig. 11. In order to calculate the entrainment ones needs to know the initial and final mass fluxes and the upstream Froude number.

The Froude number at the beginning of the channel is calculated from

$$\mathrm{Fr}_1 = \frac{Q}{b\sqrt{g{h_1}^3 \Delta T/T_a}} \tag{25}$$

where Q is the volume flux measured at the entrance Venturi device, T_a is the ambient temperature (K), $\Delta T=T_1-T_a$, T_1 is the temperature in the beginning of the channel (measured using thermocouples), b is the width of the channel (1.0 m), and h_1 is the height of the opening according to the specific experiment. The flow at the beginning of the channel is almost uniform due to the relatively large relaxation box (marked as 4 in Fig. 11). The air is supplied using a blower (marked as 1) through a heater (marked as 2) and a diffuser (marked as 3) into the relaxation box. The diffuser of a square cross section is made of several sectors with divergence angle 7 deg each, to ensure there is no separation and thus the turbulence entering the relaxation chamber is minimized.

The dimensionless mass entrainment was calculated using

$$\varepsilon_f = \frac{Q_{\mathrm{exit}}/T_{\mathrm{exit}} - Q_{\mathrm{ent}}/T_{\mathrm{ent}}}{Q_{\mathrm{ent}}/T_{\mathrm{ent}}} \tag{26}$$

where Q_{exit} and Q_{ent} are the volume flux at the exit (marked as 5) and entrance venture devices, respectively, T_{exit} and T_{ent} are the absolute temperatures at the exit and entrance respectively, approximately inversely proportional to the density. In order to prevent additional entrainment after the bump, the air flows after the bump into a second relaxation box, the smoke level in the box is kept constant at the end of the obstruction, so no entrainment occur after it.

In Fig. 12 one can see the results obtained from the experiments and the numerical simulations for $Z/h_1=2$ and Froude numbers between 3.7 and 9.5. It can be seen the good agreement between the results, and particularly, the entrainment found at the relatively low values of the Froude number, in spite of the difference between the 2D FLUENT configuration and the three-dimensional experiment.

Note that flow visualization has shown that for relatively low values of the Froude number, the jump was submerged, but in spite of that, there was entrainment, which is contrary to the assumptions of Wilkinson and Wood [2] and consistent with the results of CFD calculations.

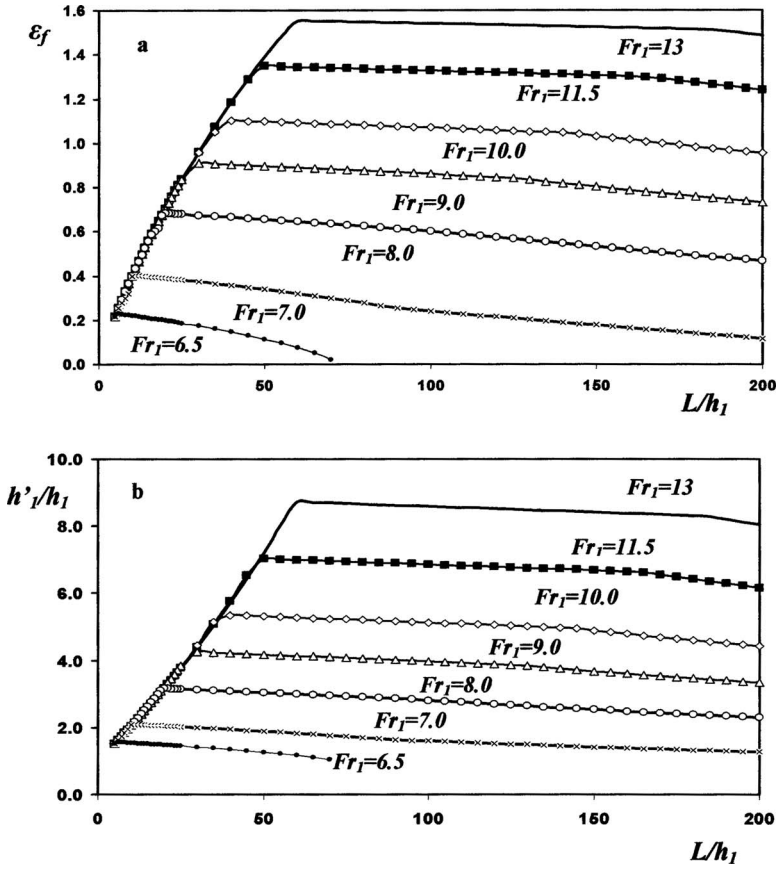

Fig. 10 (*a*) Entrainment and (*b*) dimensionless maximum height calculated from simplified model in a weir-controlled density jump as a function of the distance of the obstruction from the origin, for different Froude numbers and $Z/h_1=3.3$. If friction is neglected, ε_f is equal to for 0.30, 0.78, 1.46, 1.86, and 2.18 for $Fr_1=6.5$, 8, 10, 11.5, and 13, respectively.

3 Discussion and Conclusions

The simplified one-dimensional model for density jump flows developed in previous publications has been extended to estimate the influence of the streamwise extent of density jumps. Note that the concept of a jump—be it the classical hydraulic jump or the density jump—is somehow contradicted by the idea that it has a finite streamwise extent. However, it is shown that the streamwise extent may have an important influence on the behavior of the jump, through the influence of friction.

The results of the simplified model are similar to the ones obtained using the CFD calculation, regardless of the use of simplifying approximations, as follows:

1. The linear relationship between the dimensionless density layer height and the streamwise velocity—as derived from CFD calculations. The assumption is consistent with a vertical velocity proportional to the horizontal, the value of the proportionality constant being of the order of 0.04–0.06.
2. The assumed flat velocity and density profiles, as well as the Boussinesq approximation, are also sources of error, in the former case mainly at the immediate end of the roller region. The influence of the deviation from flat profiles was investigated by Regev and Hassid [16], and it was shown that it can be accounted by shape factors and the predicted entrainment found in good agreement with experimental results.

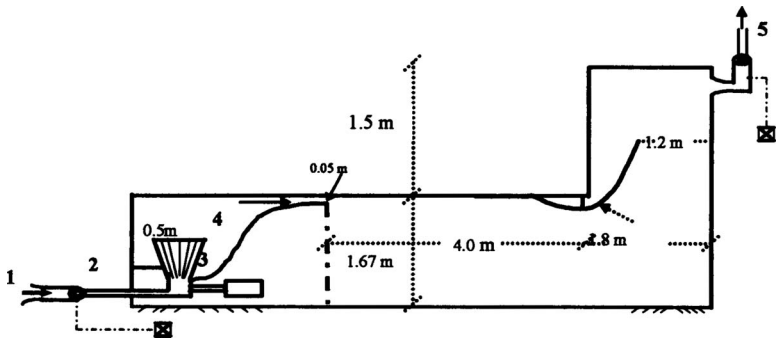

Fig. 11 Schematic diagram of the flow apparatus for visualization experiment

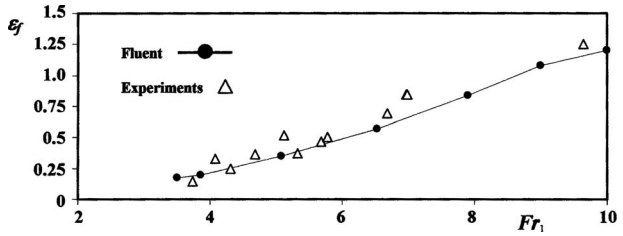

Fig. 12 Comparison of the final entrainment as a function of the upstream Froude number from numerical simulations using FLUENT and the experiments, where $Z/h_1=2$

3. The assumed constant friction factor is, in reality, dependent on the roughness of the channel or the Reynolds number for smooth channels—the dependence on the local average velocity being also the source of an additional small error.

One might of course question the results of the CFD package because of the use of a *k-e* model on the grounds that it is not suitable for flows with the strong anisotropy induced by the buoyant forces. However, as already stated, according to the works of McGuirk and Papadimitriou [10], for similar situations, the regular *k-e* model on one hand and a *k-e* model coupled with an anisotropic, buoyancy-dependent viscosity give to a large extent similar results. This can be explained on the grounds that in this case the flow is essentially influenced by the buoyancy-induced mean flow rather than turbulence-induced entrainment.

The above limitations notwithstanding, it is shown that when the density jump is controlled by an obstruction, there are three different regimes.

For short distances between the obstruction and the beginning of the jump, there is only an entrainment region, in which the mass flow rate increases with distance due to entrainment.

For larger distances, there is also a roller region. However, its development is impeded by the obstruction. At this point, the entrainment ratio reaches a maximum.

For even larger distances, the fully developed roller region is followed by a postjump region extending to the obstruction. In this case, the final entrainment slightly decreases with the distance of the obstruction from the origin, as a result of the little friction in the postdensity jump region.

The measured entrainment is shown to be in relatively good agreement with the one calculated using the CFD package FLUENT.

In all these cases, the entrainment possible is smaller than what would have resulted if friction would not be taken into account. Accordingly, the maximum value of the height immediately after the jump is reduced, relatively to the case that friction is neglected. Friction in the postjump region can be small for high Froude numbers, but its importance increases as the obstruction distance L/h_1 increases, especially for smaller Froude numbers, and sometimes there can be no jump beyond a certain value of dimensionless streamwise distance.

Another reason that the graphs of the 1D model deviate from those of the CFD calculations is the transfer to the submerged density jump status. The 1D model shows that following a certain value of Z/h_1, it is impossible to obtain a solution of the pre- and postjump equations—resulting in a submerged jump, characterized by no entrainment. The CFD model shows a gradual transfer to a submerged jump as the streamwise distance of the obstruction from the origin increases. In that case, the basic assumption that there is no entrainment in a submerged jump is not confirmed. However, the analysis of a submerged jump is beyond the scope of this work.

It can be said that the model proposed here is capable of describing adequately the main features of the density jump phenomenon, accounting for streamwise variation and friction, except for entrainment in submerged jumps, which is beyond the scope of this work.

Acknowledgment

The support of the Technion Vice President Fund for Research is acknowledged. The authors also acknowledge the advice of Professor M. Poreh.

Nomenclature

a = constant in Eq. (12)
e = turbulent energy dissipation rate
Fr_1 = Froude number at entrance, $(q/(g\Delta\rho/\rho h_1^3))^{1/2}$
Fr'_1 = Froude number at end of entrainment region, $\mathrm{Fr}_1((1+\varepsilon_f)/(h'_1/h_1))^{3/2}$
f = Fanning friction factor $(=2\tau/\rho U^2)$
g = gravity
h_1 = layer height at entrance
h'_1 = layer height at end of entrainment region
h_2 = layer height at end of roller region
H_1'' = $3(h'_1/h_1)\mathrm{Fr}_1^{2/3}/(2\mathrm{Fr}_1^2+1)$
H_2'' = $3(h'_2/h_1)\mathrm{Fr}_1^{2/3}/(2\mathrm{Fr}_1^2+1)$
k = turbulent energy
L = streamwise distance between the entrance and obstruction
L_e = streamwise extent of the entrainment region
L_p = streamwise extent of the postjump region
L_r = streamwise extent of the roller region
q = volumetric flow rate per unit width at $x=0$
$q(x)$ = volumetric flow rate per unit width at x
$q_e(x)$ = entrained volumetric flow rate per unit width
Q_{ent} = entry volume flow rate in the experiment
Q_{exit} = entry volume flow rate in the experiment
$s(x)$ = local dilution, $(\equiv 1+\varepsilon(x)=q(x)/q)$
s_f = dilution at the end of jump, $(\equiv 1+\varepsilon_f)$
T_{ent} = exit absolute temperature in experiment
T_{exit} = exit absolute temperature in experiment
v = vertical velocity
u = streamwise mean velocity at cross section
x = streamwise coordinate from entrance
x_0 = virtual streamwise coordinate at the place where $s=0$
X'' = $3[(x-x_o)/h_1]\mathrm{Fr}_1^{2/3}/(2\mathrm{Fr}_1^2+1)$
z = vertical coordinate
Z = maximum height of obstruction.

Greek

$\varepsilon(x)$ = local cumulative entrainment ratio based on the initial volume flow rate $(q_e(x)/q)$
ε_f = final entrainment ratio at the end of entrainment region $(q_e(L_e)/q)$—equal to the final flow rate too.
ξ = ratio between vertical velocity v at the edge of the density layer and horizontal mean velocity inside it u.
$\Delta\rho$ = difference between the density inside layer and the ambient region
ρ = density
τ = wall shear stress
ψ = stream function
ψ_{init} = initial stream function at upper part of inflow stream
$\psi_{\max}$ = maximum stream function inside the roller region or outside it.

References

[1] Regev, A., Hassid, S., and Poreh, M., 2006, "Calculation of Entrainment in Density Jumps," Environ. Fluid Mech., **6**, pp. 407–424.

[2] Wilkinson, D. L., and Wood, I. R., 1971, "A Rapidly Varied Flow Phenomenon in a Two-Layer Flow," J. Fluid Mech., **47**, pp. 241–256.

[3] Wood, I. R., and Simpson, J. E., 1984, "Jumps in Layered Miscible Fluids," J. Fluid Mech., **140**, pp. 329–342.

[4] Baddour, R. E., and Abbink, H., 1983, "Turbulent Underflow in a Short Channel of Limited Depth," J. Hydraul. Eng., **109**(5), pp. 722–740.

[5] Baddour, R. E., 1987, "Hydraulics of Shallow and Stratified Mixing Channel," J. Hydraul. Eng., **113**(5), pp. 630–645.

[6] Hassid, S., Regev, A., and Poreh, M., 2007, "Turbulent Energy Dissipation in Density Jumps," J. Fluid Mech., **572**, pp. 1–12.

[7] Baddour, R. E., 1987, "A Stratified Mixing Channel: Theory and Experiment," *Proceedings of the National Conference on Hydraulic Engineering*, Williamsburg, VA, pp. 135–140.

[8] FLUENT 6.3.26 Users Guide, 2006.

[9] Leschziner, M. A., 1979, "Numerical Prediction of the Internal Density Jump," *Proceedings of the 18th Congress IAHR Hydraulic Engineering in Water Resources Development and Management*, Italy, Vol. 3B.

[10] McGuirk, J. J., and Papadimitriou, C., 1985, "Buoyant Surface Layers Under Fully Entraining and Internal Hydraulic Jump Conditions," *Proceedings of the Fifth Symposium on Turbulent Shear Flows*, Cornell University.

[11] Regev, A., 2006, "Analysis of Density Jumps," D.Sc. thesis, Faculty of Civil and Environmental Engineering, Technion, Israel Institute of Technology, Haifa, Israel (in Hebrew).

[12] Engelund, F., 1981, "A Simple Theory of Weak Hydraulic Jumps," Institute of Hydrodynamics and Hydraulic Engineering, Technical University of Denmark, ISVA Progress Report No. 54.

[13] Valiani, A., 1997, "A Linear and Angular Momentum Conservation in Hydraulic Jumps," J. Hydraul. Res., **35**(3), pp. 323–355.

[14] U.S. Bureau of Reclamation, 1955, "Research Studies on Stilling Basins, Energy Dissipators, and Associated Appurtenances," Hydraulic Laboratory Report No. Hyd. 399.

[15] Chow, V. T., 1959, *Open Channel Hydraulics*, McGraw-Hill, New York, p. 398.

[16] Regev, A., and Hassid, S., 2007, "On the Velocity and Density Profiles in Density Jumps," *Proceedings of the Congres Francais de Mecanique*, Grenoble, France.

S. Duplaa
Ecole Navale IRENav,
BCRM Brest CC 600,
29240 BREST Cedex 9, France
e-mail: sebastien.duplaa@ecole-navale.fr

O. Coutier-Delgosha
e-mail: olivier.coutier@lille.ensam.fr

A. Dazin
e-mail: antoine.dazin@lille.ensam.fr

O. Roussette
e-mail: roussette@ensam.fr

G. Bois
e-mail: gerard.bois@lille.ensam.fr

G. Caignaert
e-mail: guy.caignaert@lille.ensam.fr

Arts et Métiers ParisTech/LML Laboratory,
8 Boulevard Louis XIV,
59046 Lille Cedex, France

Experimental Study of a Cavitating Centrifugal Pump During Fast Startups

The startup of rocket engine turbopumps is generally performed only in a few seconds. It implies that these pumps reach their nominal operating conditions after only a few rotations. During these first rotations of the blades, the flow evolution in the pump is governed by transient phenomena, based mainly on the flow rate and rotation speed evolution. These phenomena progressively become negligible when the steady behavior is reached. The pump transient behavior induces significant pressure fluctuations, which may result in partial flow vaporization, i.e., cavitation. An existing experimental test rig has been updated in the LML Laboratory (Lille, France) for the startups of a centrifugal pump. The study focuses on the cavitation induced during the pump startup. Instantaneous measurement of torque, flow rate, inlet and outlet unsteady pressures, and pump rotation velocity enable to characterize the pump behavior during rapid starting periods. Three different types of fast startup behaviors have been identified. According to the final operating point, the startup is characterized either by a single drop of the delivery static pressure, by several low-frequency drops, or by a water hammer phenomenon that can be observed in both the inlet and outlet of the pump. A physical analysis is proposed to explain these three different types of transient flow behavior. [DOI: 10.1115/1.4000845]

1 Introduction

Space launcher turbopumps are characterized by fast startups; actually, the time delay between the inception of the shaft rotation and the nominal flow conditions is usually close to one second. It means that the rotation speed increases from zero up to several tens of thousands of rotations per minute during a single second. Such fast startup results in severe transient effects that are mainly governed by the speed acceleration $d\omega/dt$ and the flow rate increase dQ/dt [1].

Transient effects in centrifugal pumps have been studied experimentally by several means for about 25 years: fast opening or closure of valves [2], fast startup and shutdown sequences [3,4,6–8], and /or rotation speed fluctuations [5]. It has been found in these previous studies that fast transients result in pronounced unsteady effects involving large pressure and flow rate fluctuations, which may be preponderant in front of the quasi-steady flow evolution. So, the understanding and prediction of these transient behaviors is of first importance for the design of the feed pumps of rocket engines.

For this purpose, an experimental setup has been developed in the LML Laboratory. It is presently devoted to the study of a five blades centrifugal impeller. An original startup sequence based on the use of a rapid coupling is applied in order to simulate rocket engine fast startings and the associated transient effects. Noncavitating conditions have been previously investigated [6,7] and the evolution of global parameters of the flow during the startup (flow rate, pump head, and pump rotation speed) has been obtained for various flow conditions. Local investigations have also been performed by Picavet and Barrand [6] in order to characterize the flow at the pump suction. A strong tangential velocity has been detected by visualizations at the pump inlet. Particle image velocimetry (PIV) measurements performed in the inlet pipe have confirmed the presence of this recirculation, whose length and intensity have been characterized according to the final rotation speed and flow rate [7].

These previous investigations have been mainly conducted in noncavitating flow conditions. However, pressure fluctuations involved in fast pump startups may be responsible for the development of cavitation in the impeller and in the inlet pipe. Indeed, cavitation is a recurrent source of perturbation for pumps operating at low inlet pressure and/or high rotation speed. Such conditions may be encountered during fast startups. Tanaka and Tsukamoto [2] studied the transient flow in a centrifugal pump during fast startup or shutdown sequence; they have found strong fluctuations of both the flow rates and the pressures at the inlet and outlet. While some of these fluctuations, which occur simultaneously at the pump suction and delivery, are attributed by the authors to the water hammer phenomenon, other oscillations, only detected at the pump outlet, are due to unsteady cavitation. According to the measurements reported in Ref. [2], such oscillations depend both on the value of the cavitation number τ and on the flow rate.

The objective of the present study is to analyze this transient cavitating behavior in order to characterize the influence of low inlet pressure on fast startups of pumps.

2 Experimental Device

The test rig has been initially constructed in 1993 for the study of fast startup of centrifugal pumps. It has been used since that time for the investigation of fast transients in various situations of noncavitating flows [9–11].

For the purpose of the present study, the setup has been significantly modified in order to improve its capabilities of measurement and also to enable different types of initial conditions.

Two different configurations are available (Fig. 1):

(1) Configuration No. 1: The suction and delivery pipes of the pump are connected to a single tank, so that the test rig is closed. In this situation, the flow velocity in the rig before the pump startup is zero.

Contributed by the Fluids Engineering Division of ASME for publication in the JOURNAL OF FLUIDS ENGINEERING. Manuscript received April 4, 2008; final manuscript received December 4, 2009; published online January 28, 2010. Assoc. Editor: Steven Ceccio.

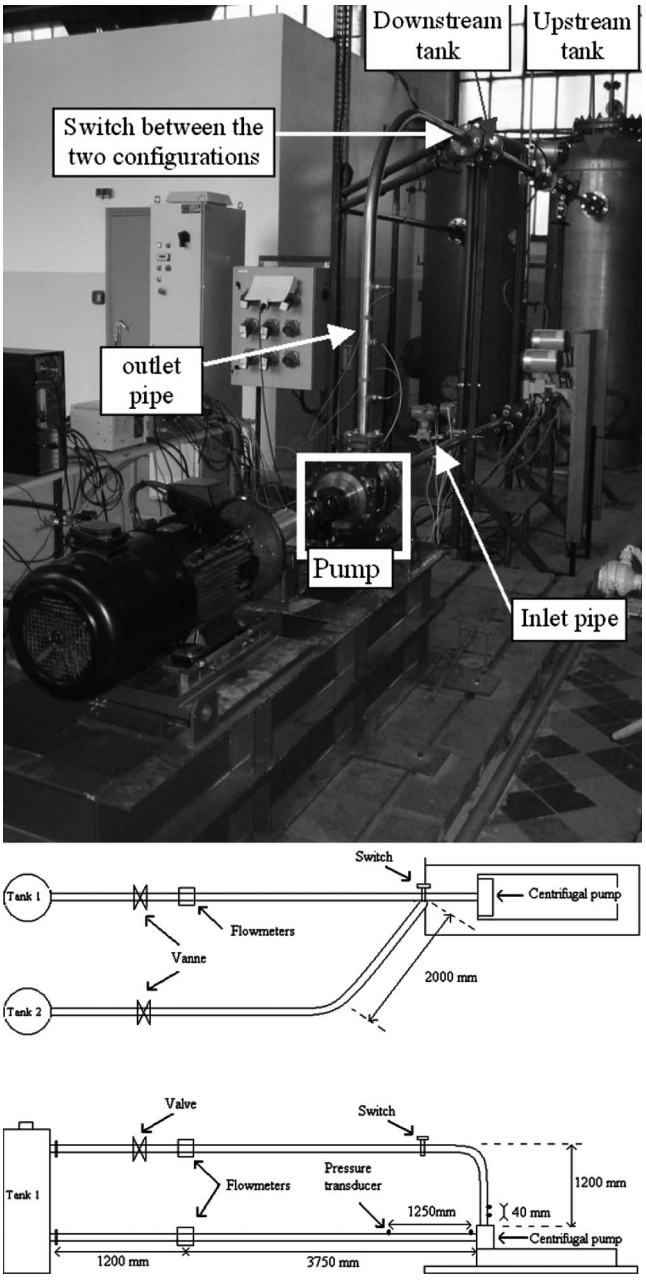

Fig. 1 Photography and scheme of the test rig

(2) Configuration No. 2: The delivery pipes are connected to a second tank, which means that the inlet and outlet initial pressures can be set independently. It enables to impose an initial flow circulation before the pump startup.

The switch between the two configurations is controlled with a valve located on the pump delivery pipe (Fig. 1). In the present study, configuration no.1 is systematically used.

In order to achieve fast starting periods, a special conception of the line of shafts is required: The pump is driven by an asynchronous electric motor through an electromagnetic clutch. The fast startups are obtained by engaging the clutch, once the motor is running at its final rotation speed. Slower startups can also be obtained by engaging the clutch before the motor is started.

A single stage vaneless diffuser single volute type radial flow pump is used for the experiments. The main specifications of the impeller are summarized in Table 1 and Fig. 2.

Table 1 Impeller specifications

Geometric specifications	
Inlet vane angle (deg)	32.2
Outlet vane angle (deg)	23
Number of vanes	5
Inlet diameter D_1 (mm)	38.5
Outer diameter D_2 (mm)	202.5
Outer width b_2 (mm)	7
Hydraulic parameters	
ω_n (rpm)	2900
ω_s	0.24
Q_n (m^3/h)	23
ΔP_n (Pa)	4.9×10^5

Several high-frequency measurements are available on the installation, in order to characterize the flow evolution during the pump fast startup:

(a) A Meiri (France) 0170MS torque meter is included between the pump and electromagnetic clutch in order to obtain the instantaneous rotation speed and torque.
(b) Four Kistler (France) 701A piezoelectric pressure transducers are located on the inlet and delivery pipes. Their signals are used to obtain the high-frequency inlet and outlet pressure evolutions as well as the inlet and outlet flow rates, according to the method initially proposed by Ghelici [9]. The transducer which is the nearest from the impeller on the suction pipe is located 50 mm upstream from the pump, while the first one on the delivery pipe is located at 100 mm downstream from the pump. More details can be found in Ref. [1] regarding this method and its accuracy.
(c) The motor shaft rotation speed is measured by a photoelectric cell.
(d) An accelerometer located on the pump casing is used to obtain the radial vibrations.

Moreover, supplementary low-frequency instrumentation is also available in order to control the final flow conditions after the transients or to characterize stabilized flow conditions. For this purpose, two Krohne (France) Optiflux 4300 flow meters are used for the flow rate control at the pump suction and delivery, and two Rosemount pressure sensors are devoted to the measurements of the inlet static pressure and pump static pressure rise, respectively.

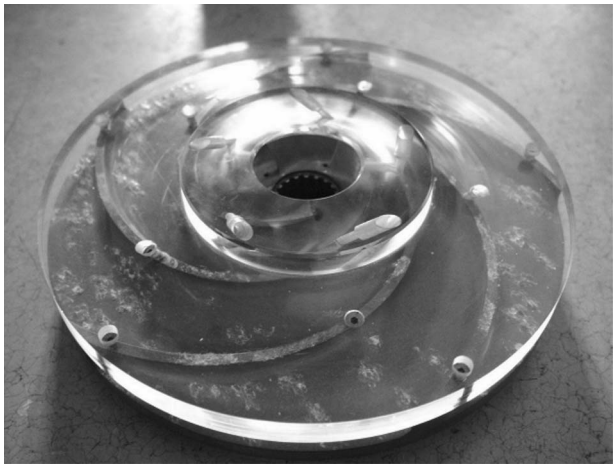

Fig. 2 Picture of the impeller

Table 2 Absolute uncertainties derived from repeatability tests (steady/transient conditions, with/without cavitation)

	P_s (Pa)		P_d (Pa)		C (Nm)		ω (rpm)	
	st	tr	st	tr	st	tr	st	tr
No cavitation	1500	3000	2000	11,000	0.15	0.5	0	45
Cavitation	1500	1500	6000	10,000	0.5	0.5	0	45

These sensors are not used for unsteady conditions measurements because their acquisition frequency is too small, i.e., 25 Hz for the flow meters, and less than 1 Hz for the Rosemount pressure sensors. Such values do not enable to catch the flow rate and the pump static pressure rise evolutions during a fast startup.

The high-frequency data from the pressure transducers and the torque meter are acquired by a National Instrument (France) PXI-PCI system equipped for the simultaneous acquisition of all signals. The sampling frequency is 10 kHz, and the acquisition duration is 5 s. In the case of fast startups, acquisition is triggered by a transistor-transistor logic (TTL) signal emitted at the engagement of the electromagnetic clutch, so that all experiments have the same reference time.

For steady state flow conditions, the uncertainty on the measurements has been evaluated from both the precision of the sensors and repeatability tests. In noncavitating conditions and a rotation speed equal to 3000 rpm, the overall relative uncertainty is 5% for the torque, 1% for the measurements of the fluctuating pressures, 0.5% for the inlet pressure and the pump head, and 4% for the flow rate, respectively. In cavitating conditions, uncertainties on torque and fluctuating pressures increase up to 6.5% and 2%, respectively.

For transient flow conditions, absolute uncertainties are given in Table 2. Indeed, relative uncertainties make no sense, since initial values of the flow rate, rotation speed are zero. In Table 2, absolute uncertainties related to steady-flow conditions are also reported in order to enable the reader to compare transient and steady-flow conditions. All values given in Table 2 correspond to the maximum uncertainties obtained during the transient from analysis of repeatability tests, for cavitating as well as noncavitating conditions. The final rotation speed is always 3000 rpm. Note that the absolute uncertainties are given for both steady (st) and transient (tr) situations. It can be seen that the precision of the measurements may decrease slightly during fast startups. The value of 45 rpm reported for the rotation speed in transient flow conditions is mainly due to a random time delay in the rotation speed increase, which is related to the variable slipping of the electromagnetic clutch when it is engaged.

Visualizations of the flow within the impeller have been performed with a high speed camera and a pulsed stroboscope. As for the other sensors, the camera and stroboscope are triggered with the electromagnetic clutch. For these measurements, an inlet pipe in plexiglas was used. The acquisition frequency equals 500 Hz, so about 250 pictures are obtained during each fast startup. The objective of these visualizations is to provide a rough estimation of the cavitation development within the impeller during the fast startups.

3 Steady Flow Measurements

The behavior of the impeller has first been characterized in configurations of stabilized flow rates and rotation speeds in noncavitating and cavitating conditions.

3.1 Noncavitating Behavior. The evolution of the pump head according to the flow rate is given in Fig. 3 for three different rotation speeds. The nominal flow rate Q_n is defined as the conditions leading to zero incidence at the blade leading edge. The corresponding flow rate coefficient is 0.021. Flow rates have been

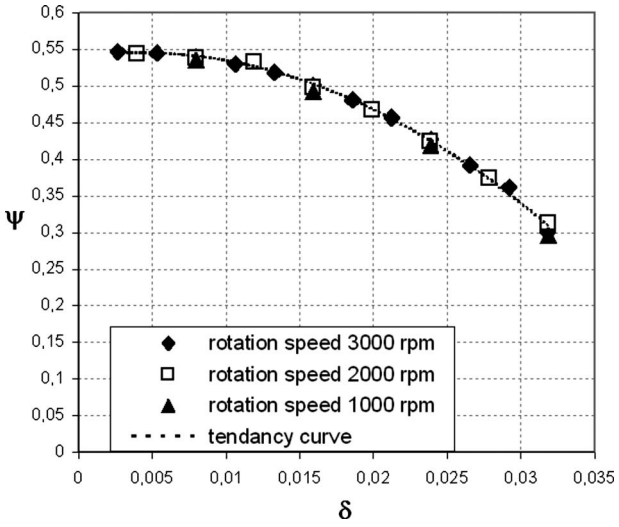

Fig. 3 Evolution of the pump elevation according to the inlet flow rate coefficient ($\Delta\Psi/\Psi=0.5\%$ and $\Delta\delta/\delta=4\%$)

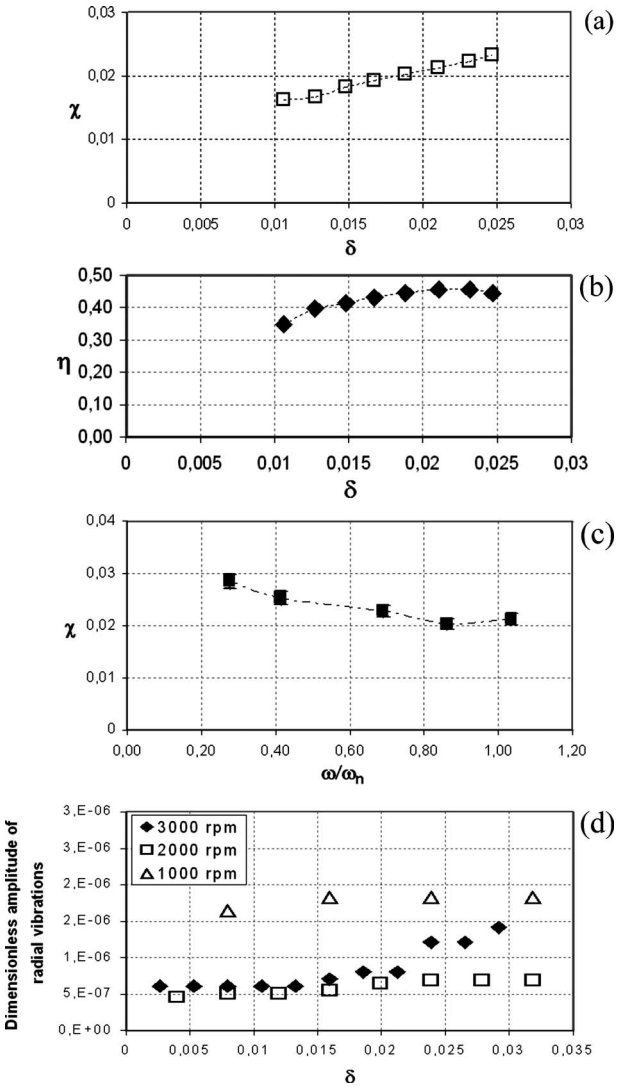

Fig. 4 Evolution of (*a*) χ according to δ at 3000 rpm ($\Delta\chi/\chi=5\%$ and $\Delta\delta/\delta=4\%$), (*b*) η according to δ at 3000 rpm ($\Delta\eta/\eta=9,5\%$), (*c*) χ according to ω/ω_n for $Q=Q_n$ ($\Delta\chi/\chi=5\%$), and (*d*) the dimensionless amplitude of the radial vibrations according to δ ($\Delta\delta/\delta=4\%$)

investigated from $0.13Q_n$ up to $1.5Q_n$. To obtain the charts drawn in Fig. 3, noncavitating conditions have been imposed by increasing the pressure level in the tank up to 3 kPa.

It can be observed in Fig. 3 that a close agreement between the three results is obtained. Only a slight decrease in the pump head can be observed at a rotation speed of 1000 rpm, in comparison with the two other speeds. It shows that for rotation speeds ranging from 1000 rpm to 3000 rpm, the noncavitating flow in the pumps matches a similarity law.

Figures 4(*a*) and 4(*b*) show the evolutions of the torque and the efficiency according to the flow rate coefficient for a rotation speed equal to 3000 rpm. Note that the efficiency of the whole pump including the volute is considered here. The variation in χ as a function of the dimensionless rotation speed ω/ω_n at nominal flow rate is given in Fig. 4(*c*). It can be observed that for rotation speeds higher than 1200 rpm ($\omega/\omega_n=0.4$), a nice similarity is obtained, while for small rotation speeds, the torque increases significantly. This poor similarity at low speed is confirmed in Fig. 4(*d*), which shows the evolution of the amplitude of radial vibrations on the pump casing according to the flow coefficient for three rotation speeds.

3.2 Cavitating Behavior. The effects of cavitation on the pump performance have been studied first in steady-flow conditions: The head drop charts have been obtained at several rotation speeds and several values of the flow coefficient by progressively decreasing the pressure in the tank. Only rotation speeds of 2500 rpm and 3000 rpm have been investigated, so that at least 20% pressure drop can be obtained. A close agreement between dimensionless charts obtained at both speeds at nominal flow rate is obtained in Fig. 5. It shows that similarity laws can be extended to cavitating behavior at such speeds.

Figure 6 displays the cavitating behavior of the pump at 3000 rpm for several flow rates. Although the pump geometry leads to a quite small value of $\omega_s=0.24$, the decrease in the pump elevation is progressive at all flow rates. Figure 7 shows the evolution of the values of τ corresponding to 3%, 10%, and 20% head drop according to the flow rate. Nearly identical slopes are obtained for the three curves, which demonstrates a similar pump behavior at all flow rates.

Figure 8 shows the decrease in the pump head according to the flow rate for constant values of the cavitation number τ. The curve corresponding to noncavitating flow conditions is also drawn in order to visualize the head drop due to cavitation. It can be observed that the head drop increases with the flow rate. It suggests that cavitation occurs also on the pressure side of the blades when the flow rate is increased over the nominal value $\delta_n=0.021$. This pressure side cavity leads to a local inversion of the pressure difference on both sides of the blades, which progressively dete-

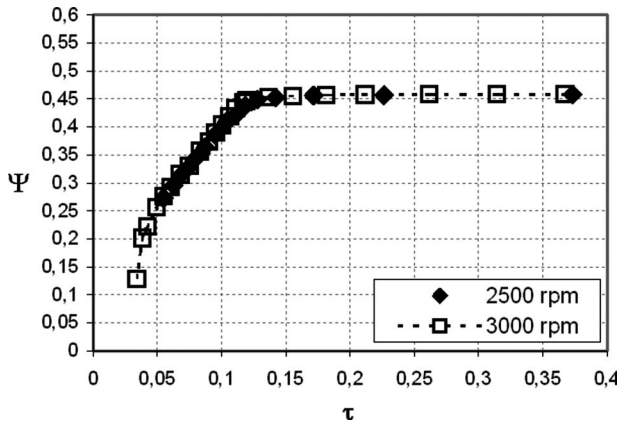

Fig. 5 Head drop charts at 2500 rpm and 3000 rpm at nominal flow rate ($\Delta\Psi/\Psi=0.5\%$ and $\Delta\tau/\tau=0.5\%$)

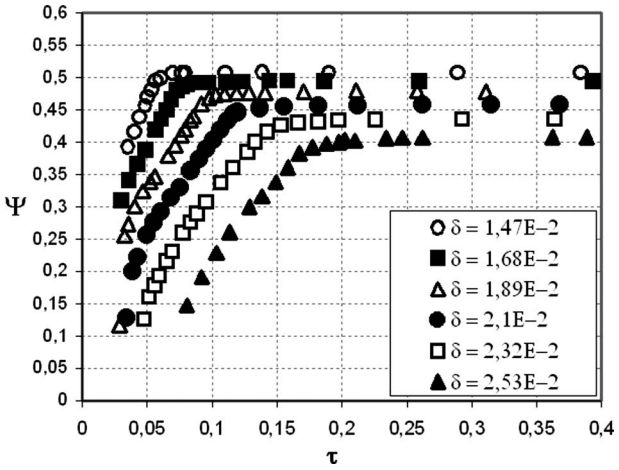

Fig. 6 Head drop charts for six inlet flow rates at 3000 rpm ($\Delta\Psi/\Psi=0.5\%$, $\Delta\tau/\tau=0.5\%$, and $\Delta\delta/\delta=4\%$)

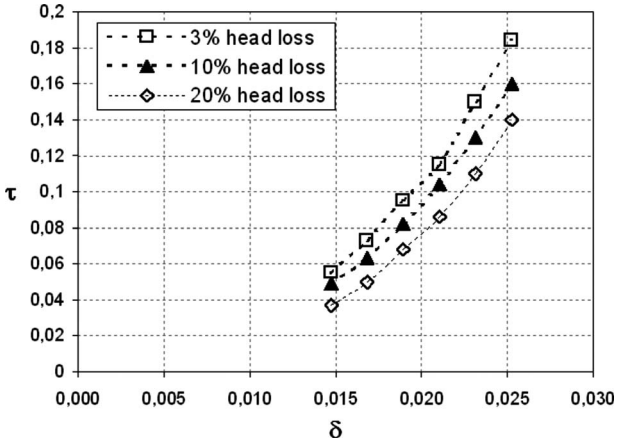

Fig. 7 Evolution of τ according to δ for 3%, 10%, and 20% head drop (3000 rpm) ($\Delta\tau/\tau=0.5\%$ and $\Delta\delta/\delta=4\%$)

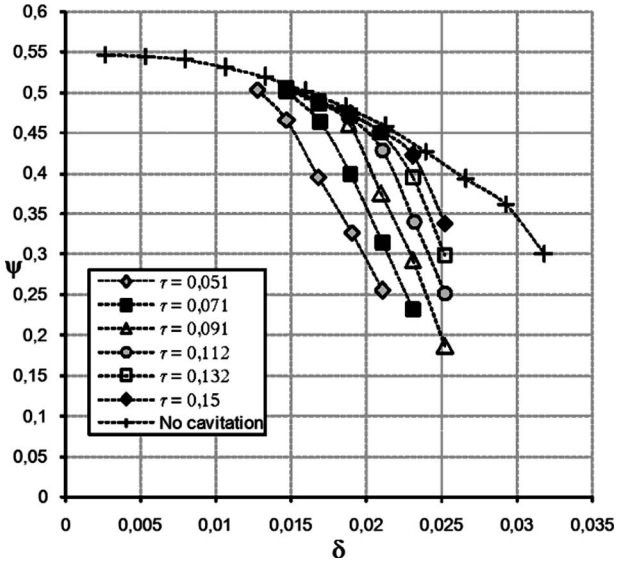

Fig. 8 Evolution of the head drop according to δ at constant value of τ ($\Delta\Psi/\Psi=0.5$, $\Delta\delta/\delta=4\%$, and $\Delta\tau/\tau=0.5\%$)

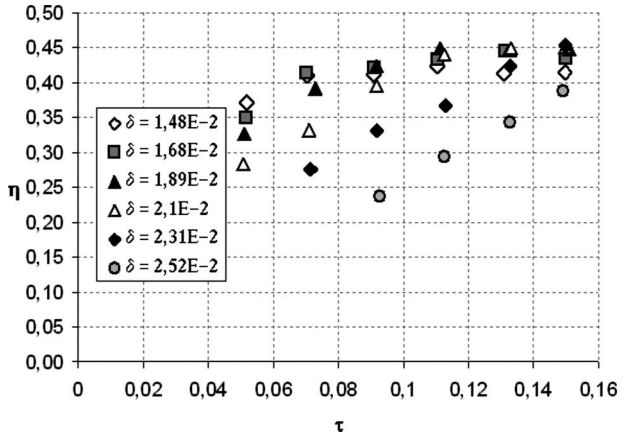

Fig. 9 Evolution of the efficiency according to τ for six values of the inlet flow rate coefficient (3000 rpm) ($\Delta\eta/\eta$=9.5% and $\Delta\tau/\tau$=0.5%)

riorates the pump elevation. However, Fig. 9 shows that the efficiency also decreases at high flow rate coefficient, which indicates that the pressure side cavity leads to a significant obstruction of the flow in the blade to blade channels. It induces also a progressive decrease in the flow coefficient corresponding to the optimal efficiency.

4 Fast Startups

Transient behaviors have been also investigated by performing fast startups of the pump at several flow rates in noncavitating and cavitating conditions.

4.1 Noncavitating Conditions. The high-frequency signals resulting from a fast startup performed at nominal flow rate are displayed in Figs. 10–12. The time evolutions of the pressure at suction (P_s) and delivery (P_d) are drawn in Fig. 10, together with the differential pressure developed by the pump ($P_d - P_s$). The startup itself corresponds to the first 0.45 s, while the second part of the signals is related to steady-flow conditions that are obtained at the end of the starting period. This is confirmed by Fig. 11, which shows the evolution of the rotation speed as a function of time. The pressure decrease in the pump suction pipe (see Fig. 10) is related to the effects of the fluid inertia in the suction pipe, according to the following relation:

$$P_s = P_{\text{tank}} - K_2^* \, \partial Q/\partial t - \xi$$

where P_{tank} is the pressure at the outlet of the upstream tank, and ξ is the pressure drop due to the unsteady head losses. It can be checked in Fig. 10 than the lowest value of P_s is obtained for the highest value of $\partial Q/\partial t$.

The torque evolution is shown in Fig. 12. Periodical fluctuations at a frequency of 50 Hz of the pump rotation are obtained in steady-flow conditions. The hydraulic torque is given hereafter [1] as

$$C = \int\int \rho r c_u c_r dS + I_{\text{fluid}} \frac{\partial}{\partial t}(\omega) - \left(\rho \int_{r1}^{r2} \frac{r}{\tan \beta} dr \right) \frac{\partial}{\partial t} Q \quad (1)$$

The first term on the right hand side is identical to the one obtained in steady-flow conditions: It corresponds to the increase in the moment of momentum in the pump. Conversely, terms 2 and 3 are due to the unsteady flow evolution: Term 2 is related to the inertial moment of the fluid (I_{fluid}) when the impeller is accelerated, while term 3 is due to the flow rate variations in the pump.

To investigate the peak that occurs at the end of the startup, the shaft inertia must be taken into account, as shown in the expression

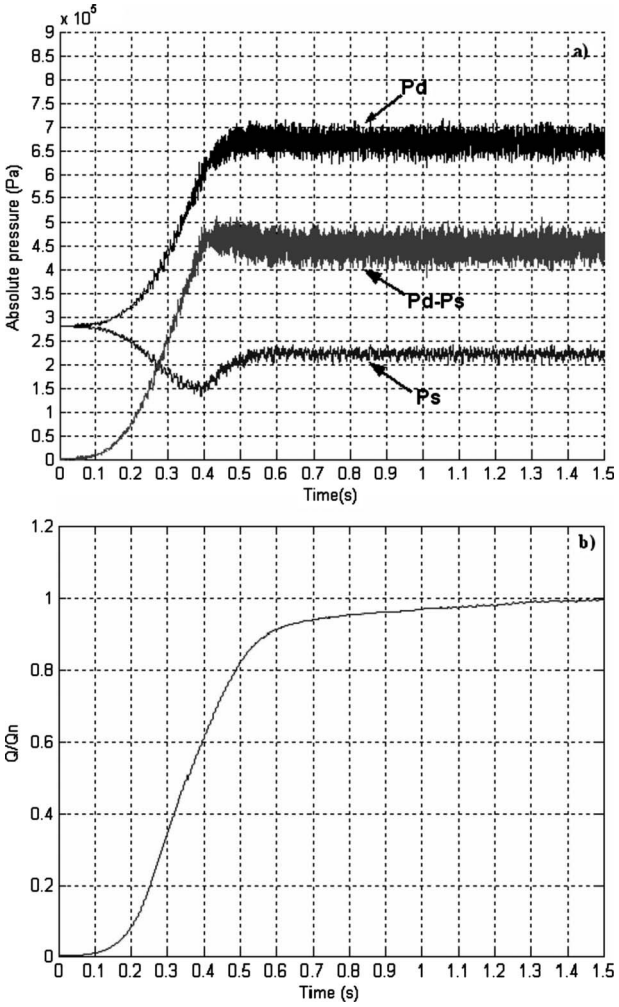

Fig. 10 (*a*) Evolution of the pump head, and the inlet and outlet pressures; (*b*) inlet flow rate evolution in the suction pipe ($Q_f = Q_n$, ω_f=3000 rpm, no cavitation)

$$C = \int\int \rho r c_u c_r dS + (I_{\text{fluid}} + I_p) \frac{\partial}{\partial t}(\omega) - \left(\rho \int_{r1}^{r2} \frac{r}{\tan \beta} dr \right) \frac{\partial}{\partial t} Q \quad (2)$$

This equation is solved numerically on the basis of the evolutions of ω and Q measured in the experiment. The comparison between the numerical result and the torque measured during the startup is

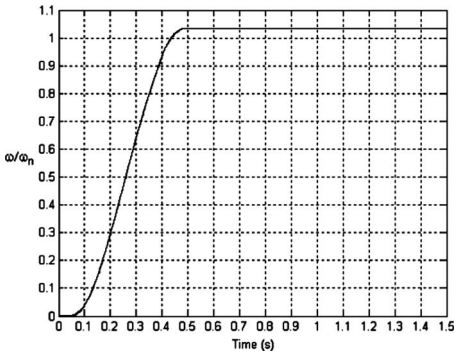

Fig. 11 Evolution of the rotation speed ($Q_f = Q_n$, ω_f=3000 rpm, no cavitation)

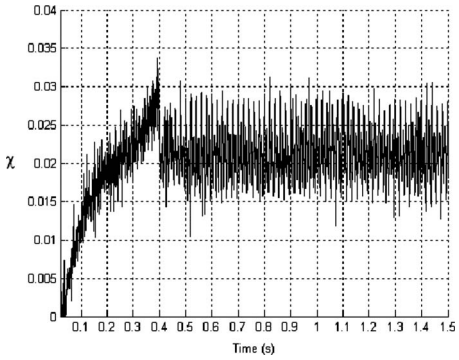

Fig. 12 Evolution of the dimensionless torque ($Q_f = Q_n$, $\omega_f = 3000$ rpm, no cavitation)

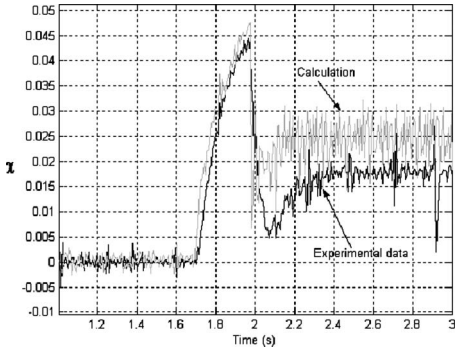

Fig. 13 Comparison between the measured and calculated dimensionless torques ($Q_f = Q_n$ and $\omega_f = 2000$ rpm)

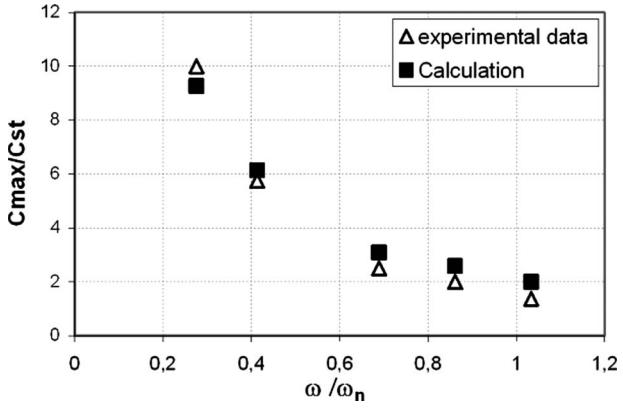

Fig. 14 Comparison between the measured and calculated values of C_{max}/C_{st} ($Q_f = Q_n$)

displayed in Fig. 13.

Although some discrepancies can be observed concerning the prediction of the steady-flow torque magnitude, a reliable agreement is obtained regarding the peak amplitude and shape.

Since the torque peak occurs for high values of $d\omega/dt$ (see Figs. 10 and 11), it is expected that the ratio C_{max}/C_{st} (where C_{max} denotes the maximum torque value and C_{st} is the torque value in steady-flow conditions) depends mainly on the fluid and solid inertia. I_p is estimated to be much higher than I_{fluid}, so C_{max}/C_{st} may be close to the following expression:

$$\frac{C_{max}}{C_{st}} \approx \frac{C_{st} + I_p \frac{\partial \omega}{\partial t}}{C_{st}} = 1 + \frac{I_p \frac{\partial \omega}{\partial t}}{C_{st}} \quad (3)$$

This expression is calculated numerically and compared with the experimental values of C_{max}/C_{st} for several rotation speeds at nominal flow rate (Fig. 14).

A close agreement between the experimental data and the calculated values is obtained for all rotation speeds. It confirms than the shaft inertia is mainly responsible for the torque peak observed at the end of the fast startups.

4.2 Cavitating Conditions. When the pressure in the tank is decreased so that cavitation is obtained during the transient or even in steady-flow conditions, three types of pressure signals displayed in Figs. 15, 17, and 18 are obtained. All data are obtained for a final rotation speed equal to 3000 rpm, since it was shown previously in Sec. 3.2 that behaviors at other rotation speeds could be derived from a single one by the similarity laws. The three different operating conditions including cavitation are given in Table 3.

Tests have been conducted for various values of flow rate and cavitation number. In most of the cases, pressure signals evolutions are similar to the one drawn in Fig. 15 (denoted as "case 2" hereafter). In comparison with noncavitating situations (see Fig. 10), the pressure at the pump suction, after the initial fall, remains completely stable during most of the startup ($0.25\ s < t$

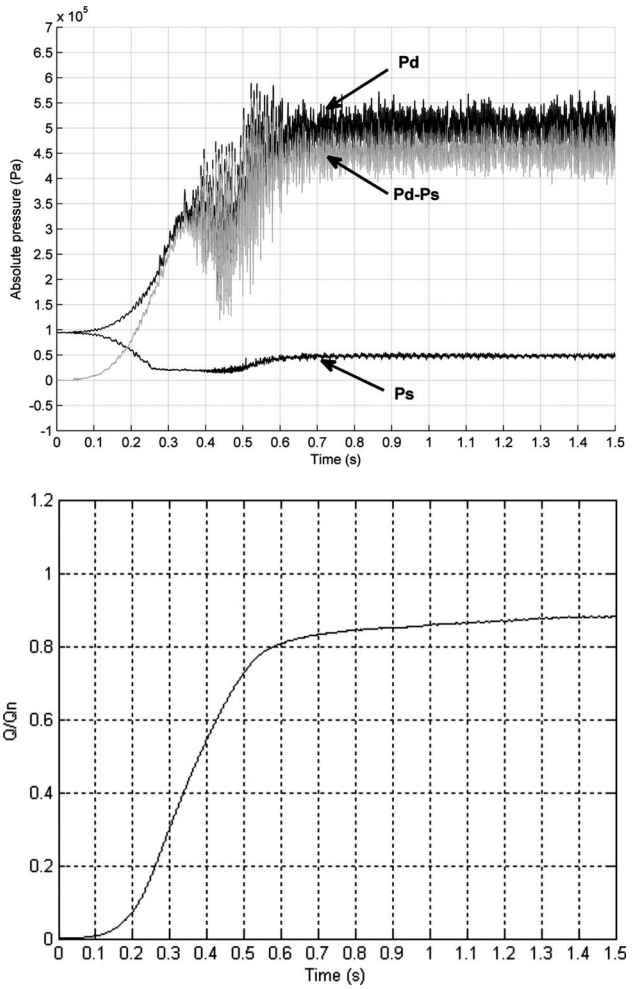

Fig. 15 Evolution of the pump head, inlet and outlet pressures, and inlet flow rate (case 2) ($\tau = 0.091$, $Q_f = 0.9 Q_n$, and $\omega_f = 3000$ rpm)

Table 3 Operating conditions in cavitation

ω_f (tr/min)	τ_f	Q_f/Q_n	Pressure evolution	Name
3000	0.091	0.9	Fig. 15	Case 2
3000	0.091	1.1	Fig. 17	Case 1
3000	0.111	0.7	Fig. 18	Case 3

<0.45 s). Its magnitude during this period is slightly higher than the vapor pressure. This behavior indicates that cavitation occurs in the pump inlet pipe and/or inside the pump. The pressure at the delivery is characterized by a significant drop at the end of the startup, which may be related to the temporary decrease in the pump head because of cavitation on the blades. The delivery signal also exhibits high-frequency fluctuations, whose maximum amplitude is about 50% of the pump head. This may be due to vapor collapse at the pump outlet.

These pressure fluctuations at the pump outlet can be associated with the drastic increase in the magnitude of the radial vibrations measured on the pump casing, in comparison with noncavitating conditions (Fig. 16). Note in Fig. 16(*b*) that the maximum amplitude of the vibrations ($0.4\ \text{s} < t < 0.5$ s) is correlated with the maximum pressure fluctuations at the pump outlet (Fig. 15).

For high flow rates (at least $1.1Q_n$) slightly different pressure signals are obtained (Fig. 17). Low frequency oscillations of the delivery pressure can be observed at the end and after the transient period. This particular behavior, denoted as "case 1" hereafter,

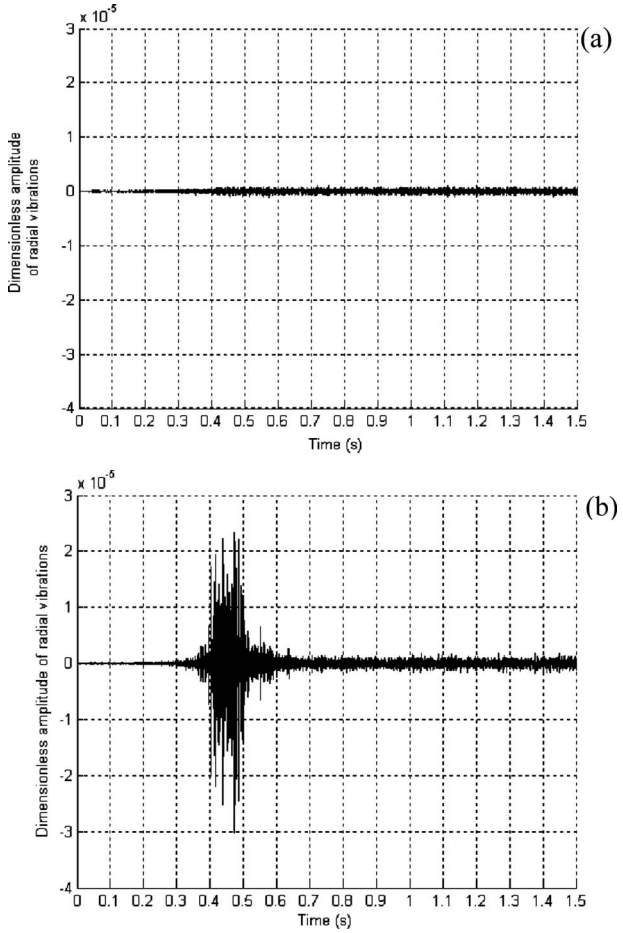

Fig. 16 Amplitude of the radial vibrations on the pump casing for ω_f=3000 rpm: (*a*) noncavitating conditions $Q_f=Q_n$; (*b*) τ =0.091 and $Q_f=0.9Q_n$

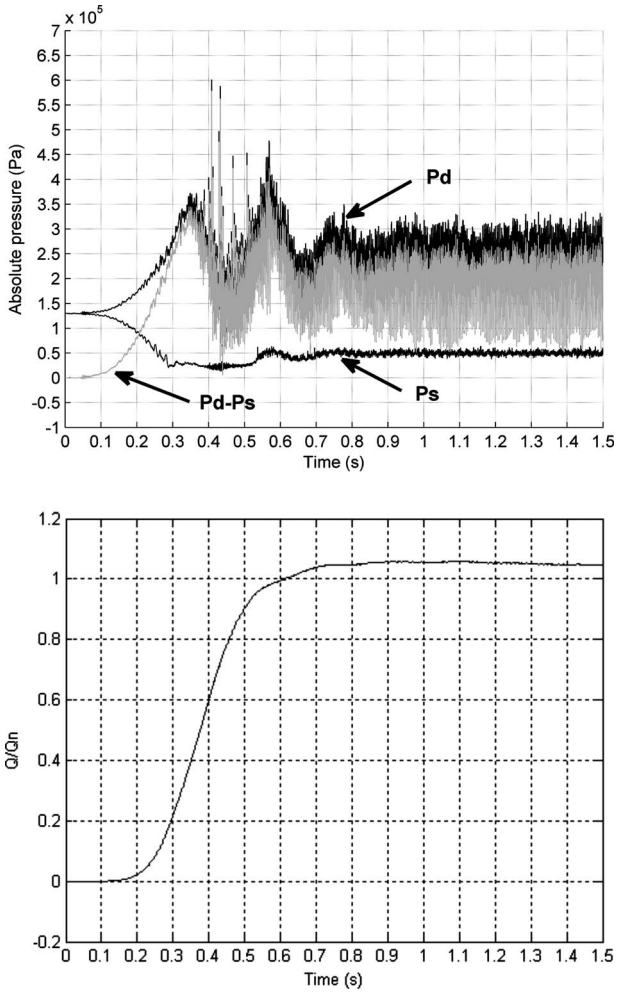

Fig. 17 Evolution of the pump head, inlet and outlet pressures, and inlet flow rate (case 1) (τ=0.091, Q_f=1.1Q_n, and ω_f =3000 rpm)

may be due to the obstruction generated by pressure side cavitation on the blades: Such blockage results in a significant decrease in the pump head, as can be seen in Fig. 8, in steady state situations. Low amplitude pressure oscillations can also be observed on the inlet pressure signal, which suggests that this phenomenon is related to a surge type instability that affects the whole pump.

A third typical pattern of the pressure signals is obtained for intermediate values of the cavitation number and lower flow rates. In such conditions of moderate cavitation, a pressure peak is obtained at the pump suction at the end of the transient (Fig. 18). Note that a peak of similar magnitude occurs also at the same time at the delivery, although it is not so visible because of high-frequency pressure fluctuations. Such simultaneous pressure jumps can be associated with the water hammer phenomenon, as it was previously stated by Tanaka and Tsukamoto [3]. These configurations will be denoted as "case 3" hereafter.

The torque fluctuations obtained in cases 1–3 are displayed in Fig. 19. As in noncavitating conditions, the dimensionless torque evolutions are characterized by a large peak that occurs at the end of the startup. This phenomenon is due, as clarified in Sec. 3.1, to the shaft inertia, so it is not related to cavitation. After this large peak, again, three different comportments of the torque can be observed before the stabilized value is reached: several low-frequency fluctuations (case 1), a progressive re-increase (case 2), or a behavior similar to the one obtained in noncavitating conditions (see Fig. 12), i.e., the stabilized value of the torque is

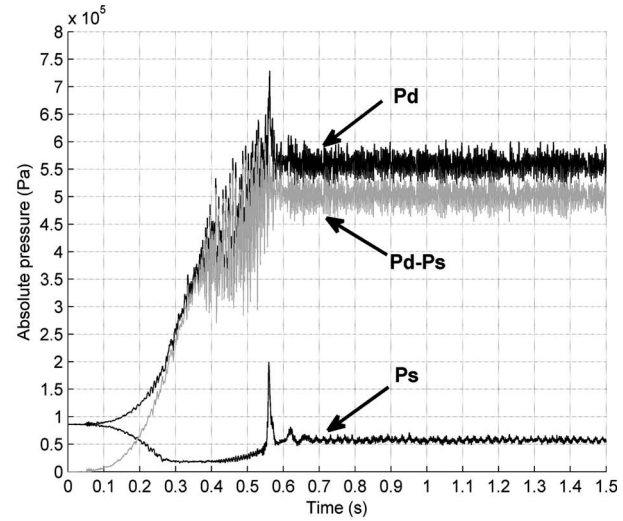

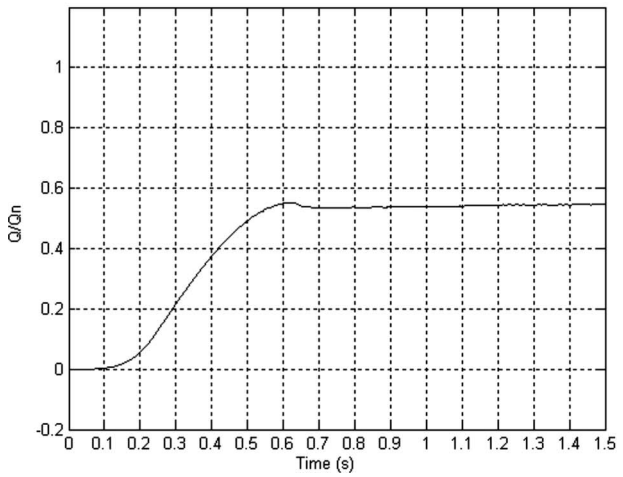

Fig. 18 Evolution of the pump head, inlet and outlet pressures, and inlet flow rate (case 3) (τ=0.111, Q_f=0.7Q_n, and ω_f =3000 rpm)

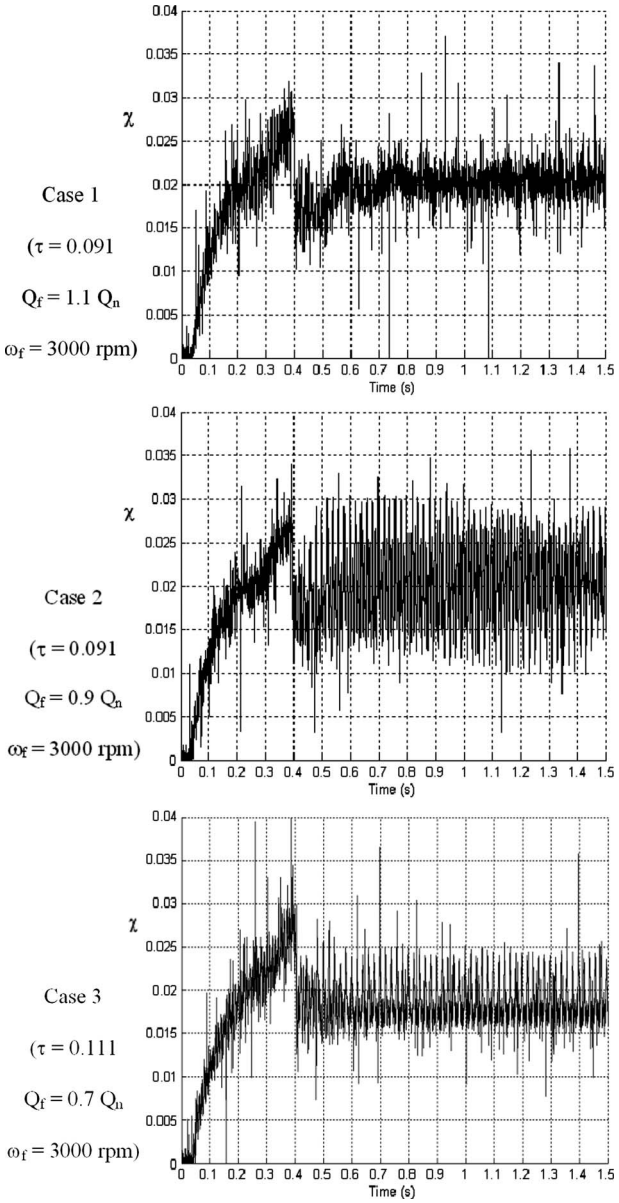

Fig. 19 Dimensionless torque evolutions in cavitating conditions

reached quasi-immediately after the large peak.

On the basis of the pressure and torque evolutions, the whole tests performed in cavitating conditions have been classified into these three different categories of transients, and the resulting map is drawn in Fig. 20. It confirms that large scale oscillations systematically occur at high flow rate and in conditions of developed cavitation, while water hammer phenomena are detected at lower flow rate and for a moderate development of cavitation. Such a classification has been proposed previously by Tanaka and Tsukamoto [3], whereas these authors investigated on a quite different range of τ and δ (Figs. 21(a) and 21(b)). Note that the parameter K used in ordinate is based on a characteristic time of the startup T_{na}, the final rotation speed N_f, and a flow rate coefficient ϕ_{nf}. $N_f \times T_{na}$ characterizes how fast the startup is, while ϕ_{nf} is related to the final flow rate in steady state conditions [3]. The present experiments are reported in the same diagram (Fig. 21(b)) in order to enable the comparison with the data reported in Ref. [3].

Tanaka and Tsukamoto also detected two types of cavitation behaviors, as follows:

(1) the first one, denoted as "no fluctuation," which exhibits only a drop of the delivery pressure at the end of the startup
(2) the second one, denoted as "oscillating cavitation," which

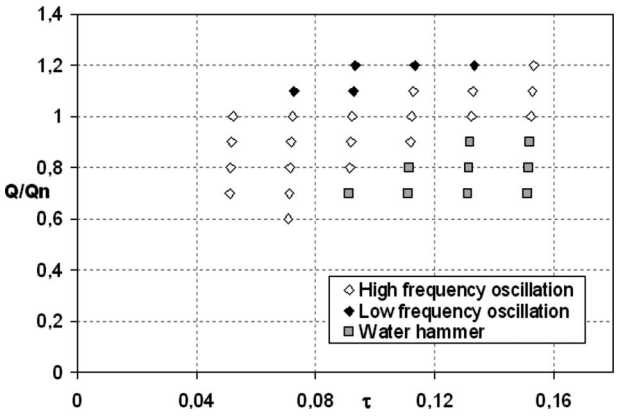

Fig. 20 Classification of the startups

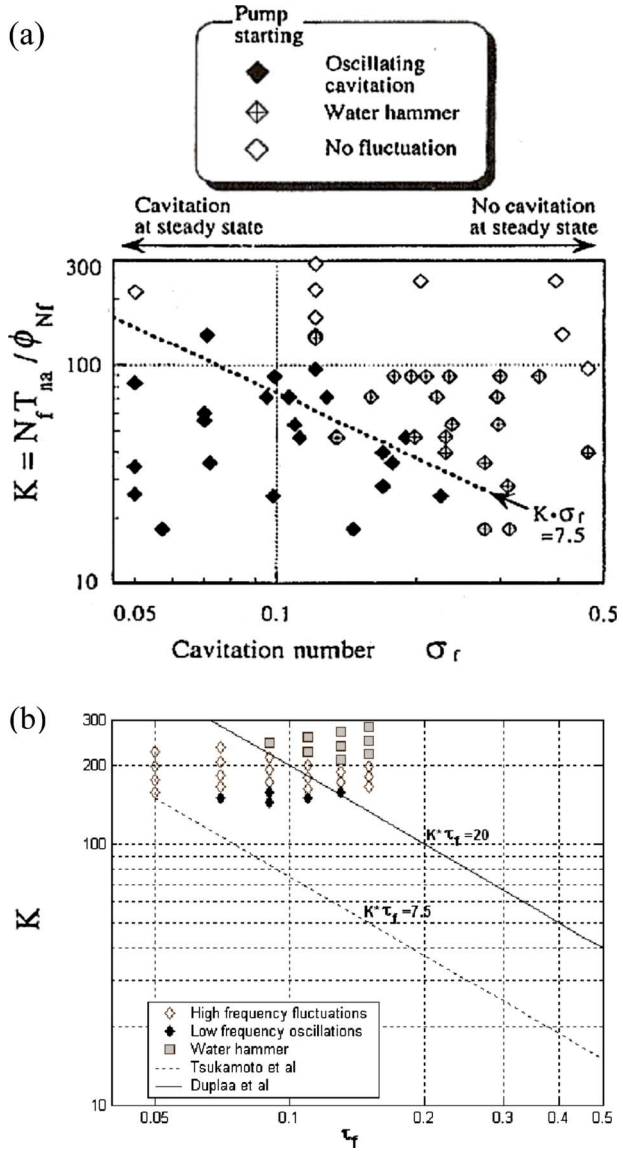

Fig. 21 Comparison between the present set of data and the previous results reported in Ref. [3]: (*a*) data from Tanaka and Tsukamoto; (*b*) present experiments

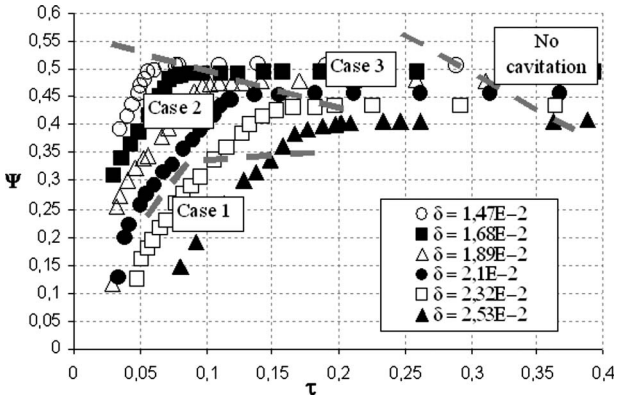

Fig. 22 Final operating points reported on the head drop curves

is obtained at large flow coefficient and low cavitation number; it involves low-frequency fluctuations both at the pump inlet and outlet

Note that in both situations, no high-frequency fluctuation is reported by the authors.

So, case 2 (Fig. 15) in the present experiments seems very close to the situation denoted as no fluctuation in Ref. [3], and case 1 (Fig. 17), which is obtained also at large flow rates and low cavitation numbers, is similar to the situation of oscillating cavitation reported in Ref. [3].

It can be observed (Fig. 21) that the present tests correspond to an area of the diagram that was not investigated by Tanaka and Tsukamoto. Moreover, the limit between the water hammer phenomena and situations of oscillations was defined by $K^*\tau=7.5$ in Ref. [3], while a significantly different value $K^*\tau=20$ is found in the present work. Such discrepancy may be related to the use of two different test rigs characterized by different pipe lengths, pipe diameters, and even pipe roughness.

To investigate the physical mechanisms involved in each type of fast startup, the final operating point corresponding to cases 1–3 is reported on the head drop curves presented in Fig. 6 (Fig. 22). It can be observed that the fast startups corresponding to case 1 ("low frequency oscillations") have their final operating point at the end of the drop, whereas the final operating points corresponding to case 3 ("water hammer") are located before the drop. The ones related to case 2 ("high-frequency fluctuations") are located between cases 1 and 3. It means that the final operating point in case 3 corresponds to low cavitating conditions, while developed cavitation is still present at the end of the startup in cases 1 and 2.

Figures 23–25 present the evolution of the cavitating number τ according to the flow rate coefficient δ for the three cases. The curves corresponding to 0%, 3%, 10%, and 20% of head drop are reported in order to visualize the evolution of the cavitating conditions during the fast startup. The rotation speed, acceleration, flow rate, and time derivate of the flow rate are also drawn in order to discuss the relative influence of the different unsteady terms on the evolution of τ and δ.

For each case, the minimum value of the cavitation number is reached simultaneously with the final rotation speed ($\delta=0.013$, for example, in Fig. 23). This point is related to the successive variations in the pressure in the pump suction pipe P_s, which is used in the definition of τ. Note that $P_s=P_{\text{tank}}-K^*(dQ/dt)-\xi$, where ξ is the regular pressure loss. During the first part of the pump startup, the flow rate increases significantly, so P_s decreases much below the pressure value in the tank. Once the final rotation speed is reached the flow rate variation dQ/dt decreases drastically, so the static inlet pressure P_s re-increases (see Fig. 15 between $t=0.5$ s and 0.6 s), which leads to a significant re-increase in the cavitation number. At the end of the fast startup (between $\delta=0.016$ and 0.019 for case 2), only the flow rates still slowly increases, while the rotation speed is constant. This leads to a progressive increase in the inlet total pressure, which has only minor influence on the cavitation number (see definition for τ).

The drop of the delivery pressure in case 2 (first drop in case 1) is correlated with the minimum value of the cavitation number, i.e., the end of the rotation speed increase. Indeed, this operating point may correspond to the most developed cavitating conditions as Fig. 26 shows it. Figures 26(*a*)–26(*d*) exhibit the cavitation development within the impeller at time $t=0.308$ s, 0.422 s, 0.520 s, and 0.728 s, respectively. The time corresponding to these different steps (Figs. 26(*a*)–26(*d*)) is indicated on the chart, showing the τ evolution in Fig. 26(*e*). From these figures it can be checked that the most developed cavitating conditions (Fig. 26(*b*)) corresponds to the minimum value of the cavitation number.

The further re-increase in the delivery pressure is mainly due to the simultaneous re-increase in the cavitation number, which leads to more moderate development of cavitation. In case 2, the nomi-

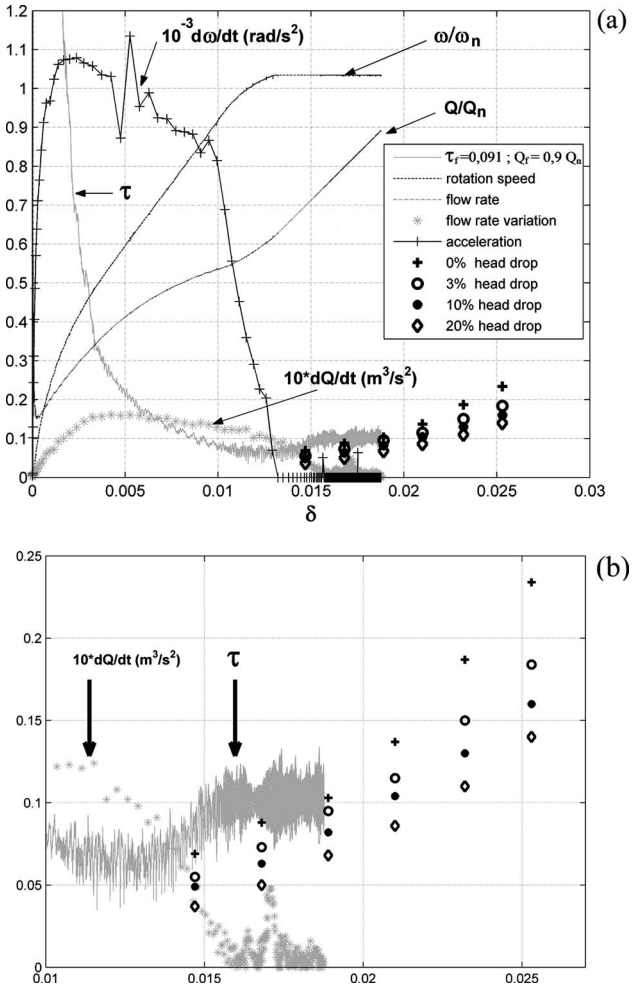

Fig. 23 Evolution of τ according to δ for case 2: (*a*) full scale; (*b*) zoom

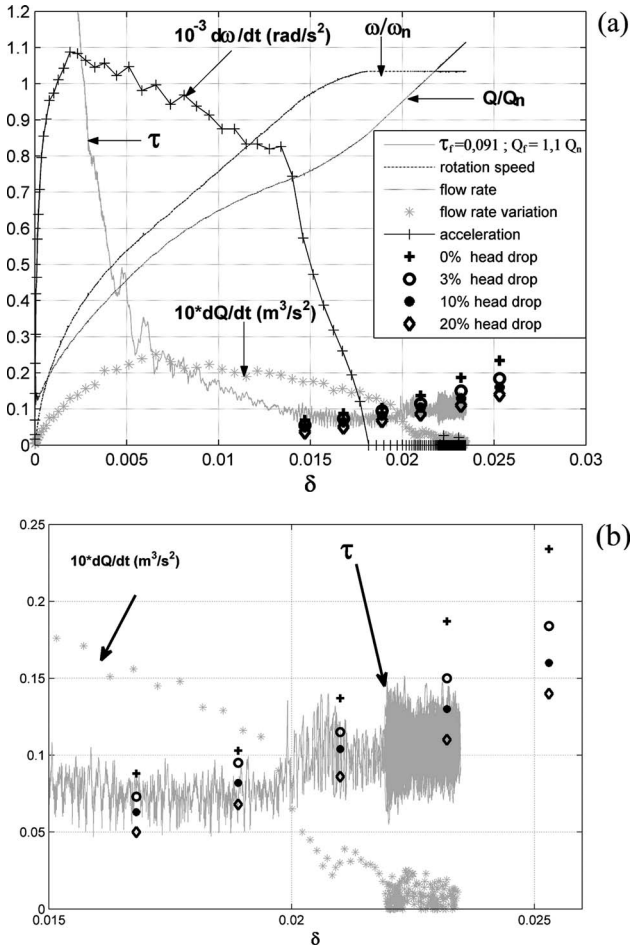

Fig. 24 Evolution of τ according to δ for case 1: (*a*) full scale; (*b*) zoom

nal pump head is progressively completely recovered: Indeed, it can be observed in Fig. 23 that the δ/τ characteristic reaches the 0% head drop curve, i.e., low cavitating conditions. Conversely, case 1 is more complex (Fig. 24): Lower cavitation conditions are first recovered (re-increase in the delivery pressure at $t=0.58$ s in Fig. 17) before a second drop occurs. This second drop is due to the high final flow rate imposed in case 1: As a result, the δ/τ characteristic crosses successively the 0%, 10%, and even 20% head drop charts (see Fig. 24). These oscillations of the delivery pressure may be associated with large fluctuations of the vapor volume in the pump and/or in the inlet pipe, which result in perturbations in the flow rate evolution: As can be seen in Fig. 24(*b*), the second drop of the delivery pressure is correlated with a slight re-increase in the dQ/dt term. The final diminution of this transient term leads to a last re-increase in the inlet pressure (between $t=0.65$ and 0.7 in Fig. 17), which probably slightly reduces the cavitation development, and thus, makes a slight re-increase in the delivery pressure before its final stabilization. These fluctuations of both inlet and delivery pressures may be interpreted as a transient surge instability due to cavitation.

In case 3 (Fig. 25), the final τ value is higher than the 0% head drop limit. This suggests that a sudden collapse of nearly all the vapor contained in the pump occurs at the end of the startup, which may be responsible for the pressure wave observed simultaneously in the inlet and delivery pressures. This water hammer type phenomenon is consistent with the interpretation proposed previously by Tanaka and Tsukamoto [2–4].

5 Conclusion

The behavior of a centrifugal pump has been studied in cavitating and noncavitating conditions. Both steady state flow situations and fast startups have been investigated. The effects of cavitation on the pump head at constant rotation speed have been characterized. Different types of unsteady behaviors have been obtained during the transients performed in cavitating conditions. At high flow rate, large scale low-frequency oscillations are obtained on the pressure signal at the delivery (case 1), whereas at a lower flow rate, only a drop at the end of the startup is detected (case 2). At moderate cavitation number and low flow rate, the water hammer phenomena are also observed.

These results are consistent with the previous data reported by Tanaka and Tsukamoto [3] with similar impeller geometry. Appropriate parameters are still to be determined to classify the different transient cavitating situations.

For cases 1–3, a physical analysis has been proposed to explain the evolution of the pump head during the startup. It has been shown that low final flow rates usually enable to reach at the end of the startup low cavitating conditions, whereas increasing the final flow rate results in more developed cavitating conditions, leading to progressive head drop of the pump. Conversely, low final flow rates result in the occurrence of the water hammer phenomena that may be related to the complete sudden collapse of the vapor in the pump and/or the inlet pipe. Supplementary global and local measurements are found to be necessary to improve the understanding of the pump transient cavitating behavior, and thus, to enrich the previous physical analysis. Therefore, local nonintrusive measurements inside the impeller will be performed by the

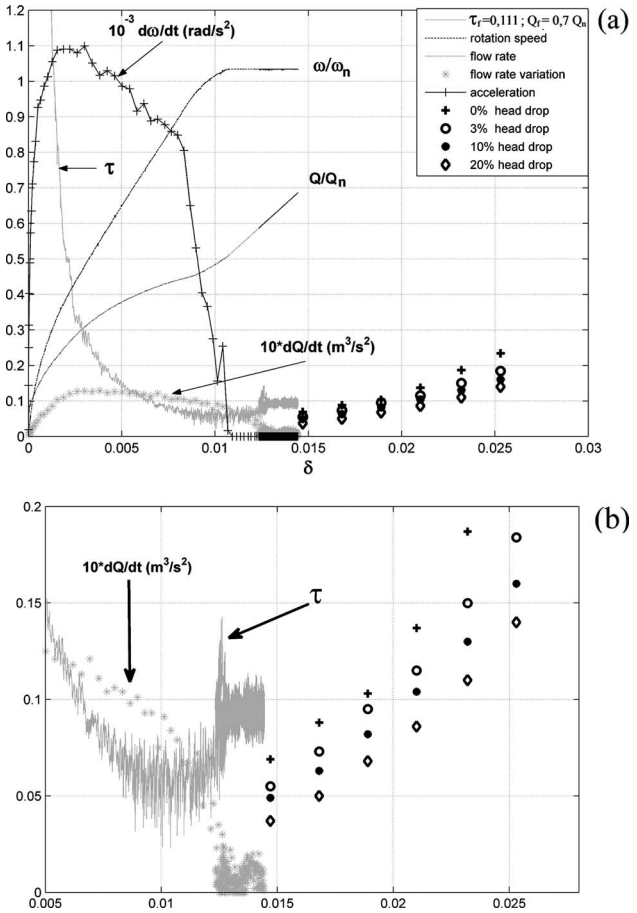

Fig. 25 Evolution of τ according to δ for case 3: (*a*) full scale; (*b*) zoom

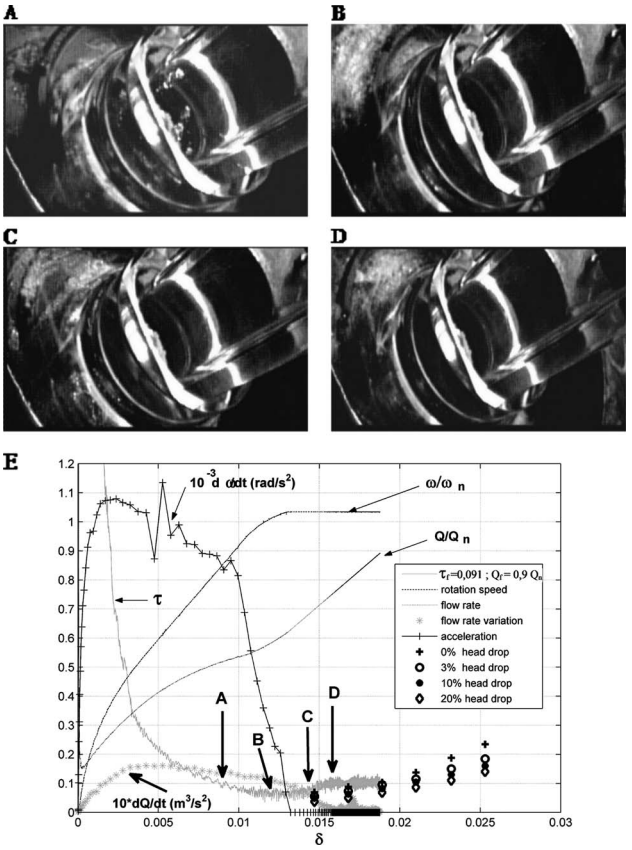

Fig. 26 Correlation between the impeller cavitation and τ evolution (case 2): (*a*) t=0.308 s; (*b*) t=0.422 s; (*c*) t=0.520 s; and (*d*) t=0.728 s

LML research team, in order to characterize more precisely the cavitation pattern obtained in the different cases detected presently.

Acknowledgment

The present work was performed in the scope of a research grant from the CNES (French Space Agency) and SNECMA Moteurs.

The authors wish to express their gratitude to SNECMA Moteurs and the CNES for their continuous support.

The authors also express their gratitude to the technical staff of the LML laboratory, especially J. Choquet and P. Olivier, who have been involved in the realization of the test facility.

Nomenclature

b = height of the blade to blade channels (m)
C_u = tangential component of the velocity (m/s)
C_r = radial component of the velocity, $=Q/(2\pi rb)$ (m/s)
C = torque (N m)
H = total head (m)
I_{fluid} = fluid inertia moment (kg m^2)
I_p = shaft inertia moment (kg m^2)
K = $\omega_f \times T_{na}/\Phi_{nf}$
P_s = static pressure in the pump suction pipe (Pa)
P_d = static pressure in the pump delivery pipe (Pa)
P_{vs} = vapor pressure (Pa)
Q = inlet volume flow rate (m^3/s)
r = impeller radius (m)
S = limit of the fluid volume in the channels (m^2)
t = time (s)
T_{na} = time to reach 63.2% of ω_f (s)
u = tip velocity, $=\omega \times r_2$ (m/s)
v = inlet pipe velocity (m/s)
β = relative flow angle
ΔP = pump static pressure rise (Pa)
χ = torque coefficient, $=C/\rho\omega^2 {r_2}^5$
δ = flow rate coefficient, $=Q/u_2 {r_2}^2$
ϕ = flow rate coefficient, $=Q/2\pi r_2 b_2 u_2$
Ψ = pressure coefficient, $=\Delta P/\rho {u_2}^2$
η = pump efficiency
ω = rotation speed (s^{-1})
ω_s = specific speed, $=\omega Q^{1/2}/(gH)^{3/4}$
τ = $=(P_s+(1/2)\rho v^2 - P_{\text{vs}})/((1/2)\rho {u_2}^2)$
ρ = density (kg/m^3)

Subscripts

f = final (steady part of the fast startup)
n = nominal
1 = impeller inlet
2 = impeller outlet
hyd = hydraulic
nf = noncavitating final condition
st = steady
tr = transient
max = maximum value

References

[1] Dazin, A., Caignaert, G., and Bois, G., 2007, "Experimental and Theoretical Analysis of a Centrifugal Pump During Fast Starting Period," ASME J. Fluids

Eng., **129**, pp. 1436–1444.
[2] Tanaka, T., and Tsukamoto, H., 1999, "Transient Behavior of a Cavitating Centrifugal Pump at Rapid Change in Operating Conditions—Part 1: Transient Phenomena at Opening/Closure of Discharge Valve," ASME J. Fluids Eng., **121**, pp. 841–849.
[3] Tanaka, T., and Tsukamoto, H., 1999, "Transient Behavior of a Cavitating Centrifugal Pump at Rapid Change in Operating Conditions—Part 2: Transient Phenomena at Pump Startup/Shutdown," ASME J. Fluids Eng., **121**, pp. 850–856.
[4] Tanaka, T., and Tsukamoto, H., 1999, "Transient Behavior of a Cavitating Centrifugal Pump at Rapid Change in Operating Conditions—Part 3: Classifications of Transient Phenomena," ASME J. Fluids Eng., **121**, pp. 857–865.
[5] Tsukamoto, H., Yoneda, H., and Sagara, K., 1995, "The Response of a Centrifugal Pump to Fluctuating Rotational Speed," ASME J. Fluids Eng., **117**, pp. 479–484.
[6] Picavet, A., and Barrand, J. P., 1996, "Fast Start-Up of a Centrifugal Pump—Experimental Study," *Proceedings of the Pump Congress*, Karlsruhe, Deutschland.
[7] Bolpaire, S., Barrand, J. P., and Caignaert, G., 2002, "Experimental Study of the Flow in the Suction Pipe of a Centrifugal Pump Impeller: Steady Conditions Compared With Fast Start-Up," Int. J. Rotating Mach., **8**(3), pp. 215–222.
[8] Lefebvre, P. J., and Barker, W. P., 1995, "Centrifugal Pump Performance During Transient Operation," ASME J. Fluids Eng., **117**, pp. 123–128.
[9] Ghelici, N., 1993, "Etude du Régime Transitoire de Démarrage Rapide d'une Pompe Centrifuge," Ph.D. thesis, Ecole Nationale Supérieure d'Arts et Métiers, Lille, France.
[10] Picavet, A., 1996, "Etude des Phénomènes Hydrauliques Transitoires lors du Démarrage Rapide d'une Pompe Centrifuge," Ph.D. thesis, Ecole Nationale Supérieure d'Arts et Métiers, Lille, France.
[11] Bolpaire, S., 2000, "Etude des Ecoulements Instationnaires dans une Pompe en Régime de Démarrage ou en Régime Etabli," Ph.D. thesis, Ecole Nationale Supérieure des Arts et Métiers, Lille, France.

Hidemasa Takana[1]
Senior Assistant Professor
Institute of Fluid Science,
Tohoku University,
2-1-1 Katahira,
Aoba-ku,
Sendai 980-8577, Japan
e-mail: takana@paris.ifs.tohoku.ac.jp

HongYang Li[2]
Department of Mechanical Systems and Design,
Graduate School of Engineering,
Tohoku University,
6-6 Aoba, Aramaki,
Aoba-ku,
Sendai 980-8579, Japan

Kazuhiro Ogawa
Associate Professor
Fracture and Reliability Research Institute,
Tohoku University,
6-6 Aoba, Aramaki,
Aoba-ku,
Sendai 980-8579, Japan

Tsunemoto Kuriyagawa
Professor
Department of Nanomechanics,
Graduate School of Engineering,
Tohoku University,
6-6 Aoba, Aramaki, Aoba-ku,
Sendai 980-8579, Japan

Hideya Nishiyama
Professor
Mem. ASME
Institute of Fluid Science,
Tohoku University,
2-1-1 Katahira, Aoba-ku,
Sendai 980-8577, Japan

Computational and Experimental Studies on Cavity Filling Process by Cold Gas Dynamic Spray

Time-dependent computational simulations on cavity filling process by cold gas dynamic spray and powder jet deposition process ranging from microscale to macroscale were carried out in order to give an insight for their advanced applications to joining, crack repair, and dental treatment. Shock wave appears in front of the substrate due to underexpansion of jet and in-flight particles interact with the shock wave before their impact. The relation between shock wave, cavity configuration, and particle in-flight behavior in supersonic jet has been discussed in detail. Based on numerical and experimental studies, it was found that when the shock wave covers up the cylindrical cavity, the cavity cannot be filled at all by deposited powders. Moreover, under the condition of shock wave appearing inside the cylindrical cavity, conical deposition was formed due to the secondary back flow jet along the cavity side wall. By adopting conical cavity, cavity can be filled completely resulting from the suppression of the secondary back flow jet along the cavity side wall. [DOI: 10.1115/1.4000802]

1 Introduction

Cold gas dynamic spray process (cold spray process) is a promising coating technology originally developed in the mid 1980s at the Institute of Theoretical and Applied Mechanics of the Siberian Branch of the Russian Academy of Science [1–3]. In the cold spray process, a wide variety of metal powders are deposited onto various substrate materials by accelerating particles through momentum transfer from supersonic gas flow [4,5]. The temperature of supersonic gas flow is always lower than the melting point of in-flight particle and then particles deposit and form the coating on a substrate in solid state. The adhesion of particles in a cold spray process occurs only when particles have large enough kinetic energy to cause their extensive plastic deformation and also the mechanochemical activation of the substrate upon impact. The previous experimental and numerical studies showed that the minimum particle impact velocity called "critical velocity" exists to create an adhesion with substrate [6]. If the particle impact velocity is below the critical velocity, the particles rebound and, as a consequence, surface abrasion occurs. Therefore, particle impact velocity is one of the key physical parameters in a cold spray process for the improvement of deposition efficiency. Because of attractive features that a cold spray process has such as low oxidation, dense coating, thick deposition, etc., cold spray process is now paid a special attention for many industrial applications. Furthermore, cold spray process has a potential to expand its application to the new joining method of structure materials or repairing of cracks by spraying on a cavity or cracks.

Recently, another room temperature and atmospheric coating process called "powder jet deposition" has been developed. It was reported that ceramics such as alumina or hydroxyapatite particles are deposited on glass and silicon substrates using powder jet deposition system [7,8]. In this powder jet deposition, particles ranging from several hundred nanometers to several microns are accelerated by room temperature high speed gas flow and make deposition on substrate upon high speed impact [7]. In this process, ceramics particles break up on the impact without deformation, which can be seen in the cold gas dynamic spray processes using metal powders. The deposition mechanism in this process still has not made clear yet. Since powder jet deposition success-

[1]Corresponding author.
[2]Present address: Mitsui Chemicals, Inc.

Contributed by the Fluids Engineering Division of ASME for publication in the JOURNAL OF FLUIDS ENGINEERING. Manuscript received December 16, 2008; final manuscript received November 16, 2009; published online February 4, 2010. Assoc. Editor: Neelesh A. Patankar. Paper presented at the 2008 ASME International Mechanical Engineering Congress & Exposition (IMECE2008), Boston, MA, October-November 6, 2008.

fully enables to form hydroxyapatite films on tooth substrate at the similar hardness to human enamel, advanced dental treatment with powder jet deposition has been highly anticipated [8].

In this study, time-dependent and realistic computational simulations on the entire cold gas dynamic spray process and powder jet deposition process were carried out by the integrated model [9–12] of flow considering shock wave, splat formation, and deposition process. First, in-flight nano-microparticle behavior in the supersonic jet impinging on a substrate with a cavity and also the interaction between a particle and shock wave were investigated in detail. Then, the influence of cavity shape on a cavity filling process was clarified both numerically and experimentally. The objective of this study is to provide a fundamental data for a high performance advanced applications of powder jet deposition process in microscale and cold gas dynamic spray process in macroscale.

2 Numerical Modeling

In order to derive the governing equations, the following assumptions are introduced.

(1) The flow is compressible and turbulent.
(2) The flow field is axisymmetric.
(3) Due to the small powder size with sufficiently large specific surface area, in-flight particles have the same temperature with gas flow.
(4) In-flight particles are without aggregation due to the sudden particle acceleration and deceleration in supersonic flow during a short residence time.
(5) In the experiments, the typical volume fraction of particles are from 8×10^{-5} to 2×10^{-4} and the influence of the particle phase on the flow must be considered. However, it is assumed that there is one-way coupling between the dispersed phase and the carrier phase for simplicity. Collision between particles is also neglected

2.1 Modeling of Particle-Laden Flow. Under the above assumptions, the governing equations for flow field are described as follows.

Continuity equation

$$\frac{\partial\rho}{\partial t}+\nabla\cdot(\rho\boldsymbol{u})=0 \tag{1}$$

Momentum equation

$$\frac{\partial(\rho\boldsymbol{u})}{\partial t}+\nabla\cdot(\rho\boldsymbol{u}\boldsymbol{u})=-\nabla p+\nabla\cdot\bar{\bar{\tau}} \tag{2}$$

Energy equation

$$\frac{\partial e}{\partial t}+\nabla\cdot[(e+p)\boldsymbol{u}]=\nabla\cdot(\lambda_f\nabla T)+\Phi_D \tag{3}$$

Equation of state

$$p=\rho RT \tag{4}$$

In this study, large eddy simulation of compressible flow [13] is carried out in order to capture the unsteady turbulent behavior during the cold gas dynamic spray and powder jet deposition process. Based on the Lagrangian approach, the particle trajectories are calculated by solving the equation of motion for the particles. To predict the in-flight behavior of nano- or microscale particle in an unsteady flow precisely, the present study applies the following particle equation of motion [14] including terms of viscous drag force, flow acceleration, added mass, Saffman lift force [15,16], and Brownian motion [17].

$$m_p\frac{d\boldsymbol{u}_p}{dt}=\boldsymbol{F}_{\text{drag}}+\boldsymbol{F}_{\text{acc}}+\boldsymbol{F}_{\text{mass}}+\boldsymbol{F}_{\text{lift}}+\boldsymbol{F}_{\text{brown}} \tag{5}$$

$$\frac{d\boldsymbol{x}_p}{dt}=\boldsymbol{u}_p \tag{6}$$

The viscous drag force is described as follows.

$$\boldsymbol{F}_{\text{drag}}=\frac{\pi}{8}d_p^2\rho C_D(\boldsymbol{u}-\boldsymbol{u}_p)|\boldsymbol{u}-\boldsymbol{u}_p| \tag{7}$$

where C_D is the drag coefficient. In this study, the drag coefficient of sphere particle considering compressible effect and Knudsen effect is adapted [18]. This representation of drag coefficient is accurate over the wide range and flow regime including continuum, slip, transition, and molecular flow at particle Mach number up to 6. The correlating equations for C_D consists of three equations; the equation represents all of the subsonic flow regimes, the equation representing the supersonic flow regime at particle Mach numbers greater than 1.75, and the linear interpolation equation for the intervening region between particle Mach number of 1 and 1.75. The detail descriptions of correlating equations for C_D are given as follows:

For subsonic flow ($M_p<1$)

$$C_{D(\text{sub})}=24\left[\text{Re}_p+S\left\{4.33+\left(\frac{3.65-1.53\frac{T_p}{T}}{1+0.353\frac{T_p}{T}}\right)\times\exp\left(-0.247\frac{\text{Re}_p}{S}\right)\right\}\right]^{-1}+\exp\left(-\frac{0.5M_p}{\sqrt{\text{Re}_p}}\right)\times\left[\frac{4.5+0.38(0.33\,\text{Re}_p+0.48\sqrt{\text{Re}_p})}{1+0.33\,\text{Re}_p+0.48\sqrt{\text{Re}_p}}+0.1M_p^2+0.2M_p^8\right]+\left[1-\exp\left(-\frac{M_p}{\text{Re}_p}\right)\right]0.6S \tag{8}$$

where Re_p and M_p are particle Reynolds number and particle Mach number based on the relative velocity between particle and gas flow, respectively. Re_p and M_p are defined as

$$\text{Re}_p=\frac{\rho d_p}{\mu}|\boldsymbol{u}-\boldsymbol{u}_p| \tag{9}$$

$$M_p=\frac{|\boldsymbol{u}-\boldsymbol{u}_p|}{\sqrt{\gamma RT}} \tag{10}$$

S is the molecular speed ratio given by $S=\sqrt{\gamma/2}$.

For supersonic flow ($M_p\geq1.75$)

$$C_{D(\text{super})}=\frac{0.9+\frac{0.34}{M_p^2}+1.86\left(\frac{M_p}{\text{Re}_p}\right)^{1/2}\left[2+\frac{2}{S^2}+\frac{1.058}{S}\left(\frac{T_p}{T}\right)^{1/2}-\frac{1}{S^4}\right]}{1+1.86\left(\frac{M_p}{\text{Re}_p}\right)^{1/2}} \tag{11}$$

For supersonic flow ($1\leq M_p<1.75$):

$$C_D(M_p,\text{Re}_p)=C_{D(\text{sub})}(1.0,\text{Re}_p)+\frac{4}{3}(M_p-1.0)[C_{D(\text{super})}(1.75,\text{Re}_p)-C_{D(\text{sub})}(1.0,\text{Re}_p)] \tag{12}$$

where $C_{D(\text{sub})}(1.0,\text{Re}_p)$ represents the coefficient calculated using Eq. (8) with $M_p=1.0$, and $C_{D(\text{super})}(1.75,\text{Re}_p)$ represents the coefficient obtained using Eq. (11) with $M_p=1.75$. The effect of temperature difference between particle and gas is considered in Eqs.

(8) and (11); however, in this simulation the temperatures of particle and flow are assumed to be the same throughout the calculation.

Other forces acting on a particle such as flow acceleration, added mass, Saffman lift force, and Brownian motion are well described in Ref. [14].

2.2 Modeling of Splat and Coating Formation for Cold Gas Dynamic Spray. The modeling of particle adhesion and deformation upon impact for cold gas dynamic spray is discussed by following models developed by Kurochkin et al. [19], Papyrin et al. [4], and Alkhimov et al. [20]. In a cold spray process, the adhesion of particle occurs when the particle adhesion energy is larger than the elastic energy at particle impact on cavity bottom. The particle adhesion and elastic energy normalized by the maximum adhesion energy $(E_{\mathrm{ad}})_{\max}$ can be expressed as follows [4].

Normalized adhesion energy

$$E_{\mathrm{ad}}^{*} = 1 - \exp\left\{ - \nu t_c \exp\left(- \frac{E_a}{kT_c} \right) \right\} \tag{13}$$

Normalized elastic energy

$$E_{\mathrm{el}}^{*} = (1 - V_m) \frac{p_d^2}{E^{*}} V_p \frac{3}{2} \left(\frac{\rho_p v_p^2}{p_d} \right)^{3/4} \frac{1}{(E_{\mathrm{ad}})_{\max}} \tag{14}$$

where

$$(E_{\mathrm{ad}})_{\max} \approx \frac{\pi d_p^2 N_{\sigma 0} E_1}{3(1 - \epsilon_p)} \tag{15}$$

The ν in Eq. (13) is the natural frequency of atoms in lattice and the value of $\nu = 1 \times 10^{13}$ Hz is the characteristic value of this parameter independent of material [4,21]. The t_c in Eq. (13) is the contact time of particle upon impact and given by $t_c = 2\epsilon_p d_p / v_p$ [4]. In this study, the activation energy E_a was decided from the previous experimental result of adhesion probability [22]. The contact temperature T_c can be formulated from the energy conservation before and after the impact. Using the ratio of kinetic energy consumed for particle heating η ($\eta = 0.75$), T_c can be given by the following relations. The rest of the particle kinetic energy is spent on thermal conduction into the substrate.

$$T_c = \begin{cases} T_p + \dfrac{\eta}{2c_p} \dfrac{v_p^2}{V_z} & (T_c < T_m) \\ T_m & \\ T_p + \left(\dfrac{\eta}{2c_p} \dfrac{v_p^2}{V_z} - \dfrac{H_m}{c_p} \right) & (T_c > T_m) \end{cases} \tag{16}$$

where V_z is the specific particle heating volume due to thermal conduction during the contact time [4] and given as

$$V_z = 1 - \left(1 - \frac{\sqrt{\lambda_p t_c}}{h_p} \right)^2 \tag{17}$$

V_m appeared in Eq. (14) represents the specific melting volume in a particle and can be estimated from the following equations.

$$V_m = \begin{cases} 0 & (T_c < T_m) \\ \dfrac{1}{H_m} \left[\eta \dfrac{v_p^2}{2} - c_p (T_m - T_p) V_z \right] & (T_c = T_m) \\ V_z & (T_c > T_m) \end{cases} \tag{18}$$

The physical properties used in the Eqs. (13)–(18) are summarized in Table 1.

In case of aluminum particle impacting on steel substrate, the configuration of splat, which attached particle forms can be approximated by parabolic profile as shown in Fig. 1. Then, by using the splat height h_p and splat diameter D_s, the splat profiles can be described as

Table 1 Physical properties (aluminum and steel pair)

Activation energy, E_a	1.40×10^{-19} J
Stress at the rebounding moment, p_d	60 MPa
Elasticity modulus, E^{*}	57 GPa
Maximum number of bonds per unit area, $N_{\sigma 0}$	12×10^{18} m^{-2}
Bonding energy between atoms, E_1	0.6×10^{-18} J
Energy conversion ratio, η	0.75
Melting point of Al, T_m	934 K
Latent heat of melting of Al, H_m	3.88×10^5 J/kg
Specific heat of Al, c_p	900 J/(kg K)
Density of Al, ρ_p	2.7 g/cm^3

$$h = - \frac{4h_p}{D_s^2} r^2 + h_p \tag{19}$$

Assuming the constant particle volume before and after splat formation, splat diameter is given by

$$D_s = \sqrt{\frac{4d_p^3}{3h_p}} \tag{20}$$

From the relation of strain induced by particle impact $\epsilon_p = 1 - h_p / d_p$, splat height is obtained as follows.

$$h_p = (1 - \epsilon_p) d_p \tag{21}$$

From the previous experiment of high speed aluminum particle impact at 400–1200 m/s, ϵ_p is formulated as [4]

$$\epsilon_p = \exp\left(- 1.4 \frac{H_p}{\rho_p v_p^2} \right) \tag{22}$$

H_p in the above equation is the dynamic hardness and $H_p = 560$ MPa.

In this above described splat formation model, particle adhesion, and elastic energy, splat profiles are all given as a function of particle impact velocity and diameter. In this computation, the adhesion energy and elastic energy are estimated form the calculated particle velocity just before the impact. When the adhesion energy is over the elastic energy, the splat profile is computed. Then, the coating is formed by adding up each splat profile [9,10] obtained from Eq. (19).

2.3 Computational Domain and Conditions. Figures 2 and 3 show the schematic illustrations of powder jet deposition model for advanced dental treatment and cold gas spray model, respectively.

As shown in Fig. 2, the inner diameter of nozzle for dental treatment is 1.0 mm and nozzle-substrate distance is 1.7 mm. The configuration of installed cavity in the substrate is 1.0 mm in diameter and 0.5 mm in depth. The working gas is nitrogen with hydroxyapatite particle. The density of hydroxyapatite particle is 3.16 g/cm^3. The particles are injected in the axial direction at $z = 5$ mm. The computational conditions for the powder jet deposition process are given in Table 2. These conditions are taken from the experimental conditions.

The configuration of the supersonic nozzle for cold spray as

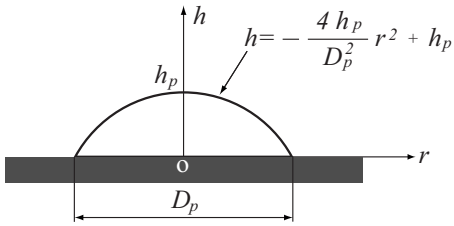

Fig. 1 Splat profile of aluminum particle impinging on a steel substrate

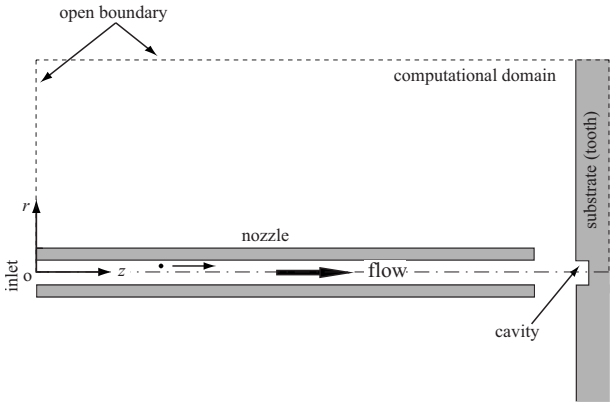

Fig. 2 Schematic Illustration of powder jet deposition system for advanced dental treatment: nozzle inner diameter is 1.0 mm and nozzle-substrate distance is 1.7 mm

shown in Fig. 3 is taken from the actual cold spray system (Dymet) manufactured in Russia. The separation distance between nozzle exit and substrate is 10 mm and particles are injected radially from the wall at $z=20$ mm. The particle and substrate materials are aluminum and steel, respectively. The computational conditions for the cold spray process taken from the experimental conditions are given in Table 3. Air is used as a working gas. The numerical study was conducted for cylindrical, spherical or conical shape cavities installed in the substrate. The center of nozzle and cavity are arranged on the same axis.

The initial conditions for a computation are pressure of 0.1 MPa and temperature of 300 K without flow. The structured rectangular grid is adopted and the number of grid points in z and r directions is 292 and 101 for cold spray computation and 180 and 99 for powder jet deposition computation, respectively. The computational grid is fine enough to capture both flow structure and particle trajectories. For coating simulation, grid points with the grid size of 5 μm are adopted on the surface of substrate to detect the particle impact location. The boundary conditions for thermofluid field are summarized below.

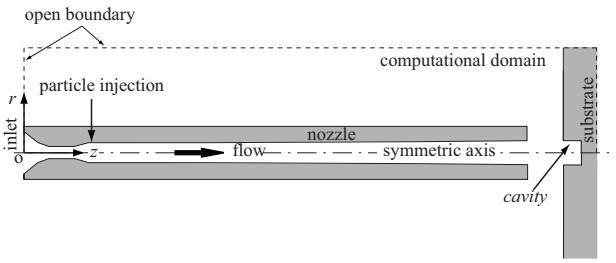

Fig. 3 Schematic illustration of cold gas dynamic spray system: nozzle inner diameters are 8.5 mm at the inlet, 2.5 mm at the throat, and 4.8 mm at the exit; nozzle-substrate distance is 10.0 mm

Table 2 Computational conditions for a powder jet deposition process

Working gas	Nitrogen
Mass flow rate	6.7×10^{-4} kg/s, 7.2×10^{-4} kg/s
Inlet cross-sectional area	7.9×10^{-7} m^2
Inlet stagnation temperature	300 K
Inlet stagnation pressure	0.35, 0.40 MPa
Ambient gas pressure	0.101 MPa
Ambient gas temperature	300 K
Particle material	Hydroxyapatite
Substrate material	Glass

Table 3 Computational conditions for a cold gas dynamic spray process

Working gas	Air
Mass flow rate	4.1×10^{-3} kg/s, 4.9×10^{-3} kg/s
Inlet cross-sectional area	5.7×10^{-5} m^2
Inlet stagnation temperature	600 K
Inlet stagnation pressure	0.52, 0.60 MPa
Ambient gas pressure	0.101 MPa
Ambient gas temperature	300 K
Particle material	Aluminum
Substrate material	Steel

$$\text{Inlet boundary:}\quad \rho=\frac{\dot{m}}{uA_{\text{in}}},\quad \frac{\gamma}{\gamma-1}\frac{pA_{\text{in}}}{\dot{m}}u+\frac{1}{2}u^2=\frac{\gamma}{\gamma-1}RT_0,$$

$$v=0,\quad \frac{\partial p}{\partial z}=0$$

$$\text{Symmetric axis:}\quad \frac{\partial \rho}{\partial r}=0,\quad \frac{\partial u}{\partial r}=0,\quad \frac{\partial p}{\partial r}=0$$

$$\text{Substrate and nozzle wall:}\quad \frac{\partial \rho}{\partial n}=0,\quad u=v=0,\quad \frac{\partial T}{\partial n}=0$$

$$\text{Open boundary:}\quad \frac{\partial \rho}{\partial n}=0,\quad \frac{\partial u}{\partial n}=\frac{\partial v}{\partial n}=0,\quad \frac{\partial T}{\partial n}=0$$

The finite volume discretization for the governing Eqs. (1)–(3) is carried out in a general curvilinear coordinate system. The numerical flux for convective term is evaluated with the third-order MUSCL type TVD scheme [23]. The second-order central difference scheme is used for spatial derivatives of viscous term. As for time integration, lower upper symmetric Gauss Seidel (LU-SGS) method [24] coupled with Crank–Nicholson method and Newtonian iterative method is used. The convergence criterion for Newtonian iteration is the residual error of 5×10^{-4}. The time-steps are chosen to be 1.82 ns for cold spray process and 9.23×10^{-2} ns for powder deposition process, respectively.

3 Experimental Measurement

Particle image velocimetry (PIV) was conducted for particulate microjet impacting on a flat glass substrate in powder jet deposition process. The operating pressure is 0.4 MPa and alumina particle with average size of 2 μm was used for PIV measurement. The laser sheet was formed by a Nd: YAG laser ($\lambda=532$ nm) light source through cylindrical lens. The time interval of laser pulses is 0.108 μs and the exposure time of high speed camera is 2.4 μm. The number of pixels and spatial resolution of this high speed camera are 1280×1024 pixel and 2.4 μm/pixel, respectively.

For the evaluation of numerical model, static pressure distribution in the nozzle and the stagnation temperature on the surface of substrate for cold gas dynamic spray are measured by piezoresistive pressure sensor and thermocouple embedded in the substrate, respectively.

4 Results and Discussion

4.1 Cavity Filling Process With Powder Jet Deposition in Microscale. Figure 4 shows the axial evolutions of the particle velocities for 800 nm and 2 μm particle, respectively. The inlet stagnation pressure is 0.35 MPa. In the figure, gas velocity at the particle location is also shown. Even in a nozzle-substrate distance of 1.7 mm, the gas flow is accelerated due to underexpansion and the shock wave is induced in front of the cavity. The particle deceleration through the shock wave is mainly by viscous drag

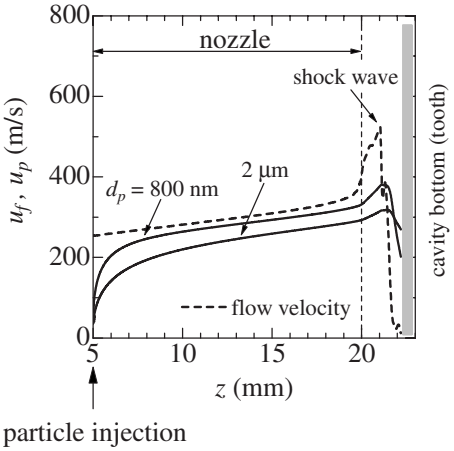

Fig. 4 Axial evolutions of velocities of 800 nm and 2 μm particles

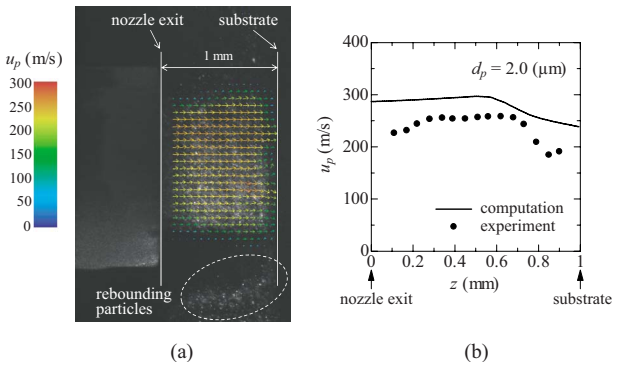

Fig. 6 (*a*) Laser sheet visualization of particle-laden jet in powder jet deposition process and (*b*) comparison of computational particle velocity with PIV measurement result

force [11,12]. Although particle velocity of 800 nm is higher than that of 2 μm in front of the shock wave due to its smaller inertia; deceleration through the shock wave is much larger for 800 nm particle compared with 2 μm particle. As a result, particle impact velocity of 2 μm particle is higher than that of 800 nm particle.

Figure 5 shows the relation between particle velocities and particle diameters in a microspace for the inlet stagnation pressure of 0.35 MPa. In the figure, particle velocity at nozzle exit and cavity bottom are denoted by open circles and closed circles, respectively. The deference between particle velocity at nozzle exit and cavity bottom for the same particle diameter is due to the deceleration by the shock wave as explained in Fig. 4. With decreasing particle diameter, particle is accelerated more at the nozzle exit. However, particles are largely decelerated by shock wave for smaller particles, which results in the decrease in particle impact velocity. The particle larger than 3 μm is not affected by the shock wave, then particle impacts the cavity bottom with keeping the velocity at nozzle exit. The highest impact velocity of 270 m/s can be obtained at 2 μm in this powder jet deposition system.

Figures 6(*a*) and 6(*b*) show the laser sheet visualization of particle-laden jet and comparison of particle velocity with PIV measurement for the particle diameter of 2.0 μm and the inlet stagnation pressure of 0.4 MPa. The nozzle-substrate distance is 1.0 mm in the experiment and powder jet impinges on flat glass substrate without a cavity. The rebounding particles from the substrate are observed near the substrate in the lower part of the photo. From the PIV measurement, particles are decelerated by

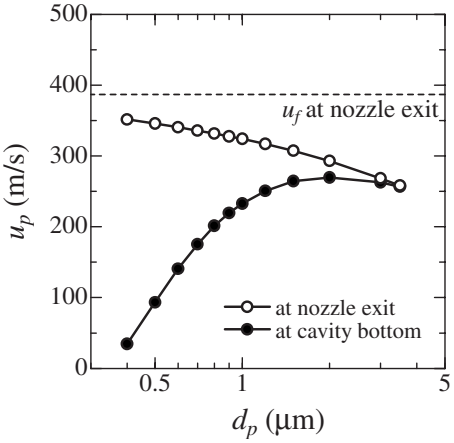

Fig. 5 Dependence of particle size on particle velocities at nozzle exit and cavity bottom in microspace

shock wave at 0.7 mm from the nozzle exit. The numerically predicted location of shock wave is approximately 0.6 mm from the nozzle exit. The numerical result shows slightly higher particle velocity. However, there is a reasonably good agreement between numerical and experimental results. Thus, the validity of this numerical computation is verified for in-flight particle behavior in the powder jet deposition process. This experiment was carried out under relatively high particle loading condition for clear observation of in-flight particles. The discrepancy between the numerical and experimental result may come from the influence of high particles loading on the gas flow and also the particle collisions, which are not considered in this computation.

4.2 Cavity Filling Process With Cold Gas Dynamic Spray in Macroscale. Figures 7(*a*)–7(*c*) show particle trajectories of 800 nm, 5 μm, and 10 μm for threee different cylindrical cavities installed in the substrate. The inlet stagnation pressure is 0.6 MPa. Two dimensional distributions of flow Mach number are also shown in the figures for each case. The diameters of each cavity are (a) 0.5, (b) 1.0, and (c) 1.5 times of nozzle exit diameter and the depth of cavities are 5.0 mm for all cases. The nozzle exit diameter is 4.8 mm in this device. The location of the shock wave strongly depends on jet-cavity configuration. In the case of d_{cav}/d_{noz}=0.5, normal shock wave covers the cavity because the jet-core diameter is over the cavity diameter, and then jet cannot flow into the cylindrical cavity. On the other hand, at d_{cav}/d_{noz} =1.0 and 1.5, the cavity diameter is large enough and shock wave appears inside the cavity. As cavity diameter increases, shock wave location approaches toward the cavity bottom as shown in Figs. 7(*b*) and 7(*c*). When the jet flows into the cavity, the flowing out gas from the cavity induces strong secondary back flow along the cavity wall. This back flow jet creates strong shear layer and supersonic jet oscillates by the interaction with shear layer. There exists the strongest back flow jet near the edge for d_{cav}/d_{noz} =1.0.

For 5 μm and 10 μm particles, particles fly straight into cavity bottom with penetrating shock wave due to their large inertia. On the other hand, the flight trajectory of 800 nm particle is deflected by shock wave. Especially in the case of d_{cav}/d_{noz}=0.5, 800 nm, the particle is captured by a strong vortex in the cavity and circulates without impacting the cavity bottom.

Figure 8 shows the particle impact velocities for various particle diameters for d_{cav}/d_{noz}=0.5, 1.0, and 1.5 under the inlet stagnation pressure of 0.6 MPa. The computed particle impact velocity for flat substrate is also shown in the figure for comparison. Moreover, the critical velocity obtained from the relation between E^*_{ad} and E^*_{el} is also shown in this figure. The optimum particle size exists for maximum particle impact velocity. Particle impact velocity decreases drastically for smaller particle resulting from strong deceleration by viscous drag behind the shock wave. With

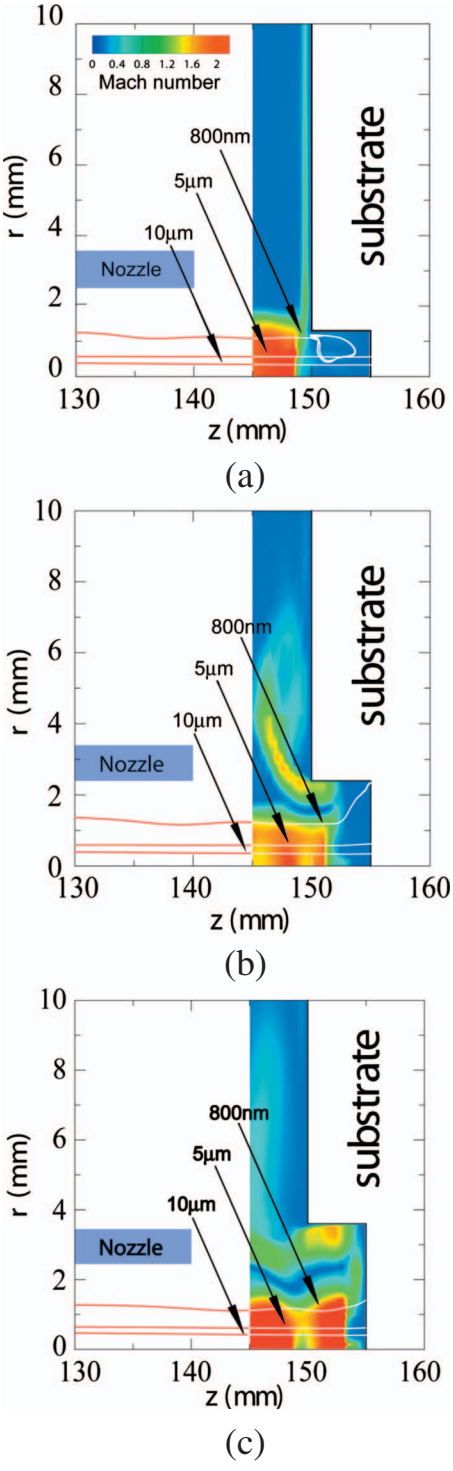

Fig. 7 Particle trajectories and Mach number distributions for (*a*) d_{cav}/d_{noz}=0.5, (*b*) 1.0, and (*c*) 1.5

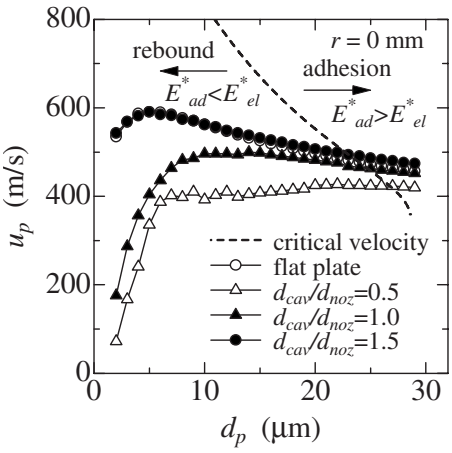

Fig. 8 Particle impact velocities as a function of particle diameter for d_{cav}/d_{noz}=0.5, 1.0, and 1.5

increasing cavity diameter, higher particle impact velocity can be obtained for all particle sizes. This is because the shock wave location shifts toward the cavity bottom for larger cavity diameter as shown in Fig. 7. Therefore, the decelerating region behind the shock wave decreases and particle deceleration can be suppressed before the impact. For d_{cav}/d_{noz}=1.5, obtained particle impact velocities are almost the same with flat substrate. It was found from this result that a particle impact velocity is not affected by a cavity configuration for a cavity with diameter 1.5 times larger than a nozzle diameter.

The critical velocity decreases with particle diameter. The minimum particle size for deposition decreases with enlarging cavity diameter. Particles larger than 23 μm deposit on the substrate when d_{cav}/d_{noz}=1.5.

Figure 9(*a*) shows the particle impact velocities and impact position at the cavity bottom and Fig. 9(*b*) shows the created coating profile in case of d_{cav}/d_{noz}=0.5. The results for d_{cav}/d_{noz}=1.5 are also shown in Fig. 10. In order to simulate the coating process, 2000 sample particles with size distribution are introduced. In the experiment, the average particle size was measured to be 27 μm with a laser scattering particle analyzer. Therefore, the size distribution of particles follows truncated normal distribution with average diameter of 25 μm at standard deviation

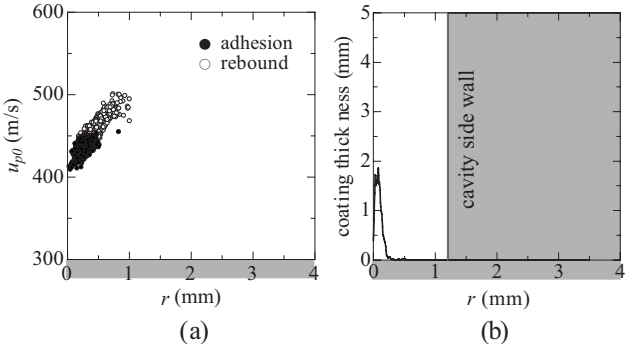

Fig. 9 (*a*) Particle impact velocities and impact positions and (*b*) created coating profile for d_{cav}/d_{noz}=0.5

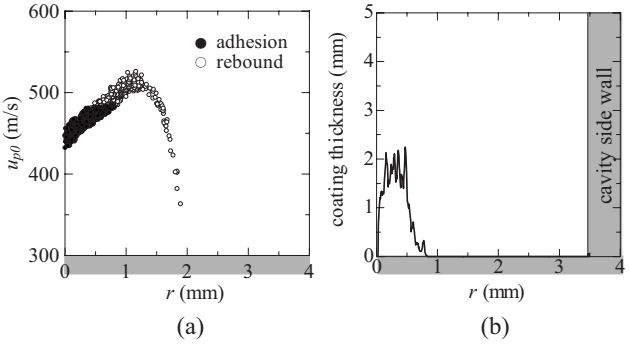

Fig. 10 (*a*) Particle impact velocities and impact positions and (*b*) created coating profile for d_{cav}/d_{noz}=1.5

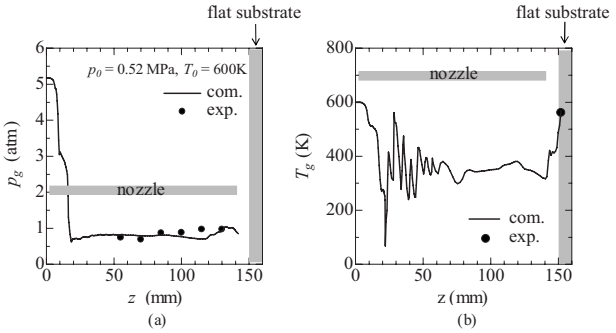

Fig. 11 Comparison with experimental results for (*a*) static pressure and (*b*) static temperature

of 8.0 by referring particles used in this experiment. The maximum and minimum particle sizes are 42 μm and 9 μm, respectively. Comparing with the case of d_{cav}/d_{noz}=0.5, radially wider coating can be formed at d_{cav}/d_{noz}=1.5. As observed from Fig. 10, for particles impacting at the radial position larger than 1.0 mm, particle impact velocity decreases toward the cavity side wall. Because the kinetic energy of impacting particle is not large enough for adhesion, coating is not formed near the cavity side wall.

In order to evaluate the validity of the numerical model, experiment has been performed with the conventional cold spray system. The inlet pressure and temperature are 0.52 MPa and 600 K, respectively, in this experiment.

Figures 11(*a*) and 11(*b*) show the comparison of wall static pressure distribution in the nozzle and gas temperature at the center of flat substrate. z=0 mm corresponds to the nozzle inlet as shown in Fig. 3. The numerical results agree qualitatively well with measured results for static pressure and temperature. As shown in Fig. 12, the numerical total pressures are larger than experimental results for all cavity diameters. The numerical computation underestimates pressure loss in this process. Neglecting the mixing of particle carrier gas flow in the nozzle could be one of the reasons for the underestimation of pressure loss.

Cavity filling process has been experimentally carried out utilizing conventional cold spray system. Figures 13(*a*)–13(*c*) and Figs. 14(*a*) and 14(*b*) show cross-sectional photo of cylindrical cavities after 20 s of spraying. For clear understanding of the cavity filling process, computed gas velocity field at the beginning of spray and gas velocity fields with considering the created deposition profiles are shown in Figs. 13 and 14, respectively. At d_{cav}/d_{noz}=0.5, coating was formed only at the tip of the cavity

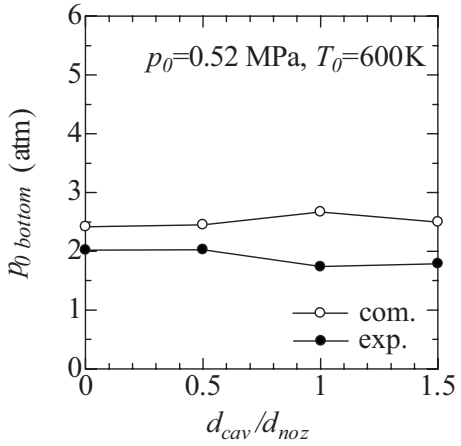

Fig. 12 Comparison with experimental results for total pressure on flat plate or at cavity bottom

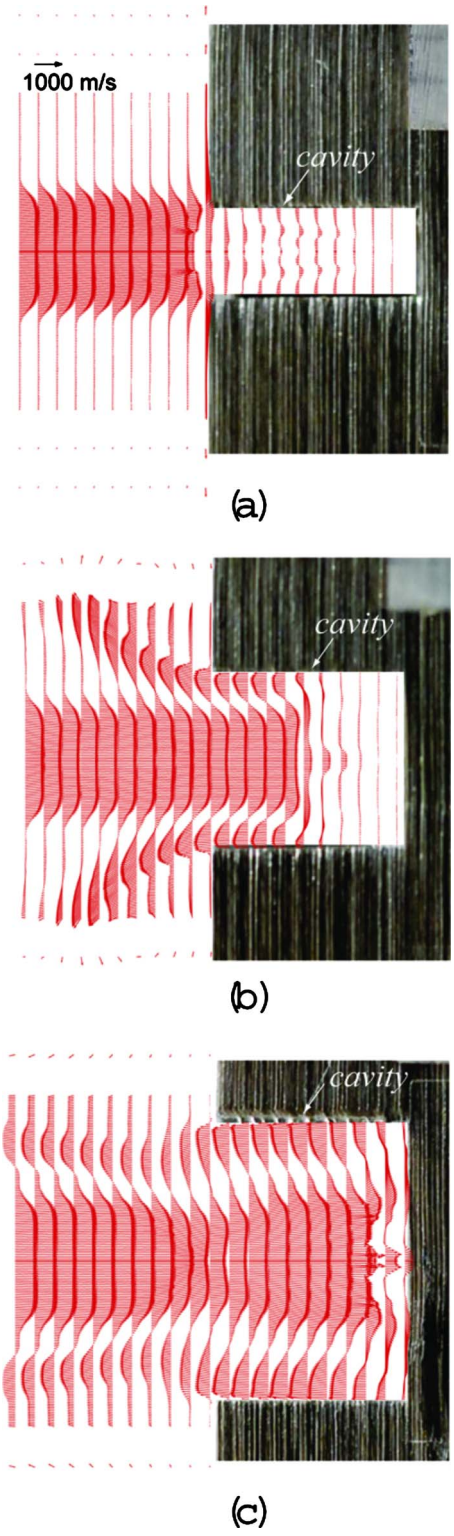

Fig. 13 Cross-sectional photos of cylindrical cavities with computed gas velocity vectors at the beginning of spray (*a*) d_{cav}/d_{noz}=0.5, (*b*) 1.0, and (*c*) 1.5

and cavity was not filled at all. As found from velocity vector profile in Fig. 13(*a*), gas velocity inside the cavity is very low since the shock wave covers up the cavity completely. Then, particles are decelerated inside the cavity and rebound at the cavity bottom due to insufficient kinetic energy for adhesion. With increasing cavity diameter as shown in Fig. 13(*b*) and 13(*c*), conical

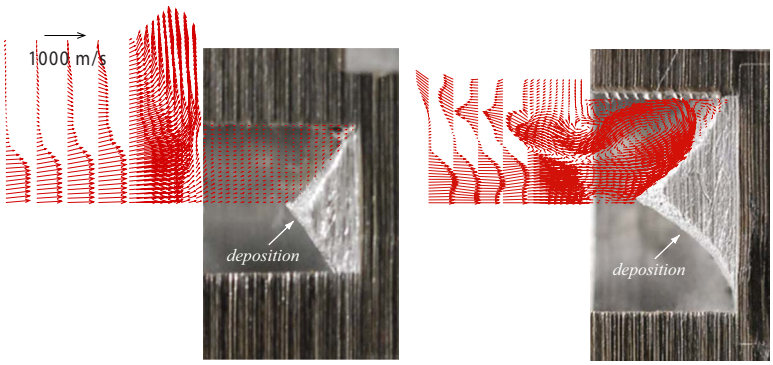

Fig. 14 Cross-sectional photos of cylindrical cavities after 20 s of spraying (*a*) $d_{cav}/d_{noz}=1.0$ and (*b*) 1.5: pictures are shown with computed gas velocity vectors after coating formation

deposition was created inside the cavity and the cavity cannot be filled completely for both cavities. According to the velocity vector profile shown in the figure, strong secondary back flow appears along the cavity side wall at the beginning of spray due to flowing out gas from the cavity. Particles flying near the cavity side wall cannot deposit on the bottom because of the deceleration by the strong secondary back flow jet. After the deposition as shown in Figs. 14, shock wave covers up the cavity for $d_{cav}/d_{noz}=1.0$. For $d_{cav}/d_{noz}=1.5$, a vortex appears near the side wall and particles are decelerated by this vortex. These results qualitatively agree well with the computational results as explained in Figs. 9 and 10.

Figures 15(*a*) and 15(*b*) show cross-sectional photos of spherical and conical cavity, respectively. The diameter of both spherical and conical cavity is 1.5 times of nozzle exit diameter. The depth of spherical cavity is 5 mm and the conical angle of conical cavity is 90 deg. The velocity vector fields at the beginning of spray are also shown in the figure. In the case of spherical cavity, secondary back flow jet also exists along the cavity side wall at the beginning of deposition process and cavity was not filled up. On the other hand in the case of conical cavity, the secondary back flow is suppressed as shown in the figure because gas flows out along the inclined cavity side wall. By adopting the conical cavity, cavity can be filled up completely.

5 Conclusions

Time-dependent and realistic computational simulations on cavity filling process by cold gas dynamic spray and powder jet deposition process ranging from microscale to macroscale were carried out in order to give an insight for their high performance advanced applications to joining, crack repair and dental treatment. The obtained results are summarized as follows.

(1) In a powder jet deposition process in a microscale, shock wave appears in front of the substrate due to underexpansion of jet. Optimal particle diameter for maximum impact velocity exists. For particles below the optimal value, particle impact velocity decreases drastically for smaller particle size resulting from deceleration by drag force behind shock wave.
(2) The location of the shock wave depends on the relation between jet-core diameter and cavity diameter. When jet-core diameter is larger than cavity diameter, shock wave covers up the cavity completely. On the other hand if jet-core diameter is smaller than cavity diameter, shock wave appears inside the cavity and its location penetrates toward the cavity bottom with increasing cavity diameter.
(3) Cavity filling process in a macroscale has been carried out with conventional cold gas dynamic spray system for a cylindrical cavity configuration. When the shock wave covers up the cavity, cavity cannot be filled at all. Under the condition of shock wave appearing inside the cavity, conical deposition is formed in the cavity attributed to the particle deceleration by strong secondary back flow jet along the cavity side wall.
(4) By adopting conical cavity with conical angle of 90 deg and diameter of 1.5 times of nozzle diameter, cavity can be filled up completely resulting from the suppression of secondary back flow jet along the cavity side wall in the conventional cold gas dynamic spray process.

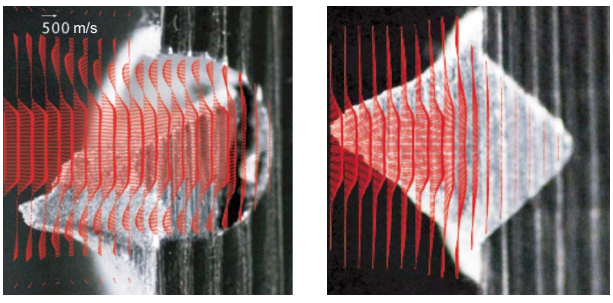

Fig. 15 Cross-sectional photos of cavities after 20 s of spraying: (*a*) spherical cavity and (*b*) conical cavity; pictures are shown with computed gas velocity vectors at the beginning of spray

Acknowledgment

Authors would like to give our sincere thanks to Mr. Kazunari Katagiri, Mr. Tomoki Nakajima, Mr. Norio Ito, Mr. Atsushi Totsuka, and Dr. Yuji Ichikawa for their consistent technical supports. The present study was partly supported by a grant-in-aid for young scientists (B), under Contract No. 20760107 from the Ministry of Education, Science, Sports, and Culture.

Nomenclature

A_{in} = Inlet cross-sectional area (m^2)
C_D = drag coefficient
d_p = particle diameter (m)
D_s = splat diameter (m)
e = stagnation internal energy per unit volume (J/m^3)
E_1 = bonding energy between atoms (J)

E^*_{ad} = normalized adhesion energy
E^*_{el} = normalized elastic energy
$\boldsymbol{F}$ = force vector (N)
h_p = splat height (m)
H_m = particle latent heat of melting (J/kg)
m_f = fluid mass (kg)
m_p = particle mass (kg)
M_p = particle Mach number
$\boldsymbol{n}$ = normal direction
$N_{\sigma 0}$ = Maximum number of bonds per unit area (m^{-2})
p = static gas pressure (Pa)
p_d = stress at the rebounding moment (Pa)
r = radius (m)
r_p = particle radius (m)
R = gas constant (J/(kg K))
Re_p = particle Reynolds number
t = time (s)
T = static gas temperature (K)
t_c = particle contact time at impact (s)
T_c = particle contact temperature (K)
T_m = particle melting temperature (K)
$\boldsymbol{u}_f$ = gas velocity vector (m/s)
$\boldsymbol{u}_p$ = particle velocity vector (m/s)
v_p = particle impact velocity (m/s)
$v_{p_{in}}$ = particle injection velocity (m/s)
V_m = specific particle melting volume at impact
V_z = specific particle heating volume at impact
x_p = particle position (m)
z = axis (m)

Greek Symbols

γ = specific heat ratio
ϵ_p = particle strain at impact
λ_f = thermal conductivity of gas (W/(m K))
λ_p = thermal conductivity of particle (W/(m K))
μ = viscous coefficient (Pa s)
ν = frequency of natural oscillations of atoms in lattice (Hz)
ρ = flow density (kg/m^3)
ρ_p = particle density (kg/m^3)
$\bar{\bar{\tau}}$ = viscosity stress tensor (Pa)
Φ = viscous dissipation (W/m^3)

References

[1] Alkhimov, A. P., Papyrin, A. N., Kosarev, V. F., and Nesterovich, N. I., 1994, "Gas-Dynamic Spraying Method for Applying Coatings," U.S. Patent No. 5,302,414.
[2] Alkhimov, A. P., Papyrin, A. N., Kosarev, V. F., and Nesterovich, N. I., 1995, "Method and Device for Coating," European Patent EP 0,484,533 B1.
[3] Tokarev, A. O., 1996, "Structure of Aluminum Powder Coatings Prepared by Cold Gasdynamic Spraying," Metal Science and Heat Treatment, **38**, pp. 136–139.
[4] Papyrin, A., Kosarev, V., Klinkov, S., Alkhimov, A., and Fomin, V., 2007, *Cold Spay Technology*, Elsevier, Amsterdam, The Netherlands.
[5] Champagne, V., 2007, *The Cold Spray Materials Deposition Process*, Woodhead Publishing Limited, Cambridge, England.
[6] Assadi, H., Gartner, F., Stoltenhoff, T., and Hreye, H., 2003, "Bonding Mechanism in Cold Gas Spraying," Acta Mater., **51**, pp. 4379–4394.
[7] Yoshihara, N., Kuriyagawa, T., Yasutomi, Y., and Ogawa, K., 2005, "Powder Jet Deposition of Ceramic Films," *Proceedings of the International Conference on Leading Edge Manufacturing in 21st Century*, pp. 833–838.
[8] Noji, M., Sasaki, K., Kuriyagawa, T., Suzuki, O., Ogawa, K., and Kanehira, M., 2005, "Creating New Interface Between Tooth and Biomaterials Using Powder-Jet Technology," International Congress Series, **1284**, pp. 302–304.
[9] Sato, T., Solonenko, O. P., and Nishiyama, H., 2002, "Optimization for Plasma Spraying Processes by Numerical Simulation," Thin Solid Films, **407**, pp. 54–59.
[10] Sato, T., Solonenko, O. P., and Nishiyama, H., 2004, "Evaluations of Ceramic Spraying Processes by Numerical Simulation," Mater. Trans., JIM, **45**, pp. 1874–1879.
[11] Takana, H., Ogawa, K., Shoji, T., Nishiyama, H., 2008, "Computational Simulation of Cold Spray Process Assisted by Electrostatic Force," Powder Technol., **185**, pp. 116–123.
[12] Takana, H., Ogawa, K., Shoji, T., and Nishiyama, H., 2008, "Computational Simulation on Performance Enhancement of Cold Gas Dynamic Spray Processes With Electrostatic Assist," ASME J. Fluids Eng., **130**(081701), pp. 1–7.
[13] Erlebacher, G., Hussainu, M., Speziale, C., and Zang, T., 1992, "Toward the Large-Eddy Simulation of Compressible Turbulent Flows," J. Fluid Mech., **238**, pp. 155–185.
[14] Karniadakis, G., Beskok, A., and Aluru, N., 2005, *Microflows and Nanoflows*, Springer, New York.
[15] Saffman, P. G., 1965, "The Lift on a Small Sphere in a Slow Shear Flow," J. Fluid Mech., **22**, pp. 385–400.
[16] Saffman, P. G., 1968, "Corrigendum to 'The Lift on a Small Sphere in a Slow Shear Flow'," J. Fluid Mech., **31**, p. 624.
[17] Li, A., and Ahmadi, G., 1993, "Deposition of Aerosols on Surfaces in a Turbulent Channel Flow," Int. J. Eng. Sci., **31**(3), pp. 435–451.
[18] Henderson, C. B., 1976, "Drag Coefficient of Spheres in Continuum and Rarefied Flows," AIAA J., **14**, pp. 707–708.
[19] Kurochkin, Y. V., Demin, Y. N., and Soldatenkov, S. I., 2002, "Demonstration of the Method of Cold Gasdynamic Spraying of Coatings," Chemical and Petroleum Engineering, **38**, pp. 245–248.
[20] Alkhimov, A. P., Klinkov, S. V., and Kosarev, V. F., 2000, "Experimental Study of Deformation and Attachment of Microparticles to an Obstacle Upon High-Rate Impact," J. Appl. Mech. Tech. Phys., **41**, pp. 245–250.
[21] Solonenko, O. P., Kudinov, V. V., Smirnov, A. V., Cherepanov, A. N., Popov, V. N., Mikhalchenko, A. A., and Kartaev, E. V., 2005, "Micro-Metallurgy of Splat: Theory, Computer Simulation and Experiment," JSME Int. J., Ser. B, **48**, pp. 366–380.
[22] Klinkov, S. V., Kosarev, V. F., and Rein, M., 2005, "Cold Spray Deposition: Significance of Particle Impact Phenomena," Aerosp. Sci. Technol., **9**, pp. 582–591.
[23] Anderson, W. K., Thomas, J. L., and Leer, B. V., 1986, "Comparison of Finite Volume Flux Splittings for the Euler Equations," AIAA J., **24**, pp. 1453–1460.
[24] Yoon, S., and Jameson, A., 1988, "Lower-Upper Symmetric-Gaiss–Seidel Method for the Euler and Navier–Stokes Equations," AIAA J., **26**, pp. 1025–1026.

Jean-Pierre Franc
e-mail: jean-pierre.franc@inpg.fr

Guillaume Boitel

Michel Riondet

LEGI,
Grenoble Institute of Technology,
Université Joseph Fourier,
Centre National de la Recherche Scientifique,
BP 53,
38041 Grenoble Cedex 9, France

Éric Janson

Pierre Ramina

Claude Rebattet

CREMHYG,
Grenoble Institute of Technology,
BP 95,
38402 Saint-Martin d'Hères Cedex, France

Thermodynamic Effect on a Cavitating Inducer—Part I: Geometrical Similarity of Leading Edge Cavities and Cavitation Instabilities

The thermodynamic effect on a cavitating inducer is investigated from joint experiments in cold water and Refrigerant 114. The analysis is focused on leading edge cavitation and cavitation instabilities, especially on alternate blade cavitation and supersynchronous rotating cavitation. The cavity length along cylindrical cuts at different radii between the hub and casing is analyzed with respect to the local cavitation number and angle of attack. The similarity in shape of the cavity closure line between water and R114 is examined and deviation caused by thermodynamic effect is clarified. The influence of rotation speed on cavity length is investigated in both fluids and analyzed on the basis of a comparison of characteristic times, namely, the transit time and a thermal time. Thermodynamic delay in the development of leading edge cavities is determined and temperature depressions within the cavities are estimated. Thresholds for the onset of cavitation instabilities are determined for both fluids. The occurrence of cavitation instabilities is discussed with respect to the extent of leading edge cavitation. The thermodynamic delay affecting the occurrence of cavitation instabilities is estimated and compared with the delay on cavity development. [DOI: 10.1115/1.4001006]

1 Introduction

The effect of fluid properties on thermal aspects of cavitation has been the subject of various investigations. It is well-known that a more or less important thermal delay in the development of cavitation can occur according to the fluid nature. It is almost zero in water at ambient temperature, but can be quite significant in other fluids such as cryogenic liquids, refrigerant liquids, or hot water.

As a whole, the physics of thermodynamic effect is well understood. Billet and co-workers [1,2] made clear that vapor is continuously entrained by the liquid flow at the rear of the cavitating region, and that an equivalent quantity of liquid changes to vapor to counterbalance this loss and ensure a stable extent of cavitation on an average. Liquid vaporization goes with a temperature drop because of the latent heat of vaporization, which is extracted to the two-phase region, whose temperature necessarily falls.

Though the phenomenology of thermodynamic effect is well documented, the quantitative prediction of temperature drop for a given industrial application remains a challenging problem. Among the most difficult parameters to evaluate, let us mention for instance the flowrate of vapor entrained in the closure region of a cavity, the heat transfer coefficient at the liquid/vapor interface, or the void fraction in the cavitating region, which all influence the phenomenon.

In the case of rocket engine inducers considered in the present work, several characteristics can be affected by thermodynamic effect as the performance of the pump, the extent of leading edge cavitation, and the tip leakage cavitation or the onset and desinence of cavitation instabilities. A major problem is the prediction of the delays caused by thermal effects to each of these phenomena and the comparative analysis of all of them.

Thermodynamic effect on cavitation performance and cavitation instabilities on a three-bladed inducer was experimentally investigated by Yoshida and co-workers [3–7] in liquid nitrogen. The length of the tip cavitation was determined from wall pressure measurements on the casing. The authors found that thermodynamic effect increases with cavity length. They noticed that thermodynamic effect suppresses cavitation surge observed in cold water. As for synchronous rotating cavitation, they reported that this regime occurs for a critical cavity length of the order of 80% of blade spacing. Cavitation instabilities were also investigated by Cervone and co-workers [8–10] on different inducers using various techniques, and in particular, visualizations by a high-speed camera. Let us also mention the observations on rotating cavitation and cavitation surge conducted by Zoladz [11] during the development of the Fastrac engine turbopump at NASA.

The thermodynamic effect on cavitating inducers was also investigated numerically (e.g., Refs. 12–16. Watanabe et al. [12,13]) developed a semianalytic model using a singularity method coupled with a heat transfer model at the cavity interface to analyze thermodynamic effects on a partially cavitating flat plate cascade. They conducted both a steady and an unsteady modeling for the analysis of mean cavity length and cavitation instabilities. Hosangadi et al. [14] developed an advanced compressible, multiphase computational fluid dynamics tool that accounts for energy balance to simulate the cavitating flow in liquid rocket turbomachinery working with cryogenic fluids. They compared the performance of a flat plate inducer in liquid hydrogen and water, and showed in particular that thermal effects result in a more gradual breakdown of head in liquid hydrogen compared with cold water. Let us also mention the simulation methods based on the use of a barotropic equation of state for the liquid-vapor mixture [15,16], which can include thermodynamic effects.

The present work, which completes an earlier work [17], is an experimental investigation of the thermodynamic effect on a four-

Contributed by the Fluids Engineering Division of ASME for publication in the JOURNAL OF FLUIDS ENGINEERING. Manuscript received September 29, 2008; final manuscript received December 14, 2009; published online February 17, 2010. Assoc. Editor: Steven Ceccio.

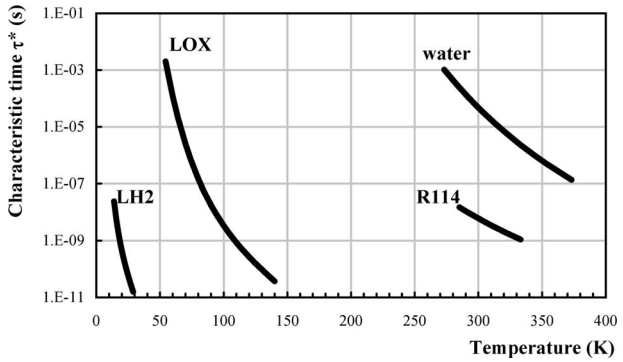

Fig. 1 Characteristic time τ^* of water, R114, liquid oxygen, and liquid hydrogen as a function of temperature

bladed cavitating inducer. It is focused on leading edge cavitation, which is investigated jointly in cold water and Refrigerant 114. Thermal delays on the development of leading edge cavitation and the occurrence of cavitation instabilities are compared. Temperature depressions within the cavities are estimated.

2 Experimental Facility and Procedure

Two sets of experiments were conducted on the experimental facilities of CREMHYG.[1] Reference tests without thermodynamic effect were carried out on a water facility at room temperature. The four-bladed inducer was operated at nominal flowrate principally and at various rotational speeds. Cavitation tests consisted in a step-by-step pressure reduction from noncavitating conditions to performance breakdown. Several pressure transducers were mounted on the casing for the detection of cavitation instabilities, especially alternate blade cavitation and supersynchronous rotating cavitation. The onset of cavitation instabilities in terms of cavitation number was determined from the emergence of the corresponding frequency in the pressure fluctuation spectrum. A special attention was paid to the development of leading edge cavities, and photographs were systematically taken and analyzed in order to determine the evolution of cavity length with cavitation number at different radii from hub to casing.

A second set of experiments was conducted on a cavitation loop, working with Refrigerant 114 as test fluid [17]. The same inducer was tested using similar experimental procedures. The fluid temperature was varied between 20°C and 40°C in order to change the magnitude of the thermodynamic effect and investigate its influence. For a brief comparison with other fluids, let us mention that the vapor pressure of R114 increases from about 1.8 bars to 3.4 bars between 20°C and 40°C. At the midtemperature of 30°C, the density of R114 is 1440 kg/m^3, its kinematic viscosity 0.25×10^{-6} m^2/s and its surface tension 0.010 N/m. The thermodynamic properties of R114 present similarities with that of liquid hydrogen used for the industrial application, but is definitely much easier to handle with regard to security requirements. As an example, the temperature drop ΔT^*, often considered as an estimate of the thermodynamic effect in cavitation, is 1.20 K for R114 at 20°C. It is close to that of liquid hydrogen at 22.2 K, which is 1.25 K and much larger than that of water at 20°C, which is only 0.01 K. The similarity between R114 and LH2 is confirmed on Fig. 1 on the basis of another related parameter τ^* (Eq. (7)) measured in time units. R114 actually proved to be quite appropriate for the investigation of thermal effects on cavitation and leads to substantial delays in cavitation development.

Cavitation tests in R114 were generally ended when vapor forms in the inlet duct, which does not happen in water. This is to avoid dangerous vibrations generated by the transit of vapor pockets through the inducer. The performance of the machine does not generally drop much since the degree of two-phase breeding is kept limited.

R114 is known to be able to dissolve a quite significant amount of air. In order to limit the effect of air relief during cavitation tests, which otherwise would interfere with the formation of vapor, a special device was developed to degas the fluid before testing. The partial pressure of oxygen, measured by an Orbisphere dissolved oxygen analyzer, drops very significantly during degassing (from typically 15 mbars to 0.6 mbar). It is difficult to know accurately the total air content in R114 because of the lack of data on the solubility of O_2 and N_2 in $C_2Cl_2F_4$. Using estimations of Henry's constants, we could estimate the total air content in R114 to be of the order of a few ppm. In the case of water tests, the water was also degassed by operating the facility for a sufficient time under cavitating conditions, and the measured air content was reduced to typically 4 ppm.

3 Theoretical Background

The driving term for the growth of a cavitation bubble is the pressure difference $p_v - p_{\min}$, where $p_{\min}$ is the minimum pressure in the original noncavitating flow. If $p_{\min}$ is smaller than p_v, the bubble will grow.

Vapor pressure has to be evaluated at the actual cavity temperature T_c, which is smaller than the liquid temperature at infinity T_∞. The real driving term is then $p_v(T_c) - p_{\min}$. It is smaller than $p_v(T_\infty) - p_{\min}$ so that cavitation development is reduced by thermal effects, as shown experimentally.

The difference in vapor pressure $\Delta p_v = p_v(T_\infty) - p_v(T_c)$ is an indicator of the thermodynamic effect. If it is negligible with respect to $p_v(T_\infty) - p_{\min}$, thermal effects will have a minor influence. The condition for negligible thermodynamic effect is then

$$\Delta p_v = \frac{dp_v}{dT}\Delta T \ll p_v(T_\infty) - p_{\min} \tag{1}$$

Temperature depression in a growing bubble ΔT can be estimated from the heat balance of the bubble. Assuming that the heat flux required for phase change is conveyed to the bubble interface by convection [19], the temperature depression ΔT necessary to get the appropriate heat flux for the growth of the bubble at rate $\dot{R}$ is

$$\Delta T = \frac{\rho_v L}{h}\dot{R} \tag{2}$$

Using this estimate of temperature depression, condition (1) for negligible thermal effects becomes

$$\frac{1}{\mathrm{Nu}}\frac{\Delta p_v^*}{\rho_\ell \alpha_\ell}\frac{\dot{R}D}{V^2} \ll \frac{-C_{p\,\min} - \sigma_v}{2} \tag{3}$$

The nondimensional numbers, which appear in this equation are the usual Nusselt number $\mathrm{Nu} = hD/\lambda_\ell$ based on a characteristic dimension of the flow D (typically the inducer diameter), minimum pressure coefficient $C_{p\,\min}$, and conventional cavitation number based on vapor pressure at temperature T_∞.

Although thermal effects tend to reduce the bubble growth rate, a first order of magnitude can be obtained on the basis of the classical asymptotic growth rate without thermodynamic effect (see, e.g., Ref. [20])

$$\dot{R} \approx \sqrt{\frac{2(p_v - p_\infty)}{3\rho_\ell}} \tag{4}$$

whose corresponding nondimensional form is

[1]Centre de Recherches et d'Essais de Machines Hydrauliques de Grenoble, France.

Table 1 Typical orders of magnitude of the transit and thermal times for cold water and Refrigerant 114 at 20°C, and for a characteristic length $D \cong 0.1$ m and a characteristic velocity $V \cong 30$ m/s ($\tau \cong 3$ ms)

	Cold water	R114 at 20°C
τ^* (s)	10^{-4}	10^{-8}
Pr (Prandtl number)	7	5.5
Re (Reynolds number)	3.0×10^{6}	1.2×10^{7}
Nu (Nusselt number)	6.7×10^{3}	1.8×10^{4}
τ_T (s)	0.67	1.8×10^{-4}
τ/τ_T	4.5×10^{-3}	17

$$\dot{\bar{R}} = \frac{\dot{R}}{V} \approx \frac{1}{\sqrt{3}}\sqrt{-C_{p\,\min} - \sigma_v} \tag{5}$$

The bubble growth rate appears to be proportional to flow velocity in a first approach.

The introduction of this first order evaluation of bubble growth rate in Eq. (3) leads to the following approximate condition for negligible thermodynamic effect:

$$\frac{1}{\mathrm{Nu}}\frac{\Delta p_v^*}{\rho_\ell \alpha_\ell}\frac{D}{V} \ll \frac{\sqrt{3}}{2}\sqrt{-C_{p\,\min} - \sigma_v} \tag{6}$$

Parameter $\tau = D/V$ is the transit time. The group of parameters

$$\tau^* = \frac{\rho_\ell \alpha_\ell}{\Delta p_v^*} \tag{7}$$

is also in time unit. It depends only upon the fluid properties and is connected to Brennen's Σ parameter [21,22] by relation $\tau^* = \sqrt{\alpha_\ell}/\Sigma$. Characteristic time τ^* was used previously by Bonnin [23,24]. Figure 1 gives the value of τ^* for a few typical fluids of practical interest in this work. At room temperature, R114 appears to have similar values for parameter τ^* than liquid hydrogen. The characteristic time $\tau_T = \mathrm{Nu}\tau^*$, which appears in Eq. (6) can be considered as a thermal time since it contains the information on heat transfer at the interface via the Nusselt number. It plays a major role in thermodynamic effect as explained below.

In practice, it is difficult to make a quantitative use of Eq. (6) to predict the importance of thermodynamic effect since the Nusselt number, which concentrates the information on heat transfer at cavity interface, is unknown. This is a difficult problem and no reliable correlation for the Nusselt number is presently available for cavitating flows, although estimates can be obtained (see, for instance, Refs. [25], [26], and [19]).

Nevertheless, Eq. (6) is used here as a guideline for the interpretation of experimental results. The following two principles should be kept in mind. (i) The influence of fluid nature is basically included in the characteristic time τ^*, and (ii) the amplitude of the thermodynamic effect depends upon the ratio τ/τ_T of the transit time to the thermal time. The larger this ratio, the larger the thermodynamic effect. These rules give a basis used later for interpreting the effect of various parameters, such as fluid properties and flow velocity, on thermal cavitation.

Let us evaluate typical orders of magnitude of the previous characteristic times. Assume $D \cong 0.1$ m, $V \cong 30$ m/s, and then a transit time $\tau \cong 3$ ms. In a preliminary approach, the Nusselt number is estimated using the classical Colburn's correlation $\mathrm{Nu} = 0.023\ \mathrm{Re}^{0.8}\ \mathrm{Pr}^{1/3}$, whose applicability to cavitating flows remains an open question. Table 1 presents typical values of the thermal time τ_T compared with the transit time τ for cold water and R114. The ratio τ/τ_T appears quite small in cold water, but much larger in R114. This confirms negligible thermal effects in water, but significant thermal effects in R114.

Let us observe that Eq. (2) takes the following nondimensional form:

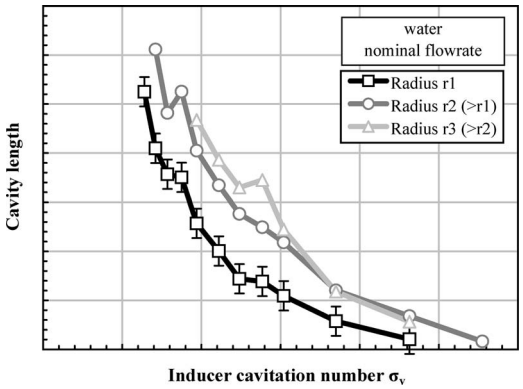

Fig. 2 Cavity length versus inducer cavitation number σ_v at three different radii, r1, r2, and r3, from hub to casing visible on Fig. 6 (water, nominal flowrate)

$$B = \frac{\mathrm{Re}\ \mathrm{Pr}}{\mathrm{Nu}}\dot{\bar{R}} \tag{8}$$

4 Cavity Length Without Thermodynamic Effect

In a preliminary analysis, the evolution of the cavity length with radius r from hub to casing has been investigated. As seen on Fig. 6(*b*), the leading edge cavity becomes longer near the blade tip before merging with the tip vortex cavitation. This trend is shown quantitatively on Fig. 2, which presents curves $\ell(\sigma)$ at three different radii (see grid on Fig. 6 for the location of corresponding cylindrical sections). It is analyzed below on the basis of a simplified 2D approach.

The cavitation number used in Fig. 2 is the standard inducer cavitation number defined by

$$\sigma_v = \frac{p_u - p_v}{\rho_\ell \omega^2 R^2} \tag{9}$$

where R is the inducer tip radius chosen as reference length and ωR is the inducer tip velocity.

In the framework of a 2D approach, it is important to observe that the relative velocity of the fluid in a cylindrical section of the machine at radius r is of the order ωr and not ωR. Following Brennen [21] and assuming that upstream pressure is uniform, a local cavitation number based on that particular velocity and then relevant of cavitation development in that particular section is defined by

$$\sigma(r) = \frac{p_u - p_v}{\rho_\ell \omega^2 r^2} \tag{10}$$

Both cavitation numbers are connected by the following equation:

$$\sigma(r) = \sigma_v\left(\frac{R}{r}\right)^2 \tag{11}$$

The local cavitation number $\sigma(r)$ decreases from hub to casing and matches with the inducer cavitation number at the tip. This decrease in cavitation number partly explains the increase in cavity length with radial position.

In addition to the change in cavitation number, the angle of attack also changes with radius because of changes in blade and flow angle. Taking into account both effects, the actual angle of attack α can easily be computed from the inlet velocity triangle. The change in angle of attack is the second reason for changes in the radial distribution of the cavity length. Let us observe that the present way of estimating the angle of attack is based on a simple two-dimensional approach, which does not take into account the detailed geometry of the leading edge such as backsweep.

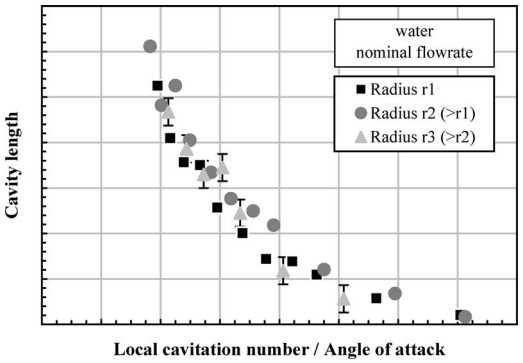

Fig. 3 Cavity length versus ratio $\sigma(r)/\alpha$ of local cavitation number to angle of attack at three different radii from hub to casing (same data as Fig. 2)

In accordance with the linearized theory of cavity flows, a decrease in the angle of attack is, to some extent, equivalent to an increase in the cavitation number, and both effects can be simultaneously accounted for by considering the ratio $\sigma(r)/\alpha$. Figure 3 shows that the consideration of this parameter actually leads to a satisfactory grouping of curves $\ell(\sigma)$ originally presented in Fig. 2.

Moreover, the evolution of cavity length with $\sigma(r)/\alpha$ is compared with that given by the linearized theory in the reference case of an isolated flat plate hydrofoil (see for instance Ref. [22]). For partial cavities much smaller than the chord length, cavity length follows the classical law

$$\ell \propto \left(\frac{\sigma}{\alpha}\right)^{-2} \tag{12}$$

Figure 4 shows that, in the inducer case, the cavity length follows an almost linear relationship with this new parameter. This trend has been observed for various operating conditions, including small variations of flowrate of $\pm 10\%$ near design.

It is concluded that the development of blade cavitation in the central part of the inducer investigated here is in reasonable agreement with conventional results. A more detailed analysis, out of the scope of the present work, would require numerical computations on the actual inducer geometry. The influence of thermodynamic effect on this basic radial evolution is examined in Sec. 6 from test results in R114.

5 Influence of Rotation Speed on Cavity Length

The influence of rotation speed is remarkably different with and without thermodynamic effect, as shown on Fig. 5. For water, there is almost no influence of rotation speed on curves $\ell(\sigma)$ in the range investigated here. The minor influence of the Reynolds

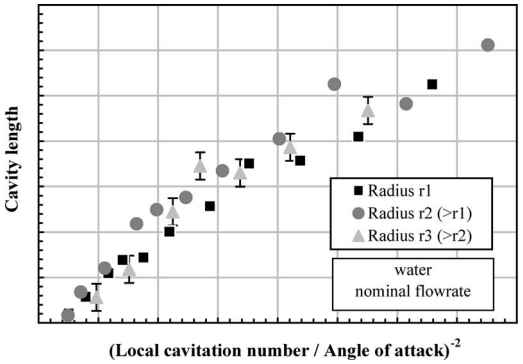

Fig. 4 Cavity length versus $[\sigma(r)/\alpha]^{-2}$ at three different radii from hub to casing (same data as Fig. 2)

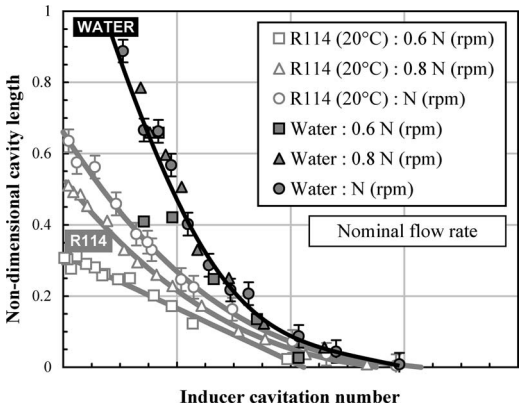

Fig. 5 Influence of rotation speed on cavity length for water and R114 at 20°C. Data are relative to nominal flowrate and cavity length is measured along medium radius r2.

number on cavity length is a common result, which has been obtained in particular on isolated hydrofoils in water tunnels.

This is no longer the case for R114, and Fig. 5 clearly indicates that the cavity length increases very significantly with rotation speed. The influence of flow velocity is easily understandable on the basis of the theoretical approach presented in Sec 3.

Transit time τ obviously varies like V^{-1}. On the other hand, assuming a dependency of the Nusselt number with Reynolds number, similar to the one given by usual correlations on classical convective heat transfer on a wall without phase change, i.e., with $\mathrm{Re}^{0.8}$, the thermal time varies like $V^{0.8}$. The ratio τ/τ_T, which is an indicator of the thermodynamic effect, should vary like $V^{-1.8}$. Consequently, thermodynamic effect is expected to decrease quite significantly when flow velocity increases. This explains qualitatively the lengthening of cavity with flow velocity, or more precisely, the deficit in shortening. The assumption that heat transfer in a cavitating flow follows the usual trend of classical convection, typically Colburn's correlation, is supported by the work of Fruman and co-workers [25,26], although not yet fully validated.

A previous discussion was focused on the analysis of the influence of rotation speed on cavity length at a constant cavitation number, i.e., along a vertical line on Fig. 5. It is also possible, from Fig. 5, to investigate the influence of rotation speed on the cavitation number along a horizontal line, i.e., for a similar development of cavitation. This allows an analysis of the effect of rotation speed on the B-factor. In a previous investigation, Franc and co-workers [17] showed that their experimental data do not exhibit any clear influence of the inducer rotation speed on the B-factor. Their analysis, based upon the same assumption of applicability of Colburn's type correlation to cavitating flows, confirmed the limited influence of flow velocity on the B-factor, typically as $V^{0.2}$. As a comparison, let us recall that the correlations of Moore and Ruggeri [27] and Hord [28], developed at NASA in the 1970s and based on experimental results, assume a dependency as $V^{0.8}$. Other aspects of the dependence of the B-factor with operating conditions are discussed in Sec. 7.

6 Thermodynamic Effect and Geometrical Similarity of Cavities

Figure 6 presents a comparison of typical leading edge cavities in water and R114 at the higher temperature investigated (40°C), where thermal effects are maximum. The operating conditions are the same, except the cavitation number. The two values of the cavitation number in water and R114 have been chosen so that cavitation has the same overall extent. Optical distortion is different for both experiments because of different sight angles and window geometries, but the grid plotted on the blades allows us to get rid of optical deformations.

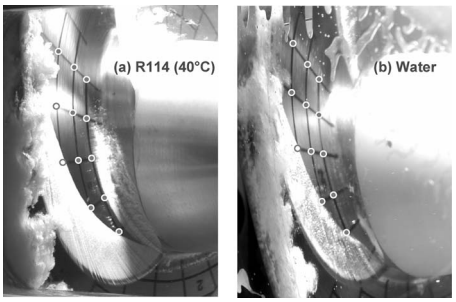

Fig. 6 Comparison of typical leading edge cavities in water (without thermodynamic effect) and Refrigerant 114 at 40°C. The value of the cavitation number for R114 is significantly smaller than that in water and was adjusted to correspond to a similar extent of cavitation

Comparison of both cavities in water and R114 demonstrates the fine similarity of the cavity shape with and without thermal effects. The main visible difference is a somewhat more developed attached cavitation on the hub in the refrigerant case, which is presently unexplained.

To analyze more precisely the similarity in cavity shape and point out possible deviations of secondary importance with respect to that basic scaling law, the shapes of the cavity closure lines were systematically compared for three typical degrees of development of cavitation. Profiles presented in Fig. 7 are actually representative of a large number of tests. They have been obtained by an averaging procedure conducted on numerous images corresponding to all operating conditions available (rpm, flowrate, and temperature in the case of R114).

Figure 7 confirms the similar expansion of the cavity from hub to casing for water and R114. However, it shows that the difference in cavity length between both ends of the domain, presently investigated from hub to casing, is systematically slightly larger in R114 than in water. This observation proves that the ideal similarity law between cavities in water and R114 mentioned above is actually affected by a deviation, which, however, remains relatively small.

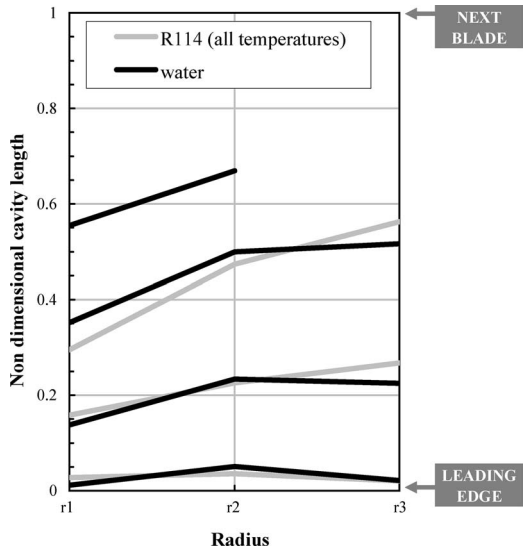

Fig. 7 Comparison, between water and R114, of the mean shape of cavity closure line for different degrees of development of cavitation. No data are available in R114 corresponding to the longer cavity shown in water because of thermodynamic effect, which shortens cavities.

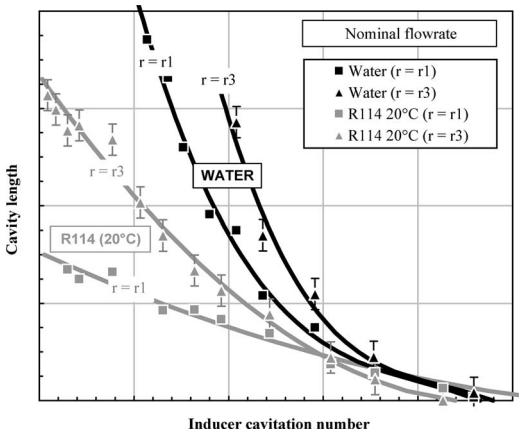

Fig. 8 Cavity length versus cavitation number for water and R114 at two different radii between hub and casing

This effect is a velocity effect similar to the one discussed in Sec. 5. The relative flow velocity ωr increases proportionally to radius r. If the characteristic length chosen for the estimate of the transit time is the local blade chord length at the same radial coordinate, it also increases proportionally to radius r. Hence, the transit time is almost independent on r. More simply, the transit time can be computed from the mean axial flow velocity and inducer length, both independent on the radial coordinate. On the other hand, heat transfer is likely increasing with flow velocity, as explained in Sec. 4, so that the thermal time should increase with the increasing radial coordinate. As a consequence, the ratio τ/τ_T, which is an indicator of thermodynamic effect, is expected to decrease with increasing radius r, causing a reduction in the thermodynamic effect from hub to casing. As a consequence, it is expected that the shortening effect due to thermal delay is smaller at the casing than at the hub. This explains qualitatively the trend observed on Fig. 7.

Even though the shape of the leading edge cavitation appears similar in water and R114, differences in texture are visible on Fig. 6, which probably depict differences in void fraction and cavity thickness. Such differences, which were also found in numerical computations (e.g., Ref. [29]), might influence the development of cavitation instabilities discussed in Sec. 8 in a manner still difficult to anticipate.

7 Estimation of Temperature Depression

Applying the procedure used by Yoshida et al. [6] and Franc et al. [17], the amplitude of temperature depression within the cavities can be estimated indirectly from visualizations. This is done independently for the three different cylindrical sections between the hub and casing considered in the present work, and the results are compared.

The procedure consists in comparing curves $\ell(\sigma)$ with and without thermodynamic effect. These curves are presented on Fig. 8 for a given set of operating conditions. Due to the thermodynamic effect, cavities are shorter in R114 than in water at constant cavitation number. In other words, the cavitation number in R114 must be lowered in comparison to water to keep the cavity length constant. The procedure is based upon the determination of this shift in cavitation number, which is an indicator of the thermodynamic effect. It allows the computation of the cavity temperature depression or B-factor of Stepanoff.

The B-factor is plotted versus the cavity length on Fig. 9 for the three investigated radii. It increases with cavity length, as reported in other works [6,17]. For a given cavity length, the B-factor for leading edge cavitation appears larger at the hub than at the casing. However, if the B-factor is plotted versus the inducer cavitation number (Fig. 10), no systematic evolution is visible with the

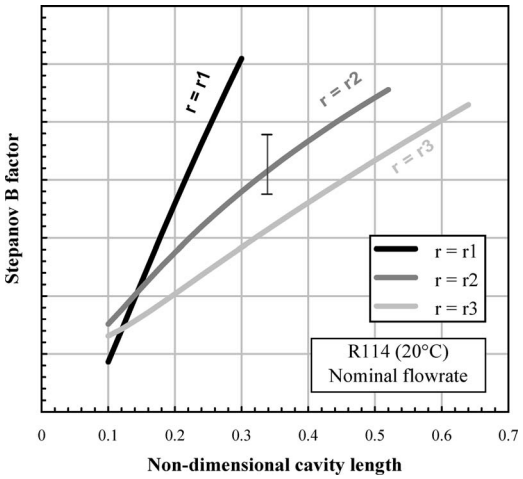

Fig. 9 B-factor of Stepanoff versus cavity length. Influence of radius between hub and casing. Cavity length is made nondimensional using blade spacing (R114 20°C, nominal flowrate).

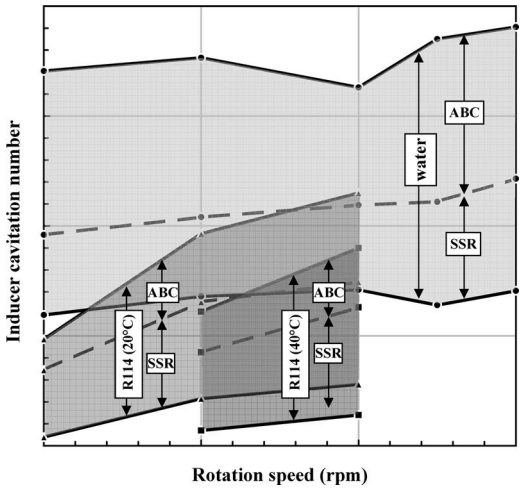

Fig. 11 Threshold values of cavitation number for onset and desinence of cavitation instabilities (ABC and SSR) for water and R114 at two different temperatures. Influence of rotation speed at nominal flowrate.

radius. Differences observed on Fig. 10 are of the order of magnitude of the uncertainty on the B-factor. Cavity temperature depression and, as a consequence, pressure inside the leading edge cavity can then be considered as independent of the radius. This conclusion, confirmed by the inspection of all other operating conditions, is quite reasonable and usually implicitly assumed.

Let us observe that, since the B-factor can be considered as constant for given operating conditions, a given test at a particular cavitation number is represented approximately by a horizontal line on Fig. 9. The increase in cavity length from hub to casing noticed previously is the reason why the three curves are separated on Fig. 9.

8 Thermodynamic Effect and Cavitation Instabilities

Thresholds for the onset of cavitation instabilities have been determined in water and R114, and are compared on Fig. 11. Regimes of alternate blade cavitation and supersynchronous rotating cavitation are delayed by the thermodynamic effect, as expected. This is visible when comparing data in water and R114, and also at different temperatures in R114.

As proposed by Tsujimoto [30], cavitation instabilities are expected to occur for a critical cavity length. This is due to the extra thickness of the cavity on a given blade, which changes the flow angle in the vicinity of the next blade. This mechanism requires that the cavity closes sufficiently near the leading edge of the following blade. Tsujimoto showed that alternate blade cavitation on a four-bladed inducer is expected to occur for a critical cavity length of the order of 65% of blade spacing.

In order to investigate the correlation between cavity length and cavitation instabilities, the critical cavity length at the onset of cavitation instabilities is plotted on Fig. 12 for all available data in water and R114. Although alternate blade cavitation occurs at a more or less constant cavity length, the critical cavity length is of the order of 10% only, which is much smaller than the expected 65%. Such a short cavity, which closes so far upstream the following blade, is unlikely to cause any substantial change in flow angle and to trigger the alternate blade cavitation instability. As for onset and, all the more, desinence of rotating cavitation, they cannot be characterized by a given critical cavity length. It is then concluded that the correlation between leading edge cavitation and cavitation instabilities is rather poor and it is conjectured that the correlation should be stronger with tip cavitation, which is not investigated here.

The lack of correlation between leading edge cavitation and cavitation instabilities is confirmed when considering thermody-

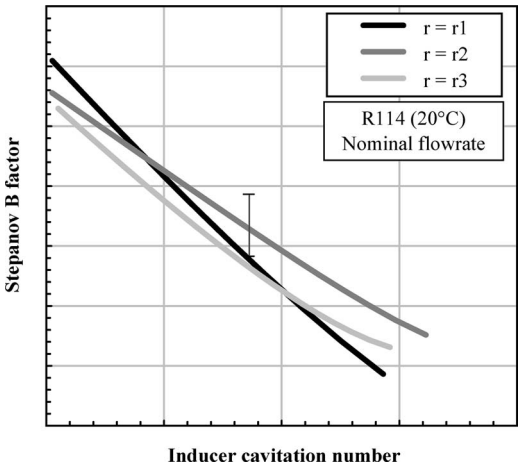

Fig. 10 B-factor of Stepanoff versus inducer cavitation number. Influence of radius between hub and casing. Cavity length is made nondimensional using blade spacing.

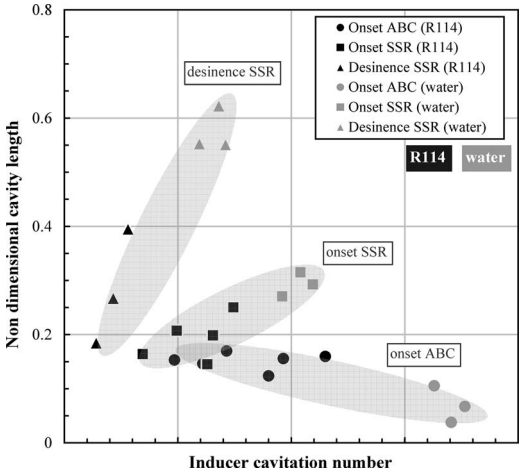

Fig. 12 Correlation between onset or desinence of cavitation instabilities (ABC and SSR) with the length of corresponding leading edge cavities for water and R114 at nominal flowrate

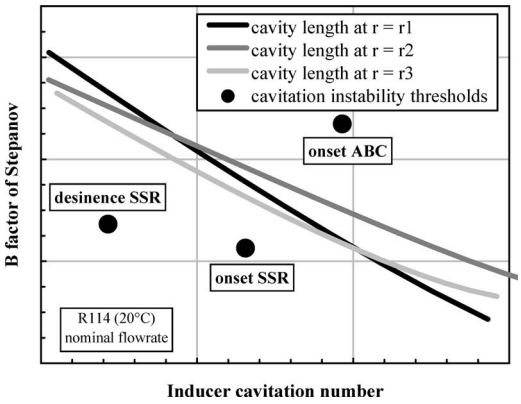

Fig. 13 Comparison of thermodynamic delay on cavity length and cavitation instabilities

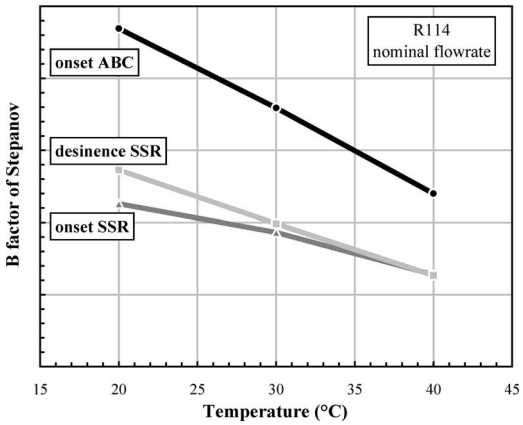

Fig. 15 Thermodynamic delay on cavitation instabilities versus liquid temperature

namic delay. The values of the B-factor of Stepanoff at the onset of alternate blade cavitation and rotating cavitation, and at the desinence of rotating cavitation, are compared with the values of the B-factor, which affect the development of leading edge cavities on Fig. 13.

The onset of alternate blade cavitation is affected by a delay significantly greater than that affecting the corresponding leading edge cavities. As for the onset of rotating cavitation, the delay is smaller than that of the associated cavities. The substantial differences in B-factors between the onset of cavitation instabilities and the corresponding leading edge cavities confirm the poor correlation between leading edge cavitation and cavitation instabilities.

The influence of rotation speed and liquid temperature on the values of the B-factor for cavitation instabilities is shown on Figs. 14 and 15, respectively. The onset of cavitation instabilities is generally delayed by an increase in rotation speed. The same trend was observed for the development of leading edge cavities.

As for the influence of liquid temperature, Fig. 15 demonstrates a clear reduction in thermodynamic delay with liquid temperature. No similar trend could be noticed for leading edge cavitation and it can be considered [17] that the delay in the development of leading edge cavities is roughly independent of liquid temperature in terms of the B-factor.

9 Conclusion

In water, i.e., without thermodynamic effect, the development of leading edge cavities on the inducer blades agrees with conventional results. In particular, cavity length is well correlated with parameter σ/α in the central most part of the machine.

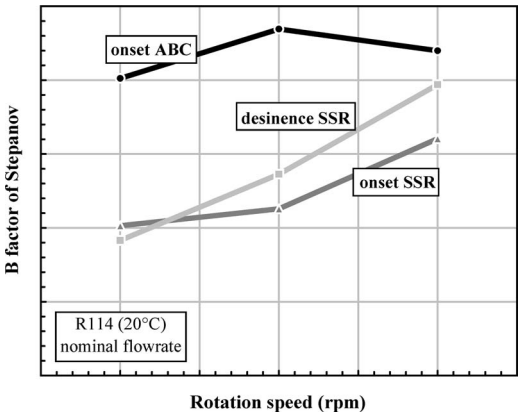

Fig. 14 Thermodynamic delay on cavitation instabilities versus rotation speed (R114 20°C, nominal flowrate)

The influence of rotation speed on cavity length is quite different with and without thermodynamic effect. In R114, the cavity length notably increases with flow velocity, whereas it is almost insensitive to velocity in water in the investigated range of rotation speed. This velocity effect is qualitatively explained by the influence of flow velocity on thermodynamic effect, which is analyzed through the consideration of two characteristic times: the transit and thermal time.

Although thermodynamic effect significantly reduces the length of leading edge cavities, the shape of cavities regarding the radial profiles of their closure line proves to be quite similar. A slight deviation to similarity has, however, been observed with a larger shortening effect at the hub relatively to the casing. This is again a velocity effect due to a smaller velocity on the hub side in comparison to casing.

The delay in the development of leading edge cavities due to thermal effects has been computed from the comparison of the cavity length with and without thermodynamic effect in the framework of a 2D analysis. The so predicted temperature depression inside the cavity appears independent of the radius of analysis, which tends to confirm the ordinary assumption of a uniform pressure in the cavity. Although a small velocity effect can be observed on the B-factor, the dominating parameter is the cavity length as pointed out by other investigations [6,17]. Direct measurements of temperature depression within the leading edge cavities are presented in a companion paper [18].

The delay on the onset of cavitation instabilities (alternate blade cavitation and rotating cavitation) increases with rotation speed, but decreases with liquid temperature. The related B-factors are significantly different from that of the corresponding cavities, so that a poor correlation between cavitation instabilities and leading edge cavities is concluded. This is confirmed by the fact that the onset of cavitation instability is not clearly associated to a given critical length of the leading edge cavities. In addition, alternate blade cavitation is observed for rather short cavities of the order of 10% of blade spacing, significantly smaller than the conventional value of 65% predicted by computations [30]. The poor correlation between leading edge cavitation and cavitation instabilities lead us to speculate that cavitation instabilities could be primarily controlled by tip leakage cavitation.

Acknowledgment

This research was supported by CNES/SNECMA (Contract No. 2005-015-I).

Nomenclature

B = B-factor of Stepanoff
$C_{p\,\min}$ = minimum pressure coefficient

$c_{p\ell}$ = liquid heat capacity
D = characteristic length
h = convection heat transfer coefficient
ℓ = cavity length
L = latent heat of vaporization
Nu = Nusselt number hD/λ_ℓ
Pr = Prandtl number
$p_{\min}$ = minimum pressure
p_u = upstream pressure
p_v = vapor pressure
r = radius of analysis between hub and casing
R = bubble radius or inducer radius
$\dot{R}$ = bubble growth rate
Re = Reynolds number
T_c = local temperature in the cavity
T_∞ = liquid temperature at infinity
V = flow velocity
α = angle of attack
α_ℓ = thermal diffusivity of the liquid
Δp_v = drop in vapor pressure (see Eq. (1))
Δp_v^* = characteristic drop in vapor pressure $\Delta T^* \cdot dp_v/dT$
ΔT = temperature drop in the cavitating flow $T_\infty - T_c$
ΔT^* = characteristic temperature drop $\rho_v L/(\rho_\ell c_{p\ell})$
λ_ℓ = thermal conductivity of the liquid
ρ_v = vapor density
ρ_ℓ = liquid density
Σ = Brennen's thermodynamic parameter
σ_v = cavitation number
ω = rotation angular velocity
τ = transit time D/V
τ^* = fluid characteristic time (see Eq. (7))
τ_T = thermal time $\mathrm{Nu}\tau^*$

References

[1] Holl, J. W., Billet, M. L., and Weir, D. S., 1975, "Thermodynamic Effects on Developed Cavitation," ASME J. Fluids Eng., **97**, pp. 507–514.
[2] Billet, M. L., Holl, J. W., and Weir, D. S., 1981, "Correlations of Thermodynamic Effects for Developed Cavitation," ASME J. Fluids Eng., **103**, pp. 534–542.
[3] Yoshida, Y., Kikuta, K., Hasegawa, S., Shimagaki, M., Nakamura, N., and Tokumasu, T., 2005, "Thermodynamic Effect on a Cavitating Inducer in Liquid Nitrogen," *Proceedings of the ASME FEDSM '05, 2005 ASME Fluids Engineering Division Summer Meeting*, Houston, TX, Jun. 19–23.
[4] Yoshida, Y., Sasao, Y., Okita, K., Hasegawa, S., Shimagaki, M., Nakamura, N., and Ikohagi, T., 2006, "Influence of Thermodynamic Effect on Synchronous Rotating Cavitation" *Proceedings of the Sixth International Symposium on Cavitation, CAV2006*, Wageningen, The Netherlands.
[5] Yoshida, S., Kikuta, K., Watanabe, M., Hashimoto, T., Nagaura, K., and Ohira, K., 2006, "Thermodynamic Effect on Cavitation Performances and Cavitation Instabilities in an Inducer" *Proceedings of the Sixth International Symposium on Cavitation, CAV2006*, Wageningen, The Netherlands.
[6] Yoshida, Y., Kikuta, K., Hasegawa, S., Shimagaki, M., and Tokumasu, T., 2007, "Thermodynamic Effect on a Cavitating Inducer in Liquid Nitrogen," ASME Trans. J. Fluids Eng., **129**, pp. 273–278.
[7] Yoshida, Y., Sasao, Y., Okita, K., Hasegawa, S., Shimagaki, M., and Ikohagi, T., 2007, "Influence of Thermodynamic Effect on Synchronous Rotating Cavitation," ASME Trans. J. Fluids Eng., **129**, pp. 871–876.
[8] Cervone, A., Bramanti, C., and Torre, L., 2007, "Setup of a High-Speed Optical System for the Characterization of Flow Instabilities Generated by Cavitation," ASME Trans. J. Fluids Eng., **129**, pp. 877–885.
[9] Cervone, A., Bramanti, C., Rapposelli, E., and d'Agostino, L., 2005, "Thermal Effects on Cavitation Instabilities in Helical Inducers," J. Propul. Power, **21**(5), pp. 893–899.
[10] Cervone, A., Bramanti, C., Rapposelli, E., Torre, L., and d'Agostino, L., 2006, "Experimental Characterization of Cavitation Instabilities in a Two-Bladed Axial Inducer," J. Propul. Power, **22**(6), pp. 1389–1395.
[11] Zoladz, T., 2000, "Observations on Rotating Cavitation and Cavitation Surge From the Development of the Fastrac Engine Turbopump," *Proceedings of the 36th AIAA/ASME/SAE/ASEE Joint Propulsion Conference*, Huntsville, AL, Jul. 17–19.
[12] Watanabe, S., Hidaka, T., Horiguchi, H., Furukawa, A., and Tsujimoto, Y., 2007, "Analysis of Thermodynamic Effects on Cavitation Instabilities," ASME Trans. J. Fluids Eng., **129**, pp. 1123–1130.
[13] Watanabe, S., Hidaka, T., Horiguchi, H., Furukawa, A., and Tsujimoto, Y., 2005, "Steady Analysis of Thermodynamic Effect of Partial Cavitation Using Singularity Method," *Proceedings of the FEDSM2005, 2005 ASME Fluids Engineering Division Summer Meeting and Exhibition*, Houston, TX, Jun. 19–23.
[14] Hosangadi, A., Ahuja, V., and Ungewitter, R. J., (2006) "Numerical Study of a Flat Plate Inducer: Comparison of Performance in Liquid Hydrogen and Water," *Proceedings of the Sixth International Symposium on Cavitation, CAV2006*, Wageningen, The Netherlands.
[15] Sinibaldi, E., Beux, F., and Salvetti, M. V., 2006, "A Numerical Method for 3D Barotropic Flows in Turbomachinery," Flow, Turbul. Combust., **76**, pp. 371–381.
[16] Coutier-Delgosha, O., Fortes-Patella, R., Reboud, J. L., Hakimi, N., and Hirsch, C., 2005, "Numerical Simulation of Cavitating Flow in 2D and 3D Inducer Geometries," Int. J. Numer. Methods Fluids, **48**, pp. 135–167.
[17] Franc, J. P., Rebattet, C., and Coulon, A., 2004, "An Experimental Investigation of Thermal Effects in a Cavitating Inducer," ASME J. Fluids Eng., **126**, pp. 716–723.
[18] Franc, J. P., Boitel, G., Riondet, M., Janson, E., and Ramina, P., 2010, "Thermodynamic Effect on a Cavitating Inducer—Part II: On-Board Measurements of Temperature Depression Within Leading Edge Cavities," ASME J. Fluids Eng., **132**, p. 021304.
[19] Franc, J. P., and Pellone, C., 2007, "Analysis of Thermal Effects in a Cavitating Inducer Using Rayleigh Equation," ASME J. Fluids Eng., **129**, pp. 974–983.
[20] Franc, J. P., and Michel, J. M., 2004, *Fundamentals of Cavitation Series: Fluid Mechanics and Its Applications*, Springer, New York, Vol. 76.
[21] Brennen, C. E., 1994, *Hydrodynamics of Pumps*, Concept ETI, Inc., Norwich, VT and Oxford University Press, New York.
[22] Brennen, C. E., 1995, *Cavitation and Bubble Dynamics*, Oxford University Press, New York.
[23] Bonnin, J., 1972, "Theoretical and Experimental Investigations of Incipient Cavitation in Different Liquids," ASME Paper No. 72-WA/FE-31.
[24] Bonnin, J., 1973, "Thermodynamic Parameters Involved in Boiling and Cavitation," *Proceedings of the 1973 Cavitation and Polyphase Flow Forum, Joint Fluids Engineering/Applied Mechanics Meeting*, Atlanta, Jun. 20–22.
[25] Fruman, D. H., Benmansour, I., and Sery, R., 1991, "Estimation of Thermal Effects on Cavitation of Cryogenic Liquids," Cavitation and Multiphase Flow Forum, ASME FED-Vol. 109, pp. 93–96.
[26] Fruman, D. H., Reboud, J. L., and Stutz, B., 1999, "Estimation of Thermal Effects in Cavitation of Thermosensible Liquids," Int. J. Heat Mass Transfer, **42**, pp. 3195–3204.
[27] Moore, R. D., and Ruggeri, R. S., 1968, "Prediction of Thermodynamic Effects of Developed Cavitation," NASA Report No. TN D-4899, Washington, DC.
[28] Hord, J., 1974, "Cavitation in Liquid Cryogens. IV. Combined Correlations for Venturi, Hydrofoil, Ogives and Pumps," NASA Report No. CR-2448, Washington, DC.
[29] Hosangadi, A., Ahuja, V., Ungewitter, J., and Busby, J., 2007, "Analysis of Thermal Effects in Cavitating Liquid Hydrogen Inducers," J. Propul. Power, **23**(6), pp. 1225–1234.
[30] Tsujimoto, Y., 2001, "Simple Rules for Cavitation Instabilities in Turbomachinery," *Proceedings of the CAV 2001 Fourth International Symposium on Cavitation*, California Institute of Technology, Pasadena, CA, Jun. 20–23.

Jean-Pierre Franc
e-mail: jean-pierre.franc@inpg.fr

Guillaume Boitel

Michel Riondet

LEGI,
Grenoble Institute of Technology,
Université Joseph Fourier,
Centre National de la Recherche Scientifique,
BP 53,
38041 Grenoble Cedex 9, France

Éric Janson

Pierre Ramina

Claude Rebattet

CREMHYG,
Grenoble Institute of Technology,
BP 95,
38402 Saint-Martin d'Hères Cedex, France

Thermodynamic Effect on a Cavitating Inducer—Part II: On-Board Measurements of Temperature Depression Within Leading Edge Cavities

Temperature depression within the leading edge cavities on a space inducer is measured in Refrigerant 114 using miniature thermocouples mounted on the rotating blades. Time-averaged values of cavity temperature depression are determined all along the descent in cavitation number and correlated with the extent of cavities. In addition to mean values, temperature fluctuations are analyzed with respect to the onset of cavitation instabilities, namely, alternate blade cavitation and supersynchronous rotating cavitation. Temperature spectra relative to a rotating frame of reference are compared with pressure spectra obtained in a fixed frame of reference. Temperature oscillations issued from different blades are compared, and phase shifts between consecutive and opposite blades are evaluated in the case of the supersynchronous instability regime.
[DOI: 10.1115/1.4001007]

1 Introduction

In cavitation, the heat required for vaporization is extracted to the two-phase region and surrounding area. As a result, the temperature in the cavitating region is smaller than that in the liquid bulk.

The amplitude of temperature depression depends particularly on the thermodynamic properties of the fluid. It may be completely negligible as in water at room temperature or quite significant as in liquid cryogens where it can be of the order of several degrees.

In a first approach, consider a two-phase mixture with quality x and suppose that vaporization occurs adiabatically so that the heat required for vaporization is taken to the liquid.[1] A small increase dx in quality will lead to temperature drop dT, which can be estimated from the following heat balance:

$$Ldx = (1 - x)c_{p\ell}dT \tag{1}$$

The group of parameters $\Delta T^* = \rho_v L/(\rho_\ell c_{p\ell})$ is generally introduced in the field of thermodynamic effect. It has the dimension of a temperature and depends only on the fluid nature. It is commonly used to make nondimensional the cavity temperature depression by introducing the Stepanoff factor (or Jakob number in the context of boiling)

$$B = \frac{\Delta T}{\Delta T^*} \tag{2}$$

Integration of heat balance (1) leads to the following relationship between B-factor and void fraction:

$$B = \frac{\rho_\ell}{\rho_v}\ln\left(1 + \frac{\alpha}{1-\alpha}\frac{\rho_v}{\rho_\ell}\right) \cong \frac{\alpha}{1-\alpha} \tag{3}$$

which is represented in Fig. 1. The interesting point is that B is of the order of unity in a wide range of void fractions except for void fractions approaching unity, i.e., for pure vapor cavities, for which this simplistic local homogeneous equilibrium approach obviously stops working. In other words, ΔT^* appears to be a relevant order of magnitude of temperature depression, which is confirmed by experiments.

Physics of thermodynamic effect is actually more complicated, and even supposing Eq. (3) were fully relevant, void fraction in cavity flows is generally unknown so that Eq. (3) is not of great use in practice to estimate temperature depression. Experiments on thermodynamic effect are then necessary to investigate the actual magnitude of temperature depression.

Hord et al. [1–4] conducted a series of experiments on several geometries (Venturi, hydrofoil, and ogives) in liquid nitrogen or hydrogen. Pressure and temperature measurements within fully developed cavities were measured. From the comparison of both types of measurements, Hord et al. [1–4] concluded that thermodynamic equilibrium generally prevails throughout the vaporous cavities.

Billet and co-workers [5,6] measured temperature depression within developed cavities on ogives in Freon 113. They showed that maximum temperature depression occurs near the leading edge of the cavity and that temperature depression decreases roughly linearly along the cavity.

Fruman et al. [7] and Belahadji et al. [8] conducted experiments on a Venturi in R114. They confirmed thermodynamic equilibrium in the front part of the cavity and also found a progressive diminution of temperature and pressure depression along the vaporous cavity toward the cavity wake where the measured temperature matches the liquid bulk temperature.

The investigations mentioned above were carried out on rather academic geometries. No temperature depression measurements are available for cavities on a rotating machinery as the liquid rocket inducer considered in the present work. Moreover, mea-

[1]The heat supplied by the vapor is usually negligible.

Contributed by the Fluids Engineering Division of ASME for publication in the JOURNAL OF FLUIDS ENGINEERING. Manuscript received September 29, 2008; final manuscript received December 14, 2009; published online February 17, 2010. Assoc. Editor: Steven Ceccio.

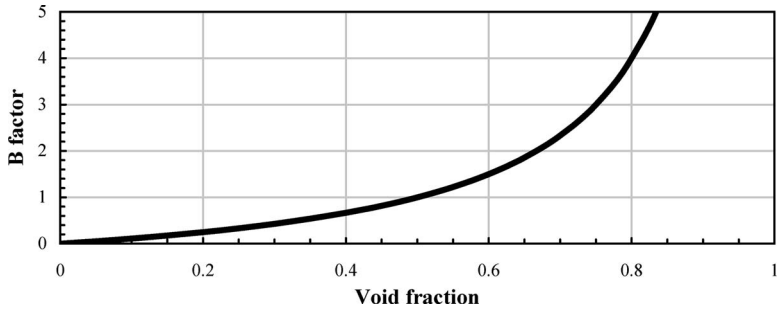

Fig. 1 *B* factor versus void fraction

surements on 2D geometries are difficult to transpose and corresponding correlations have not been validated for inducers.

The only available results on temperature depression within cavities on an inducer are indirect estimates obtained from a comparison of visualizations with and without a thermodynamic effect. Franc et al. [9,10] estimated the temperature depression within the leading edge cavities of a four-bladed inducer in Refrigerant 114 and showed that it increases roughly linearly with cavity length. Yoshida et al. [11] estimated the temperature depression within tip cavities on a three-bladed inducer in liquid nitrogen and also found a strong correlation between temperature depression and cavity length.

Up to now, there is no evidence that previous estimates of temperature depression within cavities on an inducer, based on the usual scaling law in cavitation number, are accurate estimates of the actual temperature depression. This is the reason why a direct measurement of temperature within leading edge cavities on a rotating inducer has been attempted in the present work.

2 Experimental Facility

In order to measure temperature within the leading edge cavities, a four-bladed inducer was equipped with thermocouples of 0.5 mm in diameter, as shown in Figs. 2 and 3. One of them (sensor 1 not visible on the figures) was mounted on the front bulb for the measurement of the liquid reference temperature whereas sensors 2–7 were mounted directly on the blades. Measurements as close as possible to the cavity leading edge were favored since temperature depression is expected to be maximum just downstream cavity detachment. However, because of the sharpness of the blades, they could not be mounted in too close proximity of the leading edges. Standard thermocouples of type *K* (Chromel/Alumel) were chosen. To minimize electric disturbances, the hot junction is electrically insulated from the protection tube. This unfortunately increases the response time, which is estimated to 30 ms. It corresponds to a frequency of about 33 Hz, which is enough to detect the rotating cavitation instability whose characteristic frequency is rather small in a rotating frame of reference (typically $0.16f_0$), as explained in Sec. 4.

Two different techniques were used to mount the sensors on the blades, as shown in Fig. 3. For part of them, the thermocouple protection tube emerges perpendicularly to the blade surface on about 0.5 mm. This is the length that will be immersed in the cavity. The other ones were curved along the blade on a length of 3–4 mm in the upstream direction. This second mounting technique was used to increase the immersion length and try to improve the quality of the measurement.

As a matter of fact, we did not observe any significant difference on the mean values of the cavity temperature between both cases, and curved thermocouples did not appear more accurate than straight ones for mean temperature measurements, contrary to what was expected. However, the analysis of temperature fluc-

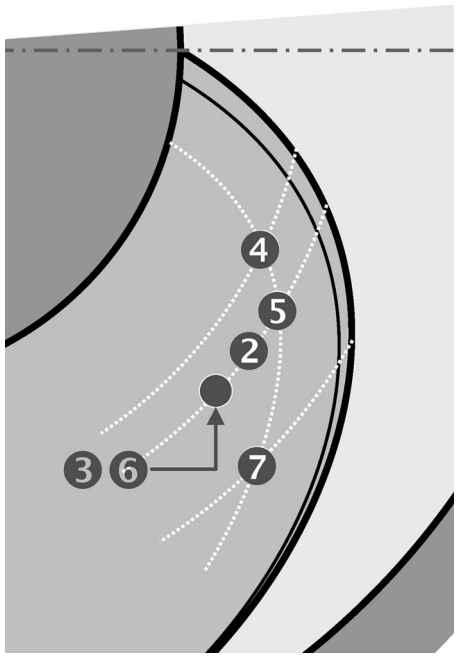

Fig. 2 Location of temperature sensors on the inducer. Sensors 3, 5, and 7 are straight whereas sensors 2, 4, and 6 are curved. Sensor 3 is on blade 1, sensor 4 is on blade 2, sensors 5, 6, and 7 are on blade 3, and sensor 2 is on blade 4.

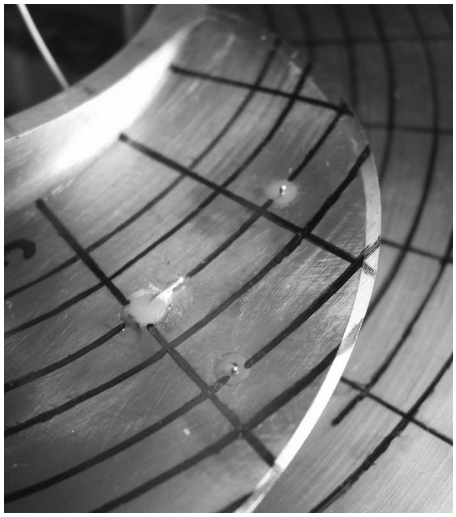

Fig. 3 View of one curved and two straight thermocouples on blade 3

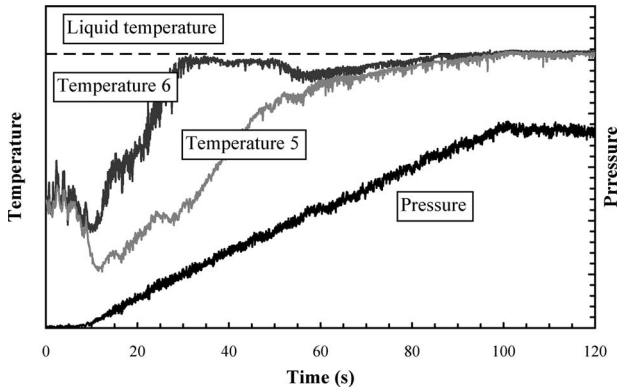

Fig. 4 Typical evolution of temperatures at the end of a cavitation test during pressure rise (R114 30°C)

tuations showed that curved thermocouples are considerably more sensitive to cavitation instabilities than straight ones, as shown in Sec. 4.

The influence of blade surface temperature was minimized by thermally insulating the thermocouple tubes from the blade using an epoxy glue filling the 3 mm holes machined in the blades.

For technical reasons, it was decided to measure independently the reference liquid temperature and the cavity temperature but not the difference. Telemetry is used for the wireless transmission of data from the rotating machinery. Eight channels are available but only seven were used since one thermocouple was broken at the beginning of the tests. On the whole, the instrumentation proved to be quite robust and all thermocouples (except one) survived to the vibrations, sometimes quite important, induced by cavitation instabilities and two-phase breeding. No pressure transducer was mounted on the blades and the thermodynamic equilibrium condition could not be checked directly.

Concerning signal acquisition, 32,000 data were taken at a sampling rate of 800 Hz during 40 s. Mean values presented in this paper are computed on the record length of 40 s. The chosen sampling rate is fully appropriate to an analysis of temperature fluctuations induced by cavitation instabilities, as shown in Sec. 4.

The protection tubes of the thermocouples could not be embedded into the blades, on their pressure side, for resistance reasons because of the small thickness of the blades. As a consequence, they induce an unwanted cavitation at low cavitation number. The slightly emerging tip of the thermocouples also induces an abnormal cavitation on the blade suction side and on the bulb. Comparisons of visualizations of attached cavities with and without instrumentation showed that the intrusive nature of the instrumentation remains quite moderate and, in particular, does not affect significantly cavity lengths.

Four additional platinum resistance temperature sensors were mounted on casing close to the inducer leading edges in order to measure the reference liquid temperature.

The measuring procedure starts with a noncavitating test by adjusting the offsets of each channel so that all thermocouples agree with Pt100 sensors. Gains were kept unchanged during all tests and deduced from a fine preliminary calibration out of the test section. Calibration has been checked in situ on several points when operating under noncavitating conditions by comparison with platinum sensors.

During cavitation tests, measured temperatures progressively decrease with the development of cavitation, as further discussed in Sec. 3. At the end of each cavitation test, it has been checked that all thermocouples recover their original level without any appreciable shift (see Fig. 4). The global uncertainty on cavity temperature measurements was estimated of the order of 5–10% of the maximal measured temperature depression.

Figure 4 presents a typical evolution of two measured temperatures at the end of a cavitation test during pressure rise together with the evolution of pressure in the test section. It shows that thermocouple 5 recovers the liquid temperature later than thermocouple 6 during the pressure rise. The reason is the following. For each sensor, the temperature rise observed in Fig. 4 corresponds to the cavity closure line passing over the sensor. Since thermocouple 5 is located upstream of thermocouple 6, it is left by the shortening cavity somewhat later during the pressure rise.

The liquid temperature measured by the thermocouple mounted on the bulb agrees fairly well with Pt100 thermometers mounted on the casing within only a few tenths of a degree. The liquid temperature chosen as a reference in this paper is actually the average of the four platinum sensors.

For liquid flows at high velocities, viscous dissipation in the boundary layer acts as a heat source, which increases the fluid temperature at the wall. In the case of an adiabatic wall, the difference between the wall temperature T_w and the liquid freestream temperature T_∞ is given by (see, e.g., Ref. [12])

$$T_w - T_\infty = r\frac{U_\infty^2}{2c_{p\ell}} \tag{4}$$

For turbulent boundary layers, the recovery factor r was found experimentally to be $r=\sqrt[3]{\mathrm{Pr}}$. The velocity to be considered in Eq. (4) is the velocity inside the leading edge cavity, which is probably an order of magnitude smaller than the liquid freestream velocity. Assuming a typical velocity of 10 m/s, Eq. (4) gives a temperature rise due to viscous dissipation of the order of 0.1 K in Refrigerant 114. This is a rough estimate since the flow is not fully wetted and the wall cannot be considered as adiabatic. In practice, it was considered that viscous dissipation within the cavities is not a major difficulty for temperature measurements especially for thermocouples emerging from the wall, and the corresponding uncertainty was included in the global uncertainty mentioned above.

3 Cavity Temperature Depression Measurements

Figure 5 presents a typical evolution of cavity temperature depression during a cavitation test. Data were obtained step by step during pressure reduction after the operating conditions have been stabilized for a few minutes following each pressure step. The decrease in cavity temperature follows four main stages.

At the beginning of the cavitation test, i.e., at high enough cavitation number, sensors are not immersed in the cavity, which is too short. In spite of this, a temperature difference is measured although it remains relatively small. This is due to cavitation generated locally by the sensor tip, which is not flush-mounted but emerges a little from the blade. The corresponding measurements have then no physical meaning with respect to leading edge cavitation since the associated cavitation spot is artificially generated.

A region of higher slope is then observed with a more rapid increase in temperature depression. This region corresponds to the arrival of cavity closure in the sensor zone. From that point and for smaller cavitation numbers, the sensor is fully immersed in the cavity and the measured temperature is actually relevant of the actual cavity temperature.

This transition region is followed by a rather flat region where cavity temperature depression does not vary much whereas the leading edge cavity continues to grow. This proves that temperature inside the cavity is not far from being constant except in the vicinity of cavity closure.

After this plateau, temperature depression drops suddenly with a further decrease in cavitation number. This corresponds to an increase in cavity temperature, which was systematically correlated with vaporization in the inlet duct. Two main reasons can be put forward to explain this trend.

First, when the incoming flow contains a fraction of vapor as it is the case when two-phase breeding occurs, it is likely that vapor bubbles generated upstream of the cavitating region partly supply

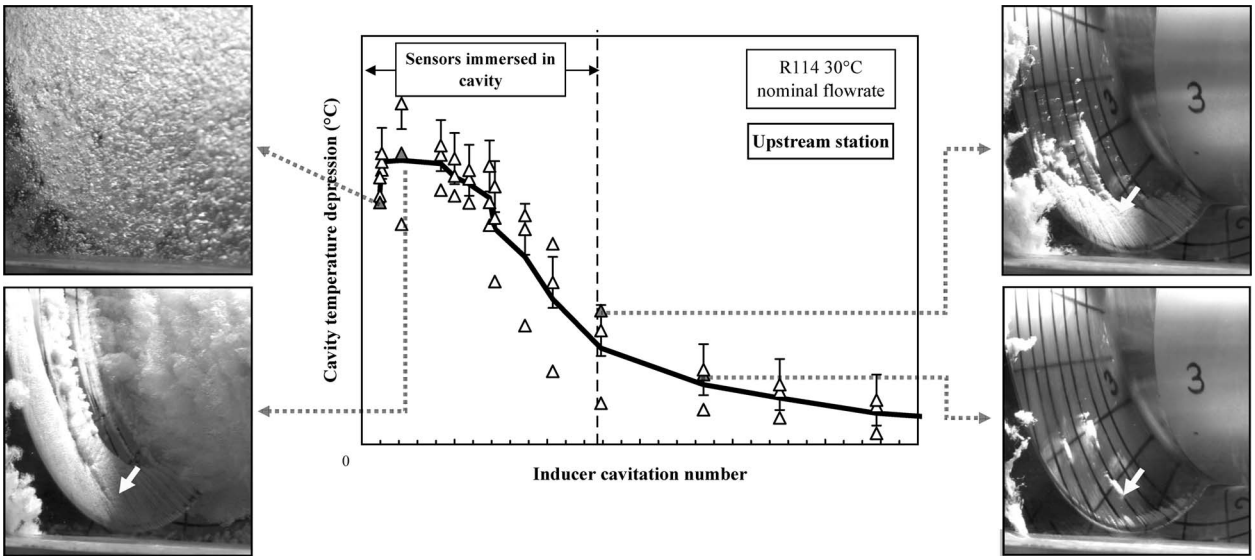

Fig. 5 Evolution of cavity temperature depression during a cavitation test at the most upstream station (sensors 4, 5, and 7) and correlation with cavity visualizations. The white arrow indicates location of sensor 5 (R114 30°C).

the leading edge cavity with vapor. This should reduce the amount of liquid to be vaporized at the interface. As a consequence, the required heat flux at the interface should be reduced and, if the heat transfer coefficient is assumed unchanged, the required temperature difference will be reduced too.

Second, heat transfer at the interface might be enhanced by two-phase breeding. For classical convective heat transfer on a wall, it is well-known that heat transfer can be significantly enhanced due to additional turbulence generated by the bubbles, as in the case of nucleate boiling. By analogy, heat transfer at the cavity interface might also be enhanced by traveling bubbles. If so, the required temperature difference for the same heat flux should be smaller. The enhancement of heat transfer by traveling bubbles together with the migration of bubbles from the liquid bulk toward the cavity are two possible explanations for the sudden increase in cavity temperature observed at the onset of two-phase breeding.

The results presented in Fig. 5 are related to sensors 4, 5, and 7, which are at the most upstream position, only a few millimeters downstream cavity leading edge (see Fig. 2). The differences between the three measurements especially near the plateau are of the order of the estimated uncertainty so that no definite trend can be deduced from the comparison of all three measurements.

Similar results but related to the most downstream position (sensors 3 and 6) are presented in Fig. 6. The two sensors (which are located on two different blades) give very comparable values.

For comparison, the mean temperature depression based on the three upstream sensors (already shown in Fig. 5) is also plotted. The rise in temperature depression related to the passage of cavity closure is shifted toward smaller cavitation numbers when moving downstream, as expected because of the increase in cavity length with a reduction in cavitation number.

The maximum temperature depression is somewhat smaller downstream, so that it could be expected that the temperature slightly increases along the cavity before matching the liquid temperature in the cavity closure region. However, the difference is of the order of the estimated uncertainty. It is then difficult to conclude about the evolution of temperature inside the cavity from present measurements. The examination of all other results obtained for different operating conditions did not allow us to point out a clear trend for temperature variation inside the cavity, more especially as all sensors were arranged deliberately within a rather small area downstream cavity detachment to better apprehend the maximum value of thermodynamic effect expected in the vicinity of cavity detachment. It was then concluded that the temperature variations within the leading edge cavities remain quite limited (and in any case smaller or of the order of the measurement uncertainty) for the most part of the cavity except near closure.

No temperature rise is measured in the cavity closure region though condensation of cavitation bubbles restores heat to the surrounding fluid. It is supposed that the high turbulent rate at closure together with the break-up of the vapor phase into many small scale structures considerably enhances heat transfer and increases the volume of liquid absorbing the latent heat. As a consequence, the temperature is expected to be almost uniform at closure and very close to the liquid freestream temperature.

4 Cavitation Instabilities and Temperature Fluctuations

In addition to mean values, temperature fluctuations were examined and compared with the onset of cavitation instabilities.

The two main regimes of instability observed on the four-bladed inducer tested here are recalled in Fig. 7 obtained from

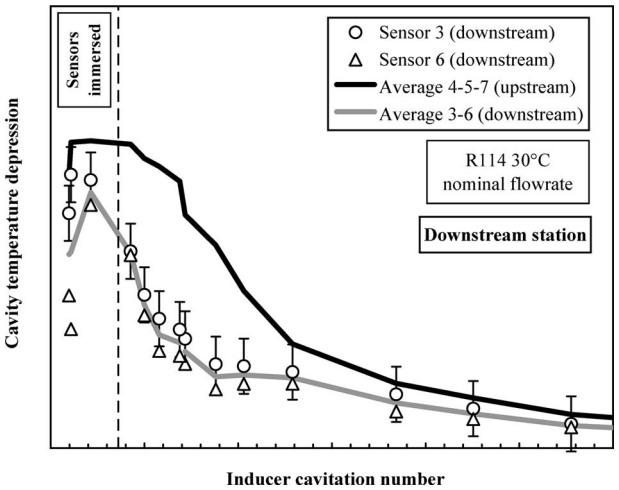

Fig. 6 Evolution of cavity temperature depression during a cavitation test at the downstream station. Comparison with upstream station (R114 30°C).

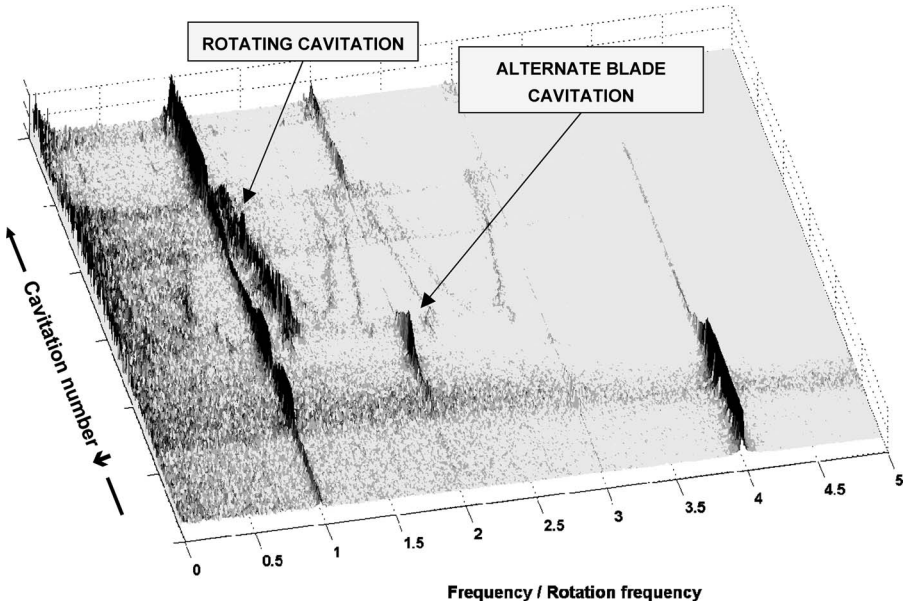

Fig. 7 Typical spectra of pressure fluctuations on the four-bladed tested inducer in water showing the two main cavitation instabilities, namely, alternate blade cavitation and supersynchronous rotating cavitation. Spectra have been obtained from a pressure transducer mounted on the casing in the neighborhood of the leading edges.

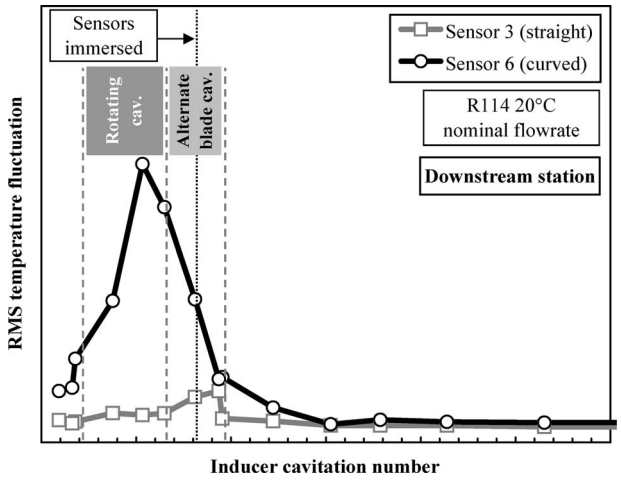

Fig. 8 Evolution of rms value of temperature fluctuations during a cavitation test (R114 20°C) and comparison with cavitation instabilities (alternate blade cavitation and supersynchronous rotating cavitation)

pressure measurements conducted in a fixed frame of reference. During the progressive reduction in cavitation number of a typical cavitation test, the alternate blade cavitation instability responsible for the peak at twice the rotation frequency is first observed. Then, rotating cavitation at a slightly supersynchronous frequency appears. The supersynchronous frequency progressively approaches the rotation frequency when the cavitation number decreases before being suddenly locked on the rotation frequency when it is close enough to it. Further details on the desinence of the supersynchronous instability are given at the end of Sec. 5 from temperature measurements conducted in the rotating frame of reference.

Figure 8 presents a typical example of the evolution of the rms value of temperature fluctuations during a cavitation test. It shows that temperature fluctuations measured by sensor 6 exhibit a serious increase in the domain of cavitation instabilities and especially when supersynchronous rotating cavitation occurs, whereas fluctuations on sensor 3 remain at a low level in spite of instabilities.

To further analyze differences, Fig. 9 presents an example of time recordings for sensors 3, 5, and 6 under the rotating cavitation instability together with the reference liquid temperature.

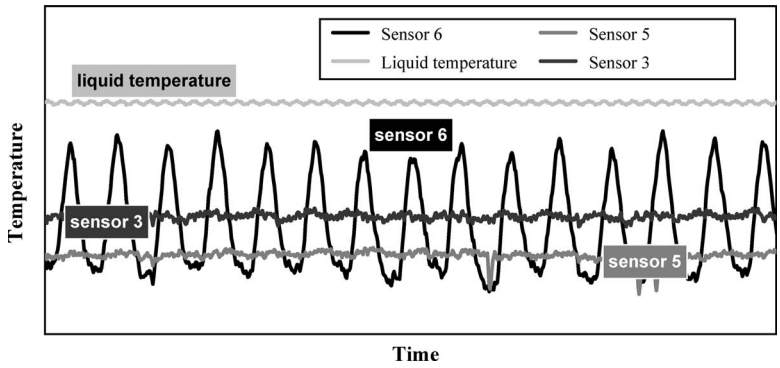

Fig. 9 Comparison of signals of sensors 5 and 6 (blade 3) and 3 (blade 1) under supersynchronous rotating cavitation (R114 20°C)

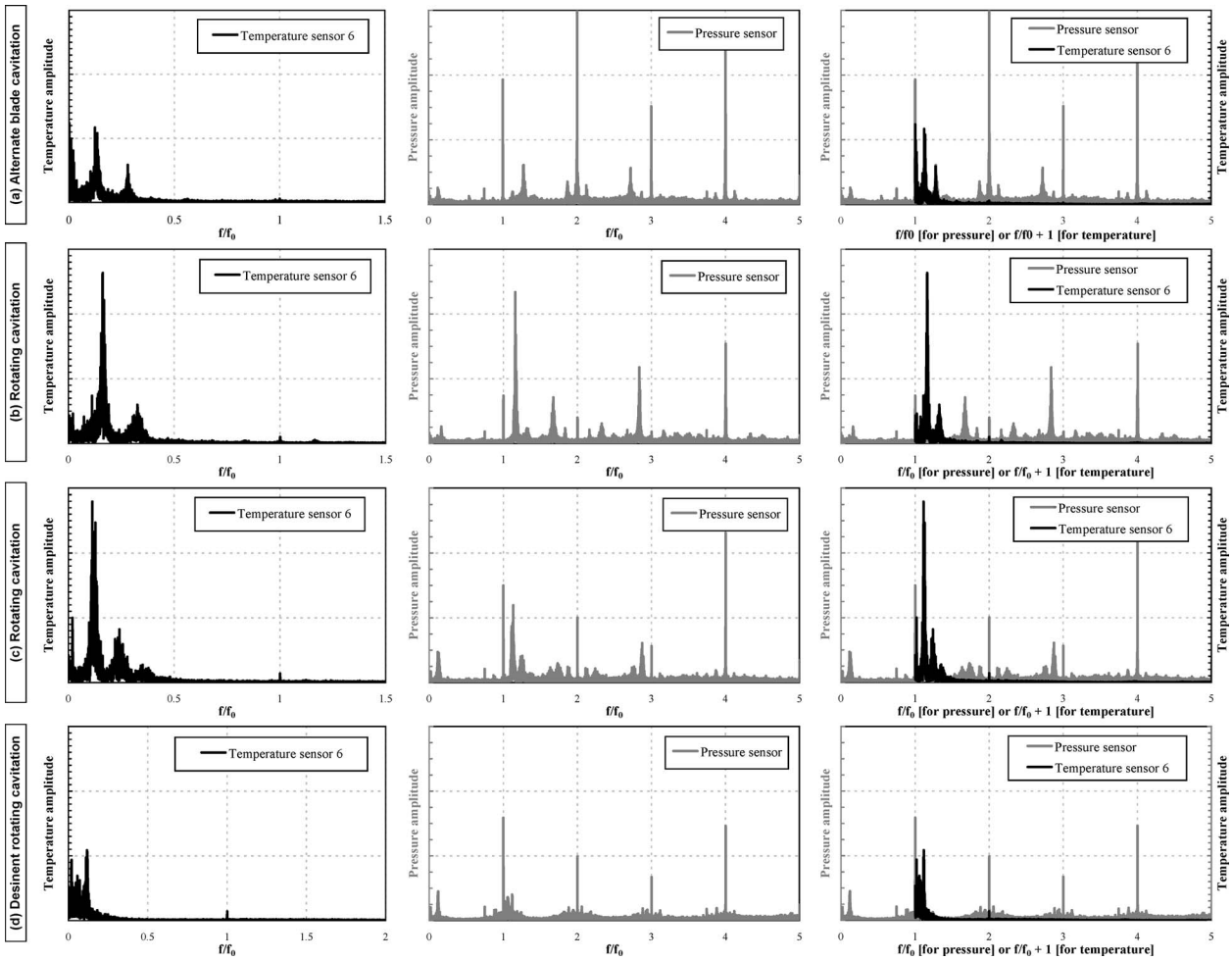

Fig. 10 Comparison between temperature and pressure spectra under alternate blade cavitation and supersynchronous rotating cavitation. For condition (*a*), cavity closes in the vicinity of temperature sensor 6 and downstream for conditions (*b*), (*c*), and (*d*). Same operating conditions as Fig. 8 (R114 20°C).

Sensor 5, which is the most upstream, presents negligible fluctuations and is supposed to give the temperature of vapor inside the cavity. Signal from sensor 6 fluctuates very regularly between nearly the cavity temperature as measured upstream by sensor 5 and a higher level somewhat below the liquid temperature. Signal from sensor 3, which is located on opposite blade but at the same station as sensor 6, is almost constant. A careful examination of Fig. 9 shows, however, that it oscillates at the same frequency but with a considerably smaller amplitude. In spite of fluctuations, the average temperature given by both sensors 3 and 6 is the same.

The reason for a different response of sensors 3 and 6, which are positioned at the same location though on opposite blades, is not yet fully understood. The main difference between both thermocouples is that sensor 3 (which is insensitive to cavitation instabilities) is straight whereas sensor 6 is curved. A much longer part of thermocouple 6 is then immersed in the cavity. In addition, due to the difference in mounting, curved sensors emerge a bit more from the blade surface than straight ones. Hence, the measurement point is closer to the cavity interface for curved sensors. These differences in mounting are probably at the origin of differences in response, but further investigations are needed to better understand the influence of mounting on sensor response.

In order to confirm that temperature oscillations are actually induced by the rotating cavitation instability, a spectral analysis has been carried out on temperature and pressure signals. Figure 10 presents a comparison of temperature and pressure spectra during a cavitation test. The comparison is focused on the domain of cavitation instabilities, from alternate blade cavitation (Fig. 10(*a*)) to rotating cavitation (Figs. 10(*b*) and 10(*c*)) whereas Fig. 10(*d*) corresponds to the desinence of the supersynchronous instability.

The temperature spectrum shown in Fig. 10(*b*) presents a dominant peak at reduced frequency $f/f_0 \cong 0.16$. As for the corresponding pressure spectrum, the major peak, which is the signature of supersynchronous rotating cavitation, is observed at $f/f_0 \cong 1.16$. The difference is exactly 1. This is due to the fact that pressure signals are relative to a fixed frame of reference since pressure transducers are mounted on the housing, whereas temperature spectra are relative to the rotating frame of reference.

For comparison, temperature and pressure spectra are superimposed after adding the inducer rotation frequency f_0 to the frequency scale of the temperature spectrum. A perfect coincidence of the dominant peak is observed, so that there is no doubt that the observed temperature fluctuations are actually caused by rotating cavitation.

This conclusion has been confirmed by the comparison of several other temperature and pressure spectra. In particular, when cavitation number is decreased (as shown in Fig. 10), both peaks keep strongly correlated until the supersynchronous frequency, which progressively decreases, becomes locked on the inducer rotation frequency and the instability vanishes.

Contrary to rotating cavitation, the alternate blade cavitation instability corresponds to a cavitation pattern fixed in the rotating frame of reference with the succession of a long and a short cavity

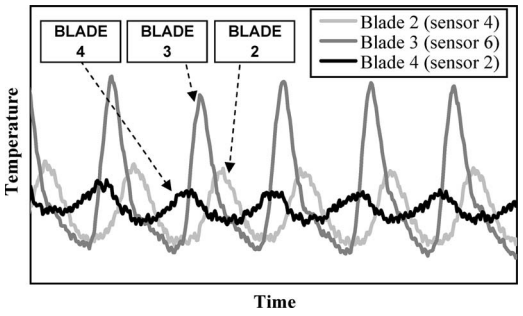

Fig. 11 Comparison of temperature fluctuations on blades 2, 3, and 4 under supersynchronous rotating cavitation (R114 20°C)

always attached to the same blades. The associated frequency, which is visible on pressure spectra at $f/f_0=2$, is unsurprisingly not detected by on-board temperature measurements (see Fig. 10(*a*)). However, the temperature spectrum presents a peak (together with a first harmonic) similar to that observed in the rotating cavitation regime, even though smaller. On the pressure spectrum, the supersynchronous frequency is hardly visible. The first harmonic is more distinct although much smaller than the dominant peak at $f/f_0=2$.

These observations show that the supersynchronous instability is more or less underlying behind the alternate blade cavitation regime, gains importance as the cavitation number is decreased, and finally becomes predominant. The transition from alternate blade cavitation to rotating cavitation could not be further analyzed from the present investigation because of a too large step in cavitation number during the descent.

5 Temperature Oscillations on Different Blades

Figure 11 presents a comparison of temperature oscillations measured on different blades in the rotating cavitation regime. The amplitudes of oscillations are different, which is probably due to the fact that the considered sensors are positioned at different locations and maybe also to possible small differences in mounting although all three sensors are of curved type. In spite of differences in amplitude, which are difficult to interpret, Fig. 11 shows that the same characteristic frequency is detected by all three sensors.

This is confirmed by Fig. 12, which shows that the normalized spectra are quite similar. Some differences, relatively to the importance of the first harmonic, in particular, are, however, observable. The first harmonic is more developed for sensor 6. This is the signature of a more pronounced dissymmetry of temperature signal coming from sensor 6 in comparison to the two other sensors as it can be observed on the signals plotted in Fig. 11. As a consequence, signals coming from different blades are not exactly superposable and correlation between them is expected to be imperfect.

As for phase differences, they are estimated below on the basis of the computation of correlation coefficients between temperature signals recorded on different blades. Figure 13 presents a typical evolution of computed correlation factors as a function of the phase difference. The phase shift, which makes correlation maximum, is plotted in Fig. 14. Because the three pressure transducers are not located exactly at the same point on the three different blades, computed optimal phase differences have been corrected considering the difference in angular location between sensors.

If it is assumed that the supersynchronous regime is a wavelike instability, which rotates at a constant angular velocity in the rotating frame of reference, the phase difference should be 90 deg between two consecutive blades and 180 deg between two opposite blades for a four-bladed inducer. Figure 14 shows that the

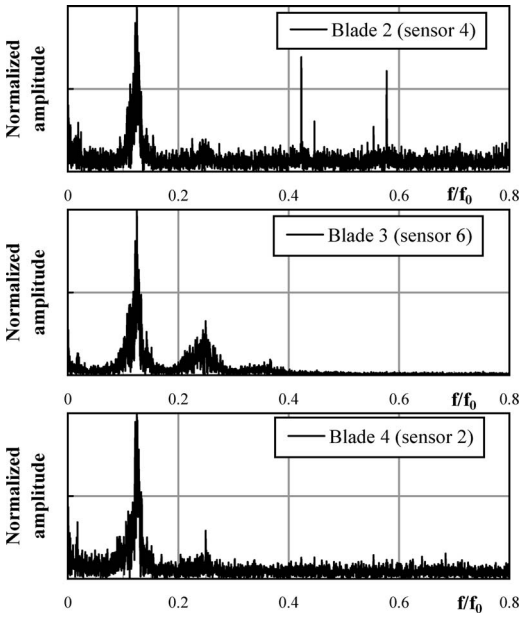

Fig. 12 Comparison of temperature spectra on blades 2, 3, and 4 under supersynchronous rotating cavitation (same operating conditions as Fig. 11)

phase difference between blades 2 and 3 is close to 90 deg whereas it is somewhat smaller for blades 3 and 4. The phase difference between blades 2 and 4 (which is the sum) is also somewhat smaller than the expected value of 180 deg.

In the present state of the investigations, it is difficult to conclude whether such differences are a significant feature of the supersynchronous instability or if they are due to other factors as differences or even deficiencies in the instrumentation. Let us recall that the transducers are not exactly at the same location on the blades and that the measured amplitudes are significantly different for unknown reasons as mentioned previously. In addition let us observe that, because of the relative flatness of the curves of Fig. 13 near their maximum, the optimal phase difference is affected by a relatively high uncertainty. Moreover, the maximum correlation, which is around 65% for two consecutive blades, drops to only 45% for opposite blades, which confirms that the shapes of the signals differ to some extent, as observed previously.

Nevertheless, present temperature measurements confirm that, in the rotating frame of reference, the supersynchronous instability rotates in the same direction as the inducer rotation and that temperature signals are approximately in quadrature for consecutive blades and in opposite phase for opposite blades. The use of

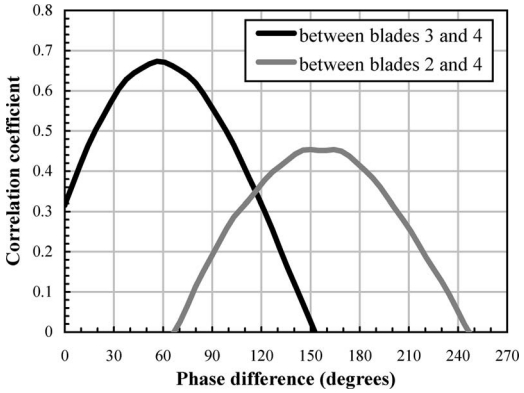

Fig. 13 Computed correlation coefficients versus phase difference for temperature signals measured on different blades

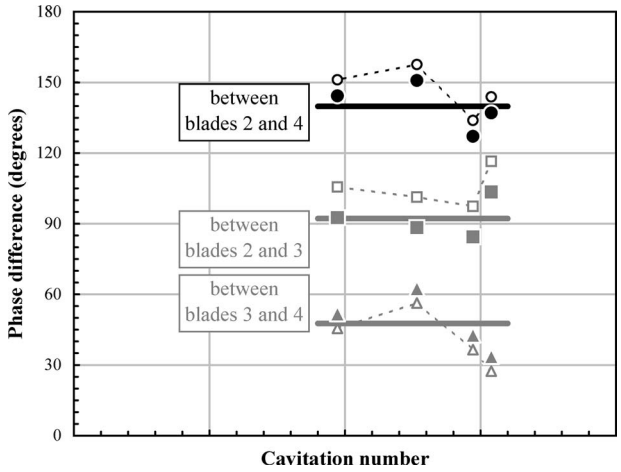

Fig. 14 Phase shift between blades 2, 3, and 4 as a function of the cavitation number under supersynchronous rotating cavitation. The dotted lines correspond to rough values, whereas the bold lines correspond to values corrected of the difference in angular location of temperature sensors.

on-board sensors appears to be a valuable means to further investigate the features of the supersynchronous instability in the rotating frame of reference, in addition to investigations in the fixed frame of reference from transducers mounted on the casing.

A final remark concerns the evolution of the shape of the temperature signal near the desinence of rotating cavitation. Figure 15 presents a comparison of typical temperature oscillations in the rotating cavitation regime and at desinence, and Fig. 16 presents the corresponding spectra. Rotating cavitation is here characterized by a major frequency of $0.125f_0$ in the rotating frame of reference with a first harmonic at $0.25f_0$, which accounts, as already mentioned, for the dissymmetry of the oscillation.

At desinence, two major changes are observed. The supersynchronous oscillation frequency is approaching 0 in a rotating frame of reference, as known from conventional investigations in a fixed frame of reference, which have shown that the supersynchronous frequency gradually approaches the rotation frequency (see, e.g., Fig. 7).

In addition, present measurements in a rotating frame of reference show that one oscillation out of two is fading away (Fig. 15). This results in a drop in the apparent frequency of oscillation, which jumps from $0.125f_0$ to about $0.050f_0$ between the two neighboring points in cavitation number considered in Fig. 15.

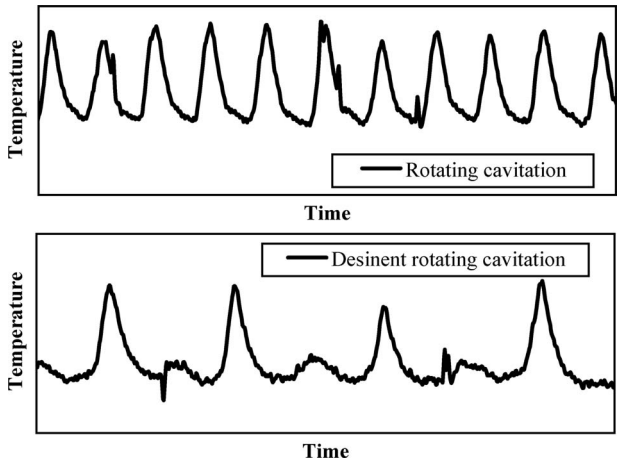

Fig. 15 Evolution of temperature oscillations near the desinence of rotating cavitation

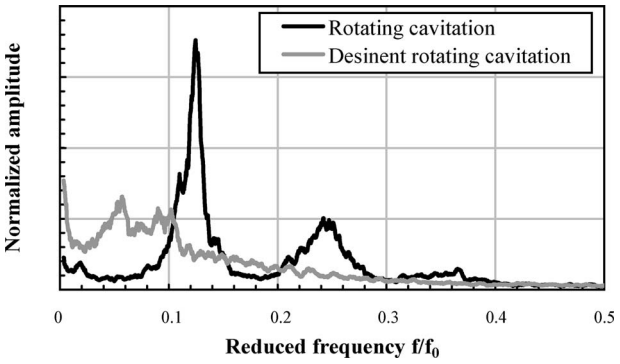

Fig. 16 Spectra of the signals presented in Fig. 15. Spectra have been smoothed and normalized so that the area under the spectra is unity.

This observation may contribute to explain the lock-in mechanism and the associated synchronization on the rotation frequency, which are responsible of the disappearance of the supersynchronous instability.

6 Conclusion

Several miniature thermocouples were mounted on the blades of an inducer in order to measure the temperature depression within leading edge cavities. Measurements were conducted using Refrigerant 114 as operating fluid, which is known to develop a significant thermodynamic effect contrary to cold water.

During a cavitation test, as the operating pressure is progressively reduced and the cavity becomes longer, temperature depression exhibits first a substantial raise when cavity closure goes over the thermocouple. Once the sensor tip is immersed in the cavity, the measured temperature remains almost constant. A drop in temperature depression is finally observed when vapor forms in the inlet pipe.

This drop in temperature depression, which depicts a sudden rise in cavity temperature, may be caused either by the enhancement of heat transfer by traveling bubbles growing in the inlet pipe or by the migration of bubbles from the liquid bulk into the cavity.

Comparison of temperature depression measured at different locations does not reveal significant variations of temperature inside leading edge cavities, except near closure.

In addition to time-averaged values, temperature fluctuations were analyzed. A number of temperature sensors displayed a noticeable increase in fluctuations when cavitation instabilities occur, especially the supersynchronous rotating cavitation instability.

A comparative spectral analysis of pressure and temperature fluctuations revealed that temperature sensors are actually able to detect the supersynchronous instability. The comparison requires taking into consideration that temperature measurements are relative to the rotating frame of reference whereas pressure measurements are relative to the fixed housing. When taking into account the corresponding shift in frequency given by the inducer rotation frequency, a fine correlation is observed between temperature and pressure spectra over the whole range in cavitation number when rotating cavitation prevails.

Temperature oscillations measured by sensors mounted on different blades have been compared under the rotating cavitation instability. Although amplitudes may differ significantly, the spectra obtained from different blades exhibit the same peak at a frequency corresponding to the supersynchronous instability. The determination of phase shifts confirms that the supersynchronous instability rotates in the same direction as the inducer rotation and that signals from consecutive blades are roughly in quadrature whereas signals from opposite blades are approximately opposite in phase.

It has been observed that, in the rotating frame of reference, the desinence of the supersynchronous instability is characterized by the extinction of one oscillation out of two. This phenomenon might contribute to explain the disappearance of the rotating cavitation regime and the lock-in mechanism, which appears when the supersynchronous frequency comes close to the rotation frequency.

Acknowledgment

This research was supported by CNES/SNECMA (Contract No. 2005-015-I).

Nomenclature

B = B-factor of Stepanoff $\Delta T/\Delta T^*$
$c_{p\ell}$ = liquid specific heat capacity
f = frequency
f_0 = inducer rotation frequency
L = latent heat of vaporization
Pr = Prandtl number
r = recovery factor
T_c = cavity temperature
T_w = wall temperature
T_∞ = liquid temperature at infinity
U_∞ = flow velocity
x = quality or vapor mass fraction
α = void fraction
ΔT = temperature drop in the leading edge cavity $T_\infty - T_c$
ΔT^* = characteristic temperature drop $\rho_v L/(\rho_\ell c_{p\ell})$
ρ_v = vapor density
ρ_ℓ = liquid density

References

[1] Hord, J., Anderson, L. M., and Hall, W. J., 1972, "Cavitation in Liquid Cryogens. I—Venturi," NASA Report No. CR-2054.
[2] Hord, J., 1972, "Cavitation in Liquid Cryogens. II—Hydrofoil," NASA Report No. CR-2156.
[3] Hord, J., 1973, "Cavitation in Liquid Cryogens. III—Ogives," NASA Report No. CR-2242.
[4] Hord, J., 1974, "Cavitation in Liquid Cryogens. IV—Combined Correlations for Venturi, Hydrofoil, Ogives and Pumps," NASA Report No. CR-2448.
[5] Billet, M. L., 1970, "Thermodynamic Effects on Developed Cavitation in Water and Freon 113," MS thesis, Pennsylvania State University, State College, PA.
[6] Holl, J. W., Billet, M. L., and Weir, D. S., 1975, "Thermodynamic Effects on Developed Cavitation," ASME J. Fluids Eng., **97**, pp. 507–514.
[7] Fruman, D. H., Reboud, J. L., and Stutz, B., 1999, "Estimation of Thermal Effects in Cavitation of Thermosensible Liquids," Int. J. Heat Mass Transfer, **42**, pp. 3195–3204.
[8] Belahadji, B., Franc, J. P., and Michel, J. M., 1997, "Analyse des effets thermiques en cavitation à partir d'essais au forane," Houille Blanche, N° 4/5–1997, pp. 117–122.
[9] Franc, J. P., Rebattet, C., and Coulon, A., 2004, "An Experimental Investigation of Thermal Effects in a Cavitating Inducer," ASME J. Fluids Eng., **126**, pp. 716–723.
[10] Franc, J. P., Boitel, G., Riondet, M., Janson, E., and Ramina, P., 2010, "Thermodynamic Effect on a Cavitating Inducer—Part I: Geometrical Similarity of Leading Edge Cavities and Cavitation Instabilities," ASME J. Fluids Eng., **132**, p. 021303.
[11] Yoshida, Y., Kikuta, K., Hasegawa, S., Shimagaki, M., and Tokumasu, T., 2007, "Thermodynamic Effect on a Cavitating Inducer in Liquid Nitrogen," ASME Trans. J. Fluids Eng., **129**, pp. 273–278.
[12] Eckert, E. R. G., and Drake, R. M., 1972, *Analysis of Heat and Mass Transfer*, McGraw-Hill, New York.

An Experimental Investigation for Bubble Rising in Non-Newtonian Fluids and Empirical Correlation of Drag Coefficient

Fan Wenyuan
Ma Youguang
Jiang Shaokun
Yang Ke

State Key Laboratory of Chemical Engineering,
School of Chemical Engineering and Technology,
Tianjin University,
Tianjin 300072, China

Li Huaizhi
Laboratoire des Sciences du Génie Chimique,
CNRS-ENSIC-INPL,
1 rue Grandville,
BP 451 54001 Nancy Cedex, France

The velocity, shape, and trajectory of the rising bubble in polyacrylamide (PAM) and carboxymethylcellulose (CMC) aqueous solutions were experimentally investigated using a set of homemade velocimeters and a video camera. The effects of gas the flowrate and solution concentration on the bubble terminal velocity were examined respectively. Results show that the terminal velocity of the bubble increases with the increase in the gas flowrate and the decrease in the solution concentration. The shape of the bubble is gradually flattened horizontally to an ellipsoid with the increase in the Reynolds number (Re), Eötvös number (Eo), and Morton number (Mo). With the increase in the Re and Eo, the rising bubble in PAM aqueous solutions begin to oscillate, but there is no oscillation phenomena for CMC aqueous solutions. By dimensional analysis, the drag coefficient of a single bubble in non-Newtonian fluids in a moderate Reynolds number was correlated as a function of Re, Eo, and Archimedes number (Ar) based on the equivalent bubble diameter. The predicted results by the present correlation agree well with the experimental data. [DOI: 10.1115/1.4000739]

Keywords: bubble, rising velocity, non-Newtonian fluid, drag coefficient, correlation

1 Introduction

The rising processes of bubbles in non-Newtonian fluids are frequently encountered in a wide variety of industrial fields such as chemical, biochemical, environmental, and food processes. Due to the inherent complexity of fluids, bubbles in non-Newtonian fluids behave in various rising velocities, shapes, and tracks under the common action of the different forces, which results in the marked influence on the contact time and contact area between two-phase gas-liquids so as to consequently lead mass, heat transfer, and chemical reactions between them. This makes the study of a single rising bubble as an essential base for better understanding of gas–liquid absorption processes with or without reactions, as well as providing important insights into the overall swarms of bubbles in non-Newtonian fluids.

A great deal of correlations for bubble rising velocity or drag coefficient in Newtonian fluids were reported in literature, but few were found for non-Newtonian fluids [1–9]. From a theoretical standpoint, since the fluid viscosity varies with shear rate, it is not possible to obtain a rigorous expression for a bubble rising freely in non-Newtonian fluids. In order to calculate the bubble terminal velocity in non-Newtonian fluids, it is necessary to know the relationship between the drag coefficient of the bubble and the correlative numbers (e.g., Re). A typical approach on the calculation of gas bubble flow velocity is based on empirical correlations or a classical concept of drag coefficient; a detailed analysis on gas bubble flow in non-Newtonian liquids in a broad range of Reynolds numbers were given in Refs. [10–16]. Chhabra [17] correlated the drag coefficient in shear thinning power law fluids by introducing the function of multinomial of index of power-law fluid. Taking into account the deformation of bubbles in various fluids, Dewsbury [18] and Margaritis [19] studied the drag coefficient variation for bubbles over a wide range of Reynolds numbers in different non-Newtonian fluids, and proposed universally applicable drag correlations by combining the Hadamard–Rybczynski equation and the equation of Turton and Levenspiel [20], which was originally proposed for solid particles in Newtonian fluids. Tzounakos et al. [21] studied the effect of surfactant concentration on the rise of gas bubbles in power law liquids and showed that the transition from a bubble with an immobile surface to a bubble with a mobile one is a function of the surfactant concentration, Reynolds number, and rheological properties of liquid. Rodrigue [22] collected a lot of the literature data and extended his previous model [23] for predicting the rise velocity of gas bubbles in Newtonian liquids to those in power law liquids. Recently, Zhang et al. [24] proposed an empirical correlation to predict drag coefficient for both accelerate motion and steady motion.

Despite remarkable progresses in the investigation of bubble rising [25], the properties of fluids, as well as bubble characteristics, were not considered fully in most of the literature on bubble drag correlation, and only limited theoretical information is available on the behavior of single bubbles in non-Newtonian fluids, especially at intermediate Reynolds numbers. In this work, by considering compositive parameters, including density, surface tension, and rheological properties of fluids, as well as velocity, size, and aspect ratio of bubble, a correlation for the drag coefficient of single bubbles moving steadily through a stagnant non-Newtonian power law liquid was proposed in virtue of the dimensional analysis. The new correlation was in good agreement with the experimental data compared with previous ones under considered experimental conditions.

2 Experimental

2.1 Apparatus. The experimental facility for measuring the velocity of bubbles in non-Newtonian fluids was sketched in Fig. 1 and included two parts: bubble generation system and velocity measurement system. Bubble generation system was mainly made of a Plexiglas square measuring tank $15.00 \times 15.00 \times 120.00$ cm^3, in which the wall effect on the shape and size of

Contributed by the Fluids Engineering Division of ASME for publication in the JOURNAL OF FLUIDS ENGINEERING. Manuscript received April 22, 2009; final manuscript received November 8, 2009; published online February 17, 2010. Assoc. Editor: Theodore Heindel.

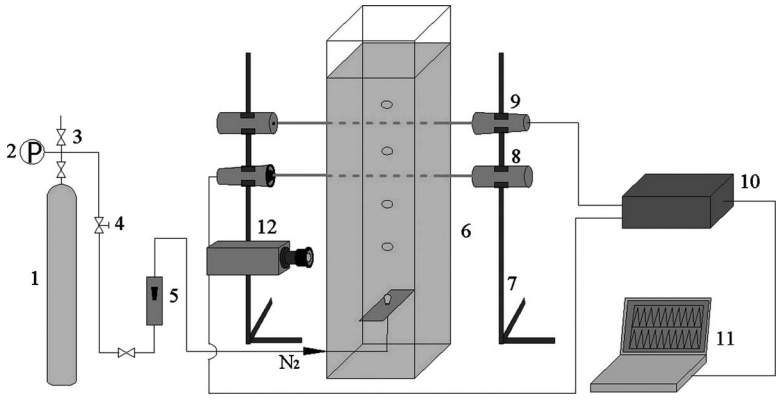

Fig. 1 Schematic diagram of the experiment system: 1—compressed nitrogen cylinder; 2—manometer; 3—valves; 4—pressure maintaining valve; 5—rotameter; 6—Plexiglass square tank; 7—tripod; 8—lasers; 9—photodiodes; 10—sampling detector; 11—computer; and 12—CCD camera

the bubble could be neglected. The test section ($15.00 \times 5.00 \times 1.00$ cm^3) with a polished orifice (diameter: 1.0 mm, 1.6 mm, or 2.4 mm) at its center also made of Plexiglas and polished well to eliminate optical distortion was placed in the middle of the tank's inner section, in parallel with the bottom of the tank, and 10.00 cm above. Stainless pipes with inner diameter of 2.0 mm were applied to the jointed Nitrogen cylinder, rotameter, and orifice. Considering the range of pressure inside the bubble, Nitrogen pressure was maintained at little more than 0.10 MPa by adjusting the decompression valve, thus, the gas flowrate could be showed accurately by the rotameter calibrated (within ± 0.01 cm^3/s). Nitrogen bubbles were always generated steadily from the submerged orifices by adjusting the gas flowrate properly.

The velocity measurement system included twin He-Ne laser beams and twin photodiodes. The Plexiglas square tank was illuminated by two horizontal and parallel laser beams, passing through the axis of the tank. The vertical distance between the beams was 20.00 ± 0.05 mm, and the laser was adjusted to focus a very fine laser beam with less than 1.00 ± 0.05 mm in diameter. Two photodiodes on either side of the tank intercepted the light beams from the lasers. Simultaneously, a digital sampling detector translated the real time signal of the passing time of the bubble and display in the computer. Especially, the bubble could not pass through the light beams sometimes when the bubbles begin to oscillate along a zigzag path in PAM aqueous solutions in high Re and Eo numbers. However, the rising bubbles will periodically pass through the beams due to the quick oscillation of trajectory; in that case, repeatable measurements was used to improve the quality of data. According to the time interval and vertical distance between the beams, the rising velocity of a single bubble could be attained with

$$u_B = \frac{\Delta z}{\Delta t} \tag{1}$$

where u_B is the mean velocity of the bubble rising in the fluid and Δz and Δt are the vertical distance and time interval of the bubble passing through dual beams, respectively. In addition, the instantaneous shape of the rising bubble in the fluid column was correspondingly recorded from one side of the test section with a digital camera. The bubble's shape and rising trajectory were then analyzed from a selected sequence of images.

2.2 Apparatus Calibration. In order to examine the reliability of the apparatus, 93% glycerin aqueous solution was used as a typical Newtonian fluid. A typical plot of the bubble velocity trend as a function of the distance from the generation point is shown in Fig. 2. From this figure, the average rising terminal velocity of a single bubble was calculated as follows. The initial 1/3 (about 37 cm) of the path was not considered. The average terminal velocity can be obtained by linearly fitting the curve of the last part of the path, in which the bubble attains a constant velocity. During the calibration, the orifice with a diameter of 1.0 mm was used, and a corresponding gas flowrate was adjusted to generate the same volume of bubbles as in Ref. [26]. It is clear that the measured velocity agrees with Raymond's results [26] very well. The results of the calibration ensure that the apparatus measures the bubble terminal velocity with high accuracy.

2.3 Experimental Conditions and Uncertainty. PAM (AR; MW:3×10^6; Sinopharm Chemical Reagent Co. (Shanghai, China)), CMC (AR; MW:5×10^6; Tianjin Kermel Chemical Reagent Co. (Tianjin, China)), glycerin (AR; Tianjin Reagent Chemicals Co. (Tianjin, China)), and distilled water were used in the experiments. Glycerin, PAM, and CMC aqueous solutions are under various conditions as follows: mass concentrations of glycerin aqueous solution: 93%; PAM aqueous solution: 0.60%, 0.80%, and 1.0%; CMC aqueous solution: 0.35%, 0.50%, and 0.70%; orifice diameter: 1.0 mm, 1.6 mm, and 2.4 mm, gas flowrate: 0.20 cm^3/s, 0.50 cm^3/s, and 0.80 cm^3/s. The range ($10-100$ s^{-1}) of shear rate of the bubble rising can be estimated

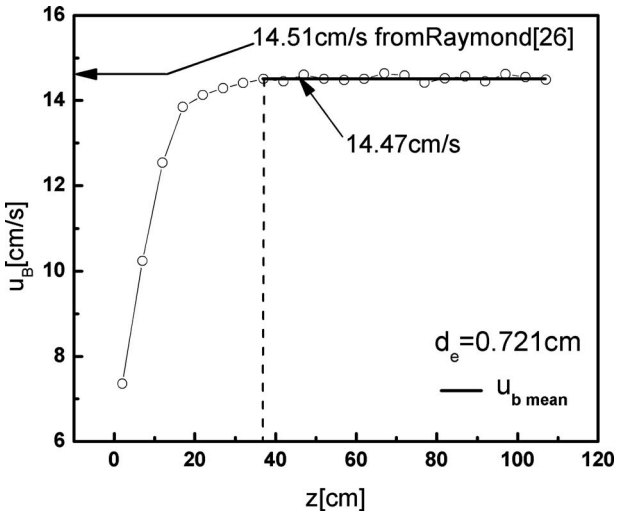

Fig. 2 Calibration curve of bubble terminal velocity in 93% Glycerin solution (uncertainty of data: ±2.1%)

Table 1 Physical properties of the solution

Fluid	Density	Surface tension	Consistency	Flow index
0.60%PAM	1.001 ± 1	72 ± 1	105	0.62
0.80%PAM	1.003 ± 1	71 ± 1	177	0.58
1.0%PAM	1.004 ± 1	69 ± 1	225	0.56
0.35%CMC	1.003 ± 1	70 ± 1	21	0.94
0.50%CMC	1.007 ± 1	69 ± 1	48	0.92
0.70%CMC	1.010 ± 1	68 ± 1	113	0.91
0.93%GL	1.230 ± 1	63 ± 1	240	1.0

by following Eq. (6), and then the rheological characteristics of PAM and CMC aqueous solutions were measured with the rheometer of StressTech (REOLOGICA Instruments AB, Sweden) for shear rates ranging from $1-300\ s^{-1}$. Power-law indices were determined by fitting the shear stress and shear rate data. The confidence interval for the best-fit curves used to determine the power law index was 95%.

Surface tensions were measured using a dynamic surface tension apparatus (DCAT21, dataphysics, Germany), which had an accuracy of 0.001 N/m. Liquid densities were determined by weighing a known volume of the fluid on an analytical balance (resolution 0.001 g). Liquid physical properties are summarized in Table 1. All experiments and physical property measurements were performed at 293.1 ± 0.1 K.

Uncertainty in the experimental results of velocity can be expressed in terms of the uncertainty in the measured parameters by propagating uncertainties through

$$\frac{U_{u_B}}{u_B} = \sqrt{\left(\frac{U_{\Delta z}}{\Delta z}\right)^2 + \left(\frac{U_{\Delta t}}{\Delta t}\right)^2} \tag{2}$$

where $U_{\Delta z}$ and $U_{\Delta t}$ are the uncertainties in determining Δz and Δt, respectively. $U_{\Delta z}$ and $U_{\Delta t}$ arise from (i) uncertainty in digitally processing the resolution, which is defined by the smallest measurable units (0.005 cm and 0.005 s), and (ii) uncertainty in repeatability of experimental data, which is obtained by computing the sample standard deviation. $U_{\Delta z}$ and $U_{\Delta t}$ are obtained by doubling the rsm of (i) and (ii) uncertainties for 95% confidence. Finally, the uncertainty in the bubble velocity is below 2.3% in a glycerin aqueous solution, and ranges from 1.8% to 5.1% in a CMC aqueous solution, but from 2.7% to 6.6% in a PAM aqueous solution because of the oscillation during bubble rising process.

3 Results and Discussion

3.1 Frequency of Bubble Formation. It is well-known that the frequency of the bubble formation has an important effect on the rise terminal velocity of bubbles in fluids. In order to relate the generation frequency with the bubble equivalent diameter and rise velocity, the Strouhal number $\mathrm{St}(=d_e f/u_B)$ was employed here. By using shift factors, the experimental data at various concentrations of PAM and CMC solutions were shifted for constructing the master curve of shifted C_D, based on 1.0% PAM, as shown in Fig. 3. From this figure, it can be seen that the present experimental data agree well with the above equation of the master curve. This implies that the frequency of the bubble formation can roughly be predicted if the size and rise velocity of bubbles are given. It is noteworthy that there is a slight interaction between two bubbles because the distance between neighboring bubbles is seven times larger than the bubble diameter, even for the highest gas flowrate [6].

3.2 Bubble Shape and Rising Trajectory. The Bubble's shape always lies on the physical properties (density, surface tension, and viscosity) of two-phase gas-liquids, bubble size, and its rising velocity. On the basis of the dimensionless treatment, Grace [27] proposed the famous map of the bubble shape shown in Fig. 4, in which the shape of the bubbles was divided into three categories: spherical, ellipsoidal, and spherical cap, according to Reynolds, Eötvös, and Morton numbers. The variation in the terminal shape of the rising bubble with a wide range of bubble sizes from 3 mm to 10 mm under the experimental condition depends on the ellipsoidal area, as shown in Fig. 4. Obviously, the bubble's shape in PAM aqueous solutions differs much from that in CMC aqueous solutions. In PAM aqueous solutions, bubbles are elongated vertically and have a teardrop shape in small Re, Eo, and Mo numbers, and with further increase in Re, Eo, and Mo numbers, bubbles take the flattened shape with always a tail behind the bubble shown as in Figs. 4(*b*)–4(*d*). But the bubble's shape in CMC aqueous solutions always present an ellipsoidal shape with the same trend flatted of that in PAM aqueous solutions as in Figs. 4(*a*), 4(*e*), and 4(*f*).

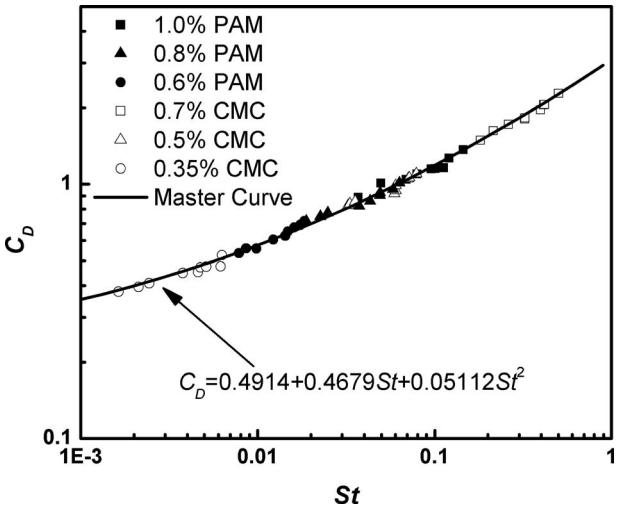

Fig. 3 Master curve of shifted C_D based on 1.0% PAM (uncertainty of data: ±8.6%)

Considering spherical or ellipsoidal bubbles in the present experiments, the aspect ratio E (defined as the ratio between equiva-

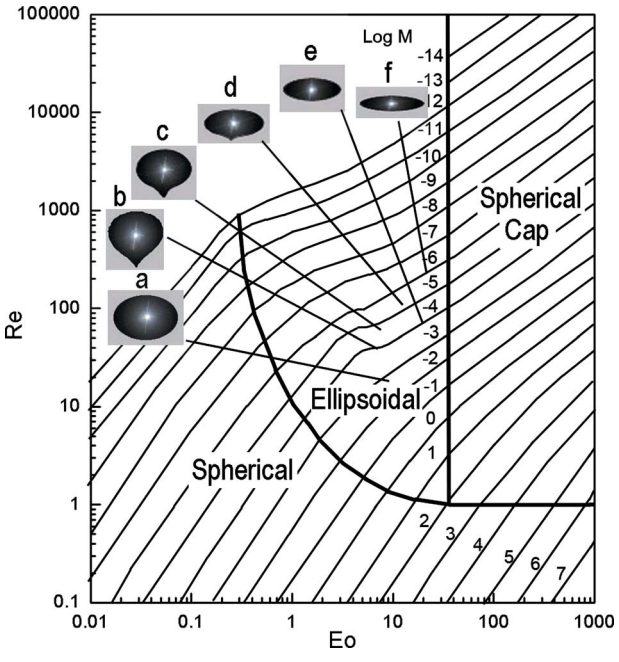

Fig. 4 Bubble shape in different non-Newtonian fluids in the diagram of Grace [27]: (*a*) 0.70%CMC, (*b*) 1.0%PAM, (*c*) 0.8%PAM, (*d*) 0.6%PAM, (*e*) 0.50%CMC, and (*f*) 0.35%CMC

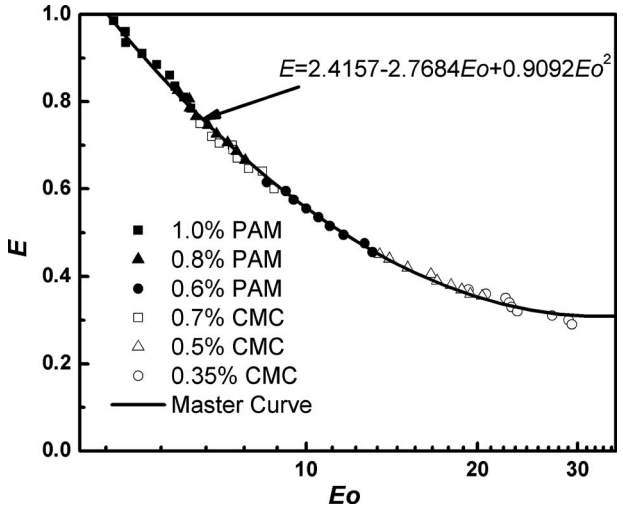

Fig. 5 Master curve with shifted *E* based on 1.0% PAM (uncertainty of data: ±6.9%)

lent diameter and max horizontal diameter of bubble) is used to characterize the bubble shape. Since the buoyancy and surface tension plays an important role in determining the bubble shape, E is plotted against the Eo in Fig. 5, and the solid lines represent the master curve based on 1.0% PAM. As indicated in the figure, E gradually decreases with the increase in Eo, and E also depends on the kind of non-Newtonian fluids. In 1.0%PAM solution, the bubble shape changes clearly from spheroid to ellipsoid when Eo increases, and in other solutions, the flatness of the ellipsoidal bubble becomes almost linear as a function of Eo. This implies that the bubble shape is governed mainly by physical properties of fluids within the considered experimental range.

In a bubble swarm, the trajectories are strongly dominated by the surrounding liquid flow, and the associated dynamics is more complex. It can be seen clearly from Figs. 6(*a*)–6(*c*) that rising

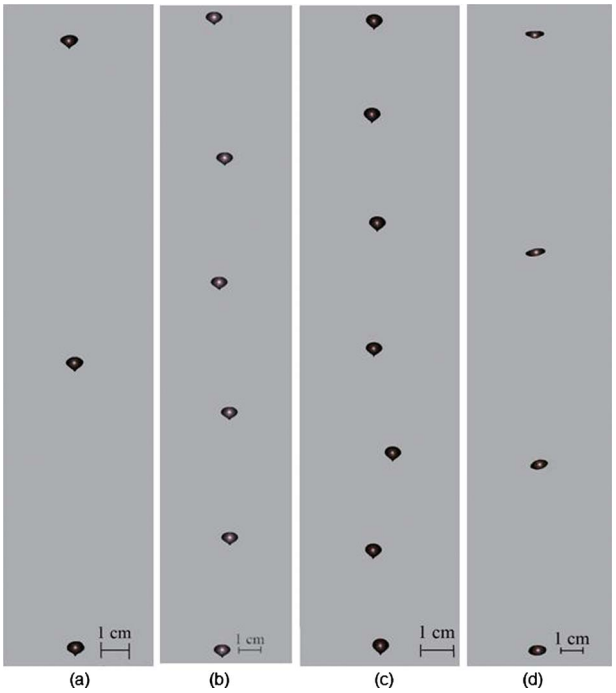

Fig. 6 Instantaneous images of bubble rising: (*a*) 0.8%PAM, Re=43, Eo=5.0; (*b*) 0.8%PAM, Re=52, Eo=5.5; (*c*) 0.8%PAM, Re=61, Eo=5.8; and (*d*) 0.35%CMC, Re=172, Eo=4.5

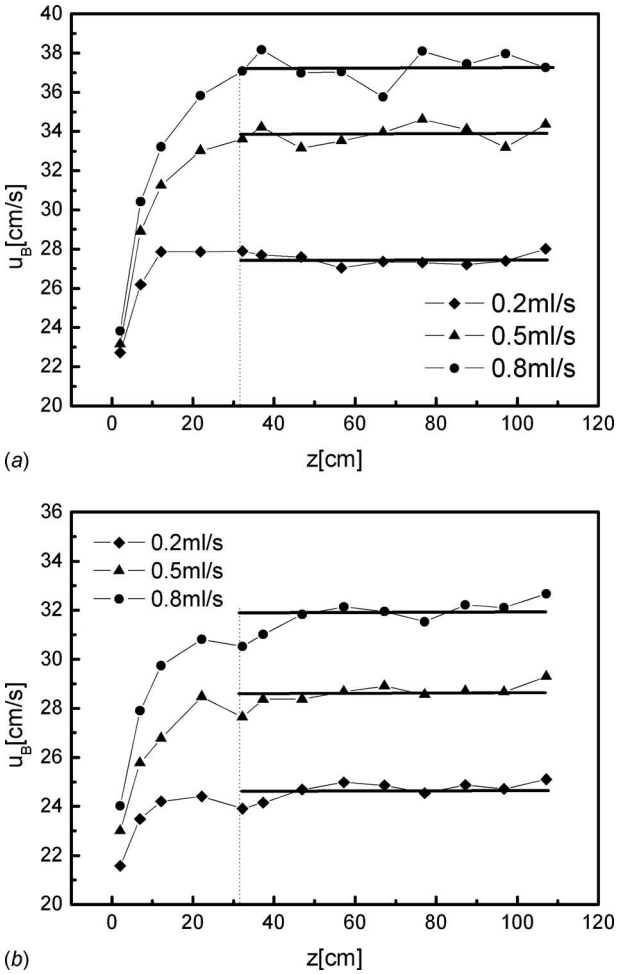

Fig. 7 Effect of gas flow rate on bubble terminal velocity: (*a*) 0.6%PAM, *d*=1.6 mm (uncertainty of data: ±5.4%); and (*b*) 0.5%CMC *d*=1 m (uncertainty of data: ±4.0%)

bubbles begin to oscillate along a zigzag path in PAM aqueous solutions with the increase in Re and Eo numbers. Distinguishingly, the rectilineal rise is always found for the CMC aqueous solution, as shown in Fig. 6(*d*). By using PIV and a classical birefringence visualization, Funfschilling and Li [28] found the coexistence of three distinct zones around bubbles rising in PAM solutions: a central downward flow behind the bubble (negative wake), a conical upward flow surrounding the negative wake zone, and an upward flow zone in front of the bubble. The residual stresses are generated by the shear between the negative wake and the conical upward flow so the trailing bubble can easily enter in the field of dominant residual stresses behind the leading bubble. The peculiar features mentioned above lead to the difference of the bubble trajectory in PAM solutions and CMC solutions.

3.3 Effect of Different Conditions on Bubble Rising Terminal Velocity

3.3.1 Gas Flow Rate. Figure 7 shows the effect of the gas flow rate on the bubble rising terminal velocity in PAM and CMC aqueous solutions. It is obviously seen that the bubble velocity gradually increases with the height of the column, levels off, and finally reaches a near constant terminal velocity. The terminal velocity increases with the gas flowrate in both PAM and CMC aqueous solutions. This could be explained from following three aspects: (1) The rise of gas flow rate results in the increase in generation frequency of bubble from the orifice, which tends to the reduce of apparent viscosity in the passage of bubble, thus, the terminal velocity rises with the fall of the viscous drag force of the

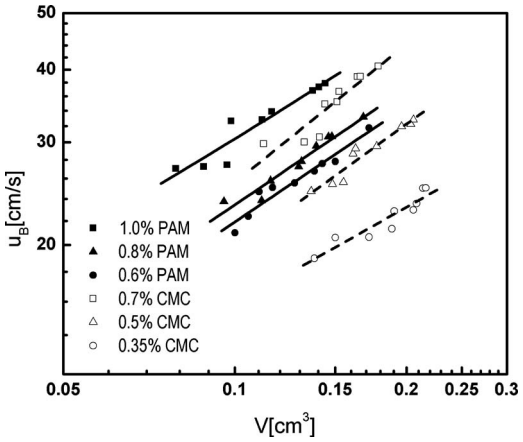

Fig. 8 Effect of bubble volume on bubble terminal velocity (uncertainty of data: ±7.8%)

fluid around the bubble. (2) From the results of the bubble formation, accretion of the gas flow rate brings to larger detachment volumes of bubbles, which almost linearly relates to the terminal velocity of the bubble, as shown in Fig. 8. (3) The relaxation of stresses induced by the memory effect of fluids may be considered as the important reason. In fact, a local deformation caused by bubble passage can lead to local stresses. The relaxation time of these stresses is determined by the rheological characteristics of the fluids. However, the accumulation of residual stress happens when the bubble's injection period T (interval between successive bubbles) is less than the relaxation time. Finally, the accumulation of residual stress increases with the decrease in T caused by high gas flowrate. The increase in residual stress leads to the decrease in local drag forces, causing the increase in the bubble rise velocity.

3.3.2 Solution Concentration. Bubble rising velocity varies with the height of the column under the condition of diverse solution concentration, as shown in Fig. 9. It can be found obviously that the bubble terminal velocity gradually decreases with increasing the solution concentration. This could be attributed to the physical properties of the PAM and CMC aqueous solutions, especially to the viscosity of the solutions. The larger viscous forces in high solution concentration reduce the possibility of the interfacial motion, which leads to the fall of the bubble terminal velocity [29].

3.4 Dimensional Analysis and Correlation of Drag Coefficient. The behavior of bubble rising in fluids is dominated mainly by several parameters like bubble size, bubble velocity, density, viscosity, and surface tension of gas-liquid systems. The conventional approach for correlating the drag coefficient is to obtain an equation between the drag coefficient and the Reynolds number based on these parameters.

The empirical analytical process used to develop the dimensionless corrections to predict drag coefficient C_D in non-Newtonian fluids is based on the Buckingham Pi theorem. The utilization of the Buckingham Pi theorem enables the important dimensionless parameters to be developed quickly and easily by describing the relation between a function to be predicted and a related function expressed in terms of dimensionless parameters. Due to $\rho_g \ll \rho_l$ and $\mu_g \ll \mu_l$, a general function of drag coefficient C_D can be expressed mathematically as relevant physical parameters and bubble characteristics

$$C_D = f[\rho_l, \mu_l(K,n), \sigma, d_e, g, u_B] \tag{3}$$

where ρ_l, μ_l, σ, d_e, g, and u_B are the density, fluids viscosity, surface tension of fluids, equivalent diameter of bubble, acceleration of gravity, and the velocity of bubble, respectively.

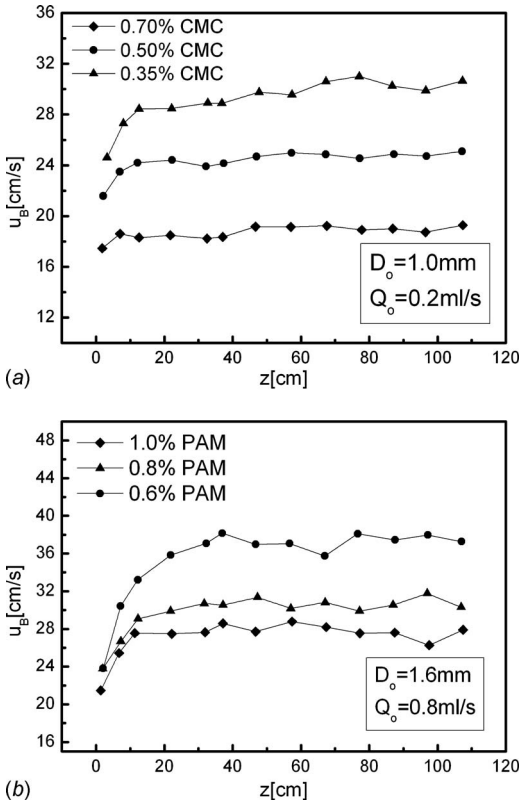

Fig. 9 Effect of solution concentration on bubble terminal velocity (uncertainty of data: (*a*) ±4.6% and (*b*) ±6.5%)

Finally, the application of the Buckingham Pi theorem of the dimensional analysis to the present case gives the following expression of C_D:

$$C_D = A\left(\frac{\rho_l d_e u_B}{\mu_l}\right)^B \left(\frac{\rho_l^2 g d_e^3}{\mu_l^2}\right)^C \left(\frac{\rho_l g d_e^2}{\sigma}\right)^D \tag{4}$$

In this paper, according to the intermediate region of shear rate, the power law model was used to describe the rheology of fluids, and thus

$$\mu_l(K,n) = K(\dot{\gamma})^{n-1} \tag{5}$$

Due to the difficulty of experimental measurement for the shear rates of bubble rising in power law fluids, it was obtained by calculating approximatively (u_B/d_e) in many literatures [30,31]. In this work, considering nonspherical characteristics of bubble, the shear rate of deformed bubbles in fluids could be expressed as follows:

$$\dot{\gamma} = \frac{u_B}{d_e E} \tag{6}$$

where $d_e = (6Q_o/f\pi)^{1/3}$ and the aspect ratio describing the nonsphericity of the bubble could be calculated by the formula $E = d_v/d_e$ (d_v is the vertical bubble diameter).

In fact, for non-Newtonian power law fluids, Reynolds, Archimedes, Eötvös numbers, and drag coefficients are respectively expressed as follows:

$$\mathrm{Re} = \frac{\rho_l d_e^n u_B^{2-n}}{K E^{1-n}} \tag{7a}$$

$$\mathrm{Ar} = \frac{\rho_l^2 g d_e^{2n+1} u_B^{2-2n}}{K^2 E^{2-2n}} \tag{7b}$$

Table 2 The constants in dimensionless correlations of C_D

Constant	A	B	C	D
Value	2.173	−1.57	0.683	−0.0931

$$\mathrm{Eo} = \frac{\rho_l g d_e^2}{\sigma} \tag{7c}$$

$$C_D = \frac{4 g d_e}{3 u_B^2 E^2} \tag{7d}$$

Therefore, Eq. (6) could be rewritten in the form

$$C_D = A\ \mathrm{Re}^B\ \mathrm{Ar}^C \mathrm{Eo}^D \tag{8}$$

Constants A, B, C, and D in Eq. (6) were obtained by fitting experimental data using the least square method, and the result is shown in Table 2.

As a result, a new correlation of drag coefficient for a bubble rising steadily in non-Newtonian fluids is obtained

$$C_D = 2.173\ \mathrm{Re}^{-1.57}\ \mathrm{Ar}^{0.683}\ \mathrm{Eo}^{-0.0931} \tag{9}$$

The validity of Eq. (9) to a single bubble in non-Netonian fluids is shown by plotting $C_D/\mathrm{Ar}^{0.683}\mathrm{Eo}^{-0.0931}$ of various systems against Re in Fig. 10. The average relative error between the predicted and measured values is below 3%.

Previously, Dewsbury et al. [18] proposed a correlation of a drag coefficient in a wide range of Reynolds numbers while rising steadily through various non-Newtonian fluids as in Eq. (10). Recently, Zhang et al. [24] considered both added mass force and history force and developed a correlation for the drag coefficient of a bubble in accelerating and steady rise as in Eq. (11)

$$C_D = \frac{16}{\mathrm{Re}}(1 + 0.173\ \mathrm{Re}^{0.657}) + \frac{0.413}{1 + 16300\ \mathrm{Re}^{-1.09}} \tag{10}$$

$$C_D = \frac{16}{\mathrm{Re}_M}(1 + 0.12\ \mathrm{Re}_M^{0.6})(1 + 0.196\ \mathrm{Ac}^{0.767}\ \mathrm{Ar}^{0.381}) \tag{11}$$

The comparison between Eqs. (9)–(11) was depicted in Fig. 11 for the range of $13 < \mathrm{Re} < 230$. It can be seen that the predictions from both Eqs. (9) and (10) are in good agreement with the experimental data for $\mathrm{Re} < 30$, and the predicted value by Eqs. (10) and (11) is respectively higher and lower than that calculated in Eq. (9). The difference of the one predicted by Eqs. (9) and (10) or Eq. (11) increases with Re. The results showed that the present model agrees better than Eqs. (10) and (11) with the experimental data in this work.

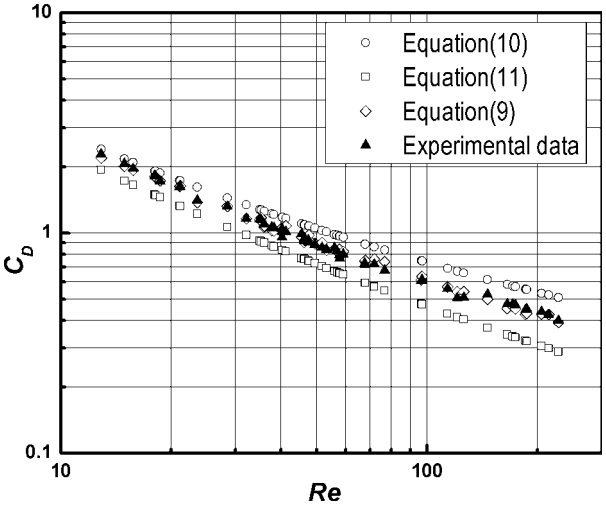

Fig. 11 Comparison between measured and predicted C_D

In addition, present correlation was also used to predict the drag coefficient for the bubble rising in 93% glycerin solution. The comparison between the measured and calculated results is shown in Fig. 12, and results show that the predicted values agree well with the experimental data within the experimental range.

4 Conclusion

The velocity, shape, and rising trajectory of a single bubble rising in a quiescent non-Newtonian fluid were investigated experimentally. Bubble shapes are dominated by the Re, Eo, and Mo numbers, and the bubble with the tear drop shape in the PAM solution and ellipsoidal shape in the CMC solution are gradually flatted horizontally with the increase in the Re, Eo, and Mo. Based on the dimensional analysis, a new correlation was developed to predict the drag coefficient of bubbles in non-Newtonian fluids within the range of $13 < \mathrm{Re} < 230$, $283 < \mathrm{Ar} < 1618$, and $3.2 < \mathrm{Eo} < 9.7$; the present model agrees better than the previous ones with the experimental data in this paper.

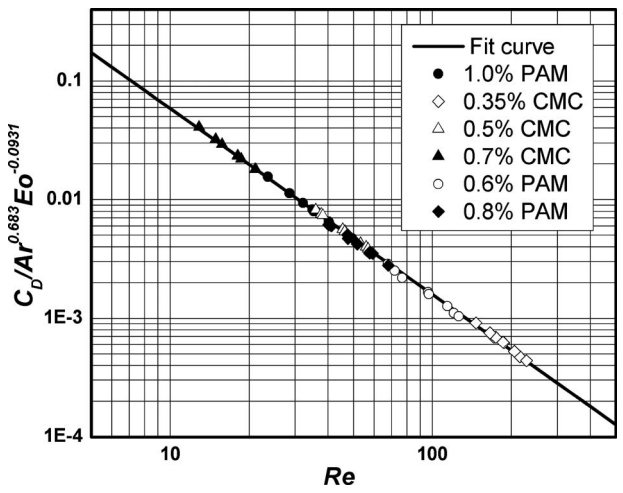

Fig. 10 Relationship between $C_D/\mathrm{Ar}^{0.683}\ \mathrm{Eo}^{-0.0931}$ and Re

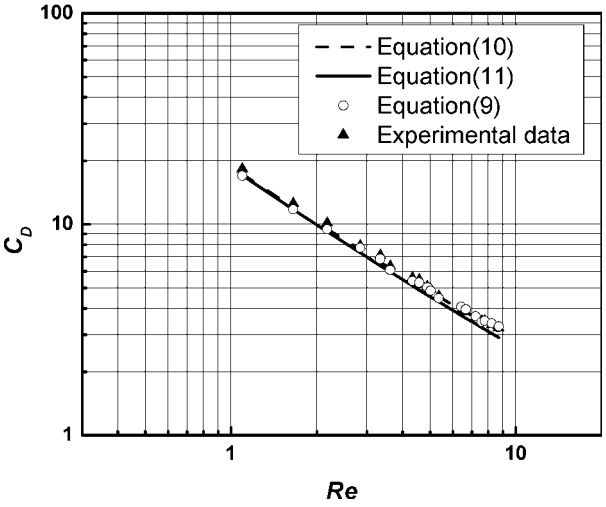

Fig. 12 Validity on present model in 93% glycerin solution

Acknowledgment

Authors wish express their appreciation for the financial support by the National Natural Science Foundation of China (Grant No. 20476073), the aid of State Key Laboratory of Chemical Engineering (Grant No. SKL-ChE-08B03), and the Programme of Introducing Talents of Discipline to Universities (Grant No. B06006).

Nomenclature

a = bubble acceleration (m/s)
A = parameter in Eq. (4)
Ac = acceleration number in Eq. (11), $\mathrm{Ac}=d_e a/u_b^2$
Ar = Archimedes number
B = parameter in Eq. (4)
C = parameter in Eq. (4)
D = parameter in Eq. (4)
E = bubble aspect ratio
C_D = drag coefficient
d_e = equivalent bubble diameter (cm)
d_v = vertical bubble diameter (cm)
Eo = Eötvös number
f = bubble frequency (s^{-1})
g = gravitational acceleration (m/s^2)
K = consistency in power law model in Eq. (5) (Pa s^n)
Mo = Morton number
n = index in power law model in Eq. (5)
Q_O = volume flow rate (cm^3/s)
Re = Reynolds number based on power law model
Re_M = Reynolds number based on Carreau model
u_b = bubble local velocity (cm/s)
u_B = bubble rise velocity (cm/s)
V = bubble volume (cm^3)

Greek Symbols

$\dot{\gamma}$ = shear rate (s^{-1})
μ_g = gas viscosity (kg/s^2 m)
μ_l = liquids viscosity (kg/s^2 m)
ρ_g = gas density (g/cm^3)
ρ_l = liquid density (g/cm^3)
σ = surface tension (mN/m)

References

[1] Abou-El-Hassan, M. E., 1986, "Correlations for Bubble Rise in Gas-Liquid Systems," *Encyclopedia of Fluid Mechanics*, N. P. Cheremisinoff, ed., Gulf, Houston, pp. 110–120.
[2] Clift, R., Grace, J. R., and Weber, M. E., 1978, *Bubbles, Drops and Particles*, Academic, New York.
[3] Miyahara, T., and Takahashi, T., 1985, "Drag Coefficient of a Single Bubble Rising Through a Quiescent Liquid," Chem. Eng. Res. Des., **25**(1), pp. 146–148.
[4] Moore, D. W., 1959, "The Rise of a Gas Bubble in a Viscous Liquids," J. Fluid Mech., **6**, pp. 113–130.
[5] Celata, G. P., Cumo, M., D'Annibale, F., Di Marco, P., Tomiyama, A., and Zovini, C., 2006, "Effect of Gas Injection Mode and Purity of Liquid on Bubble Rising in Two-Component Systems," Exp. Therm. Fluid Sci., **31**(1), pp. 37–53.
[6] Zhang, J., and Fan, L. S., 2003, "On the Rise Velocity of an Interactive Bubble in Liquids," Chem. Eng. J., **92**(1–3), pp. 169–176.
[7] Zhang, L., Yang, C., and Mao, Z. S., 2008, "Unsteady Motion of a Single Bubble in Highly Viscous Liquid and Empirical Correlation of Drag Coefficient," Chem. Eng. Sci., **63**(8), pp. 2099–2106.
[8] Hua, J., and Lou, J., 2007, "Numerical Simulation of Bubble Rising in Viscous Liquid," J. Comput. Phys., **222**(2), pp. 769–795.
[9] Liu, Z. L., and Zheng, Y., 2006, "PIV Study of Bubble Rising Behavior," Powder Technol., **168**(1), pp. 10–20.
[10] Hirose, T., and Moo-Young, M., 1969, "Bubble Drag and Mass Transfer in Non-Newtonian Fluids: Creeping Flow With Power-Law Fluids," Can. J. Chem. Eng., **47**, pp. 265–267.
[11] Macedo, I. C., and Yang, W. J., 1974, "The Drag of Air Bubbles Rising in Non-Newtonian Fluids," Jpn. J. Appl. Phys., **13**, pp. 529–533.
[12] Acharya, A., Mashelkar, R. A., and Ulbrecht, J., 1977, "Mechanics of Bubble Motion and Deformation in Non-Newtonian Media," Chem. Eng. Sci., **32**, pp. 863–872.
[13] Yamanaka, A., and Mitsuishi, N., 1977, "Drag Coefficient of a Moving Bubble and Droplet in Viscoelastic Fluids," J. Chem. Eng. Jpn., **10**, pp. 370–374.
[14] Bhavaraju, S. M., Mashelkar, R. A., and Blanch, H. W., 1978, "Bubble Motion and Mass Transfer in Non-Newtonian Fluids: Part I—Single Bubble in Power Law and Bingham Fluids," AIChE J., **24**, pp. 1063–1070.
[15] Tsukada, T., Mikami, H., and Hozawa, M., 1990, "Theoretical and Experimental Studies of the Deformation of Bubbles Moving in Quiescent Newtonian and Non-Newtonian Liquids," J. Chem. Eng. Jpn., **23**, pp. 192–198.
[16] Chhabra, R. P., 1993, *Bubbles, Drops and Particles in Non-Newtonian Fluids*, CRC, Boca Raton, FL.
[17] Chhabra, R. P., 1988, "Hydrodynamics of Bubbles and Drops in Rheologically Complex Fluids," *Encyclopedia of Fluid Mechanics*, N. P. Cheremisinoff, ed., Gulf, Houston, pp. 253–286.
[18] Dewsbury, K., Karamanev, D., and Margaritis, A., 1999, "Hydrodynamic Characteristics of Free Rise of Light Solid Particles and Gas Bubbles in Non-Newtonian Liquids," Chem. Eng. Sci., **54**(21), pp. 4825–4830.
[19] Margaritis, A., Te Bokkel, D. W., and Karamanev, D. G., 1999, "Bubble Rise Velocities and Drag Coefficients in Non-Newtonian Polysaccharide Solutions," Biotechnol. Bioeng., **64**(3), pp. 257–266.
[20] Turton, R., and Levenspiel, O., 1986, "A Short Note on the Drag Correlation for Spheres," Powder Technol., **47**, pp. 83–86.
[21] Tzounakos, A., Karamanev, D. G., Margaritis, A., and Bergougnow, M., 2004, "Effect of the Surfactant Concentration on the Rise of Gas Bubbles in Power Law Non-Newtonian Liquids," Ind. Eng. Chem. Res., **43**, pp. 5790–5795.
[22] Rodrigue, D., 2002, "A Simple Correlation for Gas Bubbles Rising in Power-Law Fluids," Can. J. Chem. Eng., **80**, pp. 289–292.
[23] Rodrigue, D., 2004, "A General Correlation for the Rise Velocity of Single Gas Bubble," Can. J. Chem. Eng., **82**(2), pp. 382–386.
[24] Zhang, L., Yang, C., and Mao, Z. S., 2008, "An Empirical Correlation of Drag Coefficient for a Single Bubble Rising in Non-Newtonian Liquids," Ind. Eng. Chem. Res., **47**, pp. 9767–9772.
[25] Kulkarni, A. A., and Joshi, J. B., 2005, "Bubble Formation and Bubble Rise Velocity in Gas-Liquid Systems: A Review," Ind. Eng. Chem. Res., **44**, pp. 5873–5931.
[26] Raymond, F., and Rosant, J. M., 2000, "A Numerical and Experimental Study of the Terminal Velocity and Shape of Bubbles in Viscous Liquids," Chem. Eng. Sci., **55**(5), pp. 943–955.
[27] Grace, J. R., 1973, "Shapes and Velocities of Bubbles Rising in Infinite Liquids," Trans. Inst. Chem. Eng., **51**(1), pp. 116–120.
[28] Funfschilling, D., and Li, H. Z., 2001, "Flow of Non-Newtonian Fluids Around Bubbles: PIV Measurement and Birefringence Visualisation," Chem. Eng. Sci., **56**(3), pp. 1137–1141.
[29] Rodrigue, D., De Kee, D., and Chan Man Fong, C. F., 1996, "An Experimental Study of the Effect of Surfactants on the Free Rise Velocity of Gas Bubbles," J. Non-Newtonian Fluid Mech., **66**(2–3), pp. 213–232.
[30] Chhabra, R. P., 1986, "Steady Non-Newtonian Flow About a Rigid Sphere," *Encyclopedia of Fluid Mechanics*, N. P. Cheremisinoff, ed., Gulf, Houston, pp. 983–1023.
[31] Li, H. Z., Mouline, Y., Choplin, L., and Midoux, N., 1997, "Rheological Simulation of In-Line Bubble Interactions," AIChE J., **43**, pp. 265–267.